AWARD NUMBER: W81XWH-19-1-0759

TITLE: **Neural Mechanisms of Neuropsychiatric Lupus**

PRINCIPAL INVESTIGATOR: Patricio Huerta

CONTRACTING ORGANIZATION: Feinstein Institutes for Medical Research

REPORT DATE: JANUARY 2023

TYPE OF REPORT: Final

PREPARED FOR: U.S. Army Medical Research and Development Command
Fort Detrick, Maryland 21702-5012

REPORT DOCUMENTATION PAGE

Form Approved
OMB No. 0704-0188

1. REPORT DATE	2. REPORT TYPE	3. DATES COVERED
JANUARY 2023	Final	15SEPT2019 - 14SEPT2022

4. TITLE AND SUBTITLE
Neural mechanisms of neuropsychiatric lupus

5a. CONTRACT NUMBER
W81XWH-19-1-0759

5b. GRANT NUMBER

5c. PROGRAM ELEMENT NUMBER

6. AUTHOR(S)
Patricio Huerta

E-Mail: phuerta@northwell.edu

5d. PROJECT NUMBER
W81XWH-19-1-0759

5e. TASK NUMBER

5f. WORK UNIT NUMBER

7. PERFORMING ORGANIZATION NAME(S) AND ADDRESS(ES)

Feinstein Institutes for Medical Research
350 Community Drive
Manhasset, New York 11030

8. PERFORMING ORGANIZATION REPORT NUMBER

9. SPONSORING / MONITORING AGENCY NAME(S) AND ADDRESS(ES)

U.S. Army Medical Research and Development Command
Fort Detrick, Maryland 21702-5012

10. SPONSOR/MONITOR'S ACRONYM(S)

11. SPONSOR/MONITOR'S REPORT NUMBER(S)

12. DISTRIBUTION / AVAILABILITY STATEMENT

Approved for Public Release; Distribution Unlimited

13. SUPPLEMENTARY NOTES

14. ABSTRACT
This is the final report for project number W81XWH-19-1-0759. It addresses neuropsychiatric systemic lupus erythematosus (NPSLE), a constellation of syndromes that affects the nervous system in subjects with lupus. A major manifestation of NPSLE is impaired cognition. This project has studied brain-related processes in murine models of lupus, with the goal of identifying brain-based biomarkers for NPSLE progression. We have tested the hypothesis that impaired cognition in NPSLE originates from synaptic and network imbalances in the brain's cognitive centers, particularly the hippocampus. Therefore, this project has determined the effect of lupus antibodies on cognitive behaviors, synaptic function, and ensemble patterns in the hippocampus. We further hypothesize that the damage inflicted by specific lupus antibodies (which we test with autoantibody-based mouse models) is exacerbated by the presence of inflammatory cytokines that are also present in SLE subjects (which we test with spontaneous lupus models). Our approach is innovative, as we study neurophysiological signals, recorded in brain regions that are the neural substrate for cognition, in NPSLE murine models. Since the current therapeutic strategies to treat NPSLE are largely immunosuppressive, novel approaches such as brain-based biomarkers are urgently needed.

15. SUBJECT TERMS
Neuropsychiatric lupus, autoantibodies, spontaneous lupus models, brain recordings, cognition, hippocampus

16. SECURITY CLASSIFICATION OF:			17. LIMITATION OF ABSTRACT	18. NUMBER OF PAGES	19a. NAME OF RESPONSIBLE PERSON USAMRDC
a. REPORT	b. ABSTRACT	c. THIS PAGE			19b. PHONE NUMBER *(include area code)*
U	U	U	UU	188	

TABLE OF CONTENTS

1. **INTRODUCTION**: *Narrative that briefly (one paragraph) describes the subject, purpose and scope of the research.*

We have studied the dysfunction of brain dynamics that occurs in neuropsychiatric systemic lupus erythematosus (NPSLE). Lupus is an autoimmune disorder that affects primarily women and disrupts several organs, such as the skin, the joints, the kidneys, and the brain. NPSLE is a constellation of symptoms centered on the nervous system, which has been recognized as a major burden as it occurs in 43–98% of SLE patients. Impaired cognition and mood disorder are among the most frequent manifestations of NPSLE and their onset and progression often occur in the absence of disease flares. Importantly, SLE patients are very assertive about the fact that cognitive problems are a major concern that severely impacts their daily lives and would like to have access to therapy that addresses such issues. Evidence in humans and mouse models indicates that NPSLE is partly caused by autoantibodies that disrupt the proper function of brain neurons. A subset of these antibodies, called DNRAbs, binds to the synaptic receptor known as N-methyl-D-aspartate receptor (NMDAR). Another subset, called anti-ribosomal P antibodies (ARPAb), binds to neuronal surface P antigen (NSPA). The purpose of this project has been to test the hypothesis that the cognitive impairment experienced by NPSLE subjects derives from synaptic and network imbalances in cognitive centers of the brain, particularly the hippocampus. We have further hypothesized that the damage inflicted by specific lupus autoantibodies can be exacerbated by the presence of inflammatory cytokines that are also present in SLE subjects. The scope of this project has been to apply a multi-level neural analysis, which has included behavioral and neurophysiological approaches, to autoantibody-based models of NPSLE (DNRAb mice) as well as mice that develop SLE spontaneously (MRL/lpr and NZBWF1 strains).

2. **KEYWORDS:** *Provide a brief list of keywords (limit to 20 words).*

Neuropsychiatric lupus, autoantibodies, mouse models of lupus, spontaneous lupus models, DNRAb, cognition, cognitive impairment, brain recordings, hippocampus.

3. **ACCOMPLISHMENTS:** *The PI is reminded that the recipient organization is required to obtain prior written approval from the awarding agency grants official whenever there are significant changes in the project or its direction.*

What were the major goals of the project?

List the major goals of the project as stated in the approved SOW. If the application listed milestones/target dates for important activities or phases of the project, identify these dates and show actual completion dates or the percentage of completion.

The main goal of this project has been to pursue several specific aims to determine the effect of lupus autoantibodies on cognitive impairment (Aim #1), synaptic function (Aim #2), and ensemble patterns within the hippocampus (Aim #3) in NPSLE murine models. Moreover, we have investigated the pathogenic role of neurotoxic antibodies transmitted from mothers to infants, to the fetal brain (annexed Aim #4). For Aim #1, we have used a battery of behavioral tasks that measure recognition memory (novel object recognition), spatial location (object-place memory) and cognitive flexibility (clockmaze) in the mouse cohorts. For Aim #2, we have used ex vivo hippocampal slices to measure glutamatergic transmission and long-term potentiation (LTP), which is thought to be the synaptic substrate of how memories are written in the brain. For Aim #3, we have studied freely behaving mice, implanted with electrode arrays, to determine the activity of hippocampal neurons and oscillatory patterns (termed theta and gamma) during attentive exploration. It is thought that these patterns are associated with memory acquisition and consolidation. For Aim #4, we have studied the maternal transmission of neurotoxic antibodies from mothers to infants, focusing on the general concept that certain maternal antibodies can have toxic effects in the developing fetal brain.

What was accomplished under these goals?

For this reporting period describe: 1) major activities; 2) specific objectives; 3) significant results or key outcomes, including major findings, developments, or conclusions (both positive and negative); and/or 4) other achievements. Include a discussion of stated goals not met. Description shall include pertinent data and graphs in sufficient detail to explain any significant results achieved. A succinct description of the methodology used shall be provided. As the project progresses to completion, the emphasis in reporting in this section should shift from reporting activities to reporting accomplishments.

The following section is divided into 13 subsections that describe the activities, objectives, outcomes, and other achievements accomplished during the duration of the project

3.2. Accomplishment of goals: For the duration of the project, we can report:

3.2.1. Major activities: Our project has proceeded in agreement with the approved Statement of Work (SOW). We have used NPSLE murine models to conduct behavioral assessments (Aim #1), synaptic studies (Aim #2), and *in vivo* neural recordings of the hippocampus of freely behaving mice (Aim #3), as well as analysis of those neural recordings and studies of maternally transferred antibodies (annexed Aim #4). We have worked at a steady pace from the start (Sept. 2019) until the end date of the award (Sept. 2022). Of notice, there have been intervals during 2020–2022 in which we were forced to work at home due to the restrictions imposed by Covid19 pandemic. During those intervals, we continued to make progress in the project by putting our effort into data analysis.

Initially, we performed a study of the DNRAb-based model of NPSLE, in a collaboration with Dr. Betty Diamond (Feinstein Institutes) and Dr. Lonnie Wollmuth (Stony Brook University). This resulted in a publication (Chan et al., 2020, *Nature Communications* 11:1403; *Appendix 9.1*) for which my team performed all the behavioral assessments and neural recordings of the DNRAb mice.

Over the course of the award, we have investigated the DNRAb model of NPSLE with behavioral assessments, electrophysiological studies, and systems-neuroscience tools. We describe our main findings below, under Specific Objectives. We are in the final steps of submitting these results to peer-reviewed journals. We have already published a report describing the analytical tools needed for our systems-neuroscience approaches (Strohl et al., 2021, *Bioelectronic Medicine* 7:17; *Appendix 9.2*)

We have examined spontaneous NPSLE models at full throttle. In a collaboration with Dr. Anne Davidson (Feinstein Institutes), we have studied how the circadian rhythm affects lupus in

NZB/WF1 mice. This resulted in a publication (Mishra et al., 2021, *Molecular Medicine* 27:99; *Appendix 9.3*), which is focused on lupus nephritis, for which my team performed all the behavioral assessments, as well as helping with the transcriptomics and data analysis. We have also examined brain-related phenotypes in spontaneous NPSLE models (which are presented below under Specific Objectives) and we plan to have this study analyzed and ready for publication during 2023.

We have published a study in which we evaluated the sex chromosomal and hormonal influences on the male bias in a murine model that was exposed in utero to a maternal antibody reactive to contactin-associated protein-like 2 (Caspr2), which was originally cloned from a mother of a child with ASD (Gata-Garcia et al., 2021, *Frontiers in Neurology* 12:721108; *Appendix 9.4*). This study is highly relevant to our analysis of NPSLE, which affects mainly females. We will use this approach in lupus-prone strains to investigate the role of the sex chromosomes in setting up the brain-related manifestations in lupus.

We have examined the maternal transfer of neurotoxic antibodies to infants in a murine model that is closely related to SLE autoimmunity. In a collaboration with Dr. Simone Mader (Feinstein Institutes and Ludwig Maximilian University of Munich), we have studied the consequences of fetal brain exposure to an antibody to the astrocytic-protein aquaporin-4 (AQP4-IgG), cloned from a patient with neuromyelitis optica spectrum disorder (NMOSD), an autoimmune disease that can affect women of childbearing age and which closely related to SLE. This resulted in a publication in *Science Translational Medicine* (*Appendix 9.5*).

3.2.2. Specific Objectives: NPSLE patients experience brain-related manifestations, including spatial memory impairment, which can be studied in mechanistic detail with the use of NPSLE mouse models. We have examined the impairment of spatial cognition in NZB/WF1 and MRL/lpr strains, which develop lupus spontaneously, as well as the DNRAb model, as stated in our Specific Aim #1. We have also studied the synaptic function of the hippocampus in NZB/WF1, MRL/lpr, and DNRAb mice, as stated in our Specific Aim #2. We have conducted in vivo electrophysiology studies in the different strains (NZB/WF1, MRL/lpr, DNRAb), as stated in Specific Aim #3.

3.2.3. Significant behavioral results with NZB/WF1 and MRL/lpr strains: We demonstrated that both NZB/WF1 and MRL/lpr mice expressed a progressive cognitive impairment, such that young animals were completely normal in task performance but they become deficient as they reach their mature state. We found that spatial memory was disrupted only in adult NZB/WF1 and MRL/lpr mice when compared to their respective control groups (Figure 1). We used the object-place memory (OPM) task, the novel object recognition (NOR) task, and the paddling pool test (PPT) in the clockmaze to assess the animals. Mice used for these procedures lived on a reverse light-dark cycle (lights off at 09:00 h, lights on at 21:00 h), for at least 10 days before testing started, with *ad libitum* access to chow and water. All behavioral experiments occurred between 10:00 h and 18:00 h, which corresponded to the dark phase of the circadian cycle, when the rodents were naturally active. Animals were handled for 15 min per day for 3 days before they were tested behaviorally. We have extensive experience in assessing animals in these different behavioral tasks. Researchers were blinded to animal's group during behavior assessment.

For the OPM task, the apparatus consisted of a square chamber (40 cm on the side, 40 cm high), with the walls painted grey. Animals were familiarized to the empty chamber (3 sessions of 15 min each). For OPM testing, mice underwent the following sequence: empty chamber (15 min), home cage (10 min), sample phase in which the chamber had two objects located at the center of the NW and NE sectors (5 min), home cage (10 min), choice phase in which the chamber had the same objects but one of them was moved from NE to the center of the SE sector (5 min). The OPM ratio was calculated during the choice phase by dividing time spent exploring the moved object minus the time spent exploring the static object by the time exploring the objects combined 5. Behavioral data were collected and analyzed using EthoVision XT (version 11, Noldus Information Technologies,

Leesburg, VA) which automatically detected the contours of the animal from a live video feed, discriminated it from the background, and tracked activity with a 3-point detection algorithm (video rate, 30 frames per second).

For the NOR task, we used a square chamber (white plastic, 25 cm on each side, 60 cm high) with open ceiling and the floor covered with bedding. Before formal testing, each mouse was familiarized to the empty chamber (15-min sessions over a period of 3 days). A trial consisted of 3 phases: sample, delay, and choice. For the sample phase, mice were allowed to explore two identical objects for a period of 5 min. For the delay phase, mice were returned to their home cage for 5 min. During this interval, the objects were replaced, so that one of them was identical to those in the sample phase ('familiar object', F) whereas the other was different ('novel object', N). The objects were placed in the same positions as the sample objects in phase one.

For the choice phase of the NOR task, mice were allowed to explore for 5 min. Object exploration was scored with a software algorithm (Ethovision-XT) that assigned a circular zone around each object and recorded the events in which the animal's snout was in proximity (<1 cm) to the object. For analysis, we defined F as time exploring the familiar object, and N as time is exploring the novel object. To determine recognition memory, we measured the NOR discrimination ratio which was defined as [(N–F) / (N+F)].

For the PPT test in the clockmaze, the apparatus was a circular base (diameter, 85 cm), surrounded by a clear wall (30 cm high). Water (18°C±1°C) was added up to 2 cm, sufficient to wet the underside of the belly of mice. The perimeter wall was pierced by 12 equidistant holes (diameter 4 cm) so that, from the top, the maze resembled the 12 positions of a clock (hence the term clockmaze). For reference memory, we sealed 11 escape holes in the clock maze, leaving one hole that led to the 'true' exit pipe. The time to find the true exit was recorded by software (Ethovision-XT). A mouse was given 60 sec to find the true exit. Mice received 4 trials per day, with an interval of ~10min between trials, for a total of 16 trials. Our ongoing behavioral assessments show a clear pattern of results (**Figure 1**) in which the lupus-prone mice are not deficient at young age (8 weeks old) in the OPM, NOR and PPT tasks, but become impaired at mature age (16 weeks and older). Of note, most of the mice were not able to perform the MWM task, including the control mice for each group. We are currently preparing these data for a publication, and plan to present the MWM data as negative results to discourage its use in lupus-prone mice.

3.2.4. Advances in synaptic studies of NPSLE mice: We demonstrated that when DNRAbs were added to hippocampal slices, they increased the synaptic responses mediated by NMDARs by binding to the extracellular mouth of the GluN2A/B subunits of the N-methyl-D-aspartate receptor (NMDARs). We have studied the process of synaptic plasticity, particularly long-term potentiation (LTP) of the synapses connecting the CA3 with the CA1 neurons of the hippocampus, a neural signaling mechanism that is critical to learning and memory, in lupus-prone strains. The sequence of events underlying LTP is well understood. Glutamate binding to the a-amino-3-hydroxy-5-methyl-4-isoxazolepropionic acid receptor (AMPAR) results in the brief opening of an ion channel, which allows Na^+ to enter the dendritic spine causing a small degree of excitation (**Figure 2**). The NMDAR does not open immediately because its pore is blocked by Mg^{2+} ions. High-frequency stimulation removes the Mg^{2+} block of the NMDAR. When the NMDAR opens, it permeates Na^+ and Ca^{2+} ions, leading to the activation of several kinases, particularly calcium-calmodulin kinase II, and to the up-regulation of AMPARs and to their trafficking into the synapse.

We prepared *ex vivo* hippocampal slices from mice of the different strains (Control NZW, Experimental NZBWF1, Control MRL/MpJ, and Experimental MRL/lpr). Transverse hippocampal slices (400 μm thick) were prepared using a Leica VT1200 brain slicer. Each slice was transferred to a recording chamber, continuously perfused with ACSF at 30°C, for electrophysiological studies. Field excitatory postsynaptic potentials (fEPSP) were recorded with borosilicate glass electrodes (2–3 MΩ tip resistance) placed in the stratum radiatum of the CA1 field exactly between two bipolar

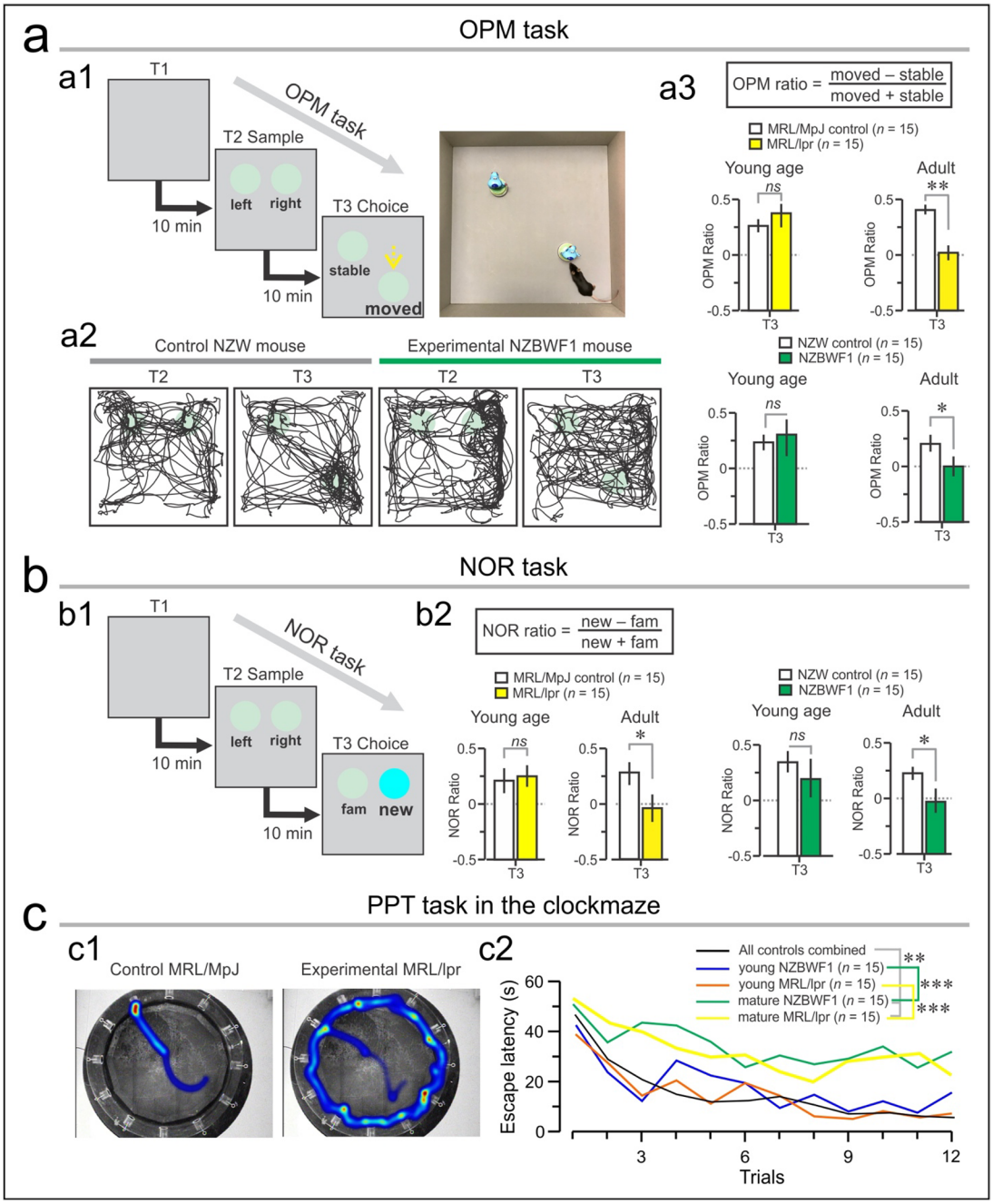

Fig. 1: Behaviors disrupted in lupus-prone mice. (A) ***a1***, schematic of the phases of the OPM task (left) and an example of a mouse exploring the moved object (right); ***a2***, representative track-plots of adult Control NZW and Experimental NZBWF1 mice. The control animal shows strong exploration of the moved object, whereas the NZBWF1 mouse explores both objects equally; ***a3***, graphs showing the OPM ratio for the different groups. Values shown are mean ± SEM (*n* = 15 mice per group). **(B)** ***b1***, schematic of the phases of the NOR task (left); ***b2***, graphs showing the NOR ratio for the different groups. Values shown are mean ± SEM (*n* = 15 mice per group). **C)** ***c1***, representatives paddling plots of adult Control MRL/MpJ and Experimental MRL/lpr mice during the last trial of the PPT; ***b2***, time series graphs showing the escape latencies across trials. Values shown are means per groups (*n* = 15 mice per group). Notice that the control groups are combined as they did not show statistical differences between groups. Statistical analysis: *ns*, non-significant, * $P < 0.05$, ** $P < 0.05$, *** $P < 0.01$, two-tailed Student t test).

stimulating electrodes (Frederick Haer & Co, Bowdoinham, ME) that activated the axons from CA3 neurons. The initial slope of the fEPSP was used as a measure of the postsynaptic response. fEPSP responses were amplified (AM Systems 1800), digitized at 10 kHz, and stored on a PC running custom software (written with AxoBasic, Axon Instruments, Union City, CA). For obtaining input-output (I-O) functions, the stimulation was reduced to a value at which no fEPSP was evoked. The stimulation was then increased incrementally to evoke steeper and larger fEPSPs. This was done until the appearance of a population spike, which reflected action potentials, generated by CA1 pyramidal cells, and defined the final point of the I-O function. For plasticity experiments, a stable baseline was obtained for at least 15 min. The baseline intensity was set to obtain a fEPSP slope that was half-maximal, as determined by I-O functions. Synaptic plasticity was induced by high-frequency stimulation (HFS), which consisted of theta burst stimulation (TBS, 10 trains of 4 pulses at 100 Hz, with 200 msec between trains). We calculated the occurrence of LTP by measuring 30 responses at 40–45 min post-HFS. For all LTP experiments, picrotoxin (100 μM) was added to block $GABA_A$ receptors.

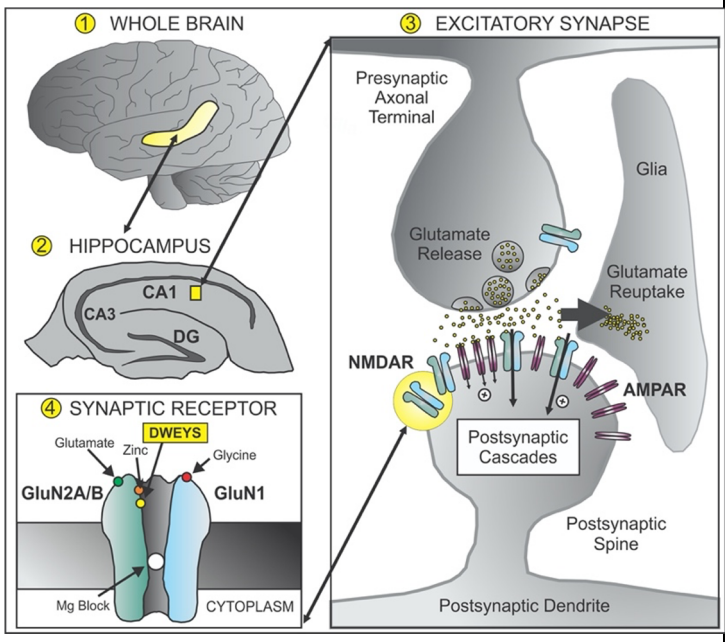

Fig. 2: Levels of analysis for long-term potentiation in the hippocampus. (1) The hippocampus is located in the temporal lobe of the mammalian brain. **(2)** Transverse hippocampal slices can be studied *ex vivo* as they maintain the neural pathways that connect the dentate gyrus (DG) with the CA3 area, and CA3 with the CA1 area. **(3)** Synaptic studies can be performed in the CA3–CA1 excitatory synapses, which release glutamate (as the neurotransmitter) and contain AMPARs and NMDARs in the cell membrane of the postsynaptic spine. Glial cells are also intimately linked to synaptic function. **(4)** The synaptic NMDAR has a glutamate-binding site and several allosteric sites, in particular the DWEYS consensus sequence to which DNRAb can bind.

We have studied several DNRAbs, which were obtained from human patients and purified as monoclonal antibodies in the Diamond Lab. The rationale for these experiments is that we can add the antibody, at an exact concentration, directly to the *ex vivo* slice and measure its effects on synaptic function instantly. We have focused on G11, an IgG1 monoclonal antibody (with Igg1 heavy chain and Igk light chain composition) derived from the B cells of a female SLE patient. We have treated *ex vivo* hippocampal slices with G11 at increasing concentrations (5 mg/ml, 15 mg/ml, and 50 mg/ml) and found that G11 at low dose (5 mg/ml) did not affect the induction of LTP, but G11 at higher doses completely blocked LTP (**Figure 3**). Remarkably, the autoantibody was applied for only 10 min, starting 5 min before the synapses were exposed to a high-frequency stimulation train that would normally be sufficient to elicit LTP. We have transitioned to testing *ex vivo* slices obtained from DNRAb mice, as well as MRL/lpr mice, and NZBWF1 mice. We expect to have these studies finished by mid-2023. Our overall objective with this part of the project is to prepare a publication by the fall of 2023 that combines the behavioral and synaptic results we have obtained in the lupus-prone mice.

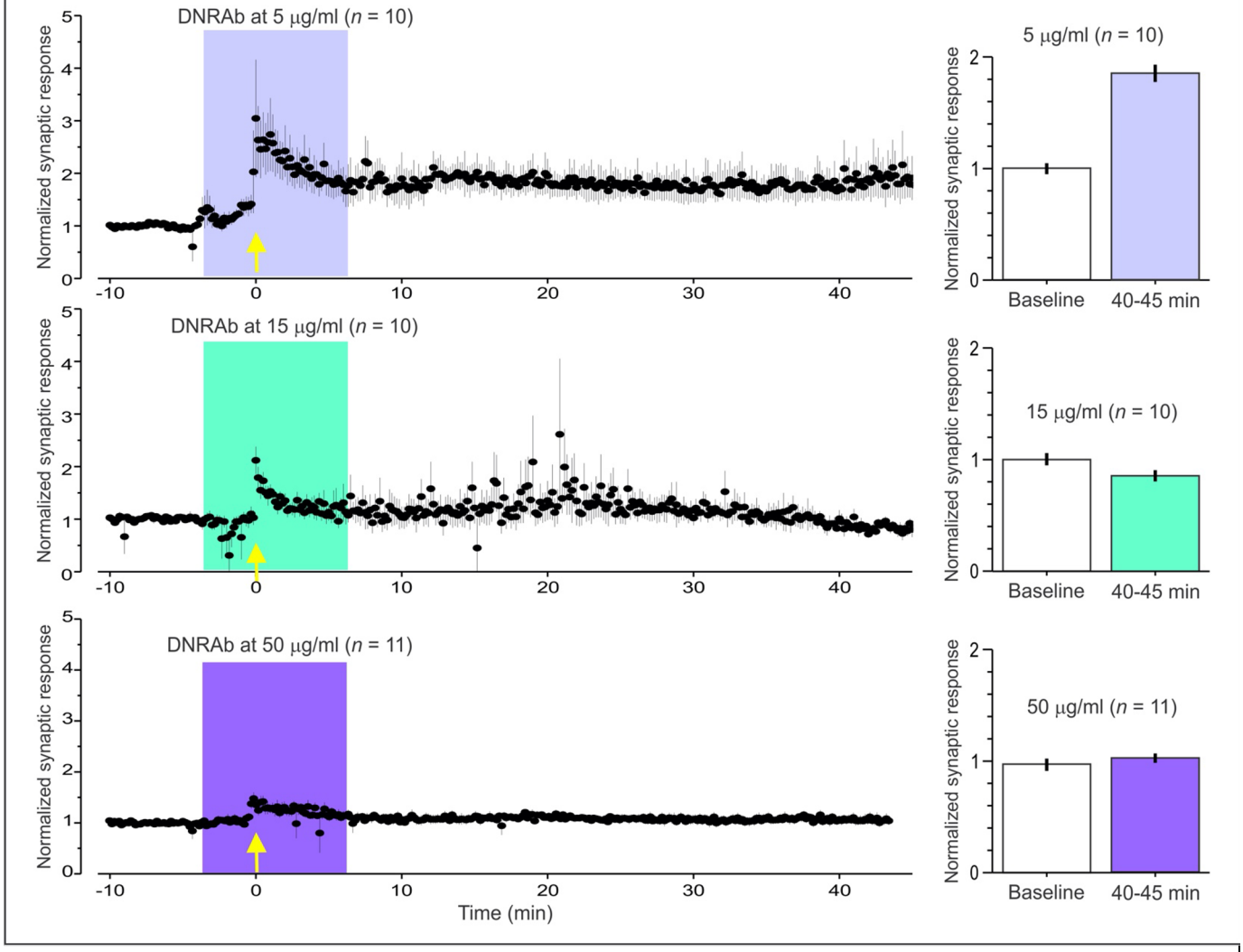

Fig. 3: Synaptic plasticity studies in ex vivo hippocampal slices treated with DNARbs. *Left*, the time-series graphs show the synaptic responses (measured as field excitatory synaptic potentials) in the CA1 area upon stimulation of the CA3 afferent axons, once every 10 sec. At time 0, a train of high-frequency stimulation (HFS) is given (indicated by yellow arrow) to trigger an increase in the synaptic responses. The top graph shows that application of DNRAb (5 mg/ml, light blue) did not disturb the induction of LTP as the synaptic responses were significantly larger than baseline 40–45 min after the HFS train. Notably, application of mid-dose DNRAb (15 mg/ml, green) and high-dose DNRAb (50 mg/ml, violet) completely blocked LTP. *Right*, the bar graphs show the mean ± SEM values at baseline (5 min before HFS) and 40–45 min post HFS.

3.2.5. Significant *in vivo* electrophysiology results with DNRAb mice: For Specific Aim #3, we wanted to determine the oscillatory patterns during attentive exploration in NPSLE mouse models, as these patterns may be critical for encoding new memories. We have found a remarkable set of results in the DNRAb mice. In a nutshell, the oscillatory patterns within the hippocampus of DNRAb mice exhibit a much higher magnitude than control mice, as they explore an environment to which they have been exposed repeated times. In the control group, the oscillatory patterns are strong when they first enter a new arena, but the oscillations become quieter as an animal gets familiarized with an arena, indicating that it has encoded this spatial arrangement as a 'recognized place'. In other words, the oscillatory patterns track faithfully the individual's level of familiarization with a given space. This is not the case in the lupus mice, for which the oscillatory patterns do not cease to be elevated. These data suggest that lupus mice never become truly familiarized with a novel environment. Furthermore, we postulate that this elevated signal in the oscillatory patterns is the neural equivalent

to the *brain fog*, an informal term that is quite common among SLE patients to refer to a state of confusion regarding their whereabouts. We are currently preparing these data for submission to the journal *Nature Communications*.

An important technical development during the second year of the project was that we created a software package that completely automates the analysis of spike data from the in vivo electrophysiology studies. This automated framework has allowed us to accelerate the research pipeline from data acquisition to complete analysis. A manuscript describing this work was published in *Bioelectronic Medicine*.

3.2.6. Altered oscillatory patterns in DNRAb mice during the open field task: C57BL/6 bred on the $H2d^{+/+}$ background were used (n = 6) as they showed eager object exploration and had robust immunized responses to the MAP-DWEYS peptide, mice exposed to the MAP-CORE peptide were used as controls (n = 7). These mice were studied following a consistent timeline (Figure 4a). The tetrodes were lowered to the stratum pyramidale in the CA1 region of the hippocampus (**Figure 4b, Figure 5a**). Mice were subjected to the open-field task, such that each implanted mouse had 4 familiarization sessions (S1–S4) that lasted 15 min each. While exploring the empty chamber, the oscillatory patterns, and place cell activity were recorded and analyzed.

From the raw oscillatory data, five key oscillation bands were demarcated: theta (6–12 Hz), beta (20–30 Hz), gamma1 (*low*, 40–50 Hz), gamma2 (*middle*, 50–90 Hz), gamma3 (*fast*, 90–150 Hz) (**Figure 4c**). The movement of the animals was tracked using an LED fixed on the top of the electrode array. Comparison of the distance traveled between control and DNRAb animals showed no significant difference between groups (**Figure 4d**). Similarly, when the mean speed in the open field was compared across control and DNRAb groups, no significant difference was observed (**Figure 4e**). Thus, the behavioral activity of DNRAb mice appears like control mice in the open-field task in terms of distance traveled and mean speed.

A striking finding of this experiment was that despite the lack of apparent behavioral changes, the DNRAb mice exhibited robust differences in the oscillatory patterns across the S1–S4 sessions. Power spectral density was calculated over the frequency range (0–150 Hz), for all recorded animals (**Figure 5b**). Spectrograms were generated depicting the frequency power over 5-min periods of time. When comparing between the first 5 min of novelty in the open field in S1 to the last 5 min of S4, the control group had relatively low theta power, while the DNRAb group demonstrated a strong increase in the theta band over time (**Figure 4f**). The theta band was then examined as power spectral density (PSD) over the frequency of theta, which revealed that in S1 the control group had higher theta PSD, while in S2–S4, DNRAb mice had higher theta PSD (**Figure 4g**).

Theta band power is known to have a positive relationship with running speed, thus we assessed whether this relationship was pertinent to our DNRAb observations. Running speed ranges (in cm/s) were slow = 0–6, medium = 6–12, fast = 12–20. Plotting theta band power over the three speed ranges showed that control mice indeed have increasing theta power over increasing speeds, yet DNRAb mice had significantly higher theta power over all speed ranges (**Figure 5c**, $P = 0.001$, mixed-effects ANOVA). When the normalized power of each band was compared over each session, a strongly significant difference was observed between control and DNRAb groups, where the normalized power of DNRAb theta, beta, and gamma1 bands markedly increased across the S4 session (**Figure 4h**, theta band $P < 0.001$; beta band, $P < 0.001$; gamma1 band, $P < 0.001$; mixed-effects ANOVA). Similarly, for gamma2 and gamma3 band power, DNRAb mice displayed significantly higher power over sessions S1–S4 (**Figure 5d**, gamma2, $P < 0.001$; gamma3, $P < 0.001$, mixed-effects ANOVA).

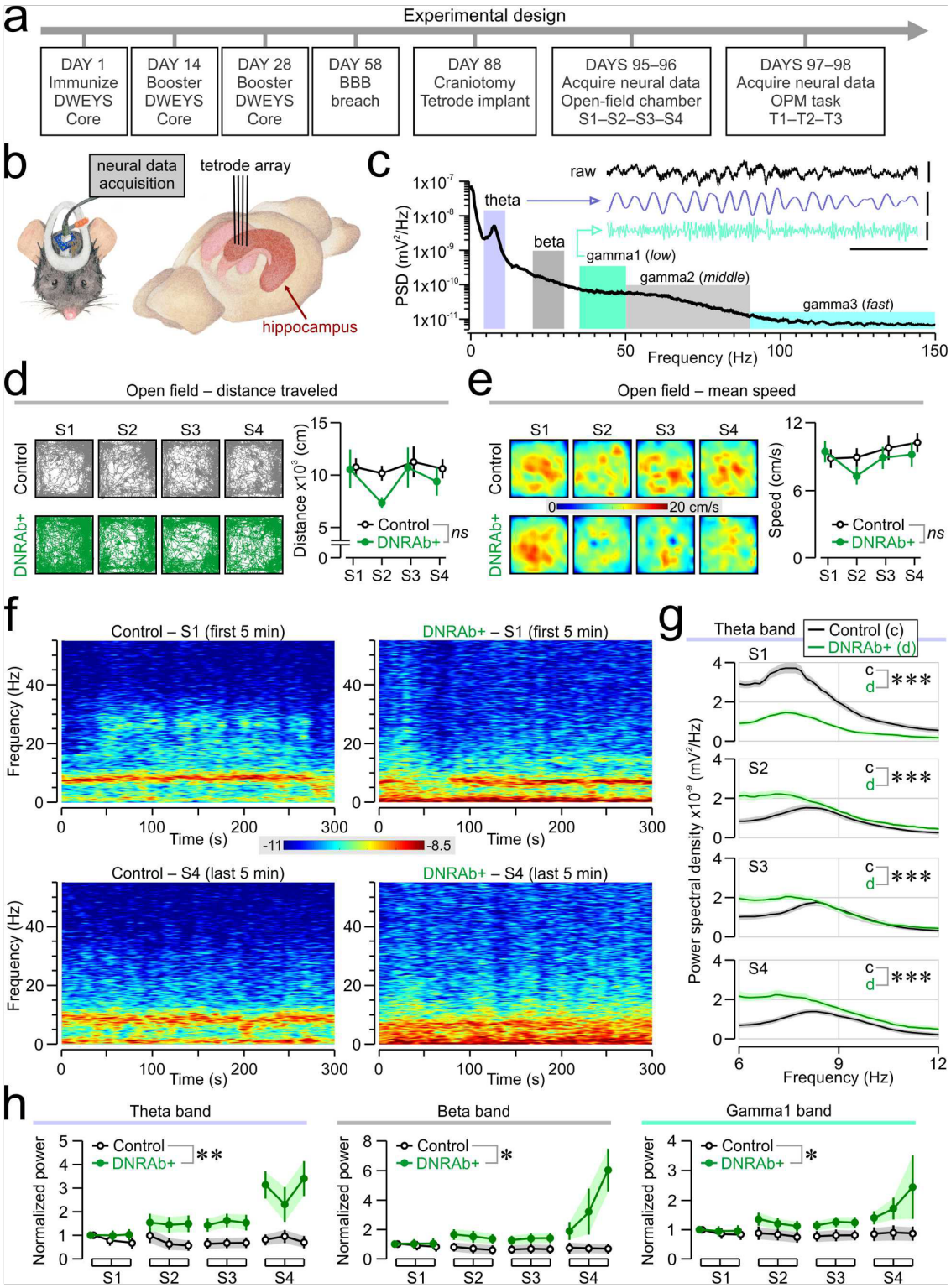

Fig. 4: Abnormal high oscillatory patterns in DNRAb mice during the open field task. (a) Overview of experimental design. **(b)** Schematic of custom in vivo electrophysiology tetrode array in the dorsal CA1 hippocampus. **(c)** Average power spectral density (PSD) of control mouse hippocampal oscillations during S1 phase of the open field test. **(d)** Representative track plots for sessions S1–S4 of open field task. Quantification of distance traveled reveals no significant difference between control and DNRAb groups. **(e)** Comparison of mean speed over S1–S4 open field sessions shows no difference between control and DNRAb groups. **(f)** Frequency spectrograms for the first 5 min of S1 and the last 5 min of S4 demonstrates an increase in the theta wave (6 – 12 Hz) power in the DNRAb group compared to control. **(g)** Power spectral density of the theta wave band reveals DNRAb mice have lower power spectral density during S1 and higher power spectral density during S4 when compared to control mice. **(h)** Quantification of the normalized power of theta band (6 – 12 Hz), beta band (20 – 30 Hz), and gamma1 band (40 – 50 Hz) demonstrates that DNRAb mice have significantly higher normalized oscillatory power when compared to control mice. Statistical analysis: *ns*, non-significant, * $P < 0.05$, ** $P < 0.05$, *** $P < 0.01$ (ANOVA, or two-tailed Student t test).

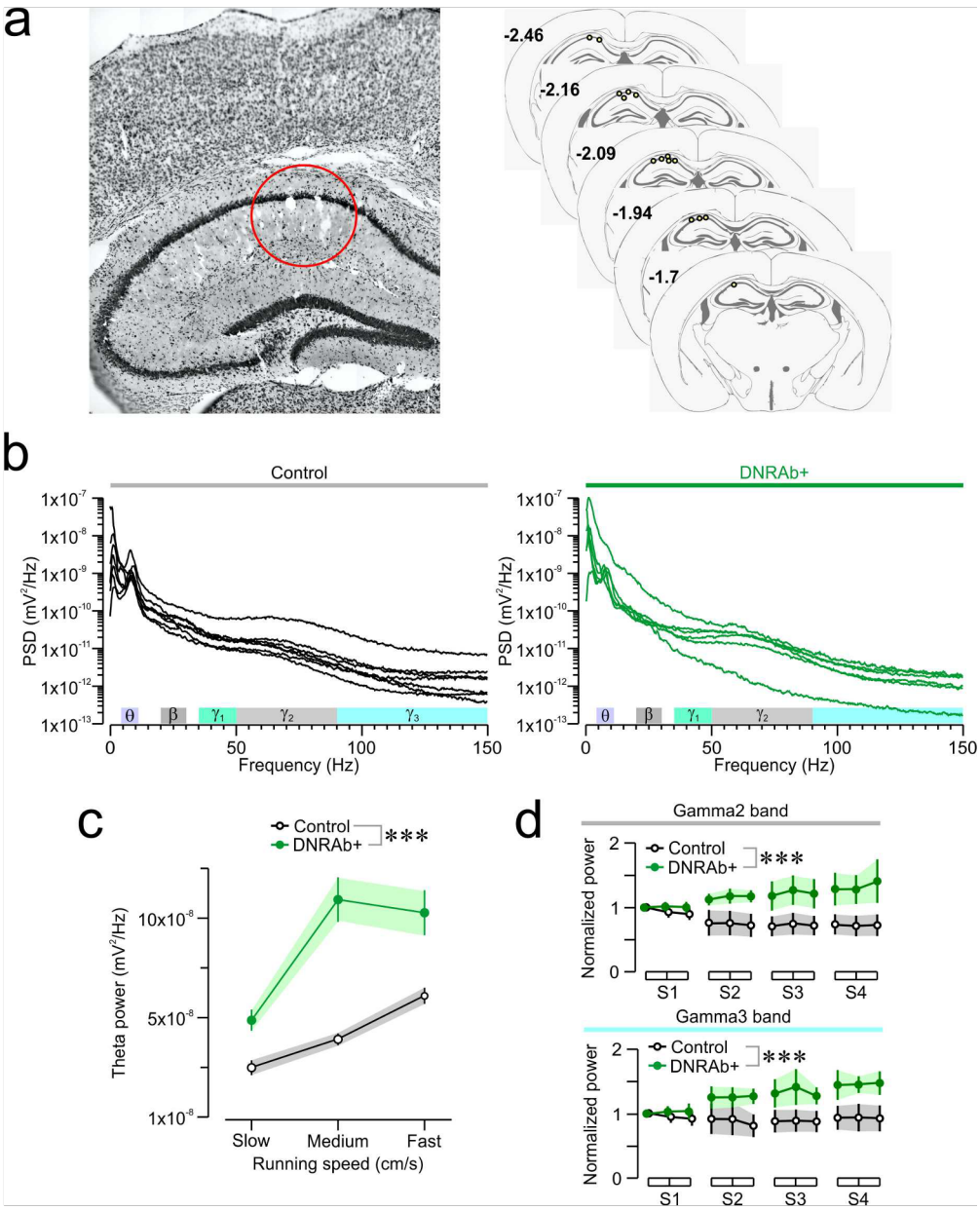

Fig. 5: Tetrode placement confirmation and power calculations across frequency bands during S1–S4. (a) Post-mortem histological assessment of implanted brains confirmed tetrode placement into CA1 hippocampus. **(b)** Overall power spectral density (PSD) as a function of frequency, for each mouse during the open field task (S1–S4). **(c)** Comparison between theta power over different running speeds (cm/s, slow = 0–6, medium = 6–12, fast = 12–20) demonstrates that DNRAb mice have significantly higher theta power over all speeds in S1–S4. **(d)** Normalized power of gamma2 and gamma3 bands are significantly higher in DNRAb mice over S1–S4. Statistical analysis: *ns*, non-significant, *** $P < 0.01$ (ANOVA).

3.2.7. Impaired behavioral performance in DNRAb mice during the object-place memory task and aberrant oscillatory patterns during object exploration: Following the open-field task, the mice were subjected to the object place memory (OPM) task in the same box. This test protocol involves three experimental phases: familiarization phase to an empty box (T1, 10 min), a sample phase where two identical objects are presented (T2, 5 min), and a choice phase where one of the objects is moved (T3, 5 min). These three phases were separated by 10-min rest sessions (**Figure 6a**). Representative track plots were generated to highlight the areas around objects (diameter 6.5 cm) that were considered as object exploration (**Figure 6d**, T2 red, T3 purple = stable and blue = moved). The bouts of object exploration, defined as the amount of time the mouse's snout was continuously in an

object's exploration area, were plotted as bout durations over the T3 session. We observed that DNRAb mice had fewer bouts of exploration of both objects and tended to spend less time exploring the objects when compared to control mice (**Figure 6b**, left). Further, when quantified as cumulative probability, the bout duration of control mice to the moved object and the stable object was significantly longer than the DNRAb mice, respectively (**Figure 6b**, top-right, control–moved *vs* DNRAb–moved, $P < 0.001$; control–stable *vs* DNRAb–stable, $P < 0.001$, Kolmogorov-Smirnov test). The OPM ratio revealed that DNRAb mice performed significantly worse in the OPM task when compared to control mice (**Figure 6b***,* bottom-right, OPM ratio, control *vs* DNRAb, $P < 0.05$, *t*-test). These results, collected form implanted mice, were consistent were compared to implanted mice. Taken together, DNRAb mice displayed an inhibition in the spontaneous investigation of the moved object in the OPM task, suggesting a disruption in healthy memory function.

We then investigated whether DNRAb mice had any abnormal oscillatory patterns as they approached and explored objects. The raw oscillatory data was parsed into theta, beta, and gamma1 bands. Representative frequency spectrograms over a 5 sec period of object approach and exploration revealed that DNRAb mice had higher overall oscillation activity during these periods (**Figure 6c**). By plotting the power spectral density (PSD) of each band during object exploration on T2, T3-stable (T3s), and T3-moved (T3m), we observed that DNRAb mice had higher PSD for T3m–theta, beta, and to a lesser extent gamma1 (**Figure 6e**). Quantification of these PSD compared across objects revealed a robust difference between DNRAb and control groups, where DNRAb mice had significantly increased wave power during object exploration (**Figure 6f,** theta control *vs* DNRAb, $P < 0.001$; beta control *vs* DNRAb, $P < 0.001$, gamma control *vs* DNRAb, $P < 0.001$, mixed-effects ANOVA). These results demonstrate that DNRAb mice display an abnormal high oscillation power for theta, beta, gamma1, gamma2 bands whenever inspecting any object. By comparison, healthy control mice only have elevated theta band power, which points to an aberrant pattern of increased oscillation power pattern in DNRAb mice.

3.2.8. Altered cross-frequency power-power coupling in DNRAb mice: Cross frequency coupling is used to investigate the intrinsic dynamics of oscillations over different frequency bands. The strength of coupling between different bands was visualized by parsing the raw signal into frequency bands over 5 s (**Figure 7a**, left). To test the correlation between theta and gamma power, we measured autocorrelograms (power vs. power across frequencies), generated spectrograms for periods of object investigation during T3, and created autocorrelation matrices where each point represents the correlation between the powers of the frequency on one axis and the frequency on the other axis. Sections of the autocorrelation matrix were delineated for defined range frequency bands (**Figure 7a**, right). These correlation matrices reveal that while exploring the moved object DNRAb mice have weak cross-frequency power-power correlation between theta and higher frequencies when compared to controls (**Figure 7b**). Quantification of frequency-band-constrained correlations demonstrated that DNRAb mice have significantly weaker cross-frequency power-power coupling between theta–beta ($P < 0.05$, one-way ANOVA), theta–gamma1 ($P < 0.05$, one-way ANOVA), theta–gamma2 ($P < 0.05$, one-way ANOVA), and theta–gamma3 ($P < 0.01$, one-way ANOVA) (**Figure 7c**). Correlation matrices for periods of exploration of the stable object showed that control mice have reduced correlation compared to period of exploration of the moved object (**Figure 7d**). Comparison of the correlation matrices of the stable object between control and DNRAb groups revealed no significant differences in the cross-frequency power-power coupling of theta to the higher bands (**Figure 7e**).

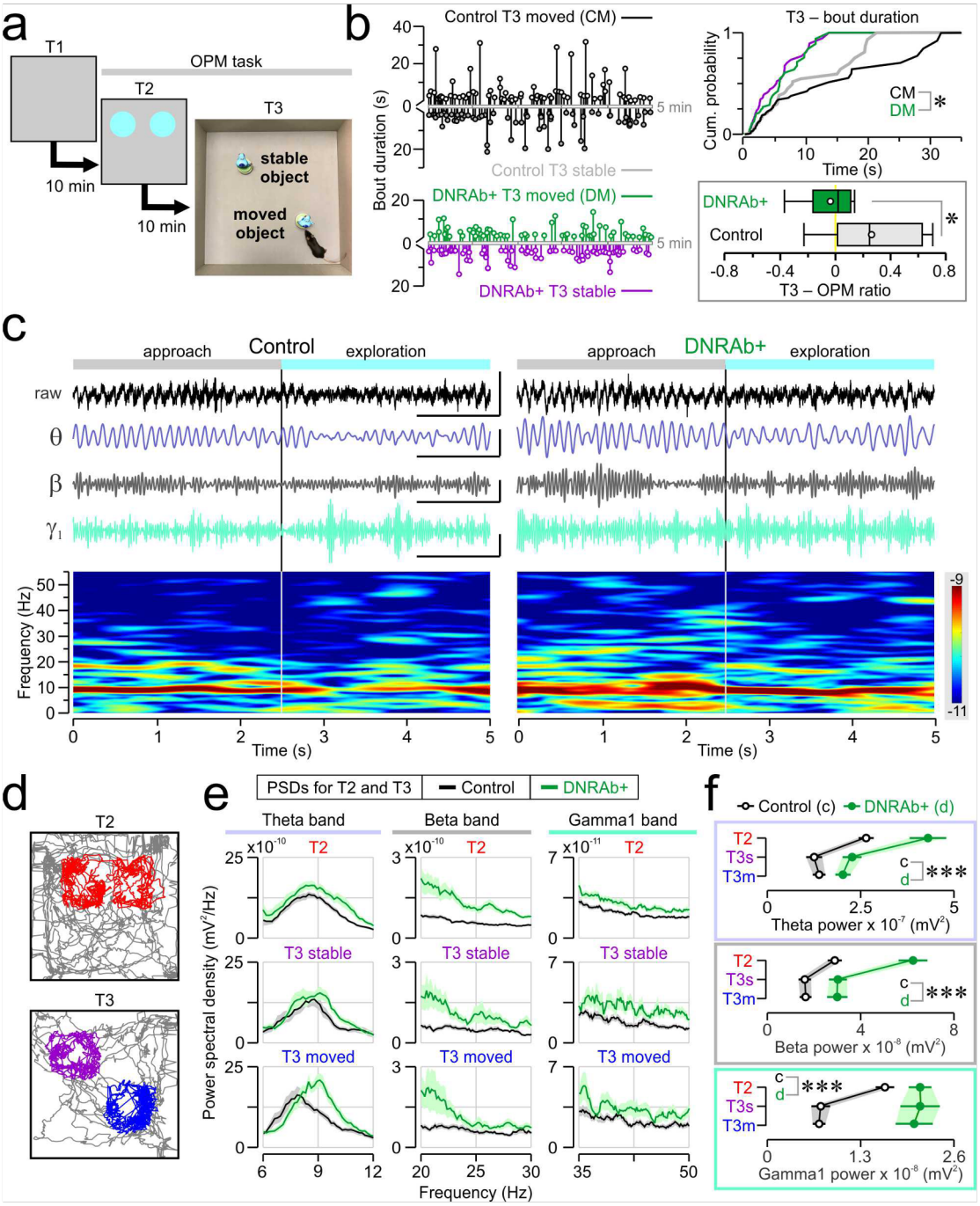

Fig. 6: Disrupted behavioral performance in DNRAb mice during the object place memory task and aberrant oscillatory patterns during object exploration. (a) Overview of the object place memory task protocol consists of three phases: familiarization (T1, 15 min), sample (T2, 5 min), and choice (T3, 5min), separated by 10 min rests. **(b)** *Left*, all bouts of object exploration (s) during the T3 phase with control moved (CM, black lines), control stable (grey), DNRAb moved (DM, green), and DNRAb (purple). *Top right*, cumulative probability of object exploration bouts during T3 reveals significant differences between control moved (CM) versus DNRAb moved (DM) bouts. *Bottom right*, T3 discrimination ratios (mean ± s.e.m.) reveal that control mice have a robust bias towards the moved object while DNRAb mice do not. **(c)** *Top*, representative data displaying oscillatory data for a 10 s period, with 5 s approaching the moved object and 5 s of exploration. Scale bars information: x-axis: 1 s, y-axis: raw (1mV), θ (0.3 mV), β (0.05 mV), and γ_1 (0.05 mV). *Bottom*, representative frequency spectrograms (Hz) of oscillatory band power for a 5 s period of exploration. **(d)** Representative track plots of OPM task. In T2 sample, red areas were analyzed as object exploration; in T3 choice, purple was stable, and blue was moved. **(e)** Plots comparing control and DNRAb oscillatory band power spectral density as a function of the frequency for theta band, beta band, and gamma1 band for T2, T3 stable, and T3 moved. Across all bands and objects conditions, DNRAb mice had higher PSD than control mice. **(f)** Quantification of band power demonstrates that across all sessions control mice have significantly lower theta power, beta power, and gamma1 power compared to DNRAb mice. Statistical analysis: *ns*, non-significant, * $P < 0.05$, ** $P < 0.05$, *** $P < 0.01$ (ANOVA, or two-tailed Student t test).

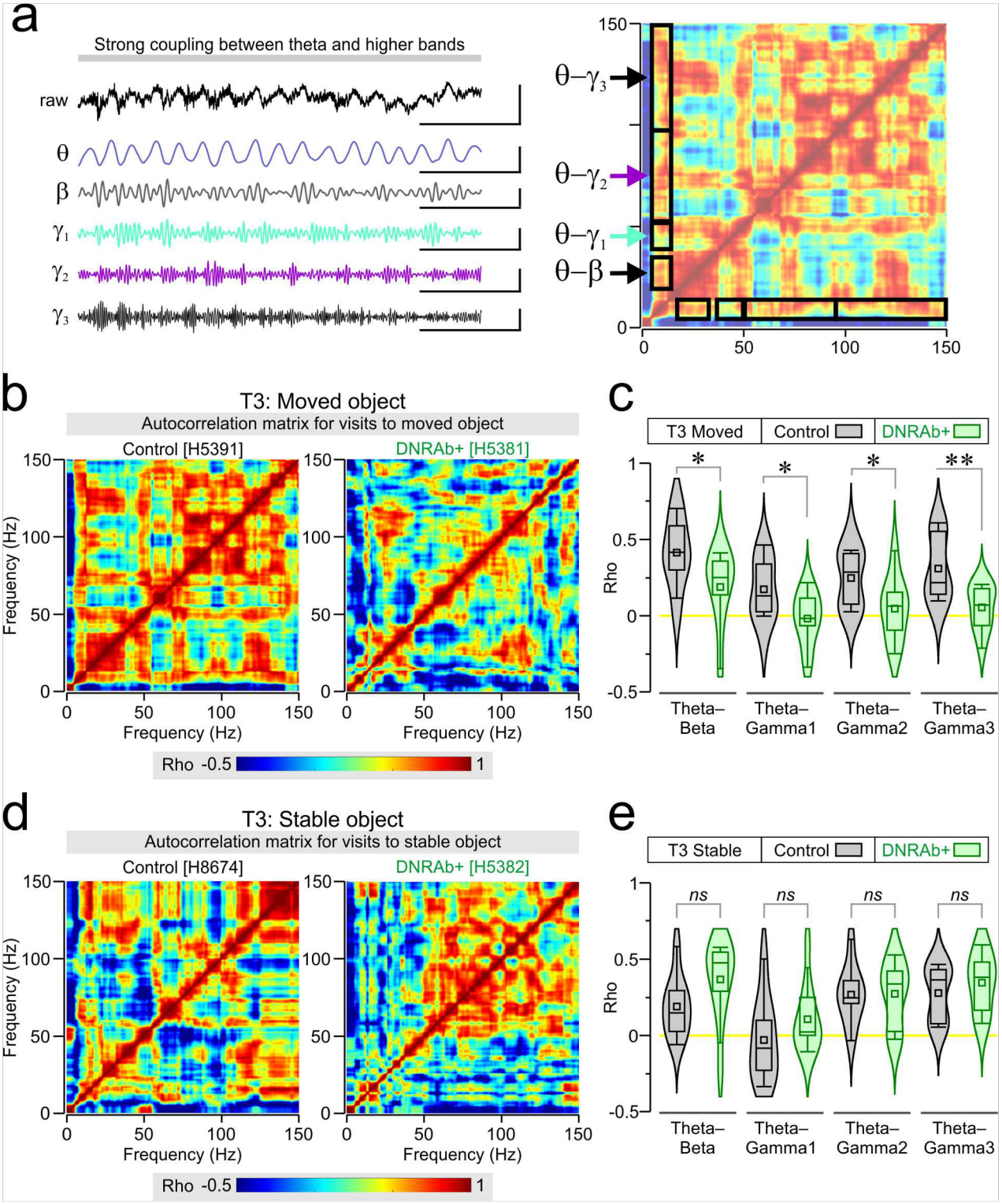

Fig. 7: DNRAb mice display altered cross-frequency power-power coupling. (a) Left, example traces showing raw LFP, and filtered bands for theta, beta, gamma1, gamma2, and gamma3 demonstrating strong coupling between theta and higher bands. Scale bars information: x-axis: 0.5 s, y-axis: raw (1mV), θ (0.3 mV), β (0.1 mV), γ_1 (0.1 mV), γ_2 (0.2 mV), and γ_3 (0.01 mV). Right, example autocorrelation delineating the frequency band constraints that were analyzed (θ–β, θ–γ_1, θ–γ_2, and θ–γ_3). **(b)** Autocorrelation matrix depicting cross-frequency power-power coupling during mouse examination of the moved object. Control mice (left) have a strong correlation between theta and higher frequencies during object examination, compared to DNRAb mice which have weaker correlations across frequencies. **(c)** DNRAb mice have significantly weaker cross-frequency power-power coupling between theta and beta, gamma1, gamma2, and gamma3. **(d)** Cross-frequency power-power coupling autocorrelation matrix for when mice are investigating the stable object. Control mice exhibit lower correlations compared to investigation of the moved object. **(e)** Cross-frequency power-power coupling across groups is not significantly different during investigation of the stable object. Statistical analysis: *ns*, non-significant, * $P < 0.05$, ** $P < 0.05$, *** $P < 0.01$ (ANOVA, or two-tailed Student t test).

3.2.9. Reduced phase-amplitude modulation in DNRAb mice during the OPM task: We calculated the modulation index (MI), which measures how much the amplitude of beta and gamma oscillations is modulated by the phase of theta. We found that DNRAb mice have a weaker MI in the region corresponding to the phase of theta and amplitude of gamma1 (Figure 8a). When quantified for constrained frequency bands, theta-beta MI is significantly lower in DNRAb mice than controls, while theta-gamma1 MI reveals that DNRAb mice have a strikingly diminished MI compared to controls (Figure 8b, theta-beta, $P < 0.05$; theta-gamma1, $P < 0.001$ mixed-effects ANOVA). Analysis of MI across each trial of the OPM task demonstrates that DNRAb oscillatory dynamics are disparate from controls in several conditions, including the moving (T1m) or resting (T1r) state of the animal during the T1 phase. DNRAb mice had significantly reduced MI during T3 (Figure 8c, theta-beta, $P < 0.05$; theta-gamma1, $P < 0.05$, ANOVA), when compared to controls. Importantly, in terms of theta-gamma1 MI, during T2 there is no difference between DNRAb and control group, but in T3 the groups separate drastically, which suggests a severe disruption in object memory encoding.

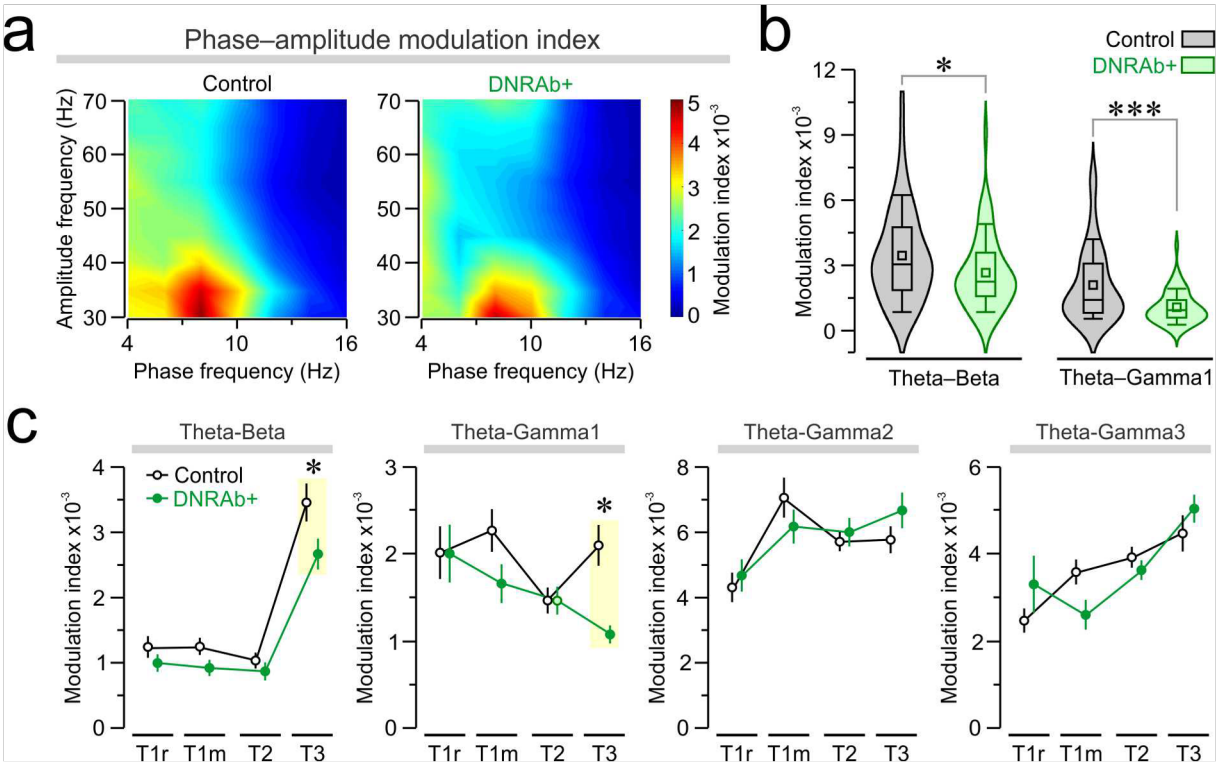

Fig. 8: Phase-amplitude coupling is diminished in DNRAb mice during object investigation. (a) Plot depicting phase-amplitude modulation index. Color at each point indicates the phase-amplitude modulation index between the phase-frequency depicted on the x-axis and the amplitude frequency depicted on the y-axis. The region corresponding to the phase of theta and the amplitude of gamma1 shows a weaker modulation index in DNRAb mice compared to controls. **(b)** The theta-beta modulation index and theta-gamma1 modulation index is significantly lower in DNRAb mice compared to controls during object investigation. **(c)** Modulation index analyzed across different phases of the OPM task: T1 moving (T1m), T1 resting (T1r), T2 and T3. Theta-beta was reduced in DNRAb mice during T3, theta-gamma1 was reduced in DNRAb mice during T3 (highlighted). No differences were found in theta-gamma2 and theta-gamma3 comparisons. Statistical analysis: *ns*, non-significant, * $P < 0.05$, ** $P < 0.05$, *** $P < 0.01$ (ANOVA, or Kolmogorov-Smirnov test).

3.2.10. Disrupted place cell dynamics and unit remapping in the CA1 region of the hippocampus in DNRAb mice: Single unit activity of pyramidal neurons in the CA1 hippocampus was recorded during the OPM task. When plotted as firing rate maps, DNRAb place cells (PCs) were found to have larger receptive fields than their control counterparts and tended to feature multiple place fields per PC. Statistical comparison demonstrated that DNRAb mice had significantly lowered spatial

information (SI) compared to controls (**Figure 9a**, $P < 0.001$, Kolmogorov-Smirnov test). PC dynamics were also investigated for each trial of the OPM task (T1–T3). Analogous to the open field results, PC firing rate maps revealed that DNRAb PCs are larger than control PCs and are prone to having multiple place fields (**Figure 9b**). DNRAb PCs exhibit several abnormalities during the OPM task compared to controls. DNRAb PCs have dramatically increased place field size, and markedly reduced SI across all phases of the OPM task (Figure 9c, place field size T1–T3, $P < 0.001$; SI T1–T3, $P < 0.001$, one-way ANOVA). DNRAb PCs have reduced mean firing rate (MFR) during T1, but increased MFR during T2 and T3 (**Figure 9c**, MFR, T1 $P < 0.05$; T2 $P < 0.05$; T3 $P < 0.001$, one-way ANOVA). In terms of peak firing rate (PFR) during OPM, DNRAb PCs are shown to have significantly increased PFR during T3 compared to controls (**Figure 9c**, PFR, T3 $P < 0.05$, one-way ANOVA).

An essential facet of place cell dynamics in the context of OPM is their tendency for their center of mass to shift in the direction of the moved object. We hypothesized that DNRAb PCs would have a diminished ability to remap towards the moved object. When the center-of-mas (COM) shift vectors between T2 and T3 were compared, we observed that DNRAb PCs had a reduced bias to move in the direction of the moved object. Instead, the DNRAb PCs had a more random distribution of vector direction when compared to control PCs (**Figure 9d**). This irregular vector behavior was further explored by plotting the vector count as a function of the absolute angular difference, away from 150º (the direction of the moved object). This representation reveals that the vector direction bias towards the moved object was diminished in DNRAb PCs (**Figure 9e**, $P < 0.05$, Kolmogorov-Smirnov test).

3.2.11. Disrupted grid cell dynamics in the medial entorhinal cortex of DNRAb mice: Another exciting development during this project is that we have been able to record a different type of spatially tuned signal from the entorhinal cortex of mice, which is called the grid cell. This type of neuron is active at different points of the environment, so that –from above– the activity looks like a hexagon. The ensemble of grid cells covers the whole environment and it provides a point-point coordinate system, not unlike a GPS. We found that DNRAb mice have a severe disturbance of the grid cell system (**Figure 10**), which deepens their abnormalities in the domain of spatial cognition. This is a completely novel result in neuroscience. We are, as far as we know, the only team to have shown that neurotoxic antibodies have a damaging effect on the GPS-grid-cell system of the brain, with our work on aquarin-4 antibodies and their disruption of the developmental program of blood vessels in the fetal brain, which transfers to abnormalities of the entorhinal cortex in adult mice (Mader et al, published in *Science Translational Medicine*). Now, we add the results from the DNRAb mice to this endophenotype. It is important to note that grid cells have been identified in humans, which makes our result a highly attractive candidate in the search for a biomarker (based on entorhinal activity), which can –in principle– be detected in SLE patients with noninvasive techniques such as EEG.

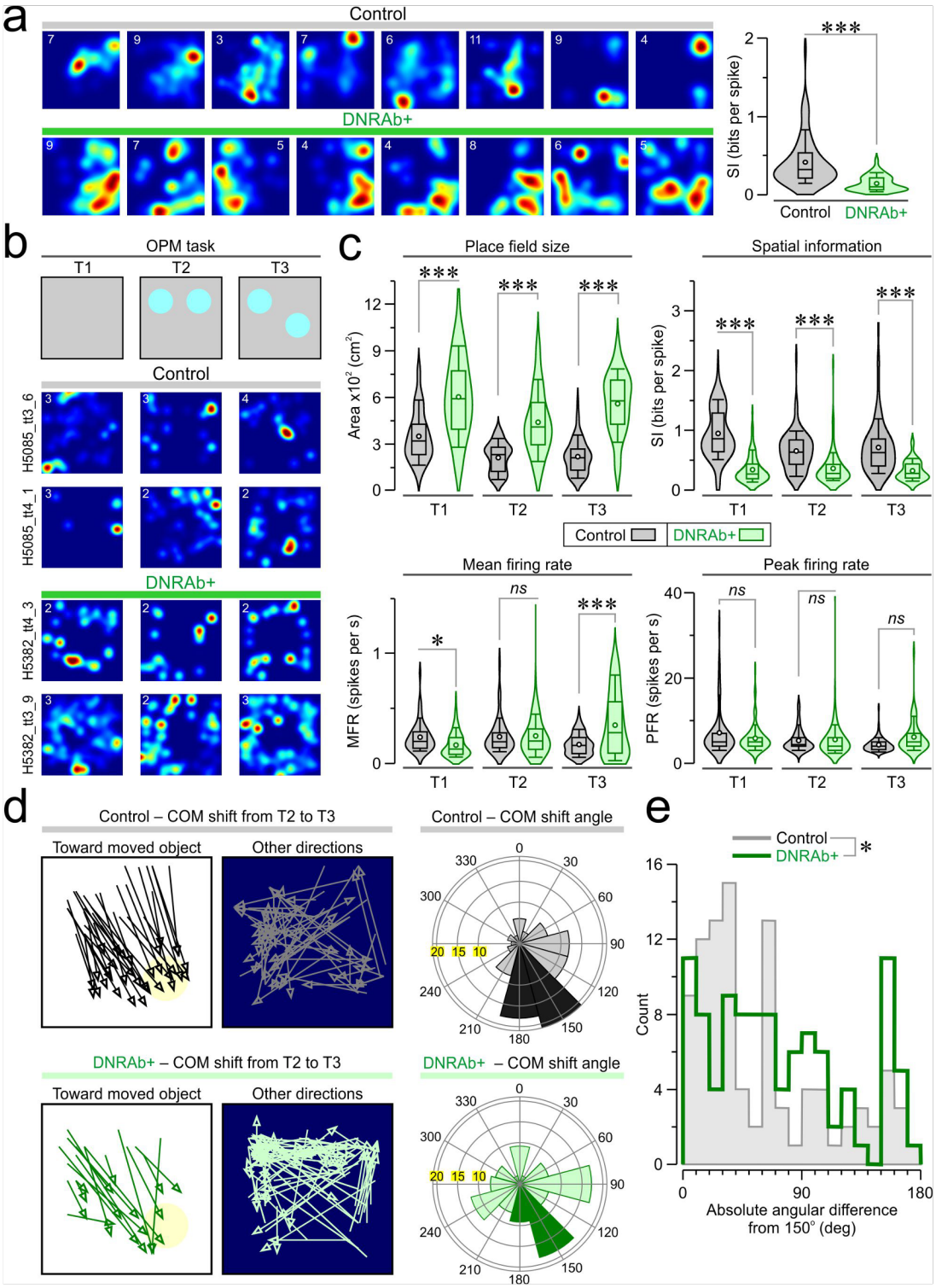

Fig. 9: Disrupted place cell dynamics in DNRAb CA1 hippocampus. (a) Left, representative place cell rate maps for control and DNRAb groups during open field task S4; the peak firing rate is noted in the top left of each map. Right, comparison of spatial information (SI) shows that DNRAb place cells have strongly reduced average SI compared to controls. **(b)** Overview of OPM task (T1–T3), with examples of control and DNRAb place cell rate maps below. DNRAb place cells tended to have more place fields relative to controls. **(c)** Analysis of place cell dynamics reveals the DNRAb place cells have larger place field size and lower SI across OPM trials T1–T3. Mean firing rate (MFR) in DNRAb mice is reduced in T1, but higher in T2 and T3, while peak firing rate (PFR) is significantly increased only in T3. **(d)** Left, visualization of place cell center of mass (COM) shift during OPM task. A higher proportion of control place cells shifted towards the moved object than DNRAb. Right, radial plots demonstrating the increased bias of COM shift angle in control compared to DNRAb place cells. **(e)** Summed count of cell COM shift angle away from 150° (direction of the moved object) demonstrates a significant difference between DNRAb and control groups.

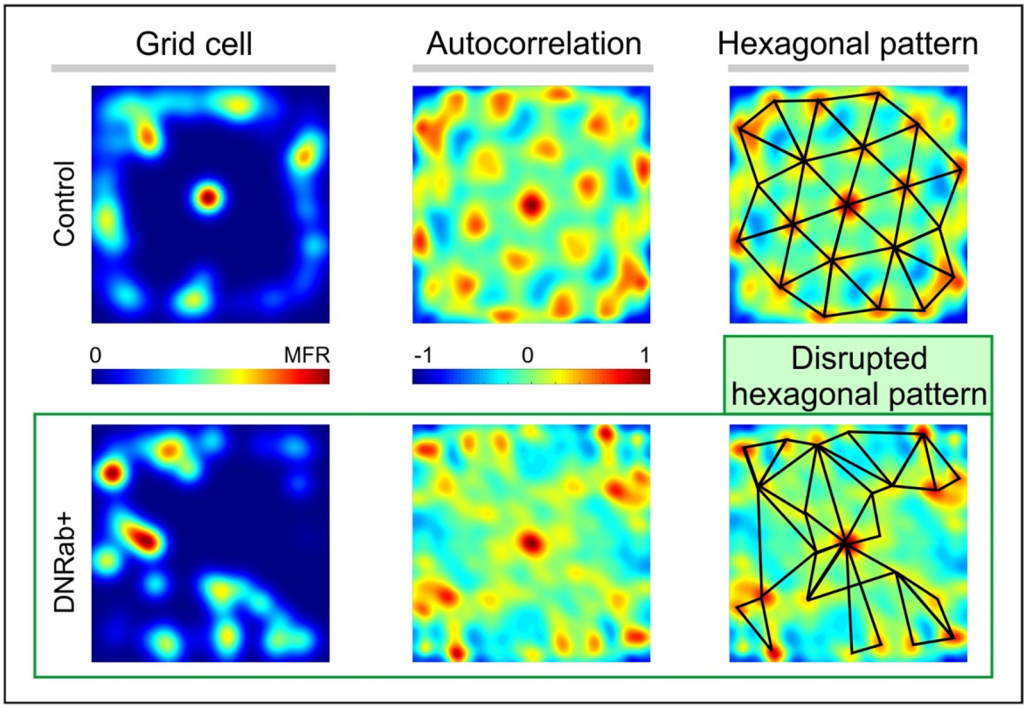

Fig. 10: Disruption of grid cell system in the entorhinal cortex of DNRAb mice. ***Left,*** representative example of grid cells recorded in the medial entorhinal cortex of control mice and DNRAb mice; MFR = maximal fire rate for a neuron. Middle, autocorrelation of the firing of the neuron at left showing local correlation peaks, color scale represents correlation level (-1 = anticorrelation, 0 = no correlation, 1 = completely correlated). Right, hexagonal structures show a neat pattern for the grid cell from the control mouse and a totally disrupted pattern for the DNRAb grid cell.

3.2.12. Other achievements. Contributions of sex chromosomes and gonadal hormones to the male bias in a maternal antibody-induced model of autism spectrum disorder. We are extremely grateful that we have been allowed to include studies on the maternal transmission of neurotoxic antibodies from mothers to infants in this Impact Award. The general concept is that certain maternal antibodies can have toxic effects in the developing fetal brain. We have made brisk progress in this annexed goal.

During the project, we have published a study (Garcia-Gata et al.) in which we evaluated the sex chromosomal and hormonal influences on the male bias in a murine model of ASD, in which mice were exposed in utero to a maternal antibody reactive to contactin-associated protein-like 2 (Caspr2), which was originally cloned from a mother of a child with ASD. In this paradigm, only male mice are affected. We used the four-core-genotypes (FCG) model in which the *Sry* gene is deleted from the Y chromosome and inserted into the autosome 3 (TgSry). Thus, by combining the Caspr2 and FCG models, we were able to differentiate the contributions of sex chromosomes and gonadal hormones to the development of fetal brain and adult behavioral phenotypes. This study is highly relevant to our analysis of NPSLE, which affects mainly females. We plan to use the FCG model in combination with the lupus-prone strains, or the DNRAb mice, to investigate the role of the sex chromosomes in setting up the brain-related manifestations in lupus.

3.2.13. Other achievements. Maternally transmitted autoantibodies can alter the brain vasculature and neural dynamics in the offspring: This set of experiments is extremely relevant to understanding how autoantibodies can be transmitted from a pregnant mother, in particular a woman that carries SLE autoantibodies, to the brain of the developing fetus during the pregnancy. The fetal brain is constantly exposed to maternal IgG prior to the formation of an effective blood-brain barrier. In this study, we examined the consequences of fetal brain exposure to an autoantibody that binds the

astrocytic protein aquaporin-4 (AQP4). The antibody was cloned as immunoglobulin G (hence it was termed AQP4-IgG) from a patient with neuromyelitis optica spectrum disorder, an autoimmune disease that can affect women of childbearing age. We first showed that embryonic radial glia in neocortex express AQP4. These glial cells are critical for blood vessel remodeling and the formation of the blood-brain barrier, through modulation of the wnt signaling pathway. Male fetuses exposed to AQP4-IgG had abnormal cortical vasculature and lower expression of wnt signaling molecules Wnt5a and Wnt7a. Positron emission tomography of adult male mice exposed *in utero* to AQP4-IgG revealed increased blood flow and leakiness of the blood-brain barrier in the entorhinal cortex. Behaviorally, the AQP4-IgG-exposed males were impaired in the object-place memory task. Neural recordings indicated that their grid cell system, within the medial entorhinal cortex, did not map the local environment appropriately. Collectively, these data implicated *in utero* binding of AQP4-IgG to radial glia as a mechanism for alterations of the developing male brain, with the entorhinal cortex a particularly sensitive area. This study, with Dr. Simone Mader as the first author, has been published in *Science Translational Medicine* and it is attached in the section of Appendices. Dr. Joshua Strohl, a member of my team, conducted all the behavioral assessments and *in vivo* recordings of the AQP4-IgG-exposed mice.

What opportunities for training and professional development has the project provided?
If the project was not intended to provide training and professional development opportunities or there is nothing significant to report during this reporting period, state "Nothing to Report."

Describe opportunities for training and professional development provided to anyone who worked on the project or anyone who was involved in the activities supported by the project. "Training" activities are those in which individuals with advanced professional skills and experience assist others in attaining greater proficiency. Training activities may include, for example, courses or one-on-one work with a mentor. "Professional development" activities result in increased knowledge or skill in one's area of expertise and may include workshops, conferences, seminars, study groups, and individual study. Include participation in conferences, workshops, and seminars not listed under major activities.

This Impact Award has opened major opportunities for training the personnel directly involved in this project, and other lab members that have helped the project to move forward, so they have all become proficient in executing all the aspects of the proposed studies. P. Huerta has mentored Dr. Joshua Strohl in performing studies in *ex vivo* hippocampal slices and *in vivo* neural recordings. Importantly, Dr. Strohl received a T32 training award from the NIH, partly because of his involvement in this project. P. Huerta has also mentored Mr. Pedro Gómez and Mr. Joshua Glynn (an M.D./Ph.D. graduate student) to perform behavioral assessments and *in vivo* neural recordings. Strohl, Gómez, and Glynn are now able to operate with independence in the completion of their tasks. P. Huerta has also trained Mr. Joseph Gallagher, a research assistant, to the point that ne reached an expert level, running experiments with no supervision. Gallagher is currently applying to several graduate programs in neuroscience. P. Huerta also trained Ms. Fatimah Copin (medical student) and Ms. Elizabeth LaRegina (high school student) who joined the Summer Intern Program at the Feinstein Institutes.

There were several professional development activities associated with P. Huerta. Importantly, the PI gave talks about the lupus work performed in the lab at several conferences. For instance, the PI talked at the 12th European Lupus Meeting (Bruges, Belgium), he participated in the symposium "NeuroSLE" at the 14th Congress on SLE and the 6th CORA Congress (Venice, Italy & Virtual), the PI talked at the 49th Meeting of the European Brain and Behaviour Society (Lausanne, Switzerland & Virtual), and he gave a talk in the FENS Forum 2022 (Paris, France). The PI gave a virtual zoom talk about the lupus work, centered on the behavioral assessments, under the name "EthoVision Mini Conference Zoom Meeting", which was organized by Collen McSweeney and Brooke April of the company Noldus.

How were the results disseminated to communities of interest?
If there is nothing significant to report during this reporting period, state "Nothing to Report."

Describe how the results were disseminated to communities of interest. Include any outreach activities that were undertaken to reach members of communities who are not usually aware of these project activities, for the purpose of enhancing public understanding and increasing interest in learning and careers in science, technology, and the humanities.

During the project, we had several scientific publications. In the first year of the project, we had a major publication by Chan et al. in *Nature Communications* (11:1403, 2020), which is entirely relevant to the specific aims of this project, and for which my laboratory contributed the behavioral assessments and *in vivo* recordings of the DNRAb mice (this paper is included in section of Appendices). In the third year of the project, we had a major publication by Mader et al. in *Science Translational Medicine* (14(641):eabe9726, 2022), which is also relevant to the specific aims of this project, and for which my laboratory contributed the behavioral assessments and *in vivo* recordings of mice (this paper is included in section of Appendices). Moreover, we would like to highlight our collaboration with Dr. Anne Davidson which produced the manuscript entitled "Reversible dysregulation of renal circadian rhythm in lupus nephritis", published in *Molecular Medicine.* (27(1):99, 2021). This work is focused on how the renal dysfunction in lupus is affected by brain-related processes that occur in day-and-night cyclical fashion (circadian rhythms). My laboratory contributed the behavioral assessments of NZB/W mice and the data analysis (this paper is included in section of Appendices).

In terms of outreach programs, we were able to accept two summer students through the Feinstein Summer Intern Program only during the summer of 2022. We were not able to accept students in the previous two years due to the physical restrictions imposed by the Covid19 pandemic. Nevertheless, the PI joined the Steering Committee for a T32 training grant in Translational Immunology, recently awarded to the Feinstein Institutes by the NIH (1T32AI155392-01A1, Project leader: Dr. Anne Davidson). The PI's is actively involved in the goal "to recruit trainees who are diverse with respect to demographics, experience and interests". The PI has contacted the appropriate persons at several colleges in New York state with a representation of minority students, with the purpose of inviting promising young students of Hispanic/Latino heritage to participate in summer research programs at the Feinstein. For instance, we have established an intern program with the coordination with Dr. Risa Stein, the Director of the Science and Technology Entry Program at Farmingdale State College. This represents an initial step in fulfilling our goal of mentoring and creating a new generation of translational immunologists of diverse backgrounds. The PI also networked informally with several patients suffering lupus and invited them to the laboratory to witness the projects going on with murine models. The patients were highly interested and supportive of the work performed in the lab, and the lab members were moved by these experiences and energized to work harder to find the cure for the disease.

What do you plan to do during the next reporting period to accomplish the goals?
If this is the final report, state "Nothing to Report."

Describe briefly what you plan to do during the next reporting period to accomplish the goals and objectives.

In the last phase of the Award, we finished our studies of the different NPSLE murine cohorts by applying a multi-level neural analysis, including behavioral and neurophysiological approaches (*ex vivo* hippocampal slices, *in vivo* neural recordings). Also, we finished our studies on maternal transfer of antibodies from the pregnant mother to the brain of the offspring, as the concept that the fetal brain might be disrupted by maternal neurotoxic antibodies has high translation potential. We are almost finished with the data analysis process and plan to submit several manuscripts during 2023.

4. **IMPACT:** D*escribe distinctive contributions, major accomplishments, innovations, successes, or any change in practice or behavior that has come about as a result of the project relative to:*

What was the impact on the development of the principal discipline(s) of the project?
If there is nothing significant to report during this reporting period, state "Nothing to Report."

Describe how findings, results, techniques that were developed or extended, or other products from the project made an impact or are likely to make an impact on the base of knowledge, theory, and research in the principal disciplinary field(s) of the project. Summarize using language that an intelligent lay audience can understand (Scientific American style).

We think this project has made highly impactful contributions to our basic knowledge on neuropsychiatric lupus and how maternally transferred antibodies can affect the developing brain. We believe our studies have the potential to open new avenues for the establishment of brain-related biomarkers for these insidious aspects of lupus. The concept that brain-related symptoms in lupus, such as impaired cognition, are localized to specific brain regions that encode and consolidate memory continues to gain momentum and it is likely to bring a deep understanding of the cellular and network processes that are affected by the disease. More generally, we think our studies in animal models of lupus can make an impact and guide the discovery of rational cures for the complex set of syndromes that define neuropsychiatric lupus in humans. An intriguing finding from our brain studies in mouse models is the observation that the phenomenon anecdotally referred to as 'brain fog' by lupus patients might have a neural substrate, at least in the spatial domain, which corresponds to aberrant oscillatory patterns that occur during episodes of memory acquisition. Moreover, the high impact of the findings that were published during this project has led the PI to being invited to give plenary talks at international conferences (listed in point 6.3), in which he has been able to highlight the role of autoimmunity on brain dysfunction.

What was the impact on other disciplines?
If there is nothing significant to report during this reporting period, state "Nothing to Report."

Describe how the findings, results, or techniques that were developed or improved, or other products from the project made an impact or are likely to make an impact on other disciplines.

Our studies also have the potential to strongly impact the discipline of neuro-immunology, which deals with the interactions between immune cells and the nervous system. Established neuro-immunology studies tend to emphasize the role of long-term inflammation within the brain as a trigger for neuro-pathologies; however, there has been an increasing interest on acute inflammation events, such as those related to the entry of autoantibodies to the brain, and the perturbances of the blood-brain barrier associated with these insults, that may help pathologies that are not necessarily linked to chronic inflammation. We think that the different lupus models, which express varying degrees of systemic inflammation (and possibly brain inflammation), offer a perfect template to study these issues.

What was the impact on technology transfer?
If there is nothing significant to report during this reporting period, state "Nothing to Report."

Describe ways in which the project made an impact, or is likely to make an impact, on commercial technology or public use, including:

- *transfer of results to entities in government or industry;*
- *instances where the research has led to the initiation of a start-up company; or*
- *adoption of new practices.*

Nothing to Report

What was the impact on society beyond science and technology?
If there is nothing significant to report during this reporting period, state "Nothing to Report."

Describe how results from the project made an impact, or are likely to make an impact, beyond the bounds of science, engineering, and the academic world on areas such as:

- *improving public knowledge, attitudes, skills, and abilities;*
- *changing behavior, practices, decision making, policies (including regulatory policies), or social actions; or*
- *improving social, economic, civic, or environmental conditions.*

Nothing to Report

5. **CHANGES/PROBLEMS:** *The PD/PI is reminded that the recipient organization is required to obtain prior written approval from the awarding agency grants official whenever there are significant changes in the project or its direction. If not previously reported in writing, provide the following additional information or state, "Nothing to Report," if applicable:*

Changes in approach and reasons for change
Describe any changes in approach during the reporting period and reasons for these changes. Remember that significant changes in objectives and scope require prior approval of the agency.

Our project proceeded as planned without major changes in the approach. However, we faced some unexpected delays in the implementation of our experiments due to the sporadic restrictions imposed by the Covid pandemic, but we were able to catch up with most of our experimental program. Under problematic issue that occurred because the Covid pandemic is that we were unable to work on the ARPAb mice, as we could not obtained the mice from our colleagues in Chile. Nevertheless, we would like to emphasize how grateful we are to the grant official for authorizing us to also report our studies on the maternal transmission of antibodies from mothers to infants, which represents an extension of our initial goals.

Actual or anticipated problems or delays and actions or plans to resolve them
Describe problems or delays encountered during the reporting period and actions or plans to resolve them.

Nothing to Report

Changes that had a significant impact on expenditures
Describe changes during the reporting period that may have had a significant impact on expenditures, for example, delays in hiring staff or favorable developments that enable meeting objectives at less cost than anticipated.

Nothing to Report

Significant changes in use or care of human subjects, vertebrate animals, biohazards, and/or select agents
Describe significant deviations, unexpected outcomes, or changes in approved protocols for the use or care of human subjects, vertebrate animals, biohazards, and/or select agents during the reporting period. If required, were these changes approved by the applicable institution committee (or equivalent) and reported to the agency? Also specify the applicable Institutional Review Board/Institutional Animal Care and Use Committee approval dates.

Significant changes in use or care of human subjects

Nothing to Report

Significant changes in use or care of vertebrate animals

Nothing to Report

Significant changes in use of biohazards and/or select agents

Nothing to Report

6. **PRODUCTS:** *List any products resulting from the project during the reporting period. If there is nothing to report under a particular item, state "Nothing to Report."*

- **Publications, conference papers, and presentations**
  Report only the major publication(s) resulting from the work under this award.

  Journal publications. *List peer-reviewed articles or papers appearing in scientific, technical, or professional journals. Identify for each publication: Author(s); title; journal; volume: year; page numbers; status of publication (published; accepted, awaiting publication; submitted, under review; other); acknowledgement of federal support (yes/no).*

Chang EH, Carreiro ST, Frattini SA, Huerta PT. Assessment of glutamatergic synaptic transmission and plasticity in brain slices: relevance to bioelectronic approaches. *Bioelectronic Medicine*. 5:6, 2019. doi: 10.1186/s42234-019-0022-2. Federal support acknowledgement.

Sankowski R, Huerta TS, Kaira R, Klein TJ, Strohl JJ, Al-Abed Y, Robbiati S, Huerta PT. Large-scale validation of the paddling pool task in the clockmaze for studying hippocampus-based spatial cognition in mice. *Frontiers in Behavioral Neuroscience.* 13:121, 2019. doi: 10.3389/fnbeh.2019.00121. Federal support acknowledgement.

Sankowski R, Strohl JJ, Huerta TS, Nasiri E, Mazzarello AN, D'Abramo C, Cheng KF, Staszewski O, Prinz M, Huerta PT, Al-Abed Y. Endogenous retroviruses are associated with hippocampus-based memory impairment. *Proceedings of the National Academy of Sciences USA*. 116(51):25982–25990, 2019. doi: 10.1073/pnas.1822164116. Federal support acknowledgement.

Chan K, Nestor J, Huerta TS, Certain N, Moody G, Kowal C, Huerta PT, Volpe BT, Diamond B, Wollmuth LP. Lupus autoantibodies act as positive allosteric modulators at GluN2A-containing NMDA receptors and impair spatial memory. *Nature Communications*. 11(1):1403, 2020. doi: 10.1038/s41467-020-15224-w. Federal support acknowledgement. [Included in the appendices]

Nasiri E, Sankowski R, Dietrich H, Oikonomidi A, Huerta PT, Popp J, Al-Abed Y, Bacher M. Key role of MIF-related neuroinflammation in neurodegeneration and cognitive impairment in Alzheimer's disease. *Molecular Medicine*. 26(1):34, 2020. doi: 10.1186/s10020-020-00163-5. No federal support acknowledgement.

Bagnall-Moreau C, Huerta PT, Comoletti D, La-Bella A, Berlin R, Zhao C, Volpe BT, Diamond B, Brimberg L. In utero exposure to endogenous maternal polyclonal anti-Caspr2 antibody leads to behavioral abnormalities resembling autism spectrum disorder in male mice. *Scientific Reports*. 10(1):14446, 2020. doi: 10.1038/s41598-020-71201-9. No federal support acknowledgement.

Mishra R, Bethunaickan R, Berthier CC, Yi Z, Strohl JJ, Huerta PT, Zhang W, Davidson A. Reversible dysregulation of renal circadian rhythm in lupus nephritis. *Molecular Medicine.* 27(1):99, 2021. doi: 10.1186/s10020-021-00361-9. Federal support acknowledgement. [Included in the appendices]

Gata-Garcia A, Porat A, Brimberg L, Volpe BT, Huerta PT, Diamond B. Contributions of sex chromosomes and gonadal hormones to the male bias in a maternal antibody-induced model of autism spectrum disorder. *Frontiers in Neurology.* 12:721108, 2021. doi: 10.3389/fneur.2021.721108. Federal support acknowledgement. [Included in the appendices]

Lara-Vasquez A, Espinosa N, Morales C, Moran C, Billeke P, Gallagher J, Strohl JJ, Huerta PT, Fuentealba P. Cortical dynamics underlying social behavior in dominance hierarchy and spatial navigation. *bioRxiv* 2020.06.12.147249; doi: https://doi.org/10.1101/2020.06.12.147249. No federal support acknowledgement.

Chan K, Nestor J, Huerta TS, Certain N, Moody G, Kowal C, Huerta PT, Volpe BT, Diamond B, Wollmuth LP. Lupus auto-antibodies act as positive allosteric modulators at NMDA receptors and induce spatial memory deficits. *bioRxiv* 202010.1101/791715; doi: https://doi.org/10.1101/791715. Federal support acknowledgement.

Strohl JJ, Gallagher JT, Gómez PN, Glynn JM, Huerta PT. Framework for automated sorting of neural spikes from Neuralynx-acquired tetrode recordings in freely-moving mice. *Bioelectronic Medicine*. 7:17, 2021; doi.org/10.1186/s42234-021-00079-3. Federal support acknowledgement. [Included in the appendices]

Mader S, Brimberg L, Vo A, Strohl JJ, Crawford JM, Bonnin A, Carrión J, Campbell D, Huerta TS, La Bella A, Dewey SL, Hellman M, Eidelberg D, Dujmovic I, Drulovic J, Bennett JL, Volpe BT, Huerta PT, Diamond B. In utero exposure to maternal anti-aquaporin-4 antibodies alters brain vasculature and neural dynamics in male mouse offspring. *Science Translational Medicine* 14(641):eabe9726, 2022. doi: 10.1126/scitranslmed.abe9726. Federal support acknowledgement. [Included in the appendices]

Books or other non-periodical, one-time publications. *Report any book, monograph, dissertation, abstract, or the like published as or in a separate publication, rather than a periodical or series. Include any significant publication in the proceedings of a one-time conference or in the report of a one-time study, commission, or the like. Identify for each one-time publication: author(s); title; editor; title of collection, if applicable; bibliographic information; year; type of publication (e.g., book, thesis or dissertation); status of publication (published; accepted, awaiting publication; submitted, under review; other); acknowledgement of federal support (yes/no).*

Strohl, Joshua J. (2020), "*Sepsis, cognition and brain dynamics*" [doctoral thesis], Department of Molecular Medicine, Donald and Barbara Zucker School of Medicine at Hofstra/Northwell, New York, April 16, 2020. No federal support acknowledgement.

Huerta, P.T. (2021), "*Discover your passion for science*". Chapter 2 in "Hispanic Role Models in Science: Advice for future scientists", Paola Mina-Osorio (editor), Part of: Hispanics in Medicine and Science (collection), Science Education Online (publisher), ISBN 978-1735172866, 2021, book. No federal support acknowledgement.

Other publications, conference papers and presentations. *Identify any other publications, conference papers and/or presentations not reported above. Specify the status of the publication as noted above. List presentations made during the last year (international, national, local societies, military meetings, etc.). Use an asterisk (*) if presentation produced a manuscript.*

Presentations by PI during award period:

Huerta, PT (2019): talk at the *48th Meeting of the European Brain and Behaviour Society*, Prague, Czech Republic (international conference).

Huerta, PT (2020): talk in the *12th European Lupus Meeting*, Bruges, Belgium (international conference)

Huerta, PT (2020): talk at the *EthoVision Mini Conference Zoom Meeting* (virtual national conference).

Huerta, PT (2021): talk entitled "Autoantibody-induced disruption of spatial encoding as a biomarker for neuropsychiatric lupus" in the *14th Congress on SLE & the 6th CORA Congress*, 6–9 October 2021, Venice, Italy & Virtual (international conference).

Huerta, PT (2021): talk entitled "Know your place. Studies of the neural substrate for spatial cognition in health and disease", Research-in-Progress talk at Northwell Health (local conference).

Huerta, PT (2022): talk entitled "Spatial cognitive impairment associated with lupus" in the *FENS Forum 2022*, 9–13 July 2022, Paris, France (international conference).

Presentations to conferences by lab members during award period:

Strohl JJ, Huerta PT (2021): presentation entitled "Disrupted neural encoding of immune signals in vagus nerve after sepsis" in the 50th Annual Meeting of the Society for Neuroscience, 8–11 November 2021 (virtual international conference).

Strohl JJ, Huerta PT (2022): presentation entitled "HMGB1 mediates disruption of spatial coding in the hippocampus of sepsis-surviving mice" in the 45th Annual Conference on Shock, 17–20 June 2022, Toronto, Canada (international conference).

Glynn JM, Gómez PN, Strohl JJ, Huerta PT (2022): presentation entitled "Gut microbiome depletion leads to altered neural dynamics and metabolism in the hippocampus" in the 45th Annual Conference on Shock, 17–20 June 2022, Toronto, Canada (international conference).

Gómez PN, Glynn JM, Strohl JJ, Huerta PT (2022): presentation entitled "Impaired cognition after sepsis is prevented by neuron-specific ablation of HMGB1" in the 45th Annual Conference on Shock, 17–20 June 2022, Toronto, Canada (international conference).

Strohl JJ, Gómez PN, Huerta PT (2022): presentation entitled "Metabolic and oscillatory disruptions of the brain fear network in long-sepsis survivors" in the FENS Forum 2022, 9–13 July 2022, Paris, France (international conference).

Glynn JM, Carrión J, Strohl JJ, Huerta PT (2022): presentation entitled "Gut microbiome depletion alters neural dynamics and metabolism in CA1 field of the hippocampus" in the FENS Forum 2022, 9–13 July 2022, Paris, France (international conference).

Gómez PN, Huerta TS, Strohl JJ, and Huerta PT (2022): presentation entitled "Disruption of hippocampus-based spatial coding in long–sepsis survivors is mediated by HMGB1. Comparisons with lupus-based cognitive impairment" in the FENS Forum 2022, 9–13 July 2022, Paris, France (international conference).

Huerta TS, Strohl JJ, and Huerta PT (2022): presentation entitled "Lupus-associated cognitive impairment linked to systems-level dysfunctions in theta-gamma coupling and place cell dynamics in the CA1 field of the hippocampus" in the FENS Forum 2022, 9–13 July 2022, Paris, France (international conference).

- **Website(s) or other Internet site(s)**
  List the URL for any Internet site(s) that disseminates the results of the research activities. A short description of each site should be provided. It is not necessary to include the publications already specified above in this section.

  Nothing to Report

- **Technologies or techniques**
  Identify technologies or techniques that resulted from the research activities. Describe the technologies or techniques were shared.

  Nothing to Report

- **Inventions, patent applications, and/or licenses**
  Identify inventions, patent applications with date, and/or licenses that have resulted from the research. Submission of this information as part of an interim research performance progress report is not a substitute for any other invention reporting required under the terms and conditions of an award.

  Nothing to Report

- **Other Products**
  Identify any other reportable outcomes that were developed under this project. Reportable outcomes are defined as a research result that is or relates to a product, scientific advance, or research tool that makes a meaningful contribution toward the understanding, prevention, diagnosis, prognosis, treatment and /or rehabilitation of a disease, injury or condition, or to improve the quality of life. Examples include:
  - *data or databases;*
  - *physical collections;*
  - *audio or video products;*
  - *software;*
  - *models;*
  - *educational aids or curricula;*
  - *instruments or equipment;*
  - *research material (e.g., Germplasm; cell lines, DNA probes, animal models);*
  - *clinical interventions;*
  - *new business creation; and*
  - *other.*

  Nothing to Report

7. PARTICIPANTS & OTHER COLLABORATING ORGANIZATIONS

What individuals have worked on the project?

Provide the following information for: (1) PDs/PIs; and (2) each person who has worked at least one person month per year on the project during the reporting period, regardless of the source of compensation (a person month equals approximately 160 hours of effort). If information is unchanged from a previous submission, provide the name only and indicate "no change".

Example:

Name:	*Mary Smith*
Project Role:	*Graduate Student*
Researcher Identifier (e.g. ORCID ID):	*1234567*
Nearest person month worked:	*5*
Contribution to Project:	*Ms. Smith has performed work in the area of combined error-control and constrained coding.*
Funding Support:	*The Ford Foundation (Complete only if the funding support is provided from other than this award.)*

Name:	Patricio T. Huerta
Project Role:	PD/PI
Researcher Identifier (ORCID ID):	0000-0003-0270-2308
Nearest person month worked:	6
Contribution to Project:	Dr. Huerta has performed behavioral assessments, electrophysiological studies in *ex vivo* slices, and *in vivo* neural recordings in freely moving mice. He has performed data analysis. He has written papers.
Funding Support:	Partial NIH/NIAID support
Name:	Joshua J. Strohl
Project Role:	Postdoctoral fellow
Researcher Identifier (ORCID ID):	N/A
Nearest person month worked:	6
Contribution to Project:	Dr. Strohl has performed the electrophysiological studies with ex vivo hippocampal slices and in vivo neural recordings in freely moving mice. He has performed data analysis.
Funding Support:	Partial NIH/NIAID support
Name:	Pedro Gómez
Project Role:	Research associate
Researcher Identifier (ORCID ID):	N/A
Nearest person month worked:	6
Contribution to Project:	Mr. Gómez has performed behavioral assessments and data analysis. He has been trained for electrophysiological studies.
Funding Support:	Partial NIH/NIAID support

Name:	Joseph Gallagher
Project Role:	Research associate
Researcher Identifier (ORCID ID):	N/A
Nearest person month worked:	6
Contribution to Project:	Mr. Gallagher has performed behavioral assessments and data analysis. He has been trained for electrophysiological studies.
Funding Support:	Most of Gallagher support is from an NIH/NIAID grant

Has there been a change in the active other support of the PD/PI(s) or senior/key personnel since the last reporting period?
If there is nothing significant to report during this reporting period, state "Nothing to Report."

If the active support has changed for the PD/PI(s) or senior/key personnel, then describe what the change has been. Changes may occur, for example, if a previously active grant has closed and/or if a previously pending grant is now active. Annotate this information so it is clear what has changed from the previous submission. Submission of other support information is not necessary for pending changes or for changes in the level of effort for active support reported previously. The awarding agency may require prior written approval if a change in active other support significantly impacts the effort on the project that is the subject of the project report.

Nothing to Report

What other organizations were involved as partners?
If there is nothing significant to report during this reporting period, state "Nothing to Report."

Describe partner organizations – academic institutions, other nonprofits, industrial or commercial firms, state or local governments, schools or school systems, or other organizations (foreign or domestic) – that were involved with the project. Partner organizations may have provided financial or in-kind support, supplied facilities or equipment, collaborated in the research, exchanged personnel, or otherwise contributed.

Provide the following information for each partnership:
Organization Name:
Location of Organization: (if foreign location list country)
Partner's contribution to the project (identify one or more)

- *Financial support;*
- *In-kind support (e.g., partner makes software, computers, equipment, etc., available to project staff);*
- *Facilities (e.g., project staff use the partner's facilities for project activities);*
- *Collaboration (e.g., partner's staff work with project staff on the project);*
- *Personnel exchanges (e.g., project staff and/or partner's staff use each other's facilities, work at each other's site); and*
- *Other.*

Nothing to Report

8. SPECIAL REPORTING REQUIREMENTS

COLLABORATIVE AWARDS: *For collaborative awards, independent reports are required from BOTH the Initiating Principal Investigator (PI) and the Collaborating/Partnering PI. A duplicative report is acceptable; however, tasks shall be clearly marked with the responsible PI and research site. A report shall be submitted to* ***https://ebrap.org/eBRAP/public/index.htm*** *for each unique award.*

QUAD CHARTS: *If applicable, the Quad Chart (available on https://www.usamraa.army.mil/Pages/Resources.aspx) should be updated and submitted with attachments.*

9. APPENDICES: *Attach all appendices that contain information that supplements, clarifies or supports the text. Examples include original copies of journal articles, reprints of manuscripts and abstracts, a curriculum vitae, patent applications, study questionnaires, and surveys, etc.*

9.1. Published paper by Chan et al.

9.2. Published paper by Strohl et al.

9.3. Published paper by Mishra et al.

9.4. Published paper by Gata-Garcia et al.

9.5. Published paper by Mader et al.

nature COMMUNICATIONS

ARTICLE

https://doi.org/10.1038/s41467-020-15224-w OPEN

Lupus autoantibodies act as positive allosteric modulators at GluN2A-containing NMDA receptors and impair spatial memory

Kelvin Chan[1,2,3,10], Jacquelyn Nestor[4,5,10], Tomás S. Huerta[4], Noele Certain[3,6], Gabrielle Moody[3,6], Czeslawa Kowal[5], Patricio T. Huerta[4,5], Bruce T. Volpe[7], Betty Diamond[5,11✉] & Lonnie P. Wollmuth[3,8,9,11✉]

Patients with Systemic lupus erythematosus (SLE) experience various peripheral and central nervous system manifestations including spatial memory impairment. A subset of autoantibodies (DNRAbs) cross-react with the GluN2A and GluN2B subunits of the NMDA receptor (NMDAR). We find that these DNRAbs act as positive allosteric modulators on NMDARs with GluN2A-containing NMDARs, even those containing a single GluN2A subunit, exhibiting a much greater sensitivity to DNRAbs than those with exclusively GluN2B. Accordingly, GluN2A-specific antagonists provide greater protection from DNRAb-mediated neuronal cell death than GluN2B antagonists. Using transgenic mice to perturb expression of either GluN2A or GluN2B in vivo, we find that DNRAb-mediated disruption of spatial memory characterized by early neuronal cell death and subsequent microglia-dependent pathologies requires GluN2A-containing NMDARs. Our results indicate that GluN2A-specific antagonists or negative allosteric modulators are strong candidates to treat SLE patients with nervous system dysfunction.

[1] Graduate Program in Neuroscience, Stony Brook University, Stony Brook, NY 11794-5230, USA. [2] Medical Scientist Training Program (MSTP), Stony Brook University, Stony Brook, NY 11794-5230, USA. [3] Department of Neurobiology & Behavior, Stony Brook University, Stony Brook, NY 11794-5230, USA. [4] Donald & Barbara Zucker School of Medicine, Hofstra University, Hempstead, NY 11549, USA. [5] Center for Autoimmune, Musculoskeletal and Hematopoietic Diseases, Feinstein Institute for Medical Research, Northwell Health, Manhasset, NY 11030, USA. [6] Graduate Program in Molecular and Cellular Pharmacology, Stony Brook University, Stony Brook, NY 11794-5230, USA. [7] Center for Biomedical Science, Feinstein Institute for Medical Research, Northwell Health, Manhasset, NY 11030, USA. [8] Department of Biochemistry & Cell Biology, Stony Brook University, Stony Brook, NY 11794-5230, USA. [9] Center for Nervous System Disorders, Stony Brook University, Stony Brook, NY 11794-5230, USA. [10] These authors contributed equally: Kelvin Chan, Jacquelyn Nestor. [11] These authors jointly supervised this work: Betty Diamond, Lonnie P. Wollmuth. ✉email: lonnie.wollmuth@stonybrook.edu; BDiamond@northwell.edu

Systemic lupus erythematosus (SLE) is an autoimmune disease characterized by the presence of autoantibodies directed against multiple self-antigens, including DNA[1]. These autoantibodies affect multiple organ systems such that SLE patients experience arthritis, renal disease, anemia, rashes, and neuropsychiatric symptoms, including memory disorders and spatial memory impairment[2–4]. The prevalence of diffuse nervous system disorders is reported from 20–90%, depending on the particular functional assessment[5–7]. These cognitive defects in both clinical and pre-clinical conditions are often associated with DNRAb, anti-double-stranded DNA (dsDNA) antibodies with cross-reactivity to NMDA receptors (NMDAR)[8–14].

The role of DNRAbs in contributing to neuropsychiatric symptoms in SLE have largely been studied in mice models that endogenously synthesize DNRAbs and in mice exposed to patient-derived DNRAbs[8,10,11]. Patient-derived DNRAbs are IgG1 antibodies cloned from patient B cells that display reactivity to dsDNA and NMDARs[15,16]. Specific regions of the brain in mice are targeted based on the experimental method used to trigger blood brain barrier permeability—lipopolysaccharide (LPS) causes DNRAbs to deposit in the hippocampus while epinephrine causes DNRAbs to deposit in the amygdala[11,17]. Non-invasive imaging of SLE patients have revealed hippocampal atrophy and parahippocampal microstructural defects, conferring an advantage to using LPS in disease models[4,18].

LPS-treated mice immunized to generate DNRAbs and patient-derived DNRAbs display a gamut of pathologies in the hippocampus: aberrant excitatory signaling, apoptosis, dendritic pruning, and microglial activation[10,11,19]. These mice also display expanded place fields in the hippocampus and defects in spatial memory[2,19]. These studies are essential to defining the pathology of the neuropsychiatric component of SLE, but do not define the specific NMDARs that mediate these effects. This information is critical to potentially develop therapies to treat and prevent neuropsychiatric symptoms associated with DNRAbs.

NMDARs are ionotropic glutamate receptors that are central to excitatory synaptic transmission in the brain. NMDARs are heterotetramers composed of two obligate GluN1 subunits and typically two GluN2 subunits of the same or different subtype (GluN2A, B, C, or D)[20,21]. DNRAbs bind to both GluN2A and GluN2B subunits, with the epitope including a pentapeptide consensus sequence, DWEYS[10,11]. This antigenic target for DNRAbs is in the extracellularly located amino-terminal domain (ATD) of GluN2, an allosteric hub for modulating NMDAR function[21,22]. NMDARs containing GluN2A or GluN2B have distinct physiological, pharmacological, and signaling properties[22]. Nevertheless, the contribution of the different GluN2 subunits to the SLE-associated neuropathologies is unclear. Knockout studies in mice have suggested GluN2A to be the primary target for DNRAb-mediated adult and fetal neuronal cell death, though the evidence was limited[23]. Specific inhibitors of GluN2B also reduced DNRAb-mediated cell death, suggesting a significant contribution of GluN2B to the DNRAb-mediated phenotype[10]. All these results are ambiguous because of uncertainty of antibody concentrations in vivo and variations of DNRAb preparations used in different passive transfer experiments.

Here, we use a combination of heterologous expression systems and animal models to show subunit-specific susceptibility to DNRAb-mediated pathological effects. For heterologous expression, we tested a DNRAb (G11 and its B1 isotype control) derived from a human patient (see "Methods") in concentrations relevant to patient CSF levels[10]. We find that DNRAbs act as positive allosteric modulators (PAMs) at both GluN2A- and GluN2B-containing NMDARs, but that GluN2A-containing receptors have a much higher intrinsic sensitivity to DNRAb-mediated potentiation than GluN2B-containing NMDARs. Using a heterologous expression system to express triheteromeric GluN1/GluN2A/GluN2B, we find that a single GluN2A subunit confers high sensitivity to DNRAbs. We find that mice with a forebrain deletion of the GluN2B subunit display the full spectrum of DNRAb-mediated pathology, including acute loss of hippocampal CA1 neurons, dendritic abnormalities in surviving neurons, microglia activation, defective place cell fields, and impaired spatial memory. Conversely, GluN2A knockout mice are protected from the effects of DNRAbs. Thus, our work identifies the GluN2A subunit as the central mediator of NMDAR-associated nervous system pathology in SLE, supporting the use of GluN2A-specific negative allosteric modulators to treat SLE patients with brain dysfunction.

Results

DNRAbs preferentially potentiate GluN2A-containing NMDARs. DNRAbs bind to both GluN2A and GluN2B subunits[2,10]. To begin to address how these subunits contribute to DNRAb-induced phenotypes, we characterized the effect of a SLE patient-derived monoclonal DNRAb, G11, on heterologously expressed NMDARs composed of human NMDAR subunits, either hGluN1-1a/hGluN2A (hN1/hN2A) or hGluN1-1a/hGluN2B (hN1/hN2B). In parallel with antibody titers found in SLE patient CSF samples, we test the DNRAbs at concentrations from 1–100 μg/ml[10]. For macroscopic or whole-cell currents, exposure of hN1/hN2A NMDARs to 10 μg/ml of G11 (green traces) strongly potentiated glutamate-gated current amplitudes compared with baseline (Fig. 1a). In contrast, a similar exposure to N2B-containing receptors had no effect on current amplitudes (Fig. 1b). A matched concentration of an isotype control antibody, B1 (gray traces), had no effect on current amplitudes for either N2A- or N2B-containing receptors.

For N2A-containing receptors, current amplitudes showed significant potentiation even at 1 μg/ml compared with its matched control (Fig. 1c). In contrast, only at 100 μg/ml, did N2B-containing receptors show significant potentiation relative to its control (Fig. 1d). Overall, these results suggest that, in terms of receptor gating, N2A-containing receptors are about 100-fold more sensitive to DNRAbs than N2B-containing receptors.

DNRAbs might potentiate NMDAR activity by acting as an agonist at the glutamate ligand-binding domain. To test this idea, we measured leak currents in the absence of glutamate in parallel to peak current amplitudes (Supplementary Table 1), but found that changes in leak current over time were not different in the presence of DNRAbs and their matched control. Hence, DNRAbs by themselves do not act as NMDAR agonists.

DNRAbs act as positive allosteric modulators (PAMs). To further verify these actions of DNRAbs, we measured single-channel activity of N2A- or N2B-containing NMDARs exposed either to control antibody B1 or to G11 (Fig. 2a–d). These recording were made in the on-cell configuration in the continual presence of glutamate and glycine (as well as 0.05 mM EDTA)[24]. The equilibrium open probability (eq. P_{open}), an index of the ease of ion channel opening, with control antibody for wild-type hN1/hN2A (0.40 ± 0.07, $n = 6$) (mean ± SEM, $n =$ cells recorded) and hN1/hN2B (0.18 ± 0.04, $n = 6$) is comparable to previously published values[25]. At 10 μg/ml of G11, hN1/hN2A single-channel activity was significantly potentiated (Fig. 2a) relative to the matched control (Fig. 2c). For hN1/hN2B, we again saw no significant effect of G11 on receptor gating at 10 μg/ml (Fig. 2b, c). At 100 μg/ml (Fig. 2c), the weak potentiation was not significant reflecting in part the variability of single-channel recordings of N2B-containing receptors. These results further indicate that N2A-containing receptors are more sensitive to DNRAbs than N2B-containing receptors.

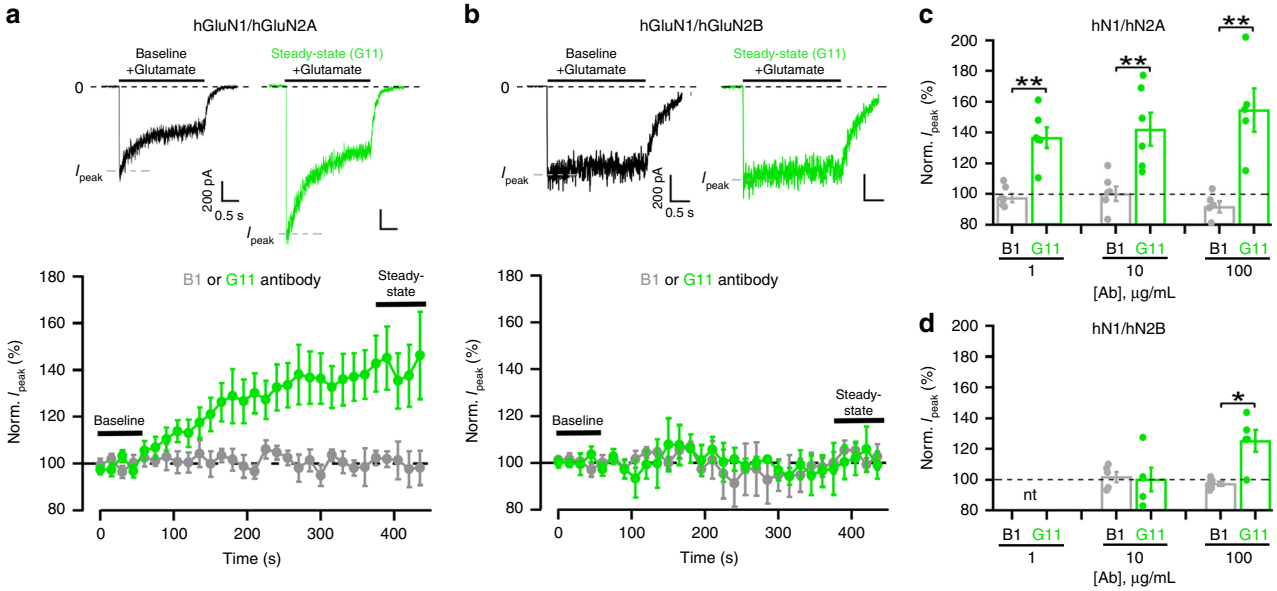

Fig. 1 Differential sensitivity of N2A- and N2B-containing NMDARs to DNRAbs. a, **b** Direct DNRAb application to NMDARs. Upper panels, whole-cell currents from HEK293 cells expressing human NMDAR subunits, either hGluN1/hGluN2A (**a**) or hGluN1/hGluN2B (**b**) at 10 µg/mL. Currents were elicited by a 2.5 s application of glutamate (1 mM) in the continuous presence of glycine (0.1 mM) (holding potential, −70 mV). Lower panels, control antibody B1 (IgG1, gray circles) or human-derived DNRAb G11 (green circles) were added 75 s after a baseline recording of five sweeps, and were included in the bath throughout the remaining period. Current amplitudes for individual recordings were normalized to its baseline. Values are mean ± SEM (hN2A + B1, $n = 6$; hN2A + G11, $n = 6$; hN2B + B1, $n = 5$; hN2B + G11, $n = 5$; n = cells recorded). Example traces in upper panels show the +G11 recordings for the initial sweep during baseline (no antibody present) or for the last sweep during steady-state (in antibody). Ca^{2+} is not present in the extracellular solution to minimize run-down over time. **c**, **d** Peak current amplitudes in N2A-containing NMDAR are more strongly potentiated than those in N2B-containing receptors. Bar graphs (mean ± SEM with dots indicating individual values) (from left to right for hN1/hN2A, $n = 6, 6, 6, 6, 5, 5$ cells recorded; and for hN1/hN2B, $n = 5, 5, 6, 5$ cells recorded) showing normalized steady-state peak current amplitudes either for control antibody (B1) or DNRAbs (G11). Significance of DNRAb values are measured relative to their respective control (*$p < 0.05$ or **$p < 0.01$, two-sided t test) (left to right for N2A, $p = 0.00137, 0.00932, 0.00906$; left to right for N2B, $p = 0.855, 0.0163$). nt, not tested.

To define how DNRAbs potentiate activity, we characterized single-channel details. Mean open time (MOT) was not significantly altered for either N2A- or N2B-containing receptors, whereas mean closed time (MCT) was significantly reduced for N2A-containing receptors at the highest concentration tested (Supplementary Table 2). Further, the frequency of opening was significantly enhanced for N2A-containing receptors (Fig. 2d). Thus, DNRAbs act by enhancing forward rates to the open state rather than by stabilizing the open channel.

A single copy of GluN2A confers high DNRAb sensitivity. At native synapses, NMDARs are typically composed of GluN1 in combination with different GluN2 subunits, often one GluN2A and one GluN2B subunit, so-called triheteromeric receptors[26,27]. We therefore tested whole-cell currents from triheteromeric receptors, where the receptor contains a single copy of GluN2A (Fig. 3a). To generate triheteromeric receptors, we used NMDAR constructs having coiled–coiled domains that permit only specific subunit combinations to reach the plasma membrane[28,29]. At 10 µg/ml of DNRAb, diheteromeric N2A-containing receptors containing the coiled–coiled domains showed significant potentiation. Diheteromeric N2B-containing receptors again showed no potentiation. In contrast, triheteromeric receptors containing a single copy of GluN2A showed significant potentiation. Thus, a single copy of GluN2A confers high sensitivity to DNRAbs.

DNRAbs modify receptor function via the DWEYS motif. DNRAb interact and presumably alter NMDAR function through the DWEYS motif in the amino-terminal domain. To directly test this idea, we introduced a charge reversal in the middle of the GluN2A DWEYS motif (DWDYS), mutating the negatively charged aspartate (D) at position 285 (DWDYS) to the positively charged lysine (K) (D285K). We avoided sites possibly involved in coordinating Zn^{2+} to mitigate confounding effects from Zn^{2+} modulation[30,31]. N2A(D285K) has no apparent effect on current properties (Supplementary Table 3). The G11 antibody shows robust binding to NMDARs (Fig. 3b, middle images). This binding is significantly attenuated in receptors containing D285K (Fig. 3b, right images, c). We did not find significant differences in the intrinsic binding of GluN2A or GluN2B-specific epitopes to G11 (Supplementary Fig. 1), suggesting that the difference in sensitivity primarily reflects gating. Receptors containing D285K are no longer significantly potentiated by DNRAbs (Fig. 3d), indicating that binding of DNRAbs to the DWEYS motif mediates the positive allosteric effect.

We also tested whether a single (triheteromeric receptor) or two (diheteromeric receptors) copies of the charge reversal are required to disrupt function. Consistent with the results for GluN2A/GluN2B triheteromeric receptors, a single copy of wild-type GluN2A confers full sensitivity to DNRAbs (Fig. 3e). Thus, in terms of stoichiometry, binding of a single DNRAbs to the DWEYS motif on GluN2A can generate the full positive allosteric effect.

GluN2A antagonists are neuroprotective against DNRAbs. Our results indicate that N2A-containing receptors are significantly more sensitive to DNRAbs than N2B-containing receptors. To see if attenuating GluN2A activity is neuroprotective, we incubated primary hippocampal cultures either in control antibody (B1) (Fig. 3f, left images) or in G11 (10 µg/mL) in the absence or presence of GluN2A antagonists (TCN-201 or MPX-004), which

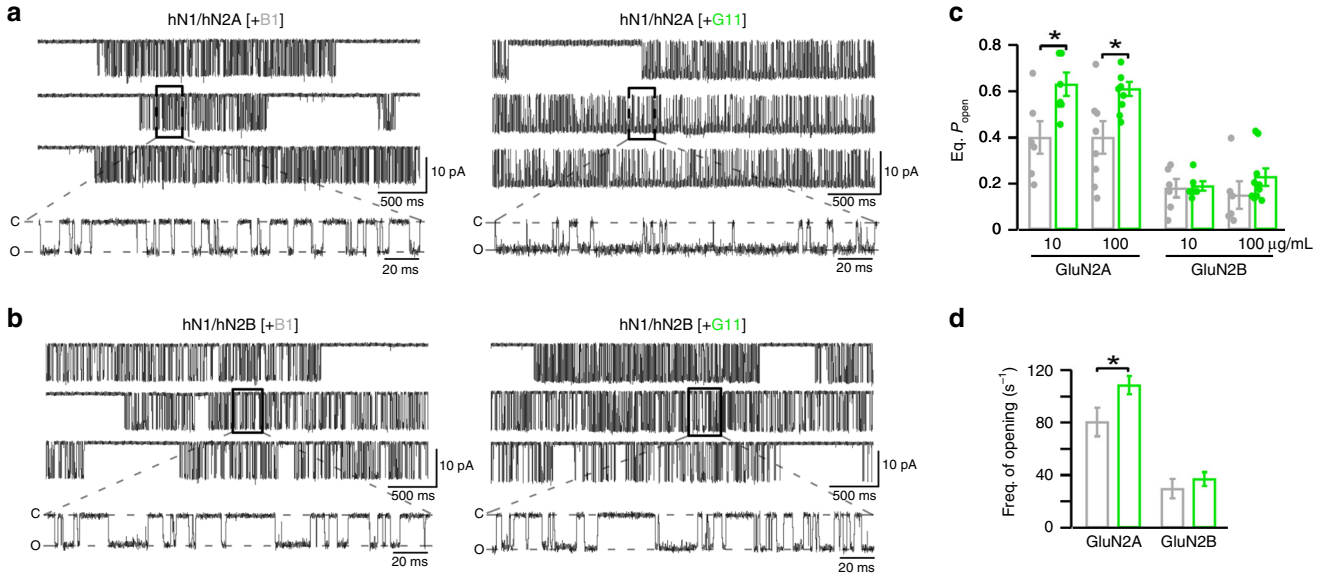

Fig. 2 Single-channel recordings of N2A- and N2B-containing NMDARs under continuous DNRAb exposure. a, **b** Example single-channel recordings of hGluN1/hGluN2A (**a**) and hGluN1/hGluN2B (**b**) with B1 (left traces) or G11 (right traces) antibodies at 10 μg/ml. Recordings were made in the on-cell configuration (holding potential, +100 mV). Downward deflections are inward currents. Low resolution top traces show 12 s of recording (filtered at 1 kHz); more high-resolution bottom traces (selection in black box) show 230 ms (filtered at 3 kHz). **c** Equilibrium open probability (Eq. P_{open}) (mean ± SEM) for N2A- or N2B-containing NMDARs (from left to right for hN1/nN2A, $n = 6, 7, 8, 8$ cells recorded; for hN1/hN2B, $n = 6, 6, 6, 10$ cells recorded). Antibody was either B1 (gray) or G11 (green) ($^*p < 0.05$, two-sided t test) (left to right for N2A, $p = 0.0335, 0.0226$; left to right for N2B, $p = 0.745, 0.0556$). **d** DNRAbs enhance forward rates of activation. Frequency of single-channel openings (mean ± SEM) derived from samples in **c** with antibody either B1 (gray) or G11 (green) ($^*p < 0.05$, one-sided t test) (left to right, $p = 0.0270, 0.212$). Test DNRAbs was 100 μg/ml.

are specific at the concentrations used here[28,32], or a GluN2B-specific negative allosteric modulator (ifenprodil) and assayed the number of DAPI-positive cells associated with activated caspase-3 activity (Fig. 3g). In the presence of DNRAb alone, apoptotic cell death was extensive, consistent with previous results[3,8,33]. This cell death was significantly attenuated in the presence of MPX-004. In contrast, ifenoprodil was less able to protect against cell death (Fig. 3f, g). Thus, specific GluN2A antagonists are neuroprotective against DNRAb-mediated cell death.

In vivo contributions of GluN2A and GluN2B to DNRAbs. To address how the different NMDAR subunits contribute to the DNRAb-induced phenotypes in vivo, we used transgenic mouse models, either with the GluN2A subunit knocked out (*grin2A*$^{-/-}$ mice, termed "N2A KO" henceforth) or with a conditional knockout of the GluN2B subunit (*grin2B*$^{fl/fl}$; *CaMKII*^{Cre} mice, termed "N2B cKO") (Fig. 4a). We used the conditional KO due to the embryonic lethality of a full GluN2B knockout[34–36]. KO mice were immunized with a decapeptide containing the pentapeptide, DWEYS, a mimetope of dsDNA and homologous to a sequence within the GluN2A and GluN2B extracellular domains, multimerized on a polylysine backbone (MAP-DWEYS) (Supplementary Fig. 2). Immunization of wild-type mice with MAP-DWEYS induces production of DNRAbs (DNRAb+ mice)[2,11,37]. As a control, mice were also immunized with the polylysine backbone alone (DNRAb− mice). Two weeks following two booster immunizations, mice were given LPS to allow transient access of antibodies to the hippocampus (Supplementary Fig. 2)[11,19].

Wild-type mice, when immunized with MAP-DWEYS, show two stages of DNRAb-induced pathology (Supplementary Fig. 2)[2,11,19]. An acute phase, assayed one week after LPS treatment, that is characterized by extensive cell death of hippocampal pyramidal neurons[11]; and a chronic phase, assayed 8 weeks post-LPS treatment, characterized by the loss of dendritic complexity in pyramidal neurons, microglia activation, and disruption of place cell function (Supplementary Fig. 2). DNRAb+ mice also display reduced spatial memory, presumably mimicking the phenotype in SLE patients[2,11]. Because LPS only transiently permeabilizes the blood brain barrier[2], the acute phase is associated with the presence of DNRAbs, whereas the chronic phase is independent of the direct presence of DNRAbs[2,19].

Mice lacking GluN2A are protected from DNRAb pathologies. Initially, we assayed the effect of DNRAbs on the acute phase of the pathology, namely the induction of pyramidal neuron cell death measured 1 week after LPS treatment[11,19]. For all in vivo experiments, we compare the effect in DNRAb+ mice to that in DNRAb− mice in the same genetic background with both of these groups treated with LPS (see Supplementary Fig. 2). DNRAb+ mice in the N2B cKO background, which still retain GluN2A, also displayed a significant loss of hippocampal neurons (Fig. 4b, c). In contrast, N2A KO mice showed no significant loss of neurons. Hence, the loss of pyramidal neurons during the acute phase is dependent on GluN2A.

Next, we characterized the chronic phase of pathology by assaying pyramidal neuron morphology 8 weeks after LPS administration (Fig. 4d–i). Compared with its control, GluN2B cKO mice exposed to DNRAbs exhibited a significant loss of dendritic complexity (Fig. 4d). In contrast, in GluN2A KO mice, DNRAbs have no significant effect on dendritic complexity (Fig. 4e). Thus, as with acute enhanced cell death, the chronic phase of SLE pathology associated with reduced dendritic complexity is also dependent on GluN2A.

DNRAbs do not activate microglia in mice-lacking GluN2A. The reduced dendritic complexity occurring during the chronic phase of DNRAb-induced pathology is dependent on microglia

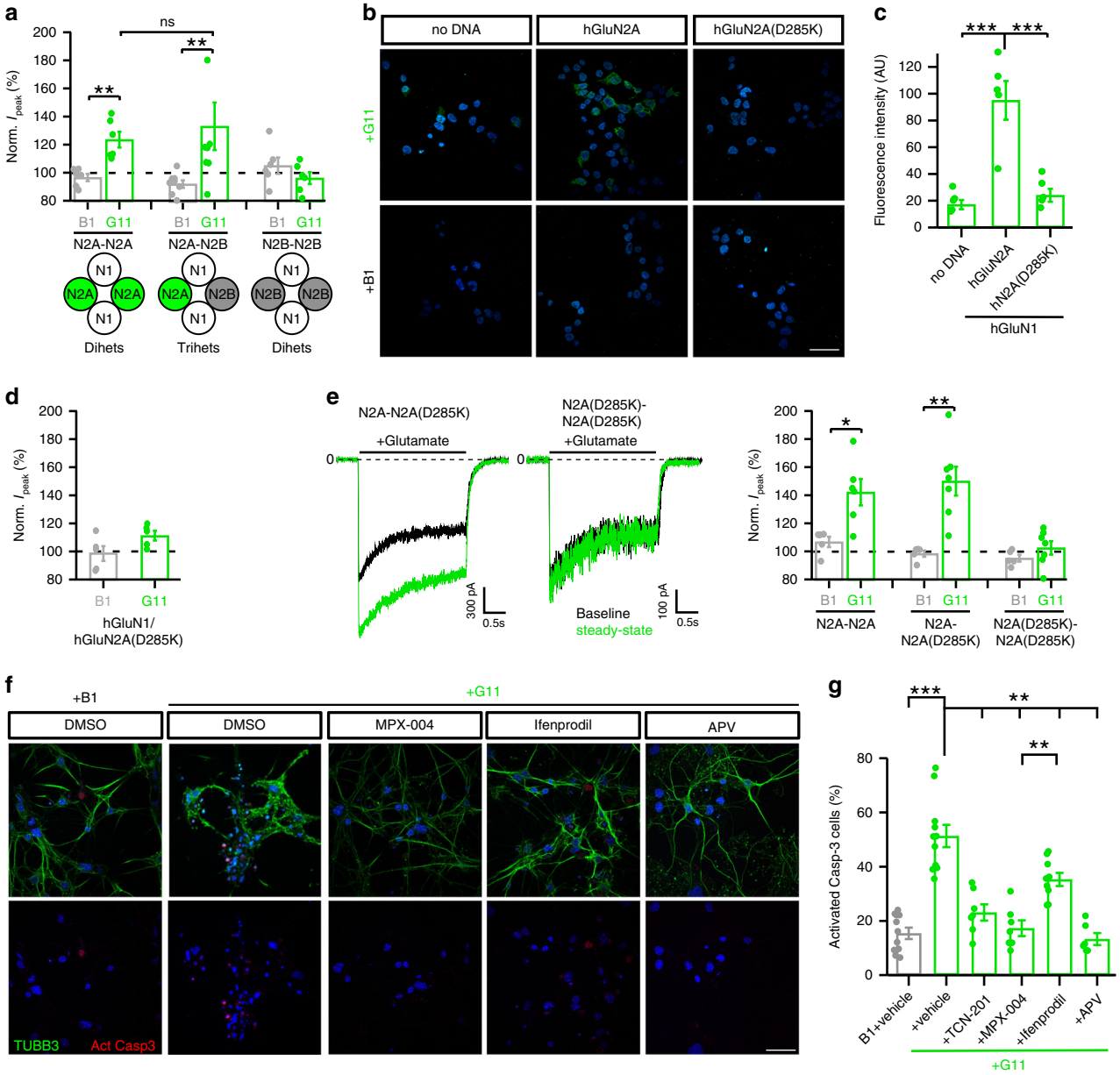

Fig. 3 A single copy of GluN2A confers high sensitivity to SLE DNRAbs. a Bar graphs (mean ± SEM) (left to right, $n = 6, 6, 8, 8, 6, 6$ cells recorded) showing normalized whole-cell peak current amplitudes for diheteromeric (N1/N2A-N2A or N1/N2B-N2B) or triheteromeric (N1/N2A-N2B) receptors at 10 μg/mL of B1 or G11 antibody (**$p < 0.01$, two-sided Mann–Whitney U test) (left to right, $p = 0.00507$, 0.00865, 0.298; for ns, $p = 0.581$). **b** Representative images from immunocytochemistry of HEK293T cells not transfected (no DNA) or transfected with GluN1/GluN2A or GluN1/GluN2A (D285K), stained with B1 or G11 (10 μg/mL) (green, Alexa-488) and DAPI (blue) counterstain. Scale (white bar): 40 μm. **c** Mean fluorescence intensity in (B) (mean ± SEM) ($n = 5$ coverslips of cells, all conditions) (***$p < 0.001$, one-way ANOVA with post-hoc Tukey's test) (Tukey's: no DNA vs hN2A, $p = 0.000156$; hN2A vs hN2A(D285K), $p = 0.000348$). **d** Single charge reversal prevents DNRAb (10 μg/mL) potentiation of whole-cell currents (mean ± SEM, $n = 5$ recorded cells, all conditions). **e** Left, current records of triheteromeric (N1/N2A-N2A(D285K)) or diheteromeric (N1/N2A(D285K)-N2A(D285K)) NMDARs. Currents displayed as in Fig. 1a. Right, bar graphs (mean ± SEM) (left to right, $n = 5, 6, 5, 7, 5, 6$ recorded cells) showing normalized current amplitude for diheteromeric and triheteromeric receptors at 10 μg/mL of B1 or G11 (*$p < 0.05$, **$p < 0.01$, two-sided Mann–Whitney U test) (left to right, $p = 0.0358$, 0.00577, 0.194). **f** Immunocytochemistry of DIV14 primary hippocampal cultures incubated either in control (B1 + vehicle) or in DNRAb (G11) at 10 μg/mL. G11 was incubated either alone (+vehicle), with TCN-201 (not shown), MPX-004, or ifenprodil at 3 μM. Upper panels, representative images of neurons stained with antibodies against neuronal β-tubulin, Tubb3 (green, Alexa-488), and activated caspase-3 (red, Alexa-647), with DAPI (blue). Lower panel, only activated caspase-3 channel. Scale (white bar): 40 μm. **g** Quantification of immunocytochemistry shown in (**f**). Proportion of DAPI and activated caspase-3-positive cells divided by total DAPI cells (mean ± SEM) (left to right, $n = 11, 11, 7, 7, 9, 6$ coverslips of cells) per treatment condition (*$p < 0.05$, **$p < 0.01$, ***$p < 0.001$, one-way ANOVA with post-hoc Tukey's test) (Tukey's: G11 + vs G11 + MPX-004, $p = 0.00282$).

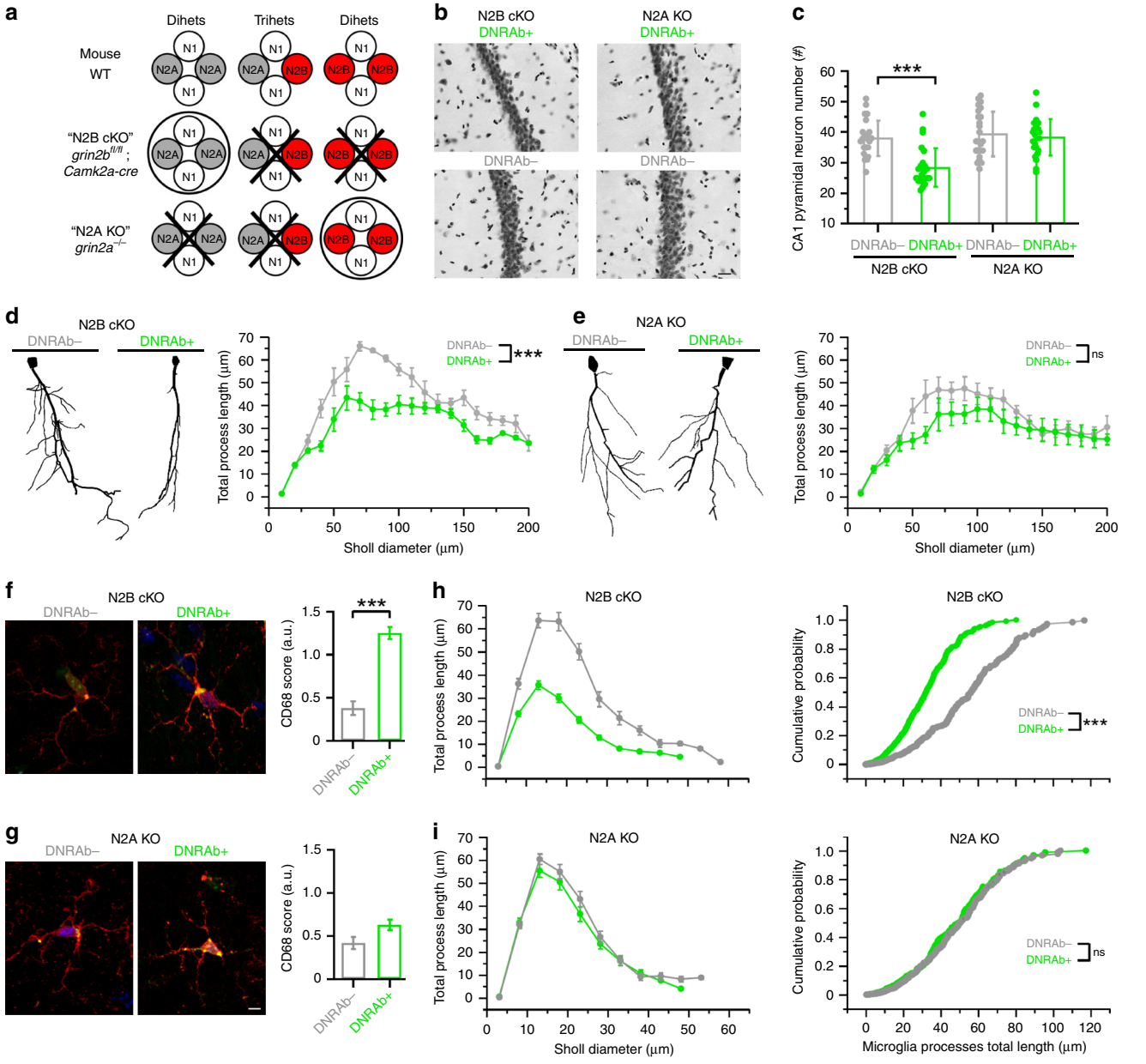

Fig. 4 DNRAbs induced neuronal loss and dendritic pruning in CA1 pyramidal neurons persist in mice-lacking GluN2B, but not in those lacking GluN2A. a Schematic of NMDAR composition expected in hippocampal pyramidal neurons in the various genetic backgrounds (Supplementary Fig. 2). **b** Micrographs of hippocampal CA1 neurons from DNRAb+ or DNRAb− N2B cKO or N2A KO mice. Scale bar, 20 µm. **c** Quantification of CA1 neurons (mean ± SEM, $n = 24$ sections per group). Each dot represents a CA1 pyramidal neuron field counted using a standard unbiased stereological protocol (eight runs of systematic random sampling in three animals per group) (***$p < 0.001$, two-sided Mann–Whitney U test) (left to right, $p = 0.0000156$, 0.765). **d**, **e** Dendritic complexity of Golgi-stained neurons. Left, tracings of CA1 pyramidal neurons from N2B cKO (**d**) or N2A KO (**e**) mice. Right, Sholl analysis for N2B cKO (**d**) or N2A KO (**e**) mice (***$p < 0.001$, two-sided Kolmogorov–Smirnov test for data converted to cumulative distribution function) (left to right, $p = 2.754 \times 10^{-16}$, 0.61). Values at concentric rings are shown as mean ± SEM. For each group, 10–20 neurons per animal, 4 animals per group. **f**, **g** Representative images of microglia from N2B cKO (**a**) or N2A KO (**b**) mice. Microglia are labeled with antibody to Iba1 (red, Alexa 594) and to CD68 (green, Alexa-488). Scale (white bar): 5 µm. Right panels, quantification of CD68 + score (mean ± SEM) (***$p < 0.001$, Kruskal–Wallis ANOVA test) (left to right, $p = 0.00000000222$, 0.0793) (see Supplementary Methods). Three animals per group; number of quantified microglia: N2B cKO, DNRAb− ($n = 42$), DNRAb+ ($n = 87$), N2A KO, DNRAb− ($n = 57$), DNRAb+ ($n = 58$). **h**, **i** Microglia process complexity and length. Left panels, Sholl analysis of process length of microglia from N2B cKO (**h**) or N2A KO (**i**) mice. Right panels, cumulative probability distribution curves of microglia process length from N2B cKO (**h**) or N2A KO (**i**) (***$p < 0.001$, two-sided Kolmogorov–Smirnov test) (top to bottom, $p = 7.16 \times 10^{-8}$, 0.999). Three animals per group; number of quantified microglia: N2B cKO, DNRAb− ($n = 33$), DNRAb+ ($n = 34$); N2A KO, DNRAb− ($n = 39$), DNRAb+ ($n = 40$).

activation[19]. We therefore characterized microglia in DNRAb+ and DNRAb− mice in the various genetic backgrounds (Fig. 4f–i).

For the N2B cKO background, and in comparison with its control, DNRAb+ mice showed enhanced expression of CD68 (Fig. 4f, right panel) and diminution of process complexity (Fig. 4h, left panel), and process length (Fig. 4h, right panel) over concentric Sholl diameters. These results are consistent with microglia activation and parallel what is observed in wild-type mice[19]. In

contrast, for the N2A KO background (Fig. 4g–i), DNRAb+ mice, in comparison with its control, did not show significant CD68 expression (Fig. 4g, right panel) or reduced complexity (Fig. 4i), suggesting a lack or reduced microglia activation. Thus, DNRAb-induced microglia activation, which is critical in dendritic morphology changes, either directly requires GluN2A and/or is dependent on acute GluN2A-induced cell death.

DNRAb-induced changes in spatial memory require GluN2A. During the chronic phase of DNRAb-induced pathology, wild-type mice exposed to DNRAb show impaired spatial memory and disrupted place cell properties in the CA1 region of the hippocampus (Supplementary Fig. 2)[2,11,19]. We therefore asked whether DNRAb+ N2A KO and N2B cKO mice, 8 weeks after LPS exposure, behaved abnormally in an object-place memory (OPM) task, which tests spatial memory (Fig. 5a)[38,39]. N2B cKO mice transiently exposed to DNRAbs performed significantly worse than its DNRAb− control in the OPM task (Fig. 5b). This parallels to what is observed in wild-type mice (Supplementary Fig. 2). In contrast, no difference in performance was detected between DNRAb+ and DNRAb− N2A KO mice. Thus, GluN2A, either directly or indirectly, is required for DNRAb-induced disruptions in spatial memory.

NMDAR-dependent spatial memory and learning is linked to hippocampal place field size[40,41]. In wild-type mice exposed to DNRAbs, place field size is aberrantly enlarged, paralleling the

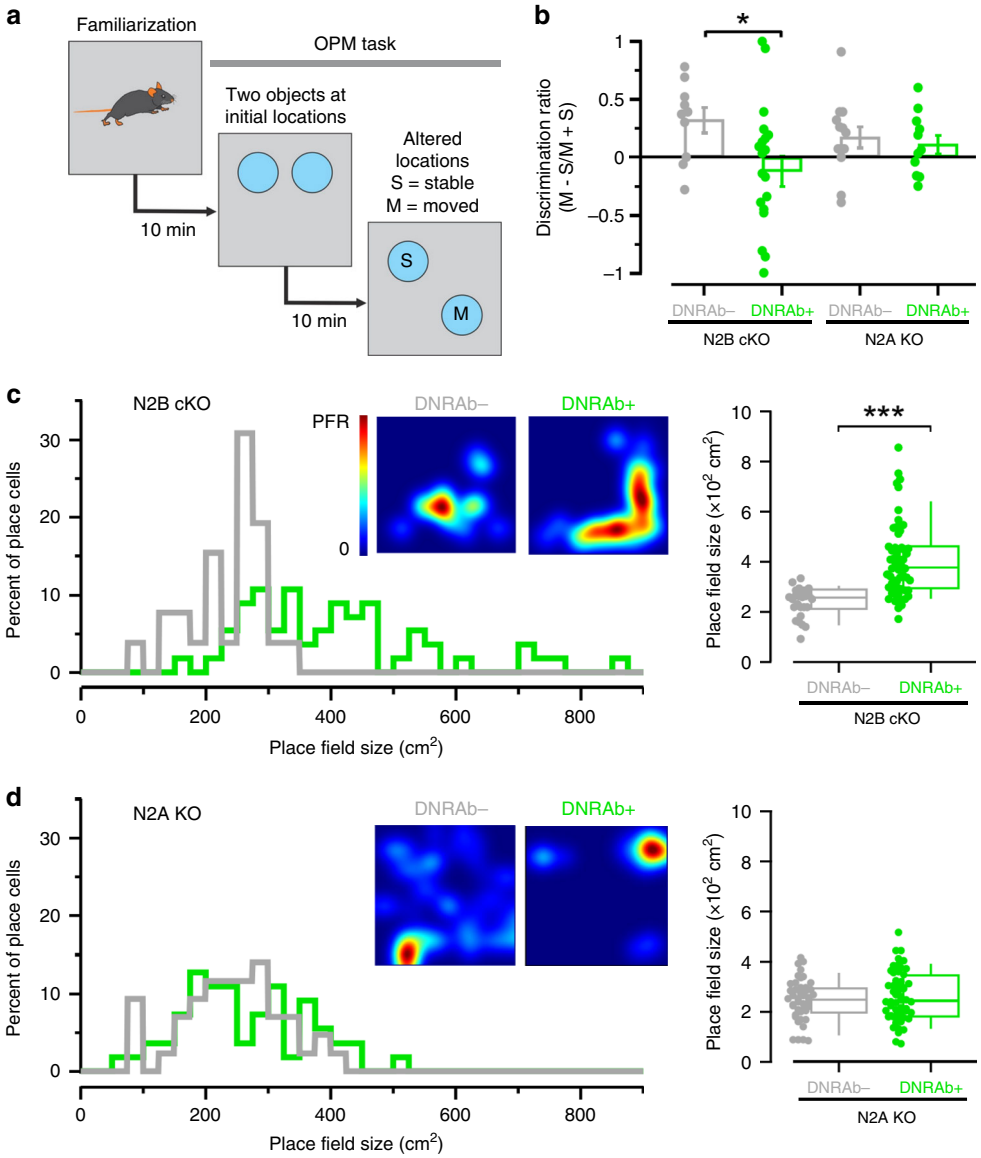

Fig. 5 Behaviors disrupted by DNRAbs persist in mice-lacking GluN2B, but not in those lacking GluN2A. a Schematic of the object-place memory (OPM) task. **b** DNRAb+ N2B cKO mice show significantly reduced exploratory behavior, relative to its control, of the moved object over the stable object (Supplementary Fig. 2). Mice were tested 8 weeks after LPS treatment. Values shown are mean ± SEM ($n = 10$, 20, 13, 11, from left to right, number of tested mice per group; $^*p < 0.05$, two-sided Mann–Whitney U test) (left to right, $p = 0.0235$, 0.524). **c**, **d** DNRAb disrupts place field size in mice-lacking GluN2B, but not in those lacking GluN2A. Left, histograms for place field sizes of all place cells recorded in DNRAb− (gray) or DNRAb+ (green) mice either N2B cKO (**c**) or N2A KO (**d**) backgrounds. Inset, heatmaps of representative place fields. Right, box plots (center: median; lower and upper box edge: 25th & 75th percentiles; with whiskers: 10th and 90th percentile), comparing place field size in N2B cKO (**c**) or N2A KO (**d**) mice ($^{***}p < 0.001$, two-sided Mann–Whitney U test) (top to bottom, $p = 0.0000000348$, 0.670). Each dot represents a single place field: for N2B cKO (**c**), DNRAb− ($n = 26$) and DNRAb+ ($n = 56$); for N2A KO (**d**), DNRAb− ($n = 43$) and DNRAb+ ($n = 55$).

reduced spatial memory in SLE patients and other neurodegenerative models[2,19,42]. To assess neuronal functional integrity, we measured place field size in freely moving mice by implanting tetrodes into the dorsal CA1 region (Fig. 5c, d). As in wild-type, DNRAb+ N2B cKO mice exhibited significantly larger place field sizes compared with DNRAb− N2B cKO mice (Fig. 5c), indicating that in the absence of GluN2B, the DNRAb-induced disruption of place field size persists. In contrast, DNRAb+ and DNRAb− N2A KO mice displayed no significant differences in place field size (Fig. 5d). Thus, the cognitive deficits associated with DNRAbs are intimately linked to GluN2A, but appear largely independent of GluN2B.

Discussion

Our experiments demonstrate that the GluN2A NMDAR subunit is required for various neuropathologies associated with lupus autoantibodies. We find that DNRAbs act as positive allosteric modulators (PAM) on NMDARs with the GluN2A subunit showing a much higher sensitivity than the GluN2B subunit (Figs. 1 and 2). DNRAb exposure manifests in two distinct phases: first, synaptic disturbances and cell death with acute exposure, and second, a loss of dendritic complexity resulting from microglia activation that occurs even after antibody is no longer detected[10,19]. Presumably, the higher sensitivity of GluN2A to DNRAbs facilitates cell death during acute exposure. The chronic phase, including the cognitive and memory defects similar to what is seen in SLE patients[2,43], are also dependent on GluN2A, but it is unknown whether it is a residual consequence of excitotoxicity encountered during the acute phase or a lasting change to NMDARs that predispose neurons to microglial-dependent pruning.

G11, the human DNRAb we tested, acts as a PAM on NMDARs via the DWEYS motif (Fig. 3b–d). DNRAbs are present in ~30–40% of SLE patients, with these DNRAbs being identified by binding to peptides containing the DWEYS motif[9,10,14,44]. Hence, we assume that the PAM action is a common feature of all DNRAbs. Consistent with this idea, polyclonal antibodies from the CSF of SLE patient with neuropsychiatric symptoms that bind the DWEYS motif induce NMDAR hyperfunction[12,33]. Nevertheless, it is possible that there are clonal variations in the magnitude of the PAM action as well as possible additional functional effects of DNRAbs, necessitating the study of more SLE patient DNRAbs.

The concentration of DNRAbs in the nervous system presumably varies during the pathophysiological course of SLE. At low concentrations, DNRAbs would affect exclusively GluN2A-containing receptors, while at high concentrations, DNRAbs would also affect GluN2B diheteromeric receptors (Fig. 1). Previous work has shown that the GluN2B-specific inhibitor, ifenprodil, can be neuroprotective[10]. However, this most likely reflects that triheteromeric GluN1/GluN2A/GluN2B NMDARs, which constitute a major portion of hippocampal synapses[26,27], are inhibited by ifenprodil[28,29]. Indeed, we find that a single copy of wild-type GluN2A confers high sensitivity to DNRAbs (Fig. 3a), a result consistent with GluN2A dominance in allosteric modulation[45,46].

The DWEYS motif is located in the amino-terminal domain (ATD) clamshell hinge region (Fig. 3b–d). GluN2A-selective PAMs and negative allosteric modulators (NAMs) have been developed to target NMDAR hypo- or hyperfunction in disease[47,48]. While most GluN2A-selective PAMs and NAMs target the ligand-binding domain (LBD), the ATD interacts with the LBD to mediate its allosteric action[49–52]. In GluN2A/GluN2B NMDARs, the GluN2A ATD interacts more extensively with the LBD than the GluN2B ATD[45,46], which may underlie the higher sensitivity of GluN2A to DNRAbs. Furthermore, the DWEYS motif is proximal to binding sites for other ATD allosteric modulators. Indeed, the sensitivity to Zn^{2+}, a NAM, may be modulated by SLE antibodies[33]. Zn^{2+} is coordinated by several residues in the ATD clamshell that are proximal to or at the DWEYS motif[30,31,53,54]. It may be that the DNRAb-induced potentiation and SLE pathology observed through GluN2A is influenced by the relief of tonic Zn^{2+} given the differences in Zn^{2+} sensitivity between GluN2A and GluN2B[31,55,56]. Nevertheless, the mechanism of action of DNRAbs to produce positive allosteric modulation and the differences in sensitivity between GluN2A and GluN2B remain unknown, but are critical to define for potential therapeutic interventions.

Our work here does not discount the possibility that DNRAbs act on additional mechanisms, independent of NMDAR gating, to exert their subunit-specific effects. The pathology of anti-NMDAR encephalitis, for example, largely does not involve receptor gating, but rather changes in cell biology: autoantibodies cause internalization of NMDARs and chronic NMDAR hypofunction[57,58], displace the interaction of NMDAR with synaptic proteins such as the EphrinB2 receptor[59,60] or disrupt the nanoscale organization of NMDARs at the synapse with subunit-selectivity[61]. DNRAbs may also engage different intracellular pathways associated with GluN2A and GluN2B. Interestingly, GluN2A signaling has been associated with cell survival through activation of the transcription factor CREB, leaving the mechanism of GluN2A-mediated potentiation to be somewhat perplexing in the context of potentiation from DNRAbs[62]. However, there is increasing evidence to suggest that GluN2A over-activation can contribute to excitotoxicity[62–64]. GluN2A contributes to both the acute and chronic phases of SLE neuropathology. While the use of GluN2A NAMs may be key to treating the neuropsychiatric symptoms of SLE, any NMDAR inhibitor may lead to undesirable side effects[20,65,66]. Uncovering the mechanistic details of DNRAb-NMDAR interactions during distinct pathophysiological phases will help us better develop and tailor therapeutic strategies for preventing neuropsychiatric symptoms in SLE patients before acute events occurs, and treating them during chronic phases of SLE.

Methods

See Supplementary Information–Supplementary Methods for details.

Animals. Mice (females, C57BL/6 strain) were housed at the Center for Comparative Physiology at the Feinstein Institute for Medical Research. All protocols were approved by the local institutional animal care and usage committee (IACUC). Mice with deletion of the GluN2A subunit (*Grin2a*$^{-/-}$) were kindly provided by Dr. M. Mishina (University of Tokyo). Mice with conditional knockout of the GluN2B subunit (*Grin2b*$^{fl/fl}$;*Camk2a-cre*) were bred in house by crossing homozygous floxed GluN2B mice (*Grin2b*$^{fl/fl}$, kind gift from Prof. Dr. H. Monyer) with a Cre line driven by CaMKIIα promoter (*Camk2a*-cre mice, B6. Cg-Tg(Camk2a-Cre)T29-1Stl/J, stock no: 005359, Jackson labs). Both groups were further bred on an H2d$^{+/+}$ background to allow antibody response to immunization. Mice are housed in a laboratory animal facility at a 12/12 h light/dark cycle, and received water and food ad libitum. Female mice aged 6–8 weeks were immunized with MAP-core and MAP-DWEYS[11].

All animal procedures at Stony Brook University were approved by the institutional animal care and usage committee (IACUC) at Stony Brook University and were in accordance with the guidelines established by the National Institutes of Health. Mice are housed in a laboratory animal facility at a 12/12 h light/dark cycle, and received water and food ad libitum. Mice (C57BL/6) were bred in house for primary cultures of hippocampal neurons at P0–P1 and glia/astrocyte feeder layers at P2–P4. Pups were not sexed for generation of primary cultures.

SLE antibodies. G11 is an IgG1 monoclonal antibody derived from a female SLE patient's B cells with Igγ1 heavy chain and Igκ light chain composition. B1 is an isotype IgG1 control derived from the same patient[16]. G11 was cloned from a B-cell binding the DWEYS peptide and B1 from a B cell that did not bind the peptide or any brain antigen. The SLE patient from whom the antibodies were derived had serum antibodies reactive to dsDNA and the DWEYS peptide[2,4].

In vitro electrophysiology. Human embryonic kidney 293 (HEK293) cells were grown in Dulbecco's modified Eagle's medium (DMEM), supplemented with 10% FBS, for 24 h before transfection. Human NMDAR-encoding cDNA constructs, were co-transfected into HEK293 cells along with a separate peGFP-Cl construct at a ratio of 4:4:1 (N1:N2:eGFP) for macroscopic recordings, and at a ratio for 4:1.5:1 for single-channel recordings using X-tremeGene HP (Roche, 06-366) (see Supplementary Methods for construct tables). Transfection of the triheteromeric NMDA receptor constructions were done with Ca^{2+} precipitation[28,29].

Macroscopic currents in the whole-cell mode were recorded at room temperature (20–23 °C) using an EPC-10 (HEKA) amplifier with PatchMaster software (version 2 × 90.2, HEKA), digitized at 10 kHz and low-pass filtered at 2.9 kHz (−3 dB) using an eight pole low-pass Bessel filter 4[67,68]. Patch microelectrodes were filled with an intracellular solution (mM): 140 KCl, 10 HEPES, 1 BAPTA, 4 Mg^{2+}-ATP, 0.3 Na^{+}-GTP, pH 7.3 (KOH), 297 mOsm (sucrose). Our standard extracellular solution consisted of (mM): 150 NaCl, 2.5 KCl, and 10 HEPES, pH 7.2 (NaOH). Pipettes had resistances of 2–6 MΩ when filled with the pipette solution and measured in the standard Na^{+} external solution. Ca^{2+} was omitted from the extracellular solution to prevent run-down over time. We did not use series resistance compensation nor did we correct for junction potentials. Currents were measured within 10 min of going whole cell. External solutions were applied using a piezo-driven double-barrel application system. Prior to use, we incubated the application system with 2% BSA (1xPBS) for two hours at 21–24 °C to minimize non-specific antibody binding. For agonist application, one barrel contained the external solution +0.1 mM glycine, whereas the other barrel contained both 0.1 mM glycine and 1 mM glutamate. For display, NMDAR currents were digitally refiltered at 500 Hz and resampled at 1 kHz.

Single-channel currents were recorded in the on-cell configuration at 20–23 °C using an integrating patch clamp amplifier (Axopatch 200B, Molecular Devices), analog filtered at 10 kHz (four-pole Bessel filter), and digitized between 25 and 50 kHz (ITC-16 interfaced with PatchMaster, HEKA)[24,69]. Patch pipettes (thick-wall, borosilicate, Sutter Instruments) were pulled and fire-polished achieving resistances between 10 and 20 MΩ when measured in the bath. At −100 mV, seal resistance ranged between 2 and 20 GΩ. For cell-attached recordings, patch pipettes were filled with the standard bath solution as well as 1 mM glutamate and 0.1 mM glycine. In total, 0.05 mM EDTA was added to minimize gating effects of divalents. Inward currents were elicited by applying a pipette potential of +100 mV. Recordings of hGluN1/hGluN2A or hGluN1/hGluN2B, either in the presence of absence of DNRAbs consisted of long clusters of activity separated by seconds-long periods of inactivity, simplifying detection of several channels in the patch. For these recordings, the relatively high equilibrium open probability (eq. Po) and duration of recordings (~10,000 to 180,000 events per recording) indicated that we were recording from single-channel patches.

Immunocytochemistry (ICC). HEK293T cells were used for ICC. Cells were fixed 48 h post-transfection, washed with 1× PBS, and then blocked with 2% bovine serum albumin (BSA) (Sigma, A9647). Incubation of primary antibody (20 µg/mL), either G11 or control B1, diluted in 2% BSA was done overnight at 4 °C.

Primary hippocampal neurons were made[70] with minor modifications (see Supplementary Methods). Pharmacological treatment occurred at DIV14. Final concentrations of antagonists were 3 µM: TCN-201 (AdooQ Bioscience, A11947), MPX-004 (Alomone Labs, M280), and Ifenprodil (Sigma, I2892). ICC was performed 24-h post treatment on DIV15. Coverslips were washed with 1× PBS, fixed, and washed again with 1× PBS and blocked/permeabilized with antibody blocking solution, consisting of 2% (w/v) BSA, 0.25% (v/v) Triton-X100 in 1xPBS, for 60 min. Coverslips were then incubated in primary antibodies, rabbit anti-activated caspase-3 (1:250, Cell Signaling, 9661), and mouse anti-β tubulin III (Tubb3) (1:400, Millipore-Sigma, MAB1637), both in antibody blocking solution overnight in 4 °C. Coverslips were washed with 1xPBS, and incubated in fluorescence-conjugated secondary antibodies, Goat anti-rabbit Alexa-647 (1:1000, ThermoFisher, A21245) and Goat anti-mouse Alexa-488 (1:1000, ThermoFisher, A21121) for 1 h at RT and mounted as described above. Post-processing and image analysis are detailed in Supplementary Methods.

Neuronal staining. Mice were anesthetized with 100 µl of Euthasol (Virbac) prior to perfusion with 0.9% sodium chloride, 0.5% sodium nitrite, and 0.1% heparin, followed by 4% paraformaldehyde (PFA) in 0.1 M phosphate buffer (PB) as before[19].

For cresyl violet staining, brains were extracted, fixed in 4% PFA for 2 h and transferred to 30% sucrose, blocked and sliced at 40 µm with a periodicity of one in four coronal sections starting at approximately Bregma −0.94 mm over the next 1600–1900 µm. Sections were mounted, dehydrated, rehydrated, and stained in cresyl violet for 3 min. Sections were dried, dehydrated, cleared (Histoclear II), and coverslipped with Permount® (Thermo Fisher) prior to imaging on an AxiophotZ1 microscope (Zeiss). Sections were imaged in 100× oil, and we focused on the soma of the stratum pyramidale around which a tiled Z-stacked (0.5 µm steps) image was generated. Stereology was performed with the sampling frame set such that an individual frame captures 2–5 targets in the photomicrograph[11,19]. Optical dissectors are then created by manipulating the level of the Z-stack, and nuclei within neurons in focus are counted as long as they are not in contact with the left or bottom part of a frame. Quantitation of CA1 neurons in image stacks was performed with the Stereo Investigator suite in Neurolucida 360 (MBF Bioscience). Neuron numbers in (Fig. 4c) represent the total number of soma captured in the systematic random sampling frame as it is placed on consecutive sections or "runs". Neuron numbers were measured per sampled tissue volume (0.20 mm^3 NR2B cKO DNRAb+; 0.19 mm^3 NR2B cKO DNRAb−; 0.20 mm^3 NR2A KO DNRAb+; 0.21 mm^3 NR2A KO DNRAb−, mean ± 0.001 mm^3, s.d.). There were three animals in each group, with eight runs for each animal.

For Golgi staining, brains were processed using FD Rapid Golgi Stain kit (FD NeuroTechnologies), and sectioned at 100 µm on a cryostat (−21 °C) that permit identification of internal anatomic landmarks to signal sample start and stop, with periodicity of one in four coronal sections across ~1200 µm (Bregma −0.94 to −2.2 mm for the dorsal hippocampus) of brain with at least five different sections being sample per animal. Sections were mounted, dried (room temperature, dark), silver nitrate stained, rinsed, dehydrated in EtOH, cleared in xylene, and coverslipped. Tissue was imaged on an AxioImager Z1 microscope (Zeiss) in 40× oil using tiling and Z-stack (2 µm steps). There were four animals in each group, and 10–20 neurons were analyzed for each animal as shown in Fig. 4d, e. Images were then analyzed using Neurolucida 360 (MBF Bioscience) dendritic tracing for Sholl analysis at 10 µm shells from the soma[2,19].

Immunohistochemistry. Mice were anesthetized as described above for cresyl violet staining. Brains were extracted, fixed, and transferred to 30% sucrose, blocked and sliced (40 µm). Sections were dried, dehydrated, cleared (Histoclear II) and coverslipped with Permount® (ThermoFisher) prior to imaging on an AxiophotZ1 microscope (Zeiss). For immunohistochemistry used in labeling microglia in Fig. 4f, g, sections were washed with PBS, permeabilized, blocked, and stained with primary antibody overnight at 4 °C. Primary antibodies were Iba1 (1:500, Wako Chemicals, 019-1 9741), CD68 (1:500, Bio-Rad, mca1957). On the following day, samples were washed with PBS and then incubated with secondary antibody, which included Donkey anti-rat Alexa Fluor 488 (1:400, Life Technologies, A21208), Chicken anti-rabbit Alexa Fluor 594 (1:300, Life Technologies, A21442). Post-processing and image analysis are detailed in Supplementary Methods.

Behavioral assessment and in vivo electrophysiology. Mice (20-24 weeks) were handled for 15 min per day for 3 days before being tested behaviorally. The object-place memory (OPM) task was performed[2,19]. The apparatus consisted of a square (40 cm) chamber 40 cm high, with the walls painted gray. Animals were familiarized to the empty chamber (three sessions of 15 min each). For OPM testing, mice underwent the following sequence: empty chamber (10 min), home cage (10 min), sample phase in which the chamber had two objects located at the center of the NW and NE sectors (5 min), home cage (10 min), choice phase, in which the chamber had the same objects but one of them was moved from NE to the center of the SE sector (5 min). The discrimination ratio was calculated during the choice phase by dividing time spent exploring the moved object minus the time spent exploring the static object by the time exploring the objects combined[2]. Data were collected and analyzed using EthoVision XT (version 11, Noldus Information Technologies).

In vivo recordings of place cells in the dorsal CA1 of the hippocampus were made[2,19]. Mice were anesthetized and implanted with a 16-channel multi-electrode array. After recovery, single unit firing was recorded using Cheetah software (version 5, Neuralynx), while the animal explored a square chamber in a schedule of four exploration runs separated by three rest sessions. Data were analyzed using Spike2 (version 8, Cambridge Electronic Design), NeuroExplorer (version 5, Nex Technologies), and MATLAB (version 9.2 R2017a, MathWorks).

Statistics. Data analysis was performed using IgorPro (version 7, WaveMetrics), QuB (version 2.0.0.30, SUNY at Buffalo), Microsoft Excel, and ImageJ. All average values are presented as mean ± SEM. For statistical analysis, we used either Origin Pro (version 9, Origin Lab) or MiniTab (version 19, Trialware). Normality was used to determine appropriate statistical tests. For normally distributed data, one-tailed or two-tailed Student's *t* tests (*t* test) as indicated or one-way ANOVAs with post-hoc Tukey's test were used as indicated. For non-normally distributed data or instances where the data were categorical variables or cumulative distribution functions, Mann–Whitney *U* tests, Kruskal–Wallis ANOVAs, and Kolmogorov–Smirnov tests were used as indicated. Significance was typically $*p < 0.05$.

We did not run a statistical test to determine sample size a priori. Sample sizes resemble those from previous publications.

Reporting summary. Further information on research design is available in the Nature Research Reporting Summary linked to this article.

Data availability

The data sets generated and analyzed during this study are available from the corresponding authors on reasonable request. The source data underlying Figs. 1–5 has been provided as a Source Data file.

Code availability

Code used for analysis is available from corresponding authors on reasonable request.

Received: 10 September 2019; Accepted: 21 February 2020;
Published online: 16 March 2020

References

1. Tsokos, G. C. Systemic lupus erythematosus. *N. Engl. J. Med.* **365**, 2110–2121 (2011).
2. Chang, E. H. et al. Selective impairment of spatial cognition caused by autoantibodies to the N-methyl-D-aspartate receptor. *EBioMedicine* **2**, 755–764 (2015).
3. Kowal, C. et al. Human lupus autoantibodies against NMDA receptors mediate cognitive impairment. *Proc. Natl Acad. Sci. USA* **103**, 19854–19859 (2006).
4. Mackay, M. et al. Metabolic and microstructural alterations in the SLE brain correlate with cognitive impairment. *JCI Insight* **4**, e124002 (2019).
5. Hanly, J. G. et al. Prospective analysis of neuropsychiatric events in an international disease inception cohort of patients with systemic lupus erythematosus. *Ann. Rheum. Dis.* **69**, 529–535 (2010).
6. Unterman, A. et al. Neuropsychiatric syndromes in systemic lupus erythematosus: a meta-analysis. *Semin. Arthritis Rheum.* **41**, 1–11 (2011).
7. Borowoy, A. M. et al. Neuropsychiatric lupus: the prevalence and autoantibody associations depend on the definition: results from the 1000 faces of lupus cohort. *Semin. Arthritis Rheum.* **42**, 179–185 (2012).
8. DeGiorgio, L. A. et al. A subset of lupus anti-DNA antibodies cross-reacts with the NR2 glutamate receptor in systemic lupus erythematosus. *Nat. Med.* **7**, 1189–1193 (2001).
9. Arinuma, Y., Yanagida, T. & Hirohata, S. Association of cerebrospinal fluid anti-NR2 glutamate receptor antibodies with diffuse neuropsychiatric systemic lupus erythematosus. *Arthritis Rheum.* **58**, 1130–1135 (2008).
10. Faust, T. W. et al. Neurotoxic lupus autoantibodies alter brain function through two distinct mechanisms. *Proc. Natl Acad. Sci. USA* **107**, 18569–18574 (2010).
11. Kowal, C. et al. Cognition and immunity; antibody impairs memory. *Immunity* **21**, 179–188 (2004).
12. Kapadia, M. et al. Effects of sustained i.c.v. infusion of lupus CSF and autoantibodies on behavioral phenotype and neuronal calcium signaling. *Acta Neuropathol. Commun.* **5**, 70 (2017).
13. Gono, T. et al. Anti-NR2A antibody as a predictor for neuropsychiatric systemic lupus erythematosus. *Rheumatol. (Oxf.)* **50**, 1578–1585 (2011).
14. Tay, S. H., Fairhurst, A. M. & Mak, A. Clinical utility of circulating anti-N-methyl-d-aspartate receptor subunits NR2A/B antibody for the diagnosis of neuropsychiatric syndromes in systemic lupus erythematosus and Sjogren's syndrome: An updated meta-analysis. *Autoimmun. Rev.* **16**, 114–122 (2017).
15. Zhang, J. et al. Identification of DNA-reactive B cells in patients with systemic lupus erythematosus. *J. Immunol. Methods* **338**, 79–84 (2008).
16. Zhang, J. et al. Polyreactive autoantibodies in systemic lupus erythematosus have pathogenic potential. *J. Autoimmun.* **33**, 270–274 (2009).
17. Huerta, P. T., Kowal, C., DeGiorgio, L. A., Volpe, B. T. & Diamond, B. Immunity and behavior: antibodies alter emotion. *Proc. Natl Acad. Sci. USA* **103**, 678–683 (2006).
18. Appenzeller, S., Carnevalle, A. D., Li, L. M., Costallat, L. T. & Cendes, F. Hippocampal atrophy in systemic lupus erythematosus. *Ann. Rheum. Dis.* **65**, 1585–1589 (2006).
19. Nestor, J. et al. Lupus antibodies induce behavioral changes mediated by microglia and blocked by ACE inhibitors. *J. Exp. Med.* **215**, 2554–2566 (2018).
20. Traynelis, S. F. et al. Glutamate receptor ion channels: structure, regulation, and function. *Pharm. Rev.* **62**, 405–496 (2010).
21. Paoletti, P., Bellone, C. & Zhou, Q. NMDA receptor subunit diversity: impact on receptor properties, synaptic plasticity and disease. *Nat. Rev. Neurosci.* **14**, 383–400 (2013).
22. Hansen, K. B. et al. Structure, function, and allosteric modulation of NMDA receptors. *J. Gen. Physiol.* **150**, 1081–1105 (2018).
23. Wang, L. et al. Female mouse fetal loss mediated by maternal autoantibody. *J. Exp. Med.* **209**, 1083–1089 (2012).
24. Talukder, I. & Wollmuth, L. P. Local constraints in either the GluN1 or GluN2 subunit equally impair NMDA receptor pore opening. *J. Gen. Physiol.* **138**, 179–194 (2011).
25. Amin, J. B., Leng, X., Gochman, A., Zhou, H. X. & Wollmuth, L. P. A conserved glycine harboring disease-associated mutations permits NMDA receptor slow deactivation and high Ca(2+) permeability. *Nat. Commun.* **9**, 3748 (2018).
26. Rauner, C. & Kohr, G. Triheteromeric NR1/NR2A/NR2B receptors constitute the major N-methyl-D-aspartate receptor population in adult hippocampal synapses. *J. Biol. Chem.* **286**, 7558–7566 (2011).
27. Tovar, K. R., McGinley, M. J. & Westbrook, G. L. Triheteromeric NMDA receptors at hippocampal synapses. *J. Neurosci.* **33**, 9150–9160 (2013).
28. Hansen, K. B., Ogden, K. K., Yuan, H. & Traynelis, S. F. Distinct functional and pharmacological properties of Triheteromeric GluN1/GluN2A/GluN2B NMDA receptors. *Neuron* **81**, 1084–1096 (2014).
29. Stroebel, D., Carvalho, S., Grand, T., Zhu, S. & Paoletti, P. Controlling NMDA receptor subunit composition using ectopic retention signals. *J. Neurosci.* **34**, 16630–16636 (2014).
30. Stroebel, D., Carvalho, S. & Paoletti, P. Functional evidence for a twisted conformation of the NMDA receptor GluN2A subunit N-terminal domain. *Neuropharmacology* **60**, 151–158 (2011).
31. Romero-Hernandez, A., Simorowski, N., Karakas, E. & Furukawa, H. Molecular basis for subtype specificity and high-affinity zinc inhibition in the GluN1-GluN2A NMDA receptor amino-terminal domain. *Neuron* **92**, 1324–1336 (2016).
32. Volkmann, R. A. et al. MPX-004 and MPX-007: new pharmacological tools to study the physiology of NMDA receptors containing the GluN2A subunit. *PLoS ONE* **11**, e0148129 (2016).
33. Gono, T. et al. NR2-reactive antibody decreases cell viability through augmentation of Ca(2+) influx in systemic lupus erythematosus. *Arthritis Rheum.* **63**, 3952–3959 (2011).
34. Sakimura, K. et al. Reduced hippocampal LTP and spatial learning in mice lacking NMDA receptor epsilon 1 subunit. *Nature* **373**, 151–155 (1995).
35. Kutsuwada, T. et al. Impairment of suckling response, trigeminal neuronal pattern formation, and hippocampal LTD in NMDA receptor epsilon 2 subunit mutant mice. *Neuron* **16**, 333–344 (1996).
36. von Engelhardt, J. et al. Contribution of hippocampal and extra-hippocampal NR2B-containing NMDA receptors to performance on spatial learning tasks. *Neuron* **60**, 846–860 (2008).
37. Putterman, C. & Diamond, B. Immunization with a peptide surrogate for double-stranded DNA (dsDNA) induces autoantibody production and renal immunoglobulin deposition. *J. Exp. Med.* **188**, 29–38 (1998).
38. Larkin, A. E. et al. Blockade of NMDA receptors pre-training, but not post-training, impairs object displacement learning in the rat. *Brain Res.* **1199**, 126–132 (2008).
39. Faust, T. W., Robbiati, S., Huerta, T. S. & Huerta, P. T. Dynamic NMDAR-mediated properties of place cells during the object place memory task. *Front Behav. Neurosci.* **7**, 202 (2013).
40. Ekstrom, A. D., Meltzer, J., McNaughton, B. L. & Barnes, C. A. NMDA receptor antagonism blocks experience-dependent expansion of hippocampal "place fields". *Neuron* **31**, 631–638 (2001).
41. McHugh, T. J., Blum, K. I., Tsien, J. Z., Tonegawa, S. & Wilson, M. A. Impaired hippocampal representation of space in CA1-specific NMDAR1 knockout mice. *Cell* **87**, 1339–1349 (1996).
42. Cacucci, F., Yi, M., Wills, T. J., Chapman, P. & O'Keefe, J. Place cell firing correlates with memory deficits and amyloid plaque burden in Tg2576 Alzheimer mouse model. *Proc. Natl Acad. Sci. USA* **105**, 7863–7868 (2008).
43. Bertsias, G. K. & Boumpas, D. T. Pathogenesis, diagnosis and management of neuropsychiatric SLE manifestations. *Nat. Rev. Rheumatol.* **6**, 358–367 (2010).
44. Fragoso-Loyo, H. et al. Serum and cerebrospinal fluid autoantibodies in patients with neuropsychiatric lupus erythematosus. Implications for diagnosis and pathogenesis. *PLoS ONE* **3**, e3347 (2008).
45. Sun, W., Hansen, K. B. & Jahr, C. E. Allosteric interactions between NMDA receptor subunits shape the developmental shift in channel properties. *Neuron* **94**, 58–64 e53 (2017).
46. Lu, W., Du, J., Goehring, A. & Gouaux, E. Cryo-EM structures of the triheteromeric NMDA receptor and its allosteric modulation. *Science* **355**, eaal3729 (2017).
47. Hackos, D. H. et al. Positive allosteric modulators of GluN2A-containing NMDARs with distinct modes of action and impacts on circuit function. *Neuron* **89**, 983–999 (2016).
48. Yi, F. et al. Structural basis for negative allosteric modulation of GluN2A-containing NMDA receptors. *Neuron* **91**, 1316–1329 (2016).
49. Tajima, N. et al. Activation of NMDA receptors and the mechanism of inhibition by ifenprodil. *Nature* **534**, 63–68 (2016).
50. Zhu, S. et al. Mechanism of NMDA receptor inhibition and activation. *Cell* **165**, 704–714 (2016).
51. Esmenjaud, J. B. et al. An inter-dimer allosteric switch controls NMDA receptor activity. *EMBO J.* **38**, e99894 (2019).
52. Gielen, M., Siegler Retchless, B., Mony, L., Johnson, J. W. & Paoletti, P. Mechanism of differential control of NMDA receptor activity by NR2 subunits. *Nature* **459**, 703–707 (2009).
53. Paoletti, P. et al. Molecular organization of a zinc binding n-terminal modulatory domain in a NMDA receptor subunit. *Neuron* **28**, 911–925 (2000).
54. Fayyazuddin, A., Villarroel, A., Le Goff, A., Lerma, J. & Neyton, J. Four residues of the extracellular N-terminal domain of the NR2A subunit control high-affinity Zn2+ binding to NMDA receptors. *Neuron* **25**, 683–694 (2000).

55. Paoletti, P., Ascher, P. & Neyton, J. High-affinity zinc inhibition of NMDA NR1-NR2A receptors. *J. Neurosci.* **17**, 5711–5725 (1997).
56. Vergnano, A. M. et al. Zinc dynamics and action at excitatory synapses. *Neuron* **82**, 1101–1114 (2014).
57. Hughes, E. G. et al. Cellular and synaptic mechanisms of anti-NMDA receptor encephalitis. *J. Neurosci.* **30**, 5866–5875 (2010).
58. Moscato, E. H. et al. Acute mechanisms underlying antibody effects in anti-N-methyl-D-aspartate receptor encephalitis. *Ann. Neurol.* **76**, 108–119 (2014).
59. Mikasova, L. et al. Disrupted surface cross-talk between NMDA and Ephrin-B2 receptors in anti-NMDA encephalitis. *Brain* **135**, 1606–1621 (2012).
60. Jezequel, J. et al. Dynamic disorganization of synaptic NMDA receptors triggered by autoantibodies from psychotic patients. *Nat. Commun.* **8**, 1791 (2017).
61. Ladepeche, L. et al. NMDA receptor autoantibodies in autoimmune encephalitis cause a subunit-specific nanoscale redistribution of NMDA receptors. *Cell Rep.* **23**, 3759–3768 (2018).
62. Hardingham, G. E. & Bading, H. Synaptic versus extrasynaptic NMDA receptor signalling: implications for neurodegenerative disorders. *Nat. Rev. Neurosci.* **11**, 682–696 (2010).
63. Zhou, X., Ding, Q., Chen, Z., Yun, H. & Wang, H. Involvement of the GluN2A and GluN2B subunits in synaptic and extrasynaptic N-methyl-D-aspartate receptor function and neuronal excitotoxicity. *J. Biol. Chem.* **288**, 24151–24159 (2013).
64. Deep, S. N., Mitra, S., Rajagopal, S., Paul, S. & Poddar, R. GluN2A-NMDA receptor-mediated sustained Ca(2+) influx leads to homocysteine-induced neuronal cell death. *J. Biol. Chem.* **294**, 11154–11165 (2019).
65. Ogden, K. K. & Traynelis, S. F. New advances in NMDA receptor pharmacology. *Trends Pharm. Sci.* **32**, 726–733 (2011).
66. Chen, H. S. & Lipton, S. A. The chemical biology of clinically tolerated NMDA receptor antagonists. *J. Neurochem* **97**, 1611–1626 (2006).
67. Yelshansky, M. V., Sobolevsky, A. I., Jatzke, C. & Wollmuth, L. P. Block of AMPA receptor desensitization by a point mutation outside the ligand-binding domain. *J. Neurosci.* **24**, 4728–4736 (2004).
68. Alsaloum, M., Kazi, R., Gan, Q., Amin, J. & Wollmuth, L. P. A Molecular determinant of subtype-specific desensitization in ionotropic glutamate receptors. *J. Neurosci.* **36**, 2617–2622 (2016).
69. Kazi, R., Dai, J., Sweeney, C., Zhou, H. X. & Wollmuth, L. P. Mechanical coupling maintains the fidelity of NMDA receptor-mediated currents. *Nat. Neurosci.* **17**, 914–922 (2014).
70. Beaudoin, G. M. 3rd et al. Culturing pyramidal neurons from the early postnatal mouse hippocampus and cortex. *Nat. Protoc.* **7**, 1741–1754 (2012).

Acknowledgements

We thank Donna Schmidt for technical assistance; Dr. Quan Gan for helpful discussions and/or comments on the paper; Drs. Stephen Traynelis and Hongjie Yuan (Emory University) for generously sharing human NMDAR constructs; Dr. Kasper Hansen (University of Montana) for supplying triheteromeric constructs; and Prof. Masayoshi Mishina (University of Tokyo) and Prof. Dr. Hannah Monyer (Universität Heidelberg) for sharing transgenic mice targeting NMDAR subunits. This work was supported by NIH Grants NRSA F30MH115618 (KC), R01 NS088479 (LPW), and P01A1073693 (BD). Created with BioRender.com.

Author contributions

K.C., J.N., P.T.H., B.T.V., B.D., and L.P.W. designed the experiments. K.C. J.N., T.S.H., N.C., G.M., C.K., and P.T.H. performed the experiments. K.C., J.N. P.T.H., B.T.V., B.D., and L.P.W. analyzed the data. K.C., P.T.H., B.T.V., B.D., and L.P.W. wrote the paper.

Competing interests

The authors declare no competing interests.

Additional information

Supplementary information is available for this paper at https://doi.org/10.1038/s41467-020-15224-w.

Correspondence and requests for materials should be addressed to B.D. or L.P.W.

Peer review information *Nature Communications* thanks Jean-Claude Béïque, George Tsokos and the other, anonymous, reviewer(s) for their contribution to the peer review of this work.

Reprints and permission information is available at http://www.nature.com/reprints

Publisher's note Springer Nature remains neutral with regard to jurisdictional claims in published maps and institutional affiliations.

SUPPLEMENTARY INFORMATION

Lupus autoantibodies act as positive allosteric modulators at GluN2A-containing NMDA receptors and impair spatial memory

Kelvin Chan, Jacquelyn Nestor, Tomás S. Huerta, Noele Certain, Gabrielle Moody, Czeslawa Kowal, Patricio T. Huerta, Bruce T. Volpe, Betty Diamond, and Lonnie P. Wollmuth

TABLE OF CONTENTS

Supplementary Table 1. In the whole-cell mode, the G11 antibody has no notable effect on current properties other than changes in peak current amplitudes (relates to Figures 1A-1D).

Subunit	Antibody	Norm. I_{peak} %	Norm. I_{leak} %	Norm. Des %	n
hGluN1/hGluN2A	100 μg/ml B1	92 ± 3.6	173 ± 44	105 ± 4	5
	100 μg/ml G11	**154* ± 14**	194 ± 95	73 ± 25	5
hGluN1/hGluN2B	100 μg/ml B1	97 ± 1.4	121 ± 12	121 ± 16	6
	100 μg/ml G11	**125* ± 7.2**	92.1 ± 13	103 ± 16	5

Values shown are mean ± SEM for changes in normalized whole-cell peak current amplitudes (Norm. I_{peak}), normalized leak current amplitudes (Norm. I_{leak}), and normalized extent desensitization (Norm. Des) for steady-state currents either in control antibody (B1) or human DNRAb (G11) (see Figures 1A & 1B).
Tagged values are significantly different (*) than their respective control condition, B1 (*$p < 0.05$, *two-tailed Student's t-test, unpaired*).

We made these measurements in 100 μg/ml where both N2A- and N2B-containing receptors were potentiated (Figures 1C & 1D). The lack of an effect on leak current indicates that DNRAbs do not themselves act as agonists. DNRAbs also do not affect desensitization.

Supplementary Table 2. Effects of DNRAbs on hGluN2A- or hGluN2B-containing NMDARs (relates to Figures 2A-2D).

Subunit	Antibody	Total events (# of patches)	*i* *pA*	eq. P_{open}	MCT *ms*	MOT *ms*
hGluN2A	10 μg/ml B1	485793 (6)	-8.3 ± 0.4	0.40 ± 0.07	5.9 ± 1.0	3.8 ± 0.6
	10 μg/ml G11	546303 (7)	-8.2 ± 0.5	**0.63* ± 0.05**	3.5 ± 0.7	6.0 ± 0.9
	100 μg/ml B1	632383 (8)	-7.1 ± 0.2	0.40 ± 0.07	8.9 ± 1.9	4.9 ± 0.7
	100 μg/ml G11	1047339 (8)	-7.5 ± 0.1	**0.61* ± 0.03**	**3.7* ± 0.4**	5.7 ± 0.4
hGluN2B	10 μg/ml B1	135134 (6)	-8.3 ± 0.3	0.18 ± 0.04	27.9 ± 12.4	4.0 ± 0.7
	10 μg/ml G11	445555 (6)	-8.5 ± 0.2	0.19 ± 0.02	16.0 ± 2.9	3.5 ± 0.3
	100 μg/ml B1	154900 (6)	-7.5 ± 0.4	0.15 ± 0.06	42.9 ± 12.9	4.8 ± 0.9
	100 μg/ml G11	332097 (10)	-7.5 ± 0.3	0.23 ± 0.04	24.0 ± 2.8	6.1 ± 0.5

Values shown are mean ± SEM for single-channel current amplitude (*i*), equilibrium open probability (P_o), mean closed time (MCT), and mean open time (MOT). Single channel currents were recorded in the on-cell mode at approximately -100 mV and analyzed in QuB (see Materials & Methods). Number of patches is in parenthesis to the right of total events. Eq P_o is the fractional occupancy of the open states in the entire single-channel recording, including long lived closed states (desensitized states). All data were idealized and fit at a dead time of 20 μs.
Tagged values are significantly different (*) than their respective isotype control antibody (Ab) condition, B1 (*$p < 0.05$, two-tailed Student's t-test, unpaired*).

Supplementary Table 3. The D285K mutation in the GluN2A DWEYS motif has no notable effect on current properties (relates to Figures 3B-3D).

Subunit	I_{ampl} *pA*	Des *%*	n
hGluN1/hGluN2A	-1200 ± 550	33 ± 12	10
hGluN1/ hGluN2A(D285K)/hGluN2A(D285K)	-970 ± 290	19 ± 10	7

Values shown are mean ± SEM for whole-cell peak current amplitude (I_{ampl}) and % desensitization (Des). Wild type and D285K recordings were alternated.

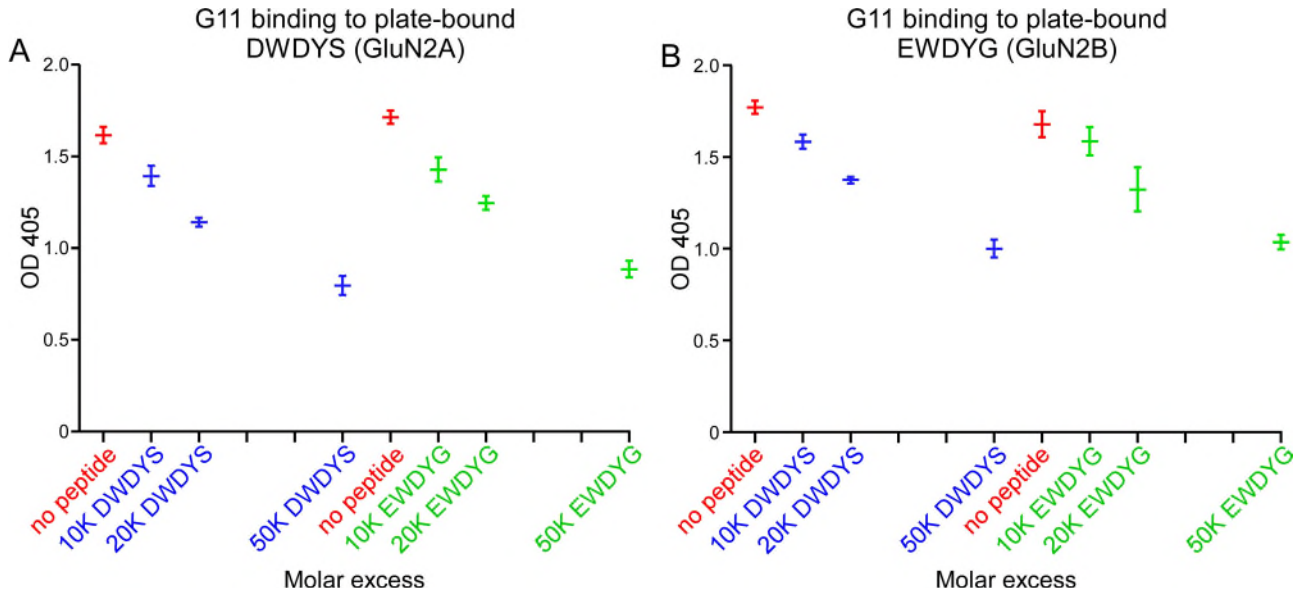

Supplementary Figure 1. Competitive ELISAs for DNRAb binding to soluble GluN2A or GluN2B epitopes (relates to Figures 3B-3E).
(A & B) Optical density (OD 405) values (mean ± SEM), measured by competitive ELISAs, for displacement of human DNRAb (G11) from plate-bound **(A)** DWDYS pentapeptide (GluN2A-specific) or **(B)** EWDYG (GluN2B-specific) by molar excess concentrations of the same soluble pentapeptides (n = 4 for each treatment condition).

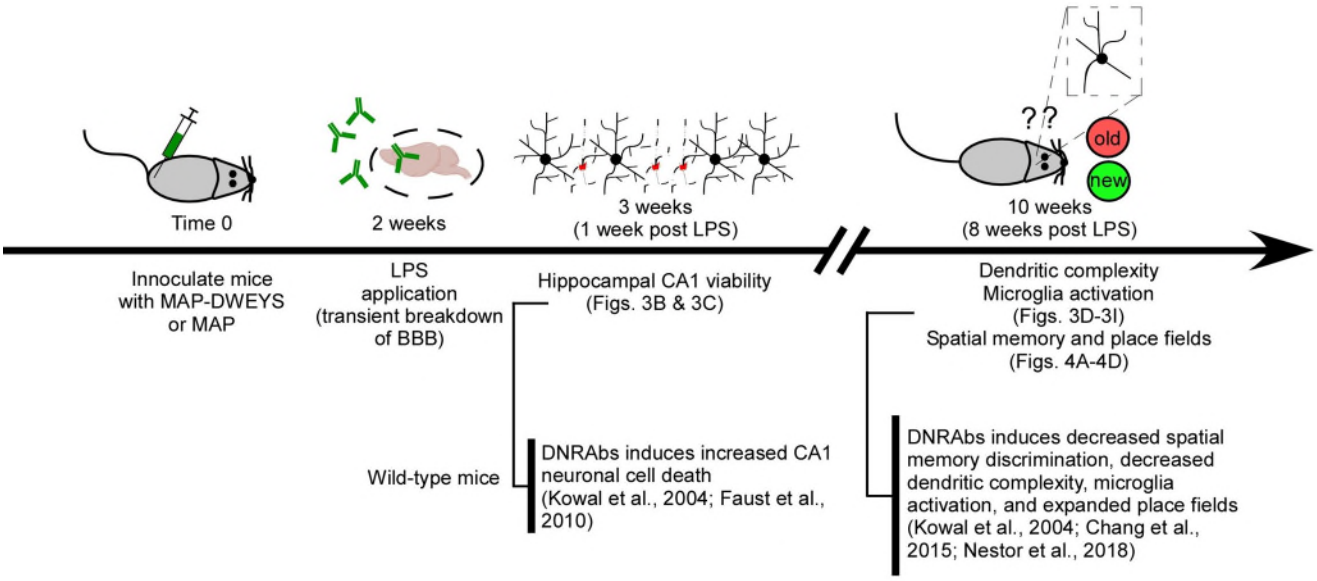

Supplementary Figure 2. Diagram of the experimental protocol used for the NPSLE mouse model (relates to Figures 4 & 5).

Female mice (6 – 8 weeks old) were immunized either with the DWEYS decapeptide multimerized on a polylysine backbone (MAP-DWEYS) or with the polylysine backbone alone (MAP). DWEYS is a mimetope of DNA and homologous to a sequence within the GluN2A and GluN2B amino-terminal domain. Immunization of wildtype mice with MAP-DWEYS induces production of DNRAbs (DNRAb+ mice) whereas MAP alone (control) does not[1]. Booster immunizations were applied two and four weeks after the first immunization. Time 0 is the final immunization with MAP-DWEYS or MAP (four weeks after initial). Two weeks after the final immunization, mice were given lipopolysaccharide (LPS) to allow transient access of antibodies to the hippocampus[2, 3]. One week after the LPS treatment subsets of mice were sacrificed for histological characterization of CA1 pyramidal cell viability (Figs. 4B & 4C)[2, 4]. At this time point following LPS treatment, DNRAbs are still present in the hippocampus[2, 5]. Two weeks post-LPS, DNRAb levels are not detectable[5]. Eight weeks post LPS, subsets of animals were tested for hippocampal anatomy (CA1 dendritic complexity and microglia activation are altered in treated wild-type mice[3] (Figs. 4D-4I). Other mice were tested for spatial memory test and implanted with tetrodes to determine place field size (Figs 5A-5D).

Use of LPS to permealize BBB. LPS by itself produces a systemic inflammatory response and neuroinflammatory effects leading to neuronal death and microglia activation[6, 7, 8]. However, for all of our *in vivo* experiments, we only make comparisons between DNRAb+ (experimental) mice and DNARb- (control) mice, with both of these groups being treated with LPS. In addition, LPS permealization localizes DNRAbs more in the hippocampus and related structures than in other brain regions[2, 9]. The major region of action of DNRAbs in patients is the hippocampus and related structures[10, 11].

SUPPLEMENTARY METHODS

Immunization

Immunization with MAP-core and MAP-DWEYS peptide was performed according to an established immunization protocol for DNRAb generation[2, 3, 5]. Female mice aged 6–8 weeks were first immunized with the multi-antigen, given in Complete Freund's Adjuvant (Becton, Dickinson, and Company, 263810), with two boosters at 2 and 4 weeks in Incomplete Freund's Adjuvant (Becton, Dickinson, and Company, 263910). At 2 weeks following the second booster, mice received two intraperitoneal injections of LPS (6 mg/kg; Millipore-Sigma, L4524) 48 h apart administered with a 500 µl intraperitoneal injection of sterile saline.

In vitro cell culture and transfection

Human embryonic kidney 293 (HEK293) cells were grown in Dulbecco's modified Eagle's medium (DMEM), supplemented with 10% FBS, for 24 h before transfection. Human NMDAR-encoding cDNA constructs (Table 1) were co-transfected into HEK293 cells along with a separate peGFP-Cl construct at a ratio of 4:4:1 (N1:N2:eGFP) for macroscopic recordings, and at a ratio of 4:1.5:1 for single channel recordings using X-tremeGene HP (Roche, 06-366). Triheteromeric NMDAR-expressing constructs (Table 1), all derived from rat, were a gift from K. Hansen and transfection with these constructs were performed with Ca^{2+} precipitation[12]. HEK293 cells were bathed in medium containing the GluN2 competitive antagonist DL-2-amino-5-phosphopentanoic acid (APV, 100 µM, Tocris), magnesium (100 µM), and the GluN1 competitive antagonist 6,7-dichlorokynuric acid (DCKA, 100 µM, Tocris). All experiments were performed 24–48 h post-transfection. Point mutations were introduced in the various GluN2A subunits using site-directed mutagenesis (SDM)[13].

Table 1. Plasmid constructs used for heterologous expression of NMDARs in HEK293 cells.

Construct	Species	Description
pCI-neo-hGluN1a	Human	Wild-type receptor subunit
pCI-neo-hGluN2A	Human	Wild-type receptor subunit
pCI-neo-hGluN2B	Human	Wild-type receptor subunit
pCI-neo-2xATG-rGluN1a-GFP	Rat	Wild-type receptor subunit with bicistronic expression of eGFP (gift from K. Hansen)
pCI-neo-rGluN2A-C1-L4	Rat	Tri-heteromeric modified subunit (Hansen et al., 2014)
pCI-neo-rGluN2A-C2-L4	Rat	Tri-heteromeric modified subunit
pCI-neo-rGluN2B-AC1-L4	Rat	Tri-heteromeric modified subunit
pCI-neo-rGluN2B-AC2-L4	Rat	Tri-heteromeric modified subunit

In vitro macroscopic recordings

Macroscopic currents in the whole-cell mode were recorded at room temperature (20–23°C) using an EPC-10 amplifier with PatchMaster software (version v2x90.2, HEKA), digitized at 10 kHz and low-pass filtered at 2.9 kHz (−3 dB) using an 8 pole low pass Bessel filter[14]. Patch microelectrodes were filled with an intracellular solution (mM): 140 KCl, 10 HEPES, 1 BAPTA, 4 Mg^{2+}-ATP, 0.3 Na^{+}-GTP, pH 7.3 (KOH), 297 mOsm (sucrose). Our standard extracellular solution consisted of (mM): 150 NaCl, 2.5 KCl, and 10 HEPES, pH 7.2 (NaOH). Ca^{2+} was omitted from the extracellular solution to prevent rundown over time. Pipettes had resistances of 2–6 MΩ when filled with the pipette solution and measured in the standard Na^{+} external solution. We did not use series resistance compensation nor did we correct for junction potentials. Currents were measured within 10 min of going whole-cell.

External solutions were applied using a piezo-driven double barrel application system. Prior to use, we incubated the application system with 2% BSA (1xPBS) for 2 h at 21–24°C to minimize non-specific

antibody binding. For agonist application, one barrel contained the external solution 0.1 mM glycine, whereas the other barrel contained both 0.1 mM glycine and 1 mM glutamate. For display, NMDAR currents were digitally re-filtered at 500 Hz and resampled at 1 kHz using IgorPro (version 7, WaveMetrics).

In vitro single channel recordings

Single channel currents were recorded in the on-cell configuration at 20–23°C using an integrating patch clamp amplifier (Axopatch 200B, Molecular Devices), analog filtered at 10 kHz (four-pole Bessel filter), and digitized between 25 and 50 kHz (ITC-16 interfaced with PatchMaster, (version v2x90.2, HEKA)[15]. Data were transferred to QuB (version 2.0.0.30, SUNY at Buffalo) for analysis.

Patch pipettes (thick-wall, borosilicate, Sutter Instruments) were pulled and fire-polished achieving resistances between 10 and 20 MΩ when measured in the bath. At −100 mV, seal resistance ranged between 2 and 20 GΩ. For cell-attached recordings, patch pipettes were filled with the standard bath solution as well as 1 mM glutamate and 0.1 mM glycine. 0.05 mM EDTA was added to minimize gating effects of divalent cations. Inward currents were elicited by applying a pipette potential of +100 mV. Recordings of hGluN1/hGluN2A or hGluN1/hGluN2B, either in the presence of absence of DNRAbs, consisted of long clusters of activity separated by seconds-long periods of inactivity, simplifying detection of several channels in the patch. For these recordings the relatively high equilibrium open probability (eq. Po) and duration of recordings (≈10,000 to 180,000 per recording) indicated that we were recording from single-channel patches.

For DNRAbs at 10 μg/ml, our standard bath (pipette) solution consisted of 150 mM NaCl, 10 mM HEPES (pH 7.2, NaOH). For DNRAbs at 100 μg/ml, our standard bath had a decreased concentration of NaCl to 140 mM to compensate for the osmotic force generated by the antibodies in solution.

Immunocytochemistry

HEK293T cells were used for immunocytochemistry (ICC). Transfections were performed in the same manner as described above with X-tremeGene HP (Roche, 06-366), without GFP co-transfection. Cells were fixed with 4% paraformaldehyde 48 h post-transfection, washed 3 times with 1xPBS, and then blocked with 2% bovine serum albumin (BSA) (Sigma, A9647) at room temperature. Incubation of primary antibody, either IgG control B1 (20 μg/mL) or human DNRAb, G11 (20 μg/mL) diluted in 2% BSA was done overnight at 4°C. Following 3 washes with 1xPBS, labeling was performed with secondary goat anti-human Alexa 488-conjugated antibodies (1:1000, ThermoFisher, A-11013) at room temperature. Coverslips were mounted with ProLong® Diamond Anti-fade mountant w/DAPI (ThermoFisher, P36962), and imaged with an Olympus FV-1000 confocal microscope with FluoView software (FV10-ASW, version 4.02, Olympus). Five fields (212 x 212 μm, 60x oil) were taken per coverslip. Mean corrected fluorescence of fields were determined on ImageJ with spectral deconvolution plugin (Seth Gammon, Washington University at St. Louis)[16, 17] and ROI background correction.

For primary hippocampal neurons used for ICC, cultures were made according to an established postnatal culture protocol with minor modifications [18]. Glia and astrocyte harvested from P2 mice were seeded at 10-14 days prior to dissection[19]. On day of dissection, glia/astrocyte cultures had media replaced with plating media, consisting of 10% (v/v) Fetal Bovine Serum (FBS) (ThermoFisher, 16140071), 0.45% (w/v) glucose, 1 mM sodium pyruvate, 2 mM glutamine, 100 U/mL penicillin/streptomycin in Basal Medium Eagle (ThermoFisher, 21010046). Hippocampi from P0-P1 C57/BL6 mice pips were dissected in ice-cold dissection media, consisting of 0.11 mg/mL sodium pyruvate, 0.1% glucose, 10 mM HEPES in HBSS, Ca^{2+} and Mg^{2+}-free (ThermoFisher, 14175095) followed by 0.25% (v/v) trypsin-EDTA digestion for 20 min at 37°C. DNase I (Sigma, DN25) was added shortly after, and incubated for 5 min at RT. Following 2 washes with plating media, tissue was triturated with an FBS-coated pipette tip 10–12 times. Cells in suspension were counted with a

hemocytometer, with approximately 150,000 cells added to 18 mm glass coverslips coated with poly-D-lysine in 12-well plates. Cultures were incubated in plating medium for 2 h at 37°C to allow for cells to adhere to coverslip. Coverslips were then flipped onto glia/astrocyte cultures, and cells were allowed to grow overnight in plating media, then switched with maintenance medium, consisting of 2% B-27 supplement (ThermoFisher, 17504044), 2 mM glutamine, 100 U/mL penicillin/streptomycin. On DIV3, 5 µM of cytosine arabinoside (Sigma, C1768) was added to cultures to inhibit mitosis of non-neuronal cells. Thereafter, half of maintenance media was replaced every 3 days until pharmacological treatment at DIV14.

Pharmacological treatment of primary hippocampal neurons occurred at DIV14. Final concentrations of antagonists were 3 µM: TCN-201 (AdooQ Bioscience, A11947), MPX-004 (Alomone Labs, M280), and ifenprodil (Sigma, I2892). These were added along with the DNRAb (G11) at 10 µg/mL, in maintenance media to neurons. DMSO was used as vehicle control for both control (B1) and DNRAb (G11) conditions.

ICC was performed 24 h post treatment on DIV15. Coverslips were washed with 1xPBS 3 times and then incubated in 4% paraformaldehyde(v/v)/4% sucrose (w/v) for 15 min. Coverslips were then washed again with 1xPBS 3 times and were blocked/permeabilized with antibody blocking solution, consisting of 2% (w/v) BSA, 0.25% (v/v) Triton-X100 in 1xPBS, for 60 min at RT. Coverslips were then incubated in primary antibodies, rabbit anti-activated caspase-3 (1:250, Cell Signaling, 9661), and mouse anti-β tubulin III (Tubb3) (1:400, Millipore-Sigma, MAB1637), both in antibody blocking solution overnight in 4°C. Coverslips were then washed with 1xPBS 3 times, and incubated in fluorescence-conjugated secondary antibodies, Goat anti-rabbit Alexa-647 (1:1000, ThermoFisher, A21245) and Goat anti-mouse Alexa-488(1:1000, ThermoFisher, A21121) for 1 h at RT. Coverslips were then mounted and imaged as described above with Olympus confocal. Number of activated caspase-3 neurons were averaged by 5 fields (212 x 212 µm, 60x oil) per biological replicate. Quantification and image analysis were done on ImageJ by researcher blinded to treatment conditions.

ELISA

Peptides were coated on COSTAR plates (Corning, CLS3690) at 20 µg/ml, 25 µl/well in 0.1 M $NaHCO_3$ pH 8.6, at 4°C, overnight. The plate was washed once with 1x PBS containing 0.05 % Tween 100 (PBS-T) and blocked with 1% BSA/PBS, 50 µl/well, for 1 hr at 37^0C. G11 antibody was used at 7.5 µg/ml which was on the linear range of binding curve established prior to the inhibition. Antibody was pre-incubated with a wide range of the inhibitory peptide in 1% BSA/PBS for 1 hr at RT and added to each well. The assay was performed twice with triplicates measurements. The well without the inhibitor peptide served as positive control. After incubation at 37°C for 1 hr, the plate was washed 6 times with PBS-T buffer. Goat anti-human secondary antibody labeled with alkaline phosphatase (IgG-AP) (SouthernBiotech, 2040-40) was added at 1:1000 dilution in 25 µl/well of 1% BSA/PBS followed by incubation at 37°C for 1 hr and by washing with PBS-T buffer. The ELISA was developed using AP substrate (Millipore-Sigma), in 50 µl/well of a buffer containing $MgCl_2$ (1 mM final), Na_2CO_3 (25 mM final) and $NaHCO_3$ (2.5 mM final). The reading was done at 405 µm using a multilabel counter from Perkin-Elmer.

Neuronal Staining

Mice were anesthetized with 100 µl of Euthasol (Virbac) prior to perfusion with 0.9% sodium chloride, 0.5% sodium nitrite, and 0.1% heparin, followed by 4% paraformaldehyde (PFA) in 0.1 M phosphate buffer (PB) as before[3].

Cresyl violet staining. Brains were extracted, fixed in 4% PFA for 2 h and transferred to 30% sucrose, blocked and sliced at 40 µm. Brains were blocked in a coronal stainless-steel template and a 4 mm slab of tissue was cut from approximately Bregma -0.94 mm with a microtome. Tissue was sampled at a thickness of 40 µm with a periodicity of one in four coronal sections over the next 1600 to 1900 µm.

Sections were mounted, dehydrated, rehydrated and stained in cresyl violet for 3 min. Sections were dried, dehydrated, cleared (Histoclear II) and coverslipped with Permount® (ThermoFisher) prior to imaging on an AxiophotZ1 microscope (Zeiss). Sections were imaged in 100x oil, and we focused on the soma of the stratum pyramidale around which a tiled Z-stacked (0.5 µm steps) image was generated. Stereology was performed with the sampling frame set such that an individual frame captures 2–5 targets in the photomicrograph[2, 3, 5]:. Then optical dissectors are created by manipulating the level of the Z-stack, and nuclei within neurons in focus are counted as long as they are not in contact with the left or bottom part of a frame[20]. Quantitation of CA1 neurons in image stacks was performed with the Stereo Investigator suite in Neurolucida 360 (MBF Bioscience) with researcher blinded to treatment conditions. Neuron numbers in Fig. 4C represent the total number of cell bodies captured in the systematic random sampling frame as it is placed on consecutive sections or "runs". There were 3 animals in each group, with 8 runs for each animal.

Golgi stain for neuronal Sholl analysis. Brains were processed using FD Rapid Golgi Stain kit (FD NeuroTechnologies), a silver staining method to visualize entire neurons[21]. Brains were extracted and submerged in the impregnation solution (Solution A + Solution B, 1:1) for 2 weeks. Impregnation solution was changed after the first 24 h. Brains were then cryoprotected in Solution C for 72 h (room temperature, dark). Solution C was exchanged after the first 24 h. After 14 days, brains were sectioned at 100 µm on a cryostat (-21°C) that permit identification of internal anatomic landmarks to signal sample start and stop, with periodicity of one in four coronal sections across ~1200 µm (Bregma -0.94 to -2.2mm for the dorsal hippocampus) of brain with at least 5 different sections being sample per animal. Sections were mounted, dried (room temperature, dark), silver nitrate stained (Solution D + Solution E, 1:1), rinsed, dehydrated in EtOH, cleared in xylene, and coverslipped. Tissue was imaged on an AxioImager Z1 microscope (Zeiss) with ZEN Blue (version 2.0, Zeiss) software in 40x oil using tiling and Z-stack (2 µm steps). There were 4 animals in each group and 10–20 neurons were analyzed for each animal as shown in Fig. 4D&E. Images were then analyzed using Neurolucida 360 (MBF Bioscience) dendritic tracing for Sholl analysis at 10 µm shells from the soma by researcher blinded to treatment conditions[3, 5].

Immunohistochemistry

For immunohistochemistry, brains were extracted and sectioned as performed for cresyl violet staining above. Sections were washed (0.1 M phosphate buffered saline, PBS), permeabilized (0.2% Triton X-100 in 1% BSA in 0.1 M PBS), blocked (1% BSA in 0.1 M PBS for 60 minutes), and stained with primary antibody overnight at 4°C in 1% BSA. Primary antibodies were rabbit anti-Iba1 (1:500, Wako Chemicals, 019-1 9741), rat anti-CD68 (1:500, Bio-Rad, mca1957). On the following day, samples were washed (0.1 M PBS), incubated with secondary antibody (0.1 M PB for 45 min). Secondary antibodies included Donkey anti-rat Alexa Fluor 488 (1:400, Life Technologies, A21208), Chicken anti-rabbit Alexa Fluor 594 (1:300, Life Technologies, A21442). Sections underwent additional washes and incubation in DAPI (0.5 µg/mL in 0.1 M PB) and mounted with Cytoseal 60 (ThermoFisher) and cover-slipped.

Tissue was imaged on an AxioImager Z1 microscope or LSM 880 confocal microscope using Airy scan parameters (Zeiss). Microglia and colocalization with CD68 were quantified using ZEN Blue (version 2.0, Zeiss) software[3, 22]. CD68 score was graded as before: "0", no or scarce expression; "1", punctate expression; "2", aggregate or punctate expression all over cell [3]. Microglia were quantitated per 106.4 μm^2 box that was placed in 6 regions of interest across the stratum radiatum of CA1 using identical Airy scan acquisition parameters (40x oil, Airy = 2X, Z-stack = 10). Images of individual microglia were transferred to Neurolucida 360 (MBF Bioscience) for quantitation. We analyzed 3 tissue sections; the periodicity was one in four 40 µm sections across the dorsal CA1 hippocampus, there were 3 animals in each group. All raw measurements were analyzed by a researcher blinded to treatment conditions and compiled for cumulative probability distributions and analyzed by Kolmogorov-Smirnov

non-parametric statistics. The mean results for each Sholl dimension from the soma were plotted for each group and displayed in 5 μm concentric circle increments.

Behavioral assessment and *in vivo* electrophysiology

Mice used for these procedures lived on a reverse light-dark cycle (lights off at 09:00 h, lights on at 21:00 h), for at least 10 days before testing started, with *ad libitum* access to chow and water. All behavioral experiments occurred between 10:00 h and 18:00 h, which corresponded to the dark phase of the circadian cycle, when the rodents were naturally active. Animals were handled for 15 min per day for 3 days before they were tested behaviorally. The object place memory (OPM) task was performed as described [3, 5]. The apparatus consisted of a square chamber (40 cm on the side, 40 cm high), with the walls painted grey. Researchers were blinded to animal's treatment group during behavior assessment. Animals were familiarized to the empty chamber (3 sessions of 15 min each). For OPM testing, mice underwent the following sequence: empty chamber (10 min), home cage (10 min), sample phase in which the chamber had two objects located at the center of the NW and NE sectors (5 min), home cage (10 min), choice phase in which the chamber had the same objects but one of them was moved from NE to the center of the SE sector (5 min). The discrimination ratio was calculated during the choice phase by dividing time spent exploring the moved object minus the time spent exploring the static object by the time exploring the objects combined [5]. Data were collected and analyzed using EthoVision XT (version 11, Noldus Information Technologies, Leesburg, VA) which automatically detected the contours of the animal from a live video feed, discriminated it from the background, and tracked activity with a 3-point detection algorithm (video rate, 30 frames per second).

The analysis of place cells in the dorsal CA1 region of the hippocampus: a mouse was anesthetized with 0.25% isoflorane and implanted with a 16 channel multi-electrode array containing 4 tetrodes[4, 5]. After recovery, single unit firing was recorded using Cheetah software (version 5, Neuralynx) while the animal explored a square chamber (40 cm on the side) in a schedule of 4 exploration runs (15 min) separated by 3 rest sessions (5 min) in the home cage. Recordings were repeated over 2 consecutive days. Acquired data were analyzed using Spike2 (version 8, Cambridge Electronic Design), NeuroExplorer (version 5, Nex Technologies), and MATLAB (version 9.2 R2017a, MathWorks).

SUPPLEMENTARY INFORMATION REFERENCES

1. Putterman C, Diamond B. Immunization with a peptide surrogate for double-stranded DNA (dsDNA) induces autoantibody production and renal immunoglobulin deposition. *J Exp Med* **188**, 29-38 (1998).

2. Kowal C, *et al.* Cognition and immunity; antibody impairs memory. *Immunity* **21**, 179-188 (2004).

3. Nestor J, *et al.* Lupus antibodies induce behavioral changes mediated by microglia and blocked by ACE inhibitors. *J Exp Med*, (2018).

4. Faust TW, *et al.* Neurotoxic lupus autoantibodies alter brain function through two distinct mechanisms. *Proc Natl Acad Sci U S A* **107**, 18569-18574 (2010).

5. Chang EH, *et al.* Selective Impairment of Spatial Cognition Caused by Autoantibodies to the N-Methyl-D-Aspartate Receptor. *EBioMedicine* **2**, 755-764 (2015).

6. Sternberg EM. Neural-immune interactions in health and disease. *J Clin Invest* **100**, 2641-2647 (1997).

7. Nolan Y, Vereker E, Lynch AM, Lynch MA. Evidence that lipopolysaccharide-induced cell death is mediated by accumulation of reactive oxygen species and activation of p38 in rat cortex and hippocampus. *Exp Neurol* **184**, 794-804 (2003).

8. Vereker E, Campbell V, Roche E, McEntee E, Lynch MA. Lipopolysaccharide inhibits long term potentiation in the rat dentate gyrus by activating caspase-1. *J Biol Chem* **275**, 26252-26258 (2000).

9. Huerta PT, Kowal C, DeGiorgio LA, Volpe BT, Diamond B. Immunity and behavior: antibodies alter emotion. *Proc Natl Acad Sci U S A* **103**, 678-683 (2006).

10. Appenzeller S, Carnevalle AD, Li LM, Costallat LT, Cendes F. Hippocampal atrophy in systemic lupus erythematosus. *Ann Rheum Dis* **65**, 1585-1589 (2006).

11. Mackay M, *et al.* Metabolic and microstructural alterations in the SLE brain correlate with cognitive impairment. *JCI Insight* **4**, (2019).

12. Hansen KB, Ogden KK, Yuan H, Traynelis SF. Distinct functional and pharmacological properties of Triheteromeric GluN1/GluN2A/GluN2B NMDA receptors. *Neuron* **81**, 1084-1096 (2014).

13. Kazi R, Dai J, Sweeney C, Zhou HX, Wollmuth LP. Mechanical coupling maintains the fidelity of NMDA receptor-mediated currents. *Nat Neurosci* **17**, 914-922 (2014).

14. Yelshansky MV, Sobolevsky AI, Jatzke C, Wollmuth LP. Block of AMPA receptor desensitization by a point mutation outside the ligand-binding domain. *J Neurosci* **24**, 4728-4736 (2004).

15. Talukder I, Wollmuth LP. Local constraints in either the GluN1 or GluN2 subunit equally impair NMDA receptor pore opening. *J Gen Physiol* **138**, 179-194 (2011).

16. Gammon ST, Leevy WM, Gross S, Gokel GW, Piwnica-Worms D. Spectral unmixing of multicolored bioluminescence emitted from heterogeneous biological sources. *Anal Chem* **78**, 1520-1527 (2006).

17. Zurek-Biesiada D, Kedracka-Krok S, Dobrucki JW. UV-activated conversion of Hoechst 33258, DAPI, and Vybrant DyeCycle fluorescent dyes into blue-excited, green-emitting protonated forms. *Cytometry A* **83**, 441-451 (2013).

18. Beaudoin GM, 3rd, *et al.* Culturing pyramidal neurons from the early postnatal mouse hippocampus and cortex. *Nat Protoc* **7**, 1741-1754 (2012).

19. Kaech S, Banker G. Culturing hippocampal neurons. *Nat Protoc* **1**, 2406-2415 (2006).

20. Gundersen HJ. Stereology of arbitrary particles. A review of unbiased number and size estimators and the presentation of some new ones, in memory of William R. Thompson. *J Microsc* **143**, 3-45 (1986).

21. Glaser EM, Van der Loos H. Analysis of thick brain sections by obverse-reverse computer microscopy: application of a new, high clarity Golgi-Nissl stain. *J Neurosci Methods* **4**, 117-125 (1981).

22. Schafer DP, *et al.* Microglia sculpt postnatal neural circuits in an activity and complement-dependent manner. *Neuron* **74**, 691-705 (2012).

Bioelectronic Medicine

METHODOLOGY Open Access

Framework for automated sorting of neural spikes from Neuralynx-acquired tetrode recordings in freely-moving mice

Joshua J. Strohl[1,2], Joseph T. Gallagher[1], Pedro N. Gómez[1], Joshua M. Glynn[1,2] and Patricio T. Huerta[1,2*]

Abstract

Background: Extracellular recording represents a crucial electrophysiological technique in neuroscience for studying the activity of single neurons and neuronal populations. The electrodes capture voltage traces that, with the help of analytical tools, reveal action potentials ('spikes') as well as local field potentials. The process of spike sorting is used for the extraction of action potentials generated by individual neurons. Until recently, spike sorting was performed with manual techniques, which are laborious and unreliable due to inherent operator bias. As neuroscientists add multiple electrodes to their probes, the high-density devices can record hundreds to thousands of neurons simultaneously, making the manual spike sorting process increasingly difficult. The advent of automated spike sorting software has offered a compelling solution to this issue and, in this study, we present a simple-to-execute framework for running an automated spike sorter.

Methods: Tetrode recordings of freely-moving mice are obtained from the CA1 region of the hippocampus as they navigate a linear track. Tetrode recordings are also acquired from the prelimbic cortex, a region of the medial prefrontal cortex, while the mice are tested in a T maze. All animals are implanted with custom-designed, 3D-printed microdrives that carry 16 electrodes, which are bundled in a 4-tetrode geometry.

Results: We provide an overview of a framework for analyzing single-unit data in which we have concatenated the acquisition system (Cheetah, Neuralynx) with analytical software (MATLAB) and an automated spike sorting pipeline (MountainSort). We give precise instructions on how to implement the different steps of the framework, as well as explanations of our design logic. We validate this framework by comparing manually-sorted spikes against automatically-sorted spikes, using neural recordings of the hippocampus and prelimbic cortex in freely-moving mice.

Conclusions: We have efficiently integrated the MountainSort spike sorter with Neuralynx-acquired neural recordings. Our framework is easy to implement and provides a high-throughput solution. We predict that within the broad field of bioelectronic medicine, those teams that incorporate high-density neural recording devices to their armamentarium might find our framework quite valuable as they expand their analytical footprint.

Keywords: Automated spike sorting, Spike clustering, MountainSort, Neuralynx, Cheetah, MATLAB, Tetrode, Electrophysiology, Mouse

* Correspondence: pato.huerta@gmail.com
[1]Laboratory of Immune & Neural Networks, Institute of Molecular Medicine, Feinstein Institutes for Medical Research, Northwell Health, Manhasset, New York, USA, 350 Community Drive, Manhasset, NY 11030, USA
[2]Department of Molecular Medicine, Zucker School of Medicine at Hofstra/Northwell, 500 Hofstra Blvd, Hempstead, NY 11549, USA

Background

Functional understanding of neural ensembles requires the ability to reliably measure the activity of single neurons, as well as to discriminate the activity of many neighboring neurons, across extended intervals of time (Buzsáki, 2004; Csicsvari, et al., 2003). In vivo electrophysiological techniques with extracellular electrodes that measure action potentials ('spikes') and subthreshold oscillations have been used to record activity from the brain of several mammalian species and have generated a tremendous amount of information (Cacucci et al., 2008; O'Keefe and Dostrovsky, 1971; O'Keefe and Nadel, 1976; Kunz, et al., 2021). Moreover, continuous technological advances have ensured the lasting relevance of this technique (Steinmetz, et al., 2021; van Daal, et al., 2021). Indeed, brain recordings with tetrode arrays have been adopted by many neuroscience laboratories all over the world (Yamamoto and Wilson, 2008). After obtaining a tetrode recording, spike sorting is a mandatory step for the isolation of neuronal units. This process begins by applying a band-pass filter followed by a voltage threshold to detect all events which fall into the frequency and voltage ranges containing neural spikes. Following event detection, spikes are brought into a spike sorting software package (Rey et al., 2015). Most spike sorting algorithms use dimensionality reduction techniques, such as principal component analysis (PCA), where the high dimensional features of spikes are represented in a 2-dimensional or 3-dimensional space for manual cluster cutting (Gray, et al., 1995; Quirk & Wilson, 1999). Other software packages implement a template matching approach (Laboy-Juárez, et al., 2019), and some, such as Spike2 (CED, Cambridge, UK), offer both PCA and template matching options. Events that cluster together are assigned to a unit with an arbitrary label, representing a putative neuron. During this process, clusters or events which are either poorly isolated or likely to correspond to background noise are removed from further analysis.

Since the introduction of XCLUST, a pioneering spike clustering program, by Matthew Wilson (Quirk & Wilson, 1999), several spike sorting packages have been developed using manual or semi-automated approaches. Some commonly used packages include KlustaKwik (Harris, et al., 2000), MClust (Redish et al., 2000), Offline Sorter (Plexon, Dallas, TX), and Spike2 (CED). While the manual approach has been the standard for decades, there are notable drawbacks. A significant concern is the lack of reliability, given that different manual operators can have variable outcomes and error rates can be as high as 30% (Harris, et al., 2000). The operator-dependent nature of the manual approach may thus negatively impact the objectivity and reproducibility of the sorted data (Wood et al., 2004). Another concern with manually-sorted spikes is the amount of time necessary to analyze datasets of any size. Cluster cutting is a time-intensive process, which effectively acts as a bottleneck in the analysis of acquired neural datasets. Early semi-automated algorithms have continued to rely on human intervention (Harris, et al., 2000; Hill et al., 2012), and some have shown poor accuracy (Pedreira, et al., 2012), resulting in a lasting dependence on manual techniques by the majority of the systems neuroscience community.

Recently, automated algorithms have been developed that are both sufficiently accurate and have the ability to sort data obtained from large arrays (Buccino et al., 2020; Chaure et al., 2018; Chung et al., 2017; Pachitariu et al., 2016; Rossant et al., 2016). Remarkably, these automated approaches have arisen during a period when advancements in electrode technology have enabled simultaneous recording from hundreds to thousands of densely packed recording sites, from which sorting data would be excruciatingly laborious with previously standard methods (Berényi et al., 2014; Chung, et al., 2019; Steinmetz, et al., 2021). Smaller arrays also benefit from automated algorithms, as the same approach can be applied to tetrodes for fast and objective results. MountainSort is a particularly attractive package as it has shown to be the most accurate method thus far to sort relatively low-channel-count datasets (Buccino et al., 2020; Chung, et al., 2017; Magland, et al., 2020) and, critically, it requires no user input or changing of parameters across recordings (Chung, et al., 2017).

While MountainSort has the potential to be an effective and highly useful spike sorting package, it is still in the development phase and does not have a fully integrated support platform for importing neural recordings obtained across different recording systems and setups. One software package in development to address this issue is SpikeInterface. This software is designed to import data across a variety of acquisition systems, and then send the data to any of the SpikeInterface-supported spike sorters (Buccino et al., 2020). While SpikeInterface is designed to be a unified framework for spike sorting, with a high degree of flexibility, our framework offers advantages in its simplicity. Using the framework presented in this study, the end-user can automatically merge files of recordings from the same mouse on the same day, and send many recordings into MountainSort in a single run. After sorting, spikes can be easily integrated into existing data analysis pipelines. This is all done automatically with no coding needed by the end-user. Thus, the purpose of this study is to provide a simple-to-execute framework for using MountainSort with Neuralynx-acquired neuronal data. Moreover, we validate this framework with a qualitative comparison of manually-sorted spikes against automatically-sorted

spikes in neural recordings of the *Cornus Ammonis* 1 (CA1) region of the hippocampus and the prelimbic (PL) cortex in freely-moving mice.

Methods

Ethical statement

Animal experiments were performed in accordance with the National Institutes of Health (NIH) Guidelines under protocols approved by the Feinstein Institutes for Medical Research Institutional Animal Care and Use Committee (IACUC). Our Animal Research Program is registered with the Department of Health and Human Services (DHHS), Office of Laboratory Animal Welfare (OLAW), U.S. Department of Agriculture (USDA #21R0107), Public Health Service (PHS #A3168–01) and New York State Department of Health (NYSDOH #A-060).

Experimental animals

All animals used in this study were male C57BL/6 mice (The Jackson Laboratory, Bar Harbor, ME) of 3 months of age. Mice were maintained on a reverse light cycle (dark: 9:00–21:00) with ad libitum access to food and water. All experiments were carried out during the dark phase of the light cycle. Prior to implanting, mice were housed in groups of four, and were single-housed after implanting. All mice were gently handled prior to surgery (15-min sessions during 3 consecutive days).

Microdrive preparation

Custom-designed microdrive bodies were fabricated using a 3D printer (Form-2, Formlabs, Somerville, MA). The design of the microdrive body was specific to the brain region being recorded. Polyimide tubing and an electrode-interface-board (Omnetics EIB-16, Neuralynx, Bozeman, MT) were attached to each microdrive body. Tetrodes were wound from 90% platinum, 10% iridium wire (diameter 17.8 μm; California Fine Wire, Grover Beach, CA) and threaded through the polyimide tubes to create a movable 4-tetrode array (Chang, et al., 2013). On the day of implantation surgery, a 'final cut' of the tetrodes was made followed by electroplating with platinum black solution (Neuralynx) to an impedance under 300 kΩ.

Surgery

All surgical procedures were performed under isoflurane anesthesia. The animal's fur was removed from the surgical site, which was then scrubbed with betadine and isopropyl alcohol. An incision was made, exposing the skull, and a layer of C&B-Metabond (Parkell, Edgewood, NY) was applied and allowed to dry. Two craniotomies were made, one over the cerebellum and the other over the region targeted for tetrode implantation. The coordinates used for dorsal CA1 were [AP, − 2.18, ML, − 1.5] from bregma, and the coordinates for the PL cortex were [AP, + 1.98, ML, − 0.25] from bregma. After installing the ground screw into the craniotomy located in the occipital bone, the microdrive was aligned so that the tetrodes were directly above the intended region, and the microdrive was secured in place with dental acrylic. As the dental acrylic hardened, mice were given injection of buprenorphine (0.05 mg per kg) and saline (0.5 mL) subcutaneously. Implanted mice were observed for three days following surgery and provided with hydrogel cups containing meloxicam for pain relief. Tetrodes were lowered to their target depth, in CA1 or PL cortex, over the course of the next three days.

Behavioral tasks

Neural recording during behavioral tasks were typically performed 7–10 days after the surgery. Mice with tetrodes targeted to CA1 (n = 4) were studied in a linear track (80 cm long). For this task, mice experienced a first 'Run' session (moving from one end of the track to the other 16 times; 8 runs 'to the left', 8 runs 'to the right'), a 'Rest' period (10 min in the homecage), and a second 'Run' session (16 times, 8 runs 'to the left', 8 runs 'to the right'), for a total of 32 runs across the length of the track. Mice with tetrodes targeted to the PL cortex (n = 4) were pre-trained in a T maze, before being implanted. The task consisted of running from the start point of the stem toward the decision point and then turning right, or left, to find a sweet food reward that was located at the end of the right arm. Mice were mildly food-deprived (food was removed for 3–4 h before testing), and were tested in the T maze until they reached a performance accuracy of 75%, which took 3–4 days (8 trials per day). One week after implantation, animals were tested in the T maze (8 trials in one day).

Data acquisition

Mice were recorded using a headstage pre-amplifier (Neuralynx), which was connected to a programmable amplifier (Lynx-8, Neuralynx) and a Windows PC running the Cheetah acquisition software (Neuralynx). In this study, we used the Cheetah system and a 16-channel setup comprising of 4 tetrodes, each featuring 4 closely spaced recording channels, along with an overhead camera. The acquisition setup generated 3 datastreams: continuously-sampled neural signals, discretely-sampled spikes, and the animal's XY location. For the continuous data, the 16 channels were acquired at 30 kHz and contained the voltage for each channel at every timestamp. For the spike data, the 16 channels were first band-pass filtered (600 Hz to 6 kHz) and only the fluctuations that surpassed the assigned voltage threshold (120 μV) were

captured. For the XY data, video tracking was achieved via a ceiling-mounted camera which tracked the position of an LED (light-emitting diode) mounted to the headstage in the Cheetah software at 30 Hz. The raw video footage was separately saved as well.

Hardware and software used for data analysis

After acquisition, data were transferred to a Linux machine (running Ubuntu 18.04.5 LTS) for sorting using the automated framework. On the Linux system, data were prepared for sorting with MountainSort, using MATLAB 2017b (MathWorks, Natick, MA), passed through the MountainSort pipeline, and the sorted spikes were saved as text files for further analysis. Spike sorting using the manual method was completed using Spike2 (version 8, Cambridge Electronic Design, Cambridge, UK) on a PC running Windows 10 (Microsoft, Redmond, WA). Sorted spikes were analyzed using NeuroExplorer version 5 (Plexon, Dallas, TX) and MATLAB on a PC running Windows 10. Final results were processed in MATLAB, Excel 2013 (Microsoft), and Origin 2019 (OriginLab, Northampton, MA).

Statistical analysis

Data are presented as mean ± standard deviation (SD), or median and quartiles (Q1 and Q3), as indicated. To examine statistical significance, which was defined as $P < 0.05$, we used two-sample ANOVA and Student's t-test in samples that were normally distributed. Normality was assessed using the Shapiro-Wilk normality test. We also used nonparametric tests, namely Mann-Whitney U test and Kolmogorov-Smirnov test, in samples that were not normally distributed. All statistical tests were performed in OriginPro software (version 2021b; OriginLab Corporation, Northampton, MA).

Results

The analysis process for neural data consists of multiple steps, using different software packages as required. A central goal of this work is to provide a roadmap for analysis of single-unit data, with a focus on how we have concatenated the Cheetah system with MATLAB and the automated spike sorting technology, MountainSort. The overall process begins with the acquisition of neural data, followed by spike sorting, and finally, the computation of spike parameters which is done in a manner specific to the phenomenon being studied. The code used in this study can be found at: GitHub: spike_sorting n.d..

Description of the cheetah file formats

The Cheetah system generates three groups of data (Fig. 1). The continuous datastream is saved in the files named `CSC1.ncs` up to `CSC16.ncs` (Neuralynx continuously sampled), which comprise the voltage at every timestamp (sample rate, 30 kHz) for each separate channel. The spike datastream is saved in the files named `TT1.ntt` up to `TT4.ntt` (Neuralynx tetrode), in which each file represents a tetrode and contains the spike information across the four channels of a particular tetrode. The XY datastream is saved in the file `VT1.nvt` (Neuralynx video tracking), which contains the position of an LED mounted onto the headstage on the animal's head.

Overview of the spike sorting methods

Both the automated spike sorting framework and manual spike sorting method follow similar overall trajectories. The raw data are saved by the Cheetah system, then brought into the spike sorting package, in which the spikes are sorted and exported for final analysis in NeuroExplorer and MATLAB, depending on the parameter in question (Fig. 1).

For the automated spike sorting framework, only the continuous channels are used (Fig. 1a). The `ncs` files are imported into MATLAB, they are merged, and then converted to the `mda` format (e.g., `raw.mda`). The files are then passed through MountainSort where preprocessing and spike sorting occur. Finally, the sorted spikes are saved as text files (e.g., `spiketimes.txt`) which allows for easy importing into most software packages. We use NeuroExplorer and MATLAB to analyze sorted data. Within NeuroExplorer, the analysis of spikes, along with the position data from the video feed (e.g., `VT1.nvt`), can be used to generate place field maps, autocorrelograms, and many other visualizations. From that point, the data can be exported into MATLAB for quantitative analysis such as calculation of place field areas or spatial information. For other forms of analysis, sorted spikes and position data are imported directly into MATLAB without passing through NeuroExplorer. Note that in order to import spikes from `spiketimes.txt` into NeuroExplorer, the correct option for importing data must be set. This can be done as follows: Open NeuroExplorer. Under the View tab, click on Data Import Options. In the window, click on the File Extensions box. Scroll down to `txt` and select the following option: Text File (pairs<channel> < timestamp>), and then click OK to exit the window.

For the manual spike sorting method (Fig. 1b), only the discrete spike channels from Cheetah are imported straight into Spike2 where file merging, spike sorting, and exporting of sorted units are completed. Our team has historically used manual spike sorting platforms such as Offline Sorter or KlustaKwik (Chang and Huerta, 2012; Faust, et al., 2013). In recent years, we

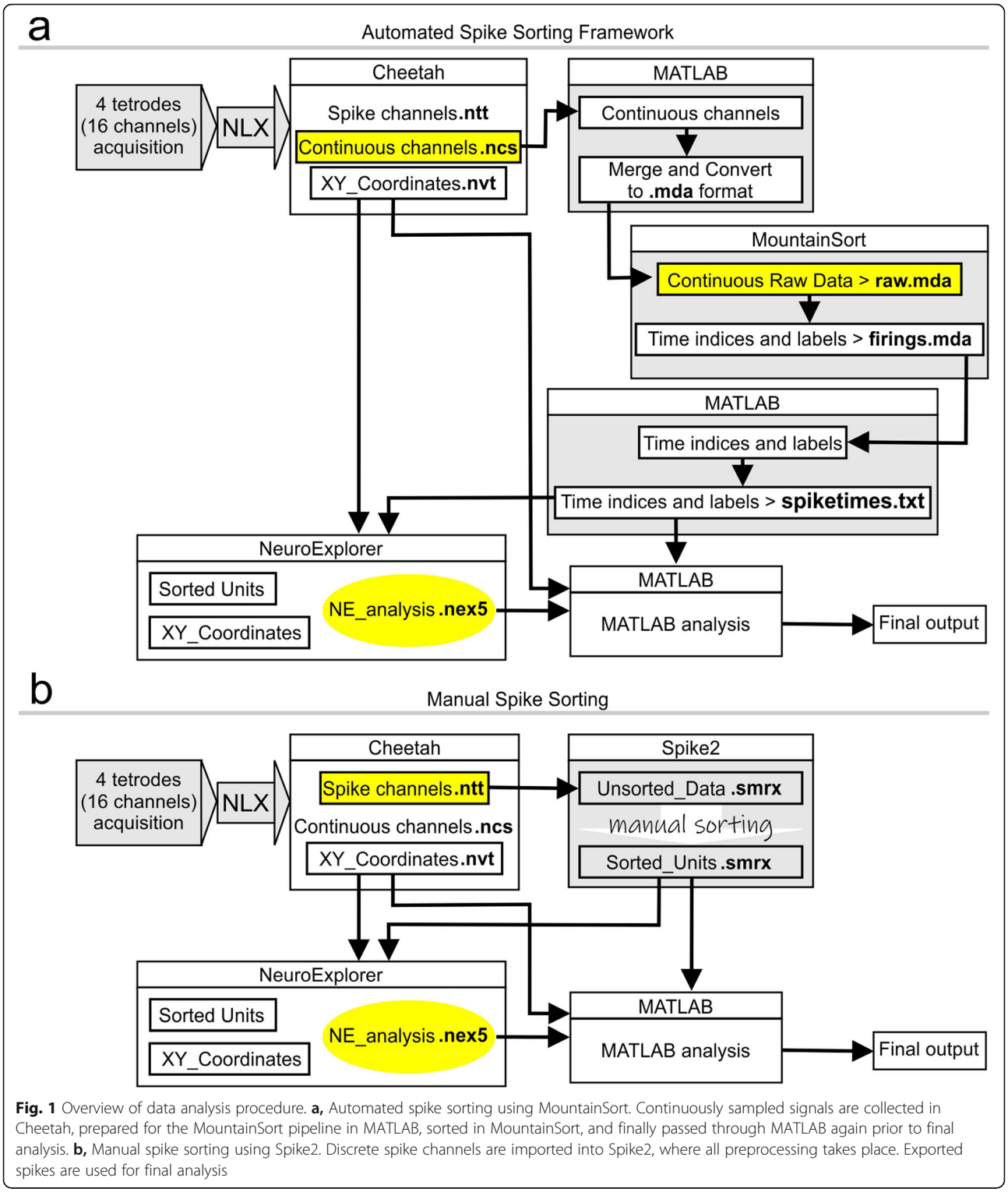

Fig. 1 Overview of data analysis procedure. **a,** Automated spike sorting using MountainSort. Continuously sampled signals are collected in Cheetah, prepared for the MountainSort pipeline in MATLAB, sorted in MountainSort, and finally passed through MATLAB again prior to final analysis. **b,** Manual spike sorting using Spike2. Discrete spike channels are imported into Spike2, where all preprocessing takes place. Exported spikes are used for final analysis

have exclusively used Spike2 which has proven to be a versatile software for sorting and visualizing spike data. In Spike2, we use PCA to generate the components for cluster cutting. The spikes can be easily viewed as either overlaid waveforms or as points across time. If different recording sessions from the same day need to be merged together for sorting and then split back into the original sessions, this is all done within the Spike2 environment. Following completion of manual sorting, the spikes are exported for downstream analysis.

Data preparation for MountainSort

The automated spike sorting process begins with the 16 continuously-sampled channels which are saved in the `ncs` format (Fig. 2a). In principle, these files contain the information about local field potential and the spike signals, but the spikes have not been isolated from the rest of the recording yet. The continuous channels are imported into MATLAB and the data files are merged according to the principle that all the recording sessions from a given mouse, obtained in the same day, are joined together. The merged files are then converted from the Neuralynx `ncs` data format into the `mda` (multi-dimensional array) format, which is compatible with MountainSort. Merging files is done so that spikes which may originate from the same neurons, can be clustered together, with the use of the `m2021_mergeandconvert.m` script (Fig. 2). This script was designed with tetrodes in mind, and the number of tetrodes used in the recording can be specified at the top of the script where indicated. If other recording configurations are used, the number of channels per n-trode may be altered as well, with 4 channels being equivalent to a tetrode. The input for this script follows a simple organization scheme. All of the experiments to be sorted need be placed into a single parent folder. Within the parent folder, recording sessions from the same mouse on the same day are grouped into individual 'mouse & day' folders (Fig. 2). Recording files go in the session folder with no additional subfolders, as is saved by default by the Cheetah system. Next, the `m2021_mergeandconvert.m` script is opened in MATLAB. The line asking for the parent folder needs to be changed to reflect the location of the parent folder stated above. Both the `m_2021_mergeandconvert.m` and `m2021_ms_out_timestamps.m` scripts require the folder `spike_sorting_dependencies` to be included in the MATLAB file path.

The `m2021_mergeandconvert.m` script first reorganizes the continuous data on a tetrode-by-tetrode basis so that each of the 4 recording channels from each tetrode is placed into an individual subfolder. Next, the `ncs` files (`CSC1.ncs` and so on) are imported into the MATLAB environment as variables using the `mex` files provided by Neuralynx. For each mouse & day folder, the raw continuous channels are imported and merged into a single [1 X M] variable. These files are then saved into the MountainSort-compatible format, as `raw.mda`, in which each file contains the 4 channels of a single tetrode for an entire mouse & day unit of recording. The `raw.mda` files are placed into folders created for each tetrode (e.g., tt1, tt2, tt3, tt4) in the mouse & day folder (Fig. 2a). Along with the `mda` files, three other files are generated for each tetrode. The first file, `geom.csv`, contains the electrode geometry for the recording, which is set to resemble the tetrode recording configuration. The second file, `params.json`, contains the sampling rate of the recording (in our case, 30 kHz) as well as the direction of spike occurrences (positive or negative). Both files are necessary for MountainSort. The third file, `t_info.csv`, gives the start and end time of each recording session for the mouse & day, and it is used (after MountainSort) to separate the merged files back into their original recording sessions (Fig. 2b). For each run of the `m2021_mergeandconvert` script, a file titled `runsort.sh` is generated. This file contains the file paths needed to input each tetrode into MountainSort, as well as paths for the output files generated by MountainSort.

After running the `m2021_mergeandconvert` script, the data are ready for the spike sorting pipeline. Prior to sorting any experiments, MountainSort needs to be installed according to: GitHub: sorting_pipeline n.d.. After installation, this pipeline can be executed by moving the `runsort.sh` file into the `sorting_pipeline` folder, and executing this file in the terminal. The `runsort.sh` file then leads MountainSort to input the `raw.mda`, `params.json`, and `geom.csv` files, run the pipeline, and generate a `firings.mda` output for each tetrode, which contains the timestamps for the firing times for each sorted unit (Fig. 3a).

Interpretation of the sorted spike data

Following MountainSort, the `firings.mda` files are saved in an appropriate format for further analysis. This is achieved by running the `m2021_ms_out_timestamps.m` script. The merged and sorted files are first split up into sessions as originally recorded (Fig. 3b). To ensure compatibility with multiple analysis programs, the output is saved as a text file titled `spiketimes.txt`. This file contains two columns, which make up [unit ID, timestamp] pairs (Fig. 3c). This file structure can be imported into a variety of analysis packages including MATLAB and NeuroExplorer. The waveforms are not exported with this dataset, allowing for fast computation and small file sizes. If waveforms need to be viewed, a MATLAB-based waveform viewer is available at: GitHub: matlab_waveforms n.d..

The waveforms are found by matching the timestamp to the `raw.mda` data for each isolated unit. From there, the waveforms are saved as `mat` files in MATLAB and can be plotted as overlaid individual waveforms, or as the average waveform for each single-unit. Other waveform viewing options are currently being developed and may be available on the GitHub page for the Flatiron Institute: GitHub: Flatiron Institute n.d..

Validation of the automated framework with CA1 recordings

Neural signals were recorded in the *stratum pyramidale* of CA1 in mice ($n = 4$) that were running along a linear

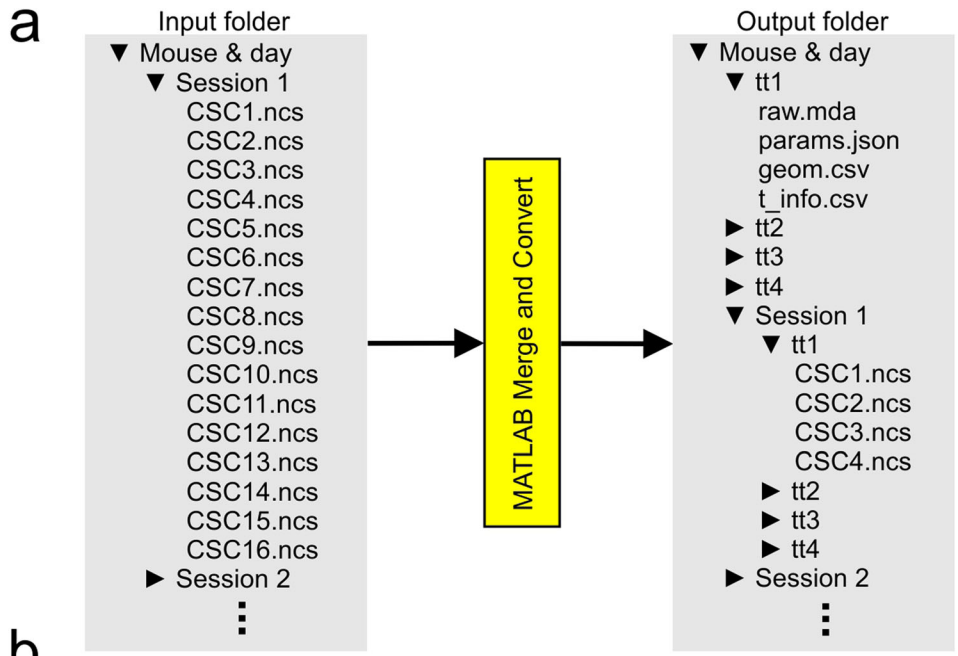


```
clear
close all
clc
%% INPUT YOUR FOLDER HERE
parent = '/home/loinn/Documents/testdata/'
%% Indicate number of recording tetrodes
num_tts = 4;
% Indicate number of channels per n-trode
num_ch_per_tt = 4;
%% Add dependencies
addpath(genpath('/home/loinn/MATLAB/spike_sorting_dependencies'))
%% Geometry file
geom = [0 0; 20 0; 0 20; 20 20];

%% Merge and save mda file for each mouse on a
% tetrode-by-tetrode basis

% Naming variable for list for mountainsort input
sortlist = cell(2,1);
sortlist_output = cell(2,1);
isort = 1;
```

Fig. 2 (See legend on next page.)

(See figure on previous page.)
Fig. 2 Merging and converting data prior to automated spike sorting. **a,** Organization and preparation of data for MountainSort pipeline. Sessions from the same mouse on the same day are placed into the same folder, with the data files organized in each session folder just as they are saved by Cheetah. The parent folder containing all of the 'mouse & day' subfolders is input into MATLAB to merge and convert the data. The output files are organized by tetrode, and saved in the mouse & day folder as they contain the signals acquired for all sessions within the folder. **b,** The `m2021_mergeandconvert.m` script imports the `CSC.ncs` files and saves the merged data as `raw.mda`. Three other files are saved; `params.json` contains the sample rate and spike direction, geom.csv indicates the tetrode geometry, and t_info.csv contains the start and end times of each recording that are used to split the merged files for session-by-session analysis. The lower panel depicts the `m2021_mergeandconvert.m` script to be run

track (Fig. 4a). The spiking activity was used to compare the output of the automated framework against a manual sorting method. We show several examples of single-units, chosen randomly, which were obtained with the MountainSort pipeline (Fig. 4b) and manually-sorted with Spike2 (Fig. 4c). Manual spike sorting was performed by experienced operators and the final results were checked for quality by two independent observers. Comparison of single-units sorted automatically and manually, during 16 recording sessions (Fig. 4d), revealed that the total number of single-units per session was not significantly different between groups (Fig. 4d**, top**; automated = 32.31 ± 11.85 [mean ± SD], range = 18–58; manual = 43.31 ± 12.35, range = 23–74; $t = 2.13$, $P = 0.05$, paired t test). However, comparison of the spike amplitudes, defined as the peak-to-peak voltage of the averaged waveform from each sorted unit, showed that the automated framework sorted single-units of significantly higher amplitude than the manual method (Fig. 4d**, bottom**; automated: median = 0.35, Q1–Q3 = 0.22–1.32; manual: median = 0.19, Q1–Q3 = 0.15–0.25; $d = 0.55$, $Z = 3.55$, $P = 3.49 \times 10^{-12}$, Kolmogorov-Smirnov test).

We used the place cell properties of the hippocampal single-units sorted automatically (MountainSort pipeline) and manually (using Spike2) for direct comparison of the output from both methods. For illustrative purposes, two pairs of single-units with place fields in close proximity across methods were selected (Fig. 5a, b). In one case (Fig. 5a), the two place cells have similar firing rates as a function of position of the mouse along the linear track (Fig. 5a**, left**) and display a well-defined place field (at ~ 70-cm on the track), with the peak firing rate occurring as the mouse moves from right to left. Moreover, their waveforms (Fig. 5a**, next-to-left**) are highly similar across the 4 channels of the tetrode when comparing the automated and the manual traces. Their autocorrelograms (Fig. 5a**, next-to-right**) show few refractory period violations but appear different depending on the sorting method, which is likely the result of MountainSort clustering more spikes into the single-unit when compared to manual sorting operators. Analysis of all spike events during a 5-min period shows that the spike amplitudes for the two sets are statistically different (Fig. 5a**, right;** automated = 0.103 ± 0.03 [mean ± SD]; manual = 0.164 ± 0.018; $F = 2.81$, $P = 6.65 \times 10^{-9}$, two-sample ANOVA). Notably, the spikes appear to fire in bursts, as would be expected of hippocampal place cells, with the automated unit showing more pronounced bursting, and also more variance, than the manual unit. This example suggests that the automated framework is more accepting toward clustering spikes of various amplitudes into a single-unit when compared to the manual method. The second example (Fig. 5b) depicts two place cells with multiple place fields, as revealed in their firing profiles (Fig. 5b**, left**). The primary place field is near the center of the track (20–40 cm), when the mouse moves from right to left, but relatively high firing rates occur in other regions of the track as well. Although the main place field is similar across sorting methods, the large differences in extraneous activity suggest that the single-units are not optimally clustered. The waveforms (Fig. 5b**, next-to-left**) show high-amplitude traces in channels 1 and 2, but the manually-sorted waveforms also have high amplitudes in channels 3 and 4 compared to the automated traces. The autocorrelograms (Fig. 5b**, next-to-right**) show few refractory period violations but the shapes are different, with the automated unit featuring more firing close to zero, which suggests a greater tendency to burst, whereas the manual unit displays a firing pattern that is spread through the autocorrelogram. Analysis of all spike events during a 5-min period of recording shows that the two sets are statistically different (Fig. 5b**, right**; automated = 0.231 ± 0.092 [mean ± SD]; manual = 0.329 ± 0.048; $F = 3.575$, $P = 1.65 \times 10^{-46}$, two-sample ANOVA). The bursting nature of the single-units is evident in both methods, but there is more variance in the amplitude of the automated unit. It is possible that in both cases, spikes arising from different neurons were clustered as the same unit. The higher extraneous firing in the manual unit, as well as the differences in the waveforms across sorting methods, strongly suggest that more inappropriate spikes were included in the manual method compared with automated sorting.

When counting the number of single-units classified as place cells across 7 sessions in the linear track, we found that the automated and manual sorting methods

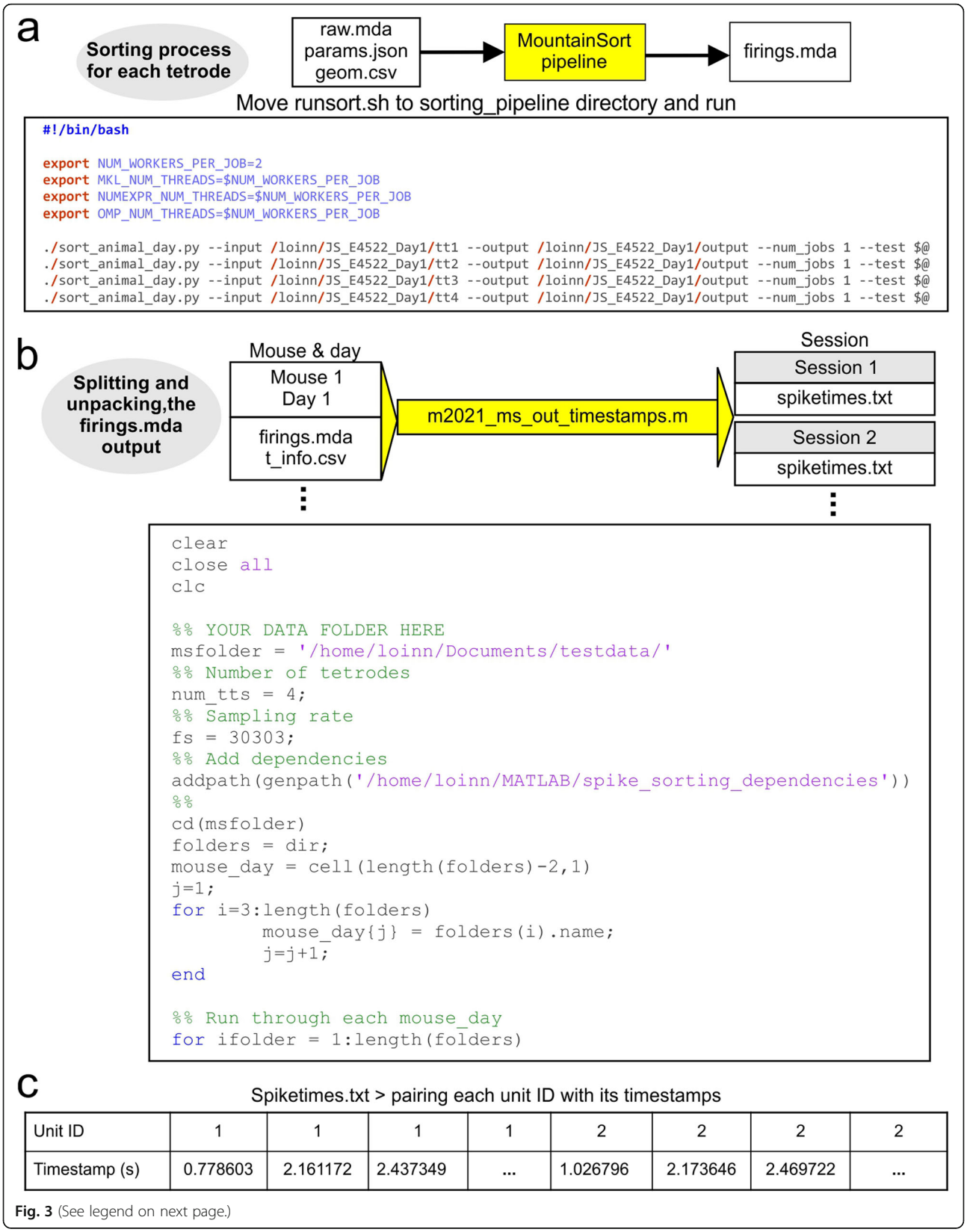

Fig. 3 (See legend on next page.)

(See figure on previous page.)
Fig. 3 Automated sorting framework. **a,** The files `raw.mda`, `params.json`, and geom.csv are imported into the MountainSort pipeline, which includes both pre-processing and spike sorting. The MountainSort pipeline outputs `firings.mda` files, which contain the unit IDs and timestamps of sorted spikes. The designated input and output folders are entered into the `runsort.sh` script, as depicted in the bottom of the panel. **b,** Using the `m2021_ms_out_timestamps.m` script, sorted files are split back up into the original recording sessions according to the `t_info.csv` file. Split files are saved as `spiketimes.txt`, for easy transfer to other software package for final analysis. The `m2021_ms_out_timestamps.m` script is shown in the bottom of the panel. **c,** Output `spiketimes.txt` files are formatted as two columns of unit ID, timestamp pairs

yielded similar quantities of single-units per recording (Fig. 5c; automated: median = 11, Q1–Q3 = 7–15; manual: median = 11, Q1–Q3 = 9–16; $U = 21$, $Z = 0.38$, $P = 0.7$, Mann-Whitney U test). Only 2 sessions behaved as outliers, with the number of single-units varying substantially across methods (Fig. 5c; automated with 30 vs. manual with 9; automated with 6 vs. manual with 17). While there are similarities and differences among spikes sorted with the two methods, neurons act together in groups, so it is important to view results at the ensemble level as well as that of the individual neuron. By normalizing the firing rates of each unit and sorting all units by

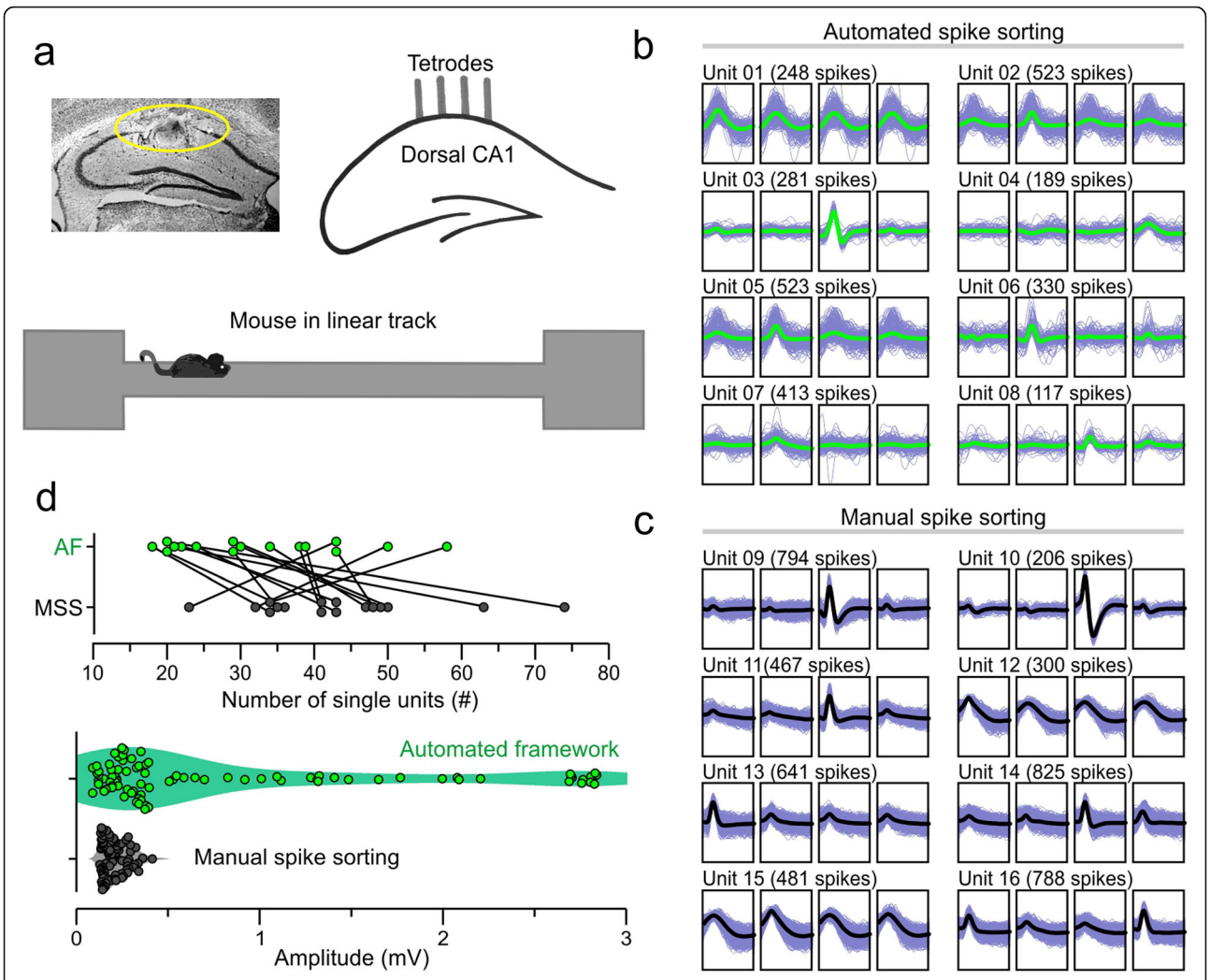

Fig. 4 Validation of the automated framework with hippocampal recordings. **a,** Schematic depicting tetrode placement in the CA1 region (indicated by yellow oval) and recording paradigm in the linear track. **b,** Representative waveform overlays of single-units sorted using the automated framework. **c,** Waveform overlays of single-units sorted using the manual method. **d,** ***Top,*** number of single-units sorted per recording session using the automated framework (AF, green) or manual spike sorting (MSS, black). ***Bottom,*** amplitudes of mean waveforms sorted using the automated framework (green) or manual method (black)

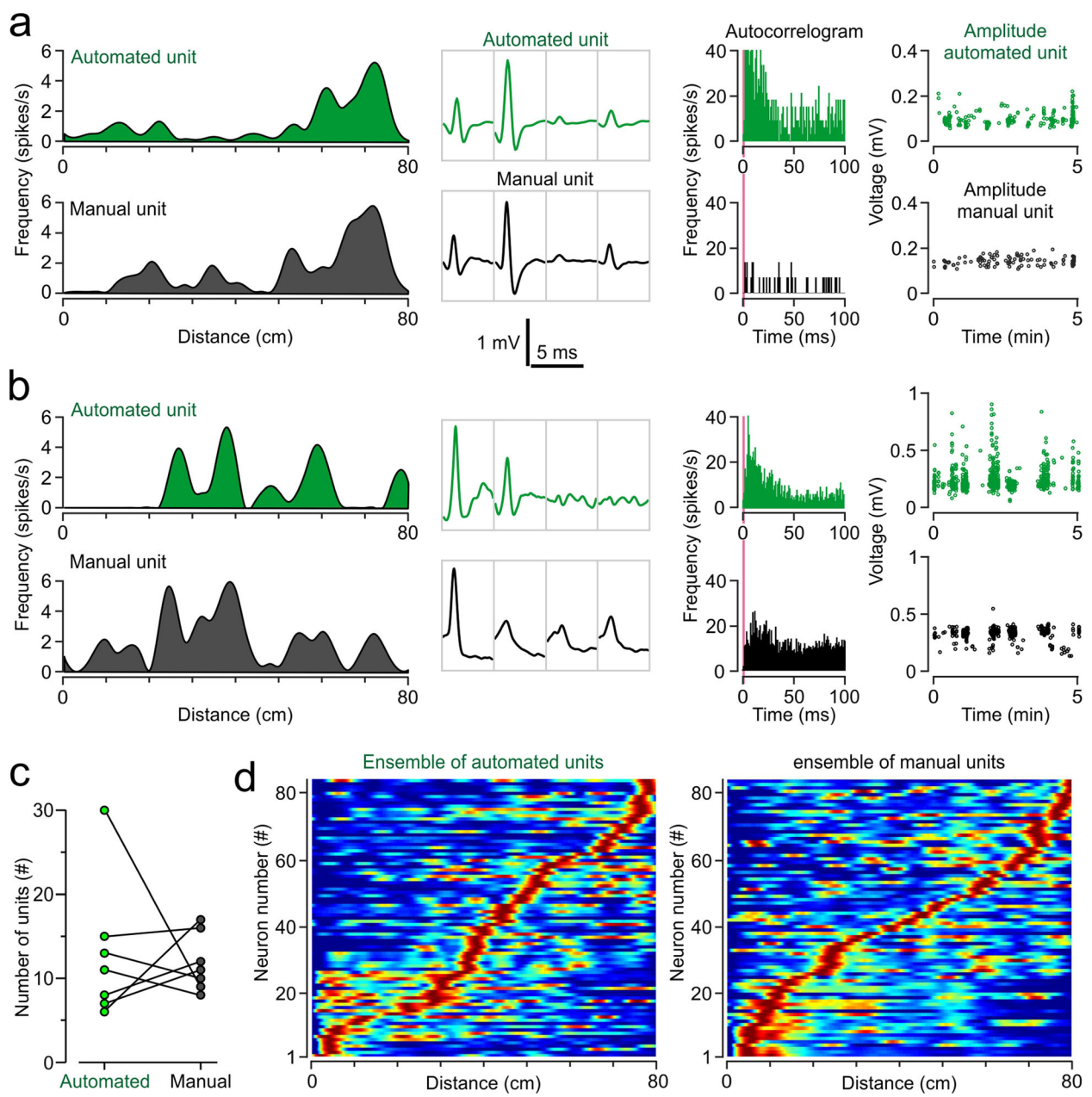

Fig. 5 Hippocampal CA1 recordings in freely-moving mice. **a, b,** Representative single-units showing the firing rates along the length of the track (left panels), average waveform in each channel of a tetrode (next-to-left panels), autocorrelogram (next-to-right panels; pink lines represent refractory period), and amplitudes of spikes over time (right panels). Automated units are displayed in green and manual units are shown in black. **a,** Representative single-units likely representing the same putative neuron sorted with automated and manual methods. **b,** Similar units likely to represent different neurons across automated and manual methods. **c,** Number of single-units per recording session using the automated framework (green) or the manual method (black). **d,** Population of place cells recorded from mice ($n = 4$) running the linear track. Each row represents normalized spike activity of one single-unit, where rows are organized by the position of the peak firing rate for each unit along the linear track. Sorted populations of place cells appear similar across automated and manual methods

the location of their peak firing rate, the activity of place cells in the linear track can be viewed as an ensemble of units (Fig. 5d). We implanted 4 mice and recorded as they ran the length of the track and generated place cell ensembles using each sorting method. Here we find that, at the ensemble level, the activity of the place cells appears similar across both methods. Remarkably, in the 'automated spike sorting' ensemble, place fields appear better isolated compared to the 'manual spike sorting' ensemble (Fig. 5d), as suggested by the reduced

extraneous activity outside of the main place fields for each unit. Importantly, both sorting paradigms result in ensembles covering the full length of the track.

Validation of the automated framework with PL cortex recordings

We sought to compare the automated framework (MountainSort pipeline) and a manual sorting method (Spike2) using recordings from the PL cortex, a region located within the medial prefrontal cortex. Prior to surgery, the mouse was trained to go to the right arm in the T maze. Tetrodes were implanted into the PL cortex, and the freely-moving mouse was tested in the T maze (Fig. 6a). We examined sorted units based on their activity as the animal navigated from the start point (in the stem) toward the reward (end of the arm). For illustrative purposes, a pair of single-units that seem to have similar properties across methods are shown (Fig. 6b). In this example, the automated unit refers to a neuron that is sorted using MountainSort (Fig. 6b**, top**) and the manual unit is sorted with the manual method (Fig. 6b**, bottom**). The waveforms from the automated unit are nearly identical to the waveforms of the manual unit, and the autocorrelograms are similar as well, although the automated unit displays more firing and bursting (Fig. 6b). By plotting the spike activity of the example

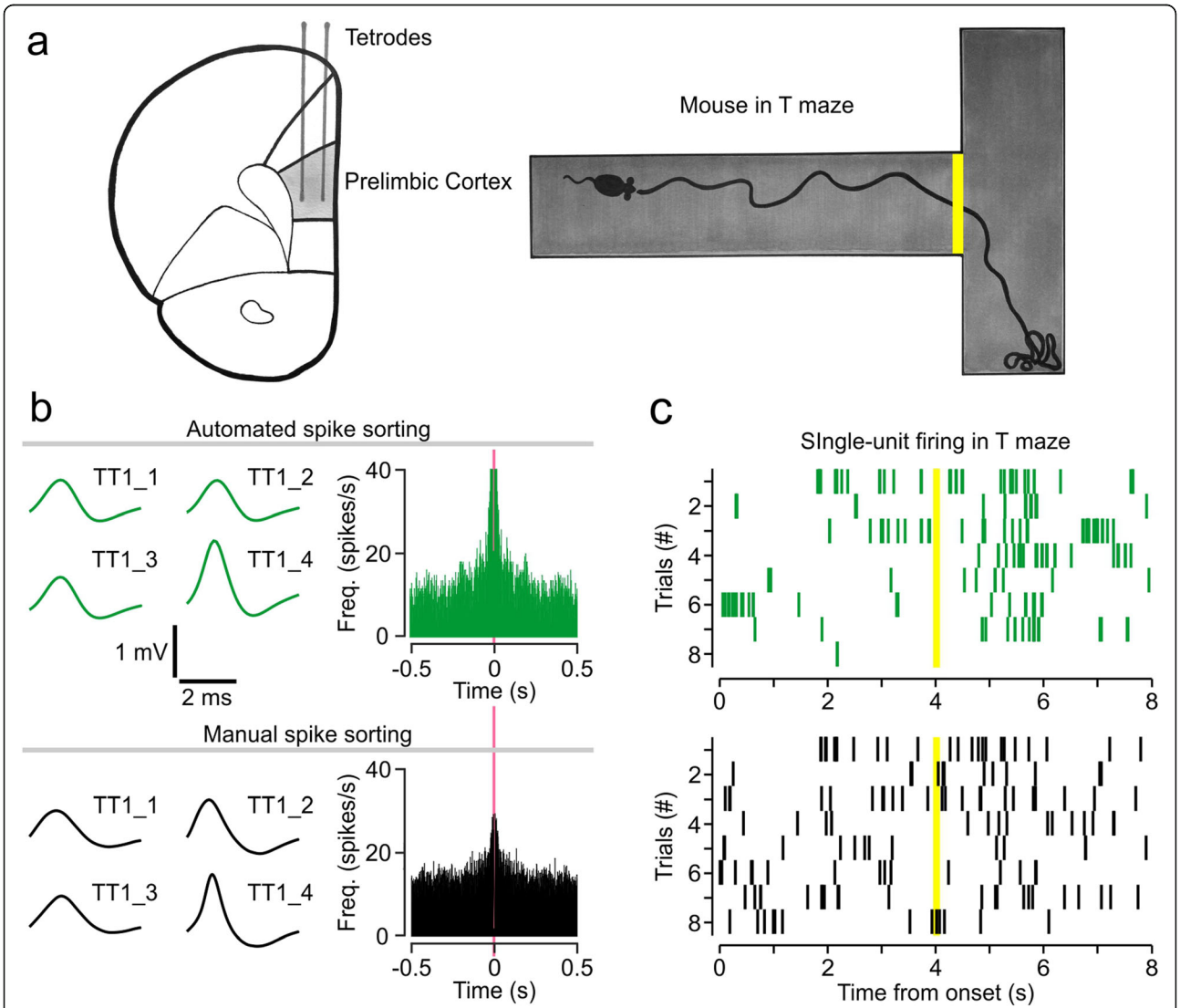

Fig. 6 Prelimbic cortex recordings in freely-moving mice. **a,** Schematic depicting tetrode placement in the PL cortex and recording paradigm in the T maze. The yellow line indicates the point at which the mouse chooses to go left or right. **b,** Representative average waveforms and autocorrelograms of sorted units, likely representing the same putative neuron, across automated and manual methods; TT1_1, and so on, indicate tetrode channel numbers. The pink line represents the refractory period. **c,** Raster plots for single-units in panel b. Each row represents a trial in the T maze and each tick is a spike. Notice that the trials are aligned to the timepoint indicated by the yellow line (4 s), which corresponds to the moment that the mouse arrives at the intersection of the stem with the arms of the T maze in each trial (as in panel a)

units as trial-by-trial raster plots, one can observe their dynamic activity (Fig. 6c). Each row of the raster represents the firing of the unit during a trial in the T maze, and the center of the plot corresponds to the time when the mouse is at the intersection of the stem and the arms of the T maze (yellow line in Fig. 6a, c). Statistical comparison shows that the numbers of isolated spikes per trial are not significantly different between the two sets (Fig. 6c; automated: median = 27.5, Q1–Q3 = 14.25–42.5; manual: median = 15.5, Q1–Q3 = 13.25–23.5; U = 45, Z = 1.315, P = 0.189, Mann-Whitney U test). Notably, the automated unit shows quite a similar pattern of activity across multiple trials, which highlights the reliability of the automated method in isolating a well-behaved unit. In contrast, the manual unit displays a more widespread pattern of spiking across the trials, which would be indicative of a poorly-isolated neuron.

Discussion

We have designed a novel framework to smoothly combine the acquisition of neuronal signals from tetrode recordings of freely-moving mice, using the Cheetah system (Neuralynx), to the automated spike sorting pipeline MountainSort (Chung et al., 2017). It is clear that automated spike sorting has become a necessity for medium and large-scale extracellular neural recordings, as it involves the extraction of (ideally) all the action potentials generated by an individual neuron from an ocean of activity in the extracellular recordings. We provide a detailed roadmap of the steps, from data acquisition to file managing between the different software platforms (Cheetah, MATLAB, MountainSort, and NeuroExplorer). In short, our solution provides full integration of MountainSort-based spike sorting to Cheetah-based acquisition of neuronal signals in mice. The framework presented in this study is not intended to be generalizable across multiple acquisition systems and spike sorters, but rather it is designed to be a specific solution for users of Neuralynx systems. The advantage of our simple approach is that in a single run, multiple recordings can be merged, sorted, and exported, with minimal user input or troubleshooting. Moreover, the framework does not require the end-user to create any new scripts of their own, which is a common necessity with other spike sorting frameworks.

The framework is intended to be completely compatible with existing analysis software; therefore, we convert sorted spikes from the `mda` format (used by MountainSort) to a simple `txt` format. While there is indeed a network of analysis tools being developed around MountainSort, these packages are still in the development phase. Furthermore, many established labs need a way to seamlessly implement state-of-the-art automated spike sorting methods in a manner compatible with existing analysis processes. In our case, we use NeuroExplorer and MATLAB, both of which are widely used programs for the analysis of neural data. Thus, we have created an original end-to-end framework to integrate the automated spike sorting technology of MountainSort with Cheetah-acquired recordings into a data analysis framework consisting of widely-used software packages.

There are several benefits to using the automated pipeline. Critically, automated spike sorting provides a repeatable and objective methodology, in contrast to manual methods which might be quite subjective. Manually sorting spikes yields variable datasets among different operators, even when the operators have significant experience with the technique. Another important benefit regards to the amount of time taken to sort datasets of almost any size. Manually sorting is a slow and user-intensive process. Each recording can take a period of user-input time ranging from several minutes up to a few hours to finish, making for a time-intensive process. In contrast, using the automated framework, multiple recordings can be quickly sorted in a single run. In this scenario, MountainSort processes each recording in a period of time shorter than the recording itself, but the user does not need to be actively working during this time period. The user only needs to set up the files to be recorded, reducing the user-input time to mere minutes per recording.

We have compared the results of the automated spike sorting framework with a manual spike sorting platform we have used for several years in our laboratory. Using either approach, we can isolate single-unit activity in two different brain regions, the hippocampus and the PL cortex. When we compared the number of units sorted per session, we found similar numbers of automated units and manual units for most sessions, but there were some exceptions. In particular, there were two sessions that stood out as outliers. For one of these outliers, the automated framework sorted more single-units, whereas for the other, the manual method sorted more single-units. While there may be differences at the level of each single-unit, we can identify units isolated with similar waveforms across both algorithms. These units also show similar activity in behaviorally relevant tasks such as the linear track or T maze. Furthermore, when viewed at the ensemble level, the datasets look largely similar with only slight variations in the precision of firing.

We think that automated spike sorting platforms are poised to become a critical component in the neuroscientist's toolkit, considering that within the next decade, we will very likely experience an exponential increase in the size of the recording arrays (Alivisatos et al. 2013;

Steinmetz et al., 2021). With the next generation of brain probes including up to thousands of recording sites, the sheer complexity of the datasets is bound to be too large for manual sorting, or even semi-automated methods, to be capable of processing them. It seems apparent that automated spike sorting needs to become easy to use and properly validated across different acquisition setups, brain regions and mammalian species. In this respect, we have presented a complete automated framework for sorting neural spike data acquired from Neuralynx-based systems. Our framework is easy to implement and provides a high-throughput solution. We predict that within the broad field of bioelectronic medicine, those teams that incorporate high-density neural recording devices to their armamentarium might find our framework quite valuable as they expand their analytical footprint.

Conclusions

- We present a complete framework for automated spike sorting using the MountainSort package, with all the code freely-available in the GitHub repository.
- The toolset delivers automatically-sorted spikes from recordings obtained with a Cheetah-based system, and exports the sorted spikes in a format which is highly compatible with existing data analysis routines.
- Integration of automated spike sorting software is a critical step in the analysis of neural data, and becomes increasingly important as the size and complexity of datasets continues to increase with new electrode technology.
- An improved understanding of the neural signals obtained with tetrode recordings within the brain will be paramount for any bioelectronic approaches targeting brain systems.

Abbreviations

AP: anterior/posterior; CA1: *Cornus Ammonis 1*; cm: centimeter; Hz: hertz; kg: kilogram; kHz: kilohertz; kΩ: kilo-ohms; LED: light-emitting diode; mg: milligram; ML: medial/lateral; min: minute; mV: millivolt; PL: prelimbic cortex; s: second

Acknowledgements

We are grateful to Elvira Strohl for the schematic drawings (Figs. 4 and 6). We thank Jeremy Magland for helpful discussions about the MountainSort software platform.

Authors' contributions

JJS, JTG, PNG, JMG, PTH contributed equally to the completion of this work, including conceptualization, data acquisition and data analysis. JJS wrote the software code and MATLAB scripts. PTH assembled the final figures. JJS and PTH prepared the manuscript. The authors read and approved the final manuscript, and agreed to its publication.

Funding

This work was supported by the National Institute of Health (NIH) grant 5P01AI102852 and NIH grant 5P01AI073693, as well as the Department of Defense (DOD) impact award W81XWH1910759, to PTH.

Availability of data and materials

The datasets used and analyzed during the current study are available from the corresponding author on reasonable request. Code used in this manuscript may be found at the following addresses:
https://github.com/HuertaLab/spike_sorting. DOI: https://doi.org/10.5281/zenodo.5537196
https://github.com/HuertaLab/spike_sorting/tree/main/sorting_pipeline
https://github.com/HuertaLab/spike_sorting/tree/main/matlab_waveforms

Declarations

Ethics approval

All animal experimentation was performed in accordance with the National Institutes of Health (NIH) Guidelines, under protocols approved by the Institutional Animal Care and Use Committee (IACUC) of the Feinstein Institute for Medical Research. Our Animal Research Program is registered with the Department of Health & Human Services (DHHS), Office of Laboratory Animal Welfare (OLAW), United States Department of Agriculture (USDA #21R0107), Public Health Service (PHS #A3168–01) and New York State Department of Health (NYSDOH #A-060).

Consent for publication

Not applicable.

Competing interests

The authors declare that they have no competing interests.

Received: 23 August 2021 Accepted: 21 October 2021
Published online: 23 November 2021

References

Alivisatos AP, Andrews AM, Boyden ES, Chun M, Church GM, Deisseroth K, et al. Nanotools for neuroscience and brain activity mapping. ACS Nano. 2013;7:1850–66. https://doi.org/10.1021/nn4012847 PMID: 23514423 PMCID: PMC3665747.

Berényi A, Somogyvári Z, Nagy AJ, Roux L, Long JD, Fujisawa S, et al. Large-scale, high-density (up to 512 channels) recording of local circuits in behaving animals. J Neurophysiol. 2014;111(5):1132–49. https://doi.org/10.1152/jn.00785.2013 PMID: 24353300; PMCID: PMC3949233.

Buccino AP, Hurwitz CL, Garcia S, Magland J, Siegle JH, Hurwitz R, et al. SpikeInterface, a unified framework for spike sorting. Elife. 2020;9:e61834. https://doi.org/10.7554/eLife.61834 PMID: 33170122; PMCID: PMC7704107.

Buzsáki G. Large-scale recording of neuronal ensembles. Nat Neurosci. 2004;7(5):446–51. https://doi.org/10.1038/nn1233 PMID: 15114356.

Cacucci F, Yi M, Wills TJ, Chapman P, O'Keefe J. Place cell firing correlates with memory deficits and amyloid plaque burden in Tg2576 Alzheimer mouse model. Proc Natl Acad Sci U S A. 2008;105(22):7863–8. https://doi.org/10.1073/pnas.0802908105 PMID: 18505838; PMCID: PMC2396558.

Chang EH, Frattini SA, Robbiati S, Huerta PT. Construction of microdrive arrays for chronic neural recordings in awake behaving mice. J Vis Exp. 2013;(77):e50470. doi: https://doi.org/10.3791/50470. PMID: 23851569; PMCID: PMC3731431.

Chang EH, Huerta PT. Neurophysiological correlates of object recognition in the dorsal subiculum. Front Behav Neurosci. 2012;6:46. https://doi.org/10.3389/fnbeh.2012.00046 PMID: 22833721; PMCID: PMC3400129.

Chaure FJ, Rey HG, Quian QR. A novel and fully automatic spike-sorting implementation with variable number of features. J Neurophysiol. 2018;120(4):1859–71. https://doi.org/10.1152/jn.00339.2018 PMID: 29995603 PMCID: PMC6230803.

Chung JE, Joo HR, Fan JL, Liu DF, Barnett AH, Chen S, et al. High-Density, Long-Lasting, and Multi-region Electrophysiological Recordings Using Polymer Electrode Arrays. Neuron. 2019;101(1):21–31.e5. https://doi.org/10.1016/j.neuron.2018.11.002 PMID: 30502044; PMCID: PMC6326834.

Chung JE, Magland JF, Barnett AH, Tolosa VM, Tooker AC, Lee KY, et al. A Fully Automated Approach to Spike Sorting. Neuron. 2017;95(6):1381–1394.e6.

https://doi.org/10.1016/j.neuron.2017.08.030 PMID: 28910621; PMCID: PMC5743236.
Csicsvari J, Jamieson B, Wise KD, Buzsáki G. Mechanisms of gamma oscillations in the hippocampus of the behaving rat. Neuron. 2003; 37(2):311–322. https://doi.org/10.1016/s0896-6273(02)01169-8. PMID: 12546825.
Faust TW, Robbiati S, Huerta TS, Huerta PT. Dynamic NMDAR-mediated properties of place cells during the object place memory task. Front Behav Neurosci. 2013;7:202. https://doi.org/10.3389/fnbeh.2013.00202 PMID: 24381547; PMCID: PMC3865705.
GitHub: Flatiron Institute n.d. https://github.com/flatironinstitute. Accessed 17 August 2021.
GitHub: matlab_waveforms. n.d. https://github.com/HuertaLab/spike_sorting/tree/main/matlab_waveforms. Accessed 17 August 2021.
GitHub: sorting_pipeline. n.d. https://github.com/HuertaLab/spike_sorting/tree/main/sorting_pipeline. Accessed 17 August 2021.
GitHub: spike_sorting. n.d.. https://github.com/HuertaLab/spike_sorting. Accessed 17 August 2021.
Gray CM, Maldonado PE, Wilson M, McNaughton B. Tetrodes markedly improve the reliability and yield of multiple single-unit isolation from multi-unit recordings in cat striate cortex. J Neurosci Methods 1995; 63(1–2):43–54. https://doi.org/10.1016/0165-0270(95)00085-2. PMID: 8788047.
Harris KD, Henze DA, Csicsvari J, Hirase H, Buzsáki G. Accuracy of tetrode spike separation as determined by simultaneous intracellular and extracellular measurements. J Neurophysiol 2000;84(1):401–414. https://doi.org/10.1152/jn.2000.84.1.401. PMID: 10899214.
Hill DN, Mehta SB, Kleinfeld D. UltraMegaSort 2000 Manual. 2012.
Kunz L, Brandt A, Reinacher PC, Staresina BP, Reifenstein ET, Weidemann CT, Herweg NA, Patel A, Tsitsiklis M, Kempter R, Kahana MJ, Schulze-Bonhage A, Jacobs J. A neural code for egocentric spatial maps in the human medial temporal lobe. Neuron. 2021:S0896–6273(21)00460–8. https://doi.org/10.1016/j.neuron.2021.06.019. Epub ahead of print. PMID: 34265253.
Laboy-Juárez KJ, Ahn S, Feldman DE. A normalized template matching method for improving spike detection in extracellular voltage recordings. Sci Rep. 2019;9(1):12087. https://doi.org/10.1038/s41598-019-48456-y. Erratum in: Sci Rep. 2019;9(1):17413. PMID: 31427615; PMCID: PMC6700190.
Magland J, Jun JJ, Lovero E, Morley AJ, Hurwitz CL, Buccino AP, et al. SpikeForest, reproducible web-facing ground-truth validation of automated neural spike sorters. Elife. 2020;9:e55167. https://doi.org/10.7554/eLife.55167 PMID: 32427564; PMCID: PMC7237210.
O'Keefe J, Nadel L. The hippocampus as a cognitive map. Oxford University Press. 1976.
O'Keefe J, Dostrovsky J. The hippocampus as a spatial map. Preliminary evidence from unit activity in the freely-moving rat. Brain Res. 1971;34(1):171–5. https://doi.org/10.1016/0006-8993(71)90358-1 PMID: 5124915.
Pachitariu M, Steinmetz N, Kadir S, Carandini M, Harris K. Kilosort: realtime spike-sorting for extracellular electrophysiology with hundreds of channels. bioRxiv. 2016; https://doi.org/10.1101/061481.
Pedreira C, Martinez J, Ison MJ, Quian QR. How many neurons can we see with current spike sorting algorithms. J Neurosci Methods. 2012;211(1):58–65. https://doi.org/10.1016/j.jneumeth.2012.07.010 Epub 2012 Jul 25. PMID: 22841630; PMCID: PMC3657693.
Quirk MC, Wilson MA. Interaction between spike waveform classification and temporal sequence detection. J Neurosci Methods. 1999;94(1):41–52. https://doi.org/10.1016/s0165-0270(99)00124-7 PMID: 10638814.
Redish AD, Rosenzweig ES, Bohanick JD, McNaughton BL, Barnes CA. Dynamics of hippocampal ensemble activity realignment: time versus space. J Neurosci. 2000;20(24):9298–309. https://doi.org/10.1523/JNEUROSCI.20-24-09298.2000 PMID: 11125009 PMCID: PMC6772998.
Rey HG, Pedreira C, Quian QR. Past, present and future of spike sorting techniques. Brain Res Bull. 2015;119(Pt B):106–17. https://doi.org/10.1016/j.brainresbull.2015.04.007 PMID: 25931392; PMCID: PMC4674014.
Rossant C, Kadir SN, Goodman DFM, Schulman J, Hunter MLD, Saleem AB, et al. Spike sorting for large, dense electrode arrays. Nat Neurosci. 2016; 19(4):634–41. https://doi.org/10.1038/nn.4268 PMID: 26974951; PMCID: PMC4817237.
Steinmetz NA, Aydin C, Lebedeva A, Okun M, Pachitariu M, Bauza M, et al. Neuropixels 2.0: A miniaturized high-density probe for stable, long-term brain recordings. Science. 2021;372(6539):eabf4588. https://doi.org/10.1126/science.abf4588 PMID: 33859006; PMCID: PMC8244810.
van Daal RJJ, Aydin Ç, Michon F, Aarts AAA, Kraft M, Kloosterman F, Haesler S. Implantation of Neuropixels probes for chronic recording of neuronal activity in freely behaving mice and rats. Nat Protoc. 2021;16(7):3322–47. https://doi.org/10.1038/s41596-021-00539-9.
Wood F, Black MJ, Vargas-Irwin C, Fellows M, Donoghue JP. On the variability of manual spike sorting. IEEE Trans Biomed Eng. 2004;51(6):912–8. https://doi.org/10.1109/TBME.2004.826677 PMID: 15188858.
Yamamoto J, Wilson MA. Large-scale chronically implantable precision motorized microdrive array for freely behaving animals. J Neurophysiol. 2008;100(4): 2430–40. https://doi.org/10.1152/jn.90687.2008 PMID: 18667539; PMCID: PMC2576215.

Publisher's Note

Molecular Medicine

RESEARCH ARTICLE

Open Access

Reversible dysregulation of renal circadian rhythm in lupus nephritis

Rakesh Mishra[1], Ramalingam Bethunaickan[1], Celine C. Berthier[2], Zhengzi Yi[3], Joshua J. Strohl[1], Patricio T. Huerta[1], Weijia Zhang[3*] and Anne Davidson[1*]

Abstract

Background: We have found disruption of expression of major transcriptional regulators of circadian rhythm in the kidneys of several mouse models of lupus nephritis. Here we define the consequence of this disturbance with respect to circadian gene expression and renal homeostatic function in a mouse model of lupus nephritis.

Methods: Molecular profiling of kidneys from 47 young and 41 nephritic female NZB/W F1 mice was performed at 4 hourly intervals over a 24 h period. Disruption of major circadian transcriptional regulators was confirmed by qPCR. Molecular data was normalized and analyzed for rhythmicity using RAIN analysis. Serum aldosterone and glucose and urine sodium and potassium were measured at 4 hourly intervals in pre-nephritic and nephritic mice and blood pressure was measured every 4 h. Analyses were repeated after induction of complete remission of nephritis using combination cyclophosphamide and costimulatory blockade.

Results: We show a profound alteration of renal circadian rhythms in mice with lupus nephritis affecting multiple renal pathways. Using Cosinor analysis we identified consequent alterations of renal homeostasis and metabolism as well as blood pressure dipper status. This circadian dysregulation was partially reversed by remission induction therapy.

Conclusions: Our studies indicate the role of inflammation in causing the circadian disruption and suggest that screening for loss of normal blood pressure dipping should be incorporated into LN management. The data also suggest a potential role for circadian agonists in the treatment of lupus nephritis.

Keywords: SLE, Nephritis, Kidney, Circadian

Introduction

Circadian rhythm is a universal phenomenon by which organisms anticipate and respond to environmental changes by regulating sleep and feeding patterns, blood pressure, metabolism, detoxification and response to pathogens. Regulation of circadian behavioral rhythms is orchestrated by a "central clock," located in the hypothalamus (Honma 2018; Mohawk et al. 2012). Core clock genes and machinery are also present in peripheral tissues (Mohawk et al. 2012) and up to 10% of cellular transcripts in any given organ oscillate in a circadian manner (Lamia et al. 2008; Panda et al. 2002).

At a molecular level, circadian rhythms are controlled by a set of core clock genes that regulate their own expression through a series of feedback loops. Clock and Bmal1 are master transcription factors that form heterodimers to induce the expression of *Per* and *Cry* genes. Per and Cry proteins translocate to the nucleus to repress *Clock /Bmal1* transcription; thus, the master clock genes inhibit their own transcription in a periodic fashion. Bmal1 and Clock also regulate the nuclear receptor genes

*Correspondence: weijia.zhang@mssm.edu; adavidson1@northwell.edu
[1] Institute for Molecular Medicine, Feinstein Institutes for Medical Research, 350 Community Drive, Manhasset, NY 11030, USA
[3] Department of Medicine, Mount Sinai Medical Center, One Gustave L. Levy Place, P.O. Box 1243, New York, NY 10029, USA
Full list of author information is available at the end of the article

Ror that activates and *Rev-erbα* (*Nrd1*) that represses *Bmal1* transcription. These core genes control the expression of many other genes which drive cascades of rhythmic gene expression (Stow and Gumz 2011; Reddy and O'Neill 2010; Levi and Schibler 2007; Kyriacou and Hastings 2010; Feng and Lazar 2012; Bechtold et al. 2010).

Renal circadian regulation influences renal blood flow, glomerular filtration rate and electrolyte excretion (Stow and Gumz 2011; Saifur Rohman et al. 2005; Firsov and Bonny 2018; Douma and Gumz 2018; Johnston and Pollock 2018; Carriazo et al. 2020). Dysfunction of renal excretory rhythms can alter renal sodium reabsorption; this is associated with loss of the normal nocturnal dip in the blood pressure which is a risk factor for cardiovascular disease and a significant predictor of chronic kidney disease (CKD) (Agarwal and Light 2009; Bankir et al. 2008; Burnier et al. 2007). There is also a link between clock output genes and drug detoxification in both the liver and kidneys with implications for delivery of therapeutic drugs (Gachon et al. 2006; Bowles et al. 2018).

In the course of molecular profiling studies of kidney mRNA from three mouse models of lupus nephritis (LN) using samples collected in the mornings we found altered expression of transcriptional regulators of circadian rhythm in nephritic kidneys (Bethunaickan et al. 2013). Here we ask whether this abnormality disrupts expression of diurnally regulated renal cellular transcripts and whether there are functional consequences with respect to homeostatic renal excretory rhythms.

Materials and methods

Mice

Mice were housed in our vivarium and maintained under conditions of 12 h light/dark periods and followed for the onset of proteinuria as previously described (Ramanujam et al. 2006; Schiffer et al. 2008). Groups of young and nephritic mice were moved to the reverse light cycle room for serum and urine collections and were acclimated for 2 weeks (Munn et al. 2011) prior to any experiments. We harvested perfused whole kidneys from 12 week old and nephritic 30–45 week old NZB/W (2–3 weeks after the onset of 300 mg/dl proteinuria and blood urea nitrogen < 25 mg/dl) mice at 4 h intervals over 24 h. To control for the general effects of age on renal circadian rhythms, kidneys were obtained from four 12-week-old and 36-week-old C57BL/6 mice at Zeitgeber time (ZT) 0 and 12 (Additional file 1: Table S1). To further control for age in the correct strain, nephritic mice aged 36–50 weeks were treated with triple CTLA4Ig, anti-CD40L and cyclophosphamide therapy from 48 to 72 h after first onset of fixed proteinuria > 300 mg/dl as previously described (Schiffer et al. 2003). Proteinuria was measured weekly and mice that maintained remission (proteinuria ≤ 30 mg/dl) were harvested after 8 weeks either at ZT0 or ZT12. For timed urine collections, mice were housed in their own cages on urine hydrophobic sand (Braintree, MA) (Hoffman et al. 2018) with gel food and gel water for up to 12 h. Urine was collected without disturbing the mice and pooled over several days for each timed collection.

Blood pressure

Blood pressure was measured longitudinally in groups of young and nephritic mice using a CODA monitor (Kent Scientific, Torrington, CT) according to manufacturers' instructions. After a 3 day period of acclimation to the apparatus, the same operator gently placed the mice in restrainers and warmed them to 35 °C for 15 min prior to measuring blood pressure. 10 cycles were measured at each time after 5 cycles of acclimation. Measurements in the dark cycle were made in a room with a red light so that the mice were not exposed to ambient light. Blood pressure measurements were performed no more than twice per individual mouse in each 24 h period and were carried out over 3–5 days.

Measurement of mouse motor activity

Each animal was individually housed in a square-base plain chamber (40 cm side, 40 cm high) containing bedding, similar to that of the home cage as well as food and water. The chamber was located in a dedicated, quiet space without confounding external stimuli. A 50-W orange-red light bulb illuminated the chamber from above. A miniature near infrared video camera (CV502-MB, Marshall Electronics) was mounted above the chamber and connected to a 4-channel high definition video capture card (DeckLink Duo 2, Blackmagic Design). After a period of acclimatization, video was recorded at 30 frames per second with a resolution of 1920 × 1080 pixels with video tracking software (Wirecast 7 Pro, Telestream) and saved to disk in.mp4 file format. Captured videos were then analyzed using a behavioral tracking software (Ethovision XT 11.5, Noldus), which tracked the activity level of the mouse on a frame by frame basis. Data was expressed as the percentage of time that the mice were active per 30 min interval.

Microarray and RNA sequencing

Total RNA was isolated from perfused mouse kidneys using TRIzol reagent (Ambion, Life Technologies). Quality of the RNA was verified on a NanoRNA chip (Agilent, Santa Clara, CA). 42 samples were run on microarray, 46 samples were run on RNASeq and 15 samples, all at ZT times 0 and 12 were run on both platforms (See Additional file 1: Table S1).

Microarray experiments using the Illumina MouseRef-8 v2.0 Expression BeadChip were performed on total RNA following standard protocols provided by the manufacturer (Illumina Inc. San Diego, CA). Whole-Genome Gene Expression Direct Hybridization assay was applied to RNA samples starting with 100 ng of total RNA for hybridization to the chips. The chips were scanned by HiScanner (Illumina Inc) and the background-subtracted intensity data was extracted by GenomeStudio Informatics System. The genes with low intensity (lowest 30% quantile of intensity values of all genes in all samples) in > 2/3 of the samples were excluded and the intensities of the remaining genes were log2 transformed and normalized at an equal global median value. Data has been submitted to GEO with the following accession number: GSE131894.

Paired-end sequencing with 150 bp read length was carried out on 73 RNA samples on HiSeq 4000 (Illumina Inc.) sequencer. The libraries were generated according to manufacturers' protocol: Briefly, mRNA was isolated from 2 μg of total RNA using oligo-dT magnetic beads and fragmented at high temperature. A cDNA library was then prepared from the fragmented mRNA by reverse transcription, second strand synthesis and ligation of specific adapters. Next generation sequencing was performed on Illumina HiSeq 4000 (Illumina Inc.) with single-ended 150 read cycles. Image analysis and bases calling was conducted in real-time by the Illumina analysis pipeline.

Good quality reads were aligned to several human reference databases including mouse genome (build 10 mm), exon, splicing junction segment and contamination database including ribosome and mitochondrial sequences using Burrows Wheeler alignment algorithm (Li and Durbin 2009). After filtering, the reads that were uniquely aligned to the exon and splicing-junction segments with a maximum of 2 mismatches for each transcript were then counted for each corresponding transcript. The genes with a read count of less than 100 across all samples were excluded. The read counts of remaining genes were log2 transformed and normalized at an equal global median value.

Both microarray analysis and RNASeq are validated methods for transcriptomic profiling with good concordance; RNASeq has a wider dynamic range and may identify more differentially expressed genes (Zhao et al. 2014; Rao et al. 2018). Before merging microarray and RNA sequencing data for downstream circadian rhythm analysis, the microarray and RNA sequencing data were each subjected to median center normalization. The data of the common genes for both microarray and RNA sequencing were merged and further normalized by quantile normalization approach. Finally, batch correction was performed between microarray and RNA sequencing data using ComBat (Johnson et al. 2007) to eliminate technical variation. These normalization steps minimized the technical variations as evident for the 15 samples with both microarray and RNA sequencing data (Additional file 1: Figure S1A, B), or all the samples (Additional file 1: Figure S1C, D) and provided more robust statistical significance (Pariollaud et al. 2018). Spearman's correlation coefficients for the 15 samples that were run on both platforms are shown in Additional file 1: Figure S1E.

To identify patterns of circadian rhythm from 6-time intervals over a 24 h period, ANOVA test was first performed to identify differentially expressed genes across intervals at an adjusted p value of ≤ 0.05 (2319 genes in young mice and 860 genes in nephritic mice). The RAIN test was furthered performed to identify the genes with a circadian rhythm pattern (2262 genes in young mice and 755 genes in nephritic mice—Additional file 1: Figure S2A) (Thaben and Westermark 2014). The enriched biological functions of the genes with circadian rhythm pattern at different time intervals were determined using Reduce and Visualize Gene Ontology (REVIGO) algorithm (Supek et al. 2011). Inflammatory genes and genes that reflect injury of stromal cells (Bethunaickan et al. 2014; Berthier et al. 1950) did not manifest a circadian pattern of expression and differences between young and nephritic mice and between nephritic and remission mice confirmed the presence of renal injury and inflammation in the nephritic mice and the induction of remission (Additional file 1: Figure S2B, C).

ELISA for Bmal1 and Per2

Snap frozen kidney was homogenized in RIPA buffer containing 1X protease inhibitor cocktail (Roche, Indianapolis, IN). After centrifugation at 19,000 *g* for 10 min at 4 °C, the supernatant was collected and the protein concentration was determined using a BCA protein assay. Fine adjustment of protein concentration was made based on the concentration of β-actin as determined by ELISA using 1:500 anti-β actin (Anti-beta Actin antibody ab8227, Abcam Cambridge, MA) in PBS to coat the plates and 1:1000 (HRP-conjugated beta Actin antibody, Proteintech, Rosemont, IL) as secondary antibody. Plates (Falcon Labware, Lincoln Park, NJ) were coated with antibodies to Bmal1 (NBP1-28802, Novus Biologics Centennial, CO) diluted at 1:500 or Per2 at 1:1000 (bs-3927R, Bioss Antibodies, Woburn, MA) in PBS overnight at 4 °C. After blocking with PBS/3% BSA, the plates were incubated with serial dilutions of kidney lysate starting at 1:3 dilution in PBS/1% BSA for 1 h at 37 °C, followed by incubation with either 1:100 anti-Bmal1 HRP (sc-365645, Santa Cruz Biotechnology, Dallas, TX) or anti-Per2

polyclonal antibody diluted at 1:5000 (AB5428P, Millipore, Burlington, MA) in PBS/1% BSA and then a 1:1 substrate solution of hydrogen peroxide and tetramethylbenzidine (R&D Systems, Minneapolis, MN) to generate the colorimetric reaction. The plates were quenched and immediately read on the plate reader at 405 nm. A liver lysate from a BMALtg mouse was run in serial dilution on each plate as a quantitation control. To confirm the validity of the ELISA, lysate from a BMAL1 deficient mouse (a gift from Dr. Garret FitzGerald, University of Pennsylvania) was used as a negative control for Bmal1. No background activity was observed in the BMAL1 deficient lysate. Because BMAL deficient mice have high levels of Per2, this lysate was also used as the positive control for titration of Per2 levels.

Serum and urine analytes

Urine Na and K levels were measured by Jackson Laboratories (Bar Harbor, ME). Serum and urine glucose were measured using a glucometer (ThermoFisher Scientific, Parsippany-Troy Hills, NJ). To correct for variations in urine dilution between samples, ratios of Na/creatinine and K/creatinine were calculated (Lee et al. 2013; Dyer et al. 1998; Mann et al. 2012; Koo et al. 2015). Creatinine was measured using a chromagenic assay (ThermoFisher Scientific). Serum and urine aldosterone were measured using a commercial inhibition ELISA assay (ENZO Life Sciences, Farmingdale, NY, USA) according to the manufacturer's instructions. Urine pH was measured using a pH Micro Electrode (Fisher Scientific).

Quantitative PCR

5ug of RNA was reverse-transcribed with SuperScript II reverse transcriptase (Invitrogen Life Technologies, Carlsbad, CA). Amplification was performed in triplicate using SYBR Green PCR Master Mix (Roche Diagnostics, Tucson, AZ) and specific primers in a LightCycler480 (Roche Diagnostics). Dissociation curve analysis confirmed amplification of one specific product per primer pair. PCR primers were as follows: Avpr1a Forward primer 5' gggataccaatttcgtttgg 3'; Reverse primer 5' aagccagtaacgccgtgat 3'; Bmal1 Set 1: Forward primer 5' gccccaccgacctactct 3'; Reverse primer 5' tgtctgtgtccatactttcttgg 3'; Set 2: Forward primer 5' ccaagaaagtatggacacagacaaa 3'; Reverse primer 5' gcattcttgatccttccttggt 3'; Clock Forward primer 5' ccagtcagttggtccatcatt 3'; Clock Reverse primer 5' tggctcctaactgagctgaaa 3'; Per1 Forward primer 5' gcttcgtggacttgacacct 3'; Per1 Reverse primer 5' tgctttagatcggcagtggt 3'; Per2 Set 1: Forward primer 5' gcttcgtggacttgacacct 3'; Reverse primer 5' tgctttagatcggcagtggt 3'; Per2 Set 2: Forward primer 5' cagcacgctggcaaccttgaagtat 3'; Per2 Reverse primer 5' cagggctggctctcactggacatta 3'; Per3: Forward primer 5' cataccaggtgcccgaga 3'; Per3 Reverse primer 5' gctgctgttccatgctctg 3'; Rev-erbα Forward primer 5' cagcatgatcaggtcaatctgt 3'; Rev-erbα Reverse primer 5' agcaaatcgtaccattaaaacctc 3'; Avpr2: Forward primer 5' ctggtgtctaccacgtctgc3'; Avpr2 Reverse primer 5' ggtctcggtcatccagtagc 3'.

Statistics

Comparisons between groups were performed using 2-tailed Mann Whitney analysis for 2 group comparisons or Kruskal–Wallis one-way analysis of variance for ≥ 3 group comparisons. Circadian rhythmicity was evaluated using Cosinor analysis (Moškon 2020) https://cosinor.online/app/cosinorOutput.php. A p value less than 0.05 was considered statistically significant.

Ethical approval information

The study was approved by the Feinstein Institute IACUC (Protocol 2015-031).

Results

Nephritic mice have a profound disturbance of diurnal variation of multiple renal genes

Diurnal expression of Bmal1and Per2 followed the normal pattern (Gachon et al. 2006; Zhang et al. 2014) in young NZB/W mice but was dysregulated in nephritic mice (Fig. 1A–D). Expression of other transcriptional regulators including *Per1, Per3, Clock* and, to a lesser extent, *Rev-erbα* (*Nr1d1*) and *Cry1* was also perturbed in the nephritic mice (Additional file 1: Figure S3A, B). Most circadian genes identified in young mice manifested a dampened pattern in the nephritic mice (Fig. 1E, F). Only 364 of 2653 diurnally regulated genes were shared between young and nephritic mice; of these 140 peaked at the same time and another 158 within 4 h with the rest being 8 or more hours off-cycle. 391 genes were expressed in a circadian fashion only in nephritic mice, but their circadian variation was generally of low amplitude (Additional file 1: Figure S3A, B).

To determine whether renal circadian disturbance is a general feature of aging, samples from 8 and 36- week-old C57BL/6 mice obtained at Zeitgeiber times (ZT) 0 and 12 were included in the RNASeq analysis. Expression of a panel of circadian regulatory genes whose diurnal variation was dampened in nephritic NZB/W mice was undisturbed in aged C57BL/6 mice (Fig. 1F–I).

To determine whether renal circadian disturbance is associated with disturbed sleep–wake cycles we observed mice over a 24 h period. Sleep–wake cycles followed a normal pattern in both young and nephritic NZB/W mice, however the nephritic mice were modestly more active during the light period and displayed diminished

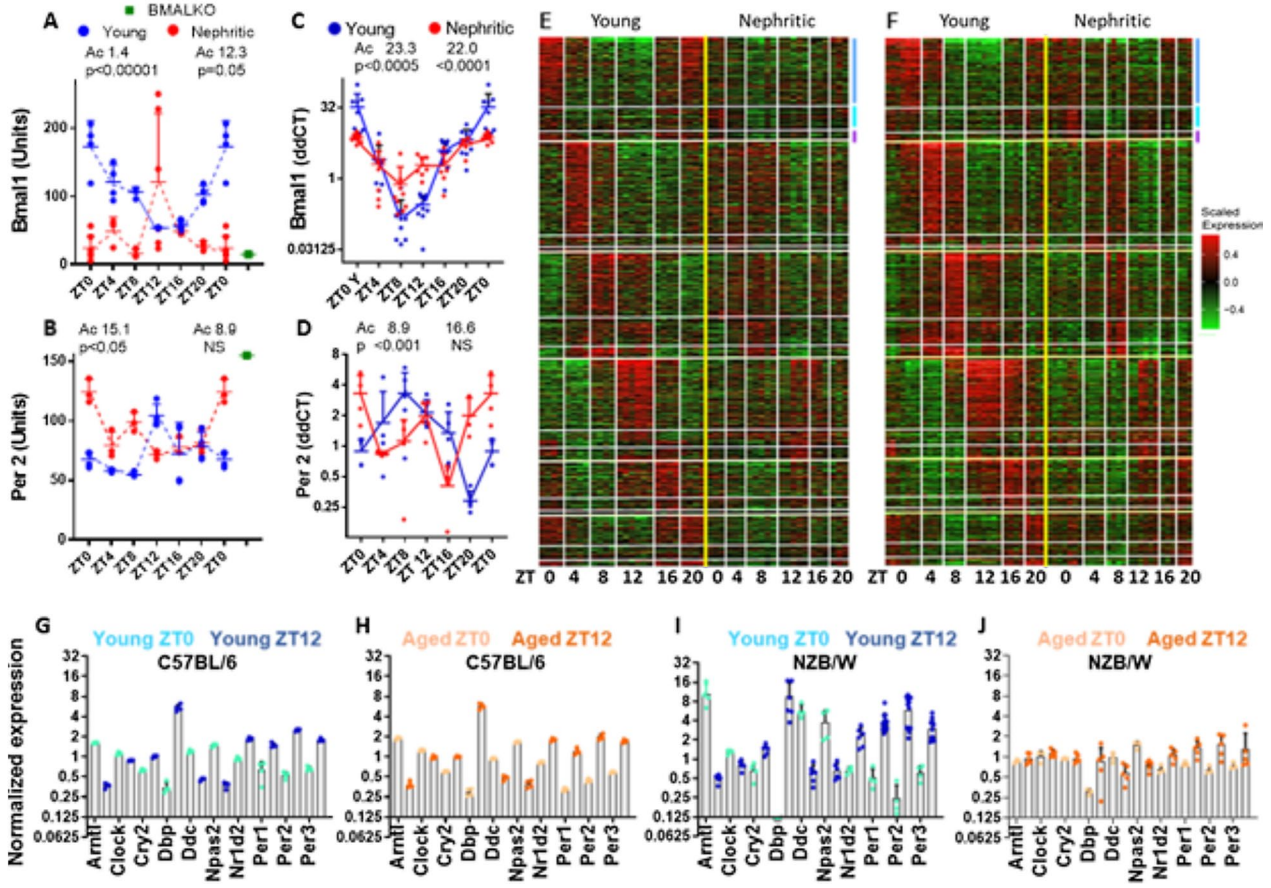

Fig. 1 **A**, **B** Bmal1 and Per2 protein expression measured in renal lysates by ELISA (shown in dashed lines); **C**, **D** Bmal1 and Per2 expression measured in whole renal mRNA by qPCR (shown in solid lines)—each symbol represents one mouse;); Ac time of acrophase, ZT Zeitgeiber time where ZT0 is the time of lights on. **E** Heatmap of all genes passing the RAIN test for circadian rhythm in young and nephritic kidneys. Complete results from the microarray analysis are on the left and from the RNASeq analysis are on the right. For each time interval, indicated by Zeitgeiber time (ZT0 = lights on, ZT12 = lights off), genes regulated in young mice are shown in the upper panel (blue bar), those regulated in nephritic mice are shown in the middle panel (aqua bar) and those regulated in common between the two groups are shown in the lower panel (purple bar). **F**–**I** RNASeq data of circadian transcriptional regulators in young (light and dark blue—**F**, **H**) and old (light and dark orange—**G**, **I**) C57BL/6 mice at ZT0 (light colors) and ZT12 (dark colors) **F**, **G** compared with young (light and dark blue) and nephritic (light and dark orange) NZB/W kidneys **H**, **I**—each symbol represents one mouse

activity during the dark period compared with young mice (Additional file 1: Figure S3C, D).

Pathways affected by circadian dysfunction in nephritic mice

To determine which functional pathways were perturbed in the kidneys of nephritic mice, Enriched Gene Functions were discovered at each time interval using REVIGO program (Fig. 2, Additional file 1: Figures S4A–F). In young mice, organ morphogenesis and cell growth predominated towards the end of the active phase at ZT20 and ZT0, whereas metabolic and cell transport processes predominated towards the end of the rest period at ZT8 and ZT12. By contrast, functional pathways in nephritic mice were dominated by processes related to protein modification and catabolism and responses to DNA damage.

Since abnormal metabolic processes are associated with CKD, we performed more detailed analysis of genes involved in metabolic functions (Additional file 1: Table S2). Many genes involved in fatty acid metabolism, particularly fatty acid synthesis and beta oxidation followed diurnal rhythms in young mice with peak expression at ZT8 and ZT12. By contrast, circadian oscillation of these genes was flattened in the nephritic mice (Fig. 3A). Heightened rhythmicity of the transcription factor *Srebp1* is associated with an increase in fatty acid synthesis in mice with fatty liver (Guan et al. 2018). By

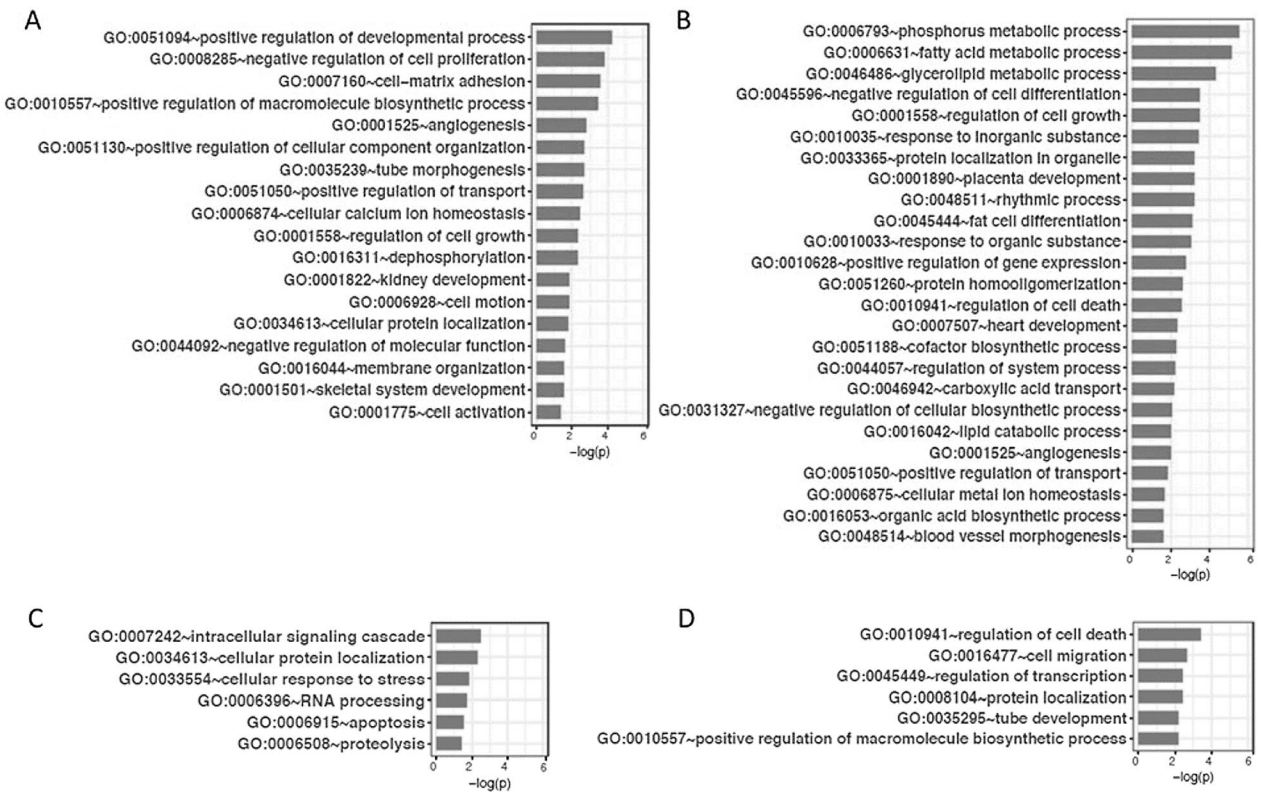

Fig. 2 Renal functions that are regulated in a circadian fashion in NZB/W kidneys. **A** Young mice ZT0; **B** Young mice ZT12; **C** Nephritic mice ZT0; **D** Nephritic mice ZT12

contrast, rhythmic expression of *Srebp1* was dampened in the kidneys of nephritic compared with young mice. In addition, overall expression levels of genes involved in fatty acid metabolism were lower in the nephritic mice than the young mice. These findings are consistent with the observed decrease in tubular fatty acid metabolism in mice with CKD (Kang et al. 2015).

Normal renal proximal tubule cells have low glycolytic activity which can increase as a consequence of renal tubular insult (Lan et al. 2016). The kidney is also responsible for ≈ 20% of total body gluconeogenesis. We noted robust circadian regulation of three enzymes involved in gluconeogenesis (*Idh1, G6pc* and *Pck1*) in young but not nephritic kidneys (Fig. 3B). By contrast, nephritic kidneys acquired an increase in expression and rhythmicity of both *G6pdx* and *H6pd*, enzymes that catalyze the first step of the pentose phosphate pathway (Fig. 3B). Only few genes involved in mitochondrial respiration were regulated in a circadian fashion even in young kidneys (Fig. 3C).

The Slc superfamily of solute carriers is a large family of membrane proteins that regulate ion fluxes and facilitate amino acid, sugar and nucleotide transport in and out of cells and cellular organelles. 85 Slc family members displayed diurnal variations in the young mice compared with 21 in the nephritic mice, of which only 10 overlapped between the two groups (Fig. 3D, Additional file 1: Table S3).

Effect of circadian dysfunction on renal homeostatic functions

Diurnal variations of sodium and potassium excretion are regulated by oscillations of renal tubule transporters involved in water and ion transport (Douma and Gumz 2018; Gumz 2016). In young mice Na + and K + excretion was highest at ZT16 and ZT20 as expected (Nikolaeva et al. 2012). However, in nephritic mice the increase in excretion of both ions at the end of the active period did not occur (Fig. 4A, B). Similarly, the normal circadian variation in urine pH was dysregulated in nephritic mice and the urine pH was lower during the rest period than in young mice (Fig. 4C). There was no difference in urine creatinine between young and nephritic mice to account for these differences (Additional file 1: Figure S5).

Global deficiencies of some circadian transcriptional regulators are associated with a hypotensive and/or non-dipping blood pressure phenotype whereas others are associated with a hyperaldosterone state (Richards

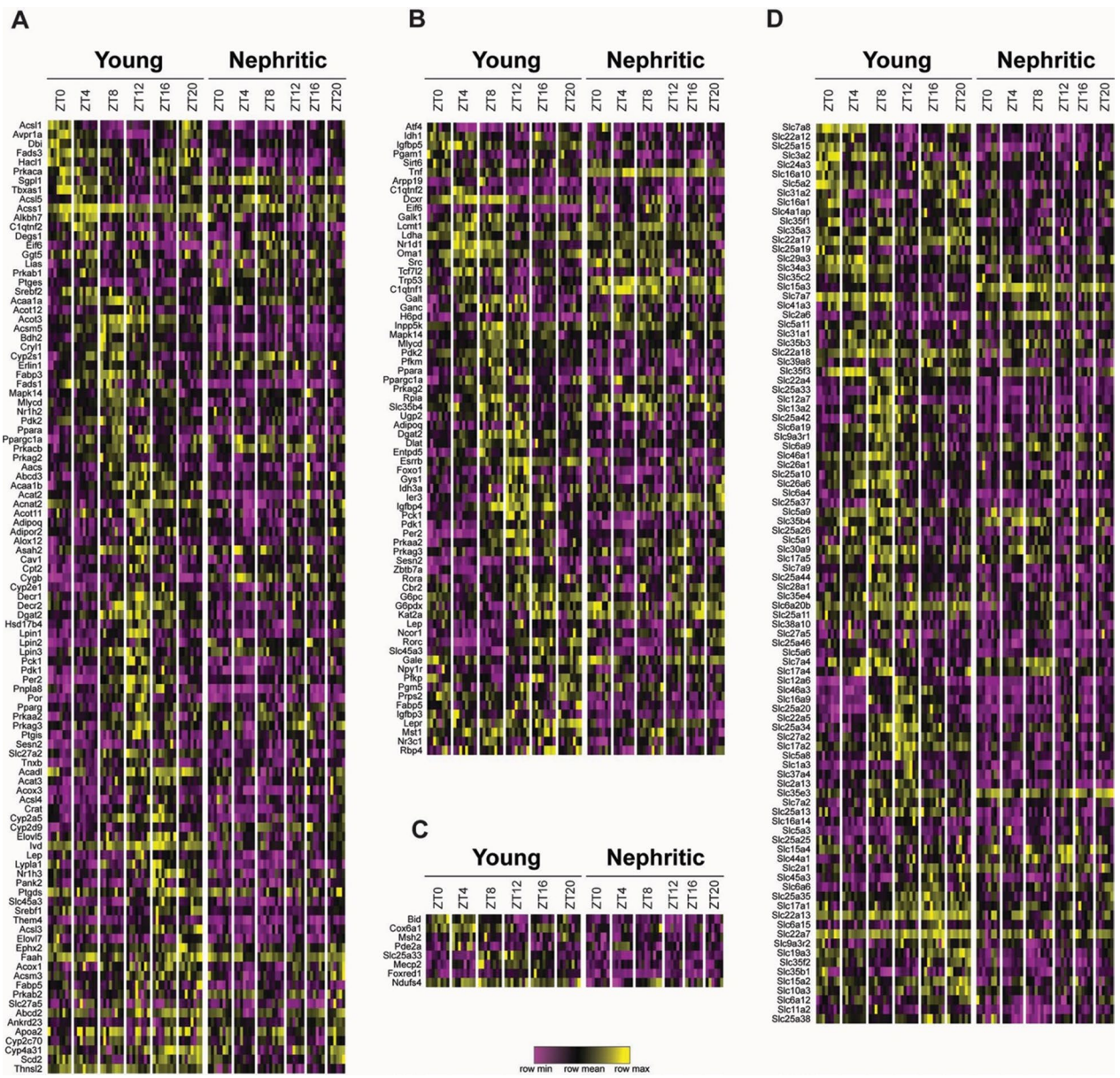

Fig. 3 Heatmaps of genes involved in metabolic pathways in young and nephritic mice. **A** Fatty acid metabolism; **B** glycolysis; **C** Mitochondrial oxidation and respiration; **D** Slc family of transporters. Samples are the same as those shown in Additional file 1: Figure S2

et al. 2013; Solocinski et al. 2017). Young mice displayed normal regulation of their blood pressure. By contrast, the nephritic mice displayed a reverse dipping pattern (Fig. 4D, E). Serum levels of aldosterone were highest at ZT12 in young mice as previously described (Nikolaeva et al. 2012). Nephritic mice, however, displayed high serum levels of aldosterone, especially during the day (Fig. 4F). This was associated with an increase in expression and circadian dysregulation of the β subunit of the epithelial sodium transporter (*Scnn1b)* in nephritic mice (Fig. 4G). Other genes involved in blood pressure control also demonstrated abnormal circadian regulation in nephritic mice. Expression of Angiotensin receptor 1a (*Agtr1*) and *Vegfc* was decreased throughout the day with a flattened rhythm, whereas expression of endothelin 1 (*Et1*), *Pdgfb*, *Adrb2, Cygb*, and *PtPro* was increased. Flattened rhythm of *Avpr1a, Cyp11b, Sgk1, Aqp3* and *Tsc22d3* (Gilz) was also observed in nephritic mice (Fig. 4G). These data in sum, suggest that in addition to the salt retention induced by the

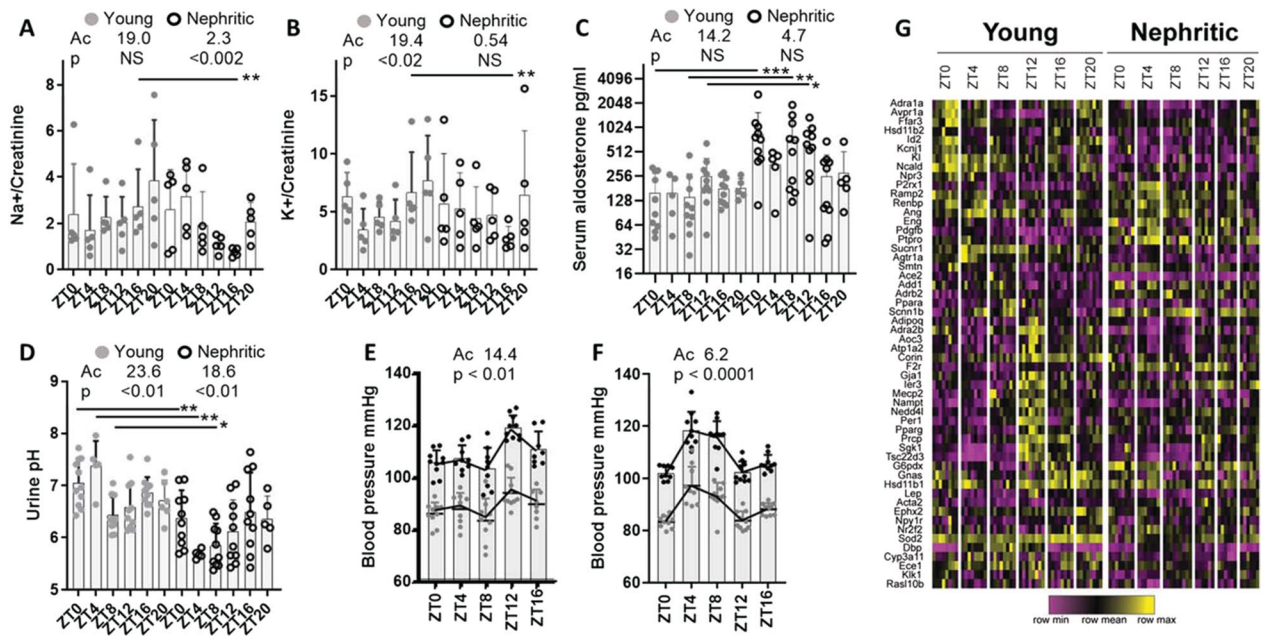

Fig. 4 Dysregulated circadian regulation of renal salt excretion and blood pressure in nephritic mice **A** Urine Na+/Creatinine ratio; **B** Urine K+/Creatinine ratio Urine pH; **C** Serum aldosterone; **D** Urine pH; **E, F**: systolic (black) and diastolic (grey) blood pressure in young (**E**) and nephritic (**F**) mice shows reverse dipping pattern in nephritic mice;—each symbol represents one mouse. **G** Heatmap of genes that contribute to regulation of blood pressure. Samples are the same as those shown in Additional file 1: Figure S2. Rhythmicity was evaluated by Cosinor analysis (Ac = acrophase)

hyperaldosterone state, the disturbance of blood pressure dipping in the nephritic mice could be influenced by changes in expression of multiple renal genes that regulate blood pressure.

Glucose reabsorption in renal tubules is crucial for glucose homeostasis. We found robust circadian rhythm of the major proximal tubule glucose co-transporter *Slc5a2* (Sglt2) in young mice with a peak at ZT8 that was dampened in the nephritic mice. By contrast, there was an increase in expression of *Slc2a6* (Glut6) in the nephritic mice. Complete deficiency of Sglt2 has been associated with glycosuria (Ansary et al. 2019). Young mice fed ad libitum had a normal dip in serum blood glucose levels during the active period that was dampened in the nephritic mice. Nevertheless, serum and urine glucose levels remained within the physiologic range in both groups. (Additional file 1: Figure S6).

Several other transporter families, including amino acid transporters, L-carnitine transporters and mitochondrial transporters manifested diurnal regulation in young but not in nephritic mice (Fig. 3C, Additional file 1: Table S3). Of interest, *Slc25a33* and *Slc25a42* that provide substrates for mitochondrial oxidative phosphorylation and fatty acid oxidation respectively (Palmieri 2014), had a robust circadian regulation in young mice that was dampened in the nephritic mice.

Induction of disease remission reverses circadian dysfunction

To determine whether the chronodisruption of renal functions in nephritic NZB/W mice is reversible, we administered a combination of cyclophosphamide, CTLA4Ig and anti-CD40L to nephritic mice that developed fixed proteinuria of > 300 mg/dl. We have extensively reported that this combination induces robust clinical, histologic and molecular disease remission in ≈ 80% of nephritic NZB/W mice (Schiffer et al. 1950b; Bethunaickan et al. 2014). ELISA analysis of renal lysates from mice that maintained clinical remission (proteinuria ≤ 30 mg/dl) 8 weeks after induction with this regimen indicated restoration of the normal pattern of Bmal1 and Per2 expression at ZT0 and 12 (Fig. 5A–D). To determine whether this was associated with correction of diurnal variation of genes involved in renal homeostatic functions, we identified a panel of 320 diurnally regulated genes that had ≥ 25% difference in expression between times ZT0 and ZT12 in young mice (at an adjusted p value of < 0.05) and ≥ 25% difference in the ZT0:ZT12 ratio between young and nephritic mice. Of these genes, 148 showed at least 50% correction in the remission kidneys (Fig. 5E), and 172 did not correct (Fig. 5F, Additional file 1: Tables S4 and S5, Figure S7). Two weeks after the mice achieved remission of proteinuria, there was a reversal of the blood pressure abnormality in 5/5 mice,

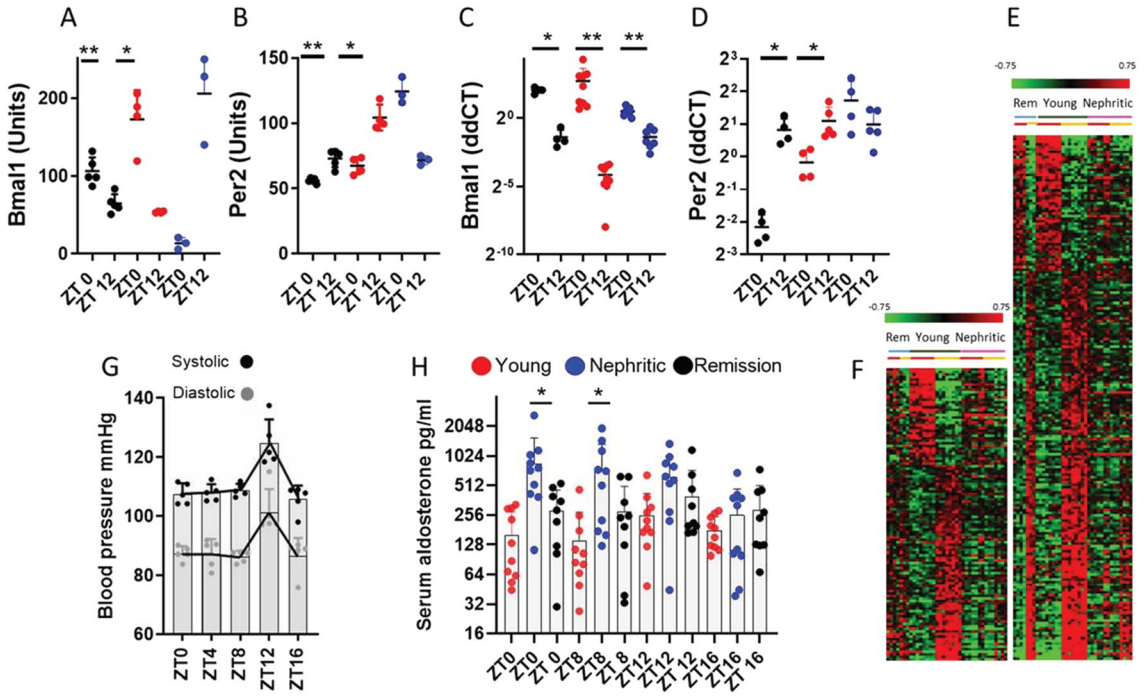

Fig. 5 Partial correction of circadian dysfunction by remission induction therapy. **A, B** Bmal1 and Per2 protein expression measured in renal lysates by ELISA; **C**, **D** Bmal1 and Per2 expression measured in whole renal mRNA by qPCR; **E**, **F** Heatmap of 320 genes that differed between ZT0 (red bars) and ZT12 (Orange bars) in young but not nephritic kidneys showing correction of 205 genes (**E**) and failure to correct 115 genes (**F**). **G** Blood pressure in remission mice shows normalization of dipping pattern; **H** Correction of serum aldosterone in remission mice. *p < 0.05. Red symbols: young mice; Blue symbols: nephritic mice; Black symbols: remission mice—each symbol represents one mouse

with normalization of the dipping pattern (Fig. 5G) and correction of the hyperaldosterone state (Fig. 5H).

Discussion

Circadian dysregulation in CKD includes disturbed sleep, failure of blood pressure dipping and renal electrolyte abnormalities and it has significant health consequences, including an increase in cardiovascular risk. Little is currently known about the role of renal intrinsic dysregulation of circadian rhythm in causing these physiologic disruptions (Firsov and Bonny 2018; Carriazo et al. 2020). We report here a general dampening of renal circadian rhythm in lupus nephritis kidneys that can be partially reversed with remission inducing immune therapy. Inflammatory mediators such as TNF, IL1β and endotoxin suppress circadian genes in multiple cell types (Haimovich et al. 2009; Guo et al. 2015; Cavadini et al. 2007; Curtis and Fagundes 2015) and induce degradation of Rev-erbα in tissues (Pariollaud et al. 2018). TGFβ may also influence renal wound healing, and epithelial cell proliferation via the regulation of master clock regulators Per1 and Dec2 by Smad3 (Sato et al. 2019). In inflammatory bowel disease, expression of major clock transcriptional regulators is dampened in affected tissue; in this model, an agonist of the circadian regulator Rev-erbα, attenuated the disease (Wang 2018). Similarly, both Rev-erbα and Per2 agonists prevented severe injury of the heart in rodent models of cardiac ischemia reperfusion (Stujanna et al. 2017; Pourcet et al. 2018). Finally, there is increasing recognition that disturbance of peripheral organ clocks may cause feedback disruption to central clock functions (Carriazo et al. 2020; Myung et al. 2019). These findings, together with our new observations in the lupus kidney support the notion that local circadian disruption is a general feature of inflammation that contributes to organ dysfunction and that reversal of this process could be of therapeutic benefit.

Our study reveals that mice with active lupus nephritis have a reversal of the normal blood pressure dipping pattern. Global deficiency of *Bmal1, Clock* or *Per1* confers a hypotensive phenotype and/or changes in blood pressure dipping status, whereas deficiency of *Cry1/2* confers increased salt sensitivity and a non-dipping pattern (Doi et al. 2010); in the case of *Cry1/2*, there is also a hyperaldosterone state (Richards et al. 2013; Solocinski et al. 2017). Reverse dipping in humans is an extreme phenotype that occurs in patients with hypertension, type 2 diabetes mellitus and chronic

kidney disease and is associated with cardiac dysfunction (Cuspidi et al. 2017; Tadic et al. 2020a, b). We show here that there are complex effects of nephritis on circadian regulation of renal genes that regulate blood pressure, with a hyperaldosterone state and increased expression of genes that regulate vasoconstriction. Other factors, including the effects of inflammation on systemic vascular function (Dinh et al. 2014; Savoia and Schiffrin 2006) could also contribute to the blood pressure abnormalities found in nephritic mice. Importantly, the reverse dipping blood pressure pattern in aged nephritic mice could be normalized by remission induction.

We also show circadian dysregulation of genes involved in renal metabolism. Renal tubular cells are dependent on fatty acid oxidation for their energy supply. We noted a significant dysregulation of diurnal variation of fatty acid transporters and of molecules involved in mitochondrial fatty acid oxidation and fatty acid synthesis. A defect in fatty acid metabolism in both mouse and human CKD and in nephritic NZB/W mice has previously been associated with a decrease in expression of the master transcriptional regulator Pparγc1α that regulates mitochondrial biogenesis and fatty acid oxidation (Kang et al. 2015). Our data suggests a more extensive defect in fatty acid synthesis and oxidation that is a major metabolic abnormality in the nephritic kidneys.

We also detected a decrease in diurnal variation of several genes involved in gluconeogenesis that reversed upon remission induction and an increase in the two rate limiting enzymes for the pentose phosphate pathway in the nephritic mice. A reduction in gluconeogenesis and an increase in renal hexokinase activity is induced by LPS in rodent kidneys perhaps reflecting an increased need for NADPH in the oxidatively stressed kidney (Smith et al. 2014) and/or provision of precursors for nucleotide synthesis that are important for cell growth (Lunt and Vander Heiden 2011). An induction of the pentose phosphate pathway has been observed in human inflammatory renal disease including LN and is correlated with inflammation (Grayson et al. 2018).

Another major role of kidney tubule transporters is to prevent the loss of amino acids in the urine (Makrides et al. 2014). We show here that there is a robust circadian regulation of transporters of the Slc6, Slc7/3 and Slc15 families in young NZB/W mice that is abrogated in the nephritic mice. Disturbances in regulation of amino acid transporters could contribute to tubular proteinuria in nephritic mice. We also observed disturbances in circadian regulation of organic anion/cation tubular transporters that could influence the renal toxicities of xenobiotics and other renally excreted drugs (Zhao et al. 2020).

One caveat of our studies is that it is difficult to control for the effects of age in NZB/W mice in which disease onset is stochastic and renal inflammation precedes the onset of proteinuria. Renal circadian dysregulation was not detected in aged non-autoimmune C57BL/6 mice. To further control for the effects of age we used kidneys from aged NZB/W mice from which collections were timed from complete responders after remission induction. We found that remission induction in aged NZB/W mice corrected the diurnal variation of more than 50% of the dysregulated genes. The effects of this treatment on blood pressure were striking, with concordance between complete remission of proteinuria and correction of the abnormal blood pressure dipper phenotype. This finding is of particular human relevance since nocturnal hypertension is an under-appreciated feature of active lupus nephritis that correlates with disease activity and interstitial damage and may be missed by day-time blood pressure measurements (Canpolat et al. 2013; Sabio et al. 2015). Ambulatory blood pressure monitoring (ABPM) is needed to detect such changes. Abnormal nocturnal blood pressure dipping is a major predictor of major adverse coronary events and its recognition and correction by timing of anti-hypertensive treatment attenuates cardiovascular morbidity and mortality as well as progression of CKD (Hermida et al. 2020). These findings suggest a need for ABPM in patients with LN and appropriate correction of abnormal blood pressure patterns. Further studies will be needed to understand the relevance of our findings to human LN and to determine whether reversal of nocturnal hypertension is a predictor for good renal outcome.

Conclusions

Overall, our study reveals an underappreciated effect of renal inflammation on renal circadian rhythms in LN kidneys in NZB/W mice with multiple adverse effects on renal homeostasis and metabolism as well as blood pressure dipper status. Although we only used one LN mouse strain, similar disturbance of circadian master transcriptional regulators was observed in 2 other LN strains (Bethunaickan et al. 2013). Dampening of circadian rhythm in inflamed organs has recently been reported and agonists of the negative transcriptional regulators Rev-erbα and Per2 have broad anti-inflammatory functions and metabolic effects in vivo, especially when used before the onset of inflammation (Wang 2018). It is not yet clear whether this is due to modulation of local or systemic circadian circuits and the effects of such an approach in the setting of chronic inflammation have not yet been studied. We found modest disruption of renal diurnal rhythm of *Rev-erbα* and marked dysregulation of both *Per1* and *Per2* in the nephritic kidneys suggesting that these could

be potential targets for circadian modulating therapy in lupus nephritis.

Abbreviations
ZT: Zeitgeber time (ZT0 is lights on and ZT12 is lights off); CKD: Chronic kidney disease; Slc: Solute carrier family; REVIGO: Reduce and visualize gene ontology; ABPM: Ambulatory blood pressure monitoring.

Supplementary Information

The online version contains supplementary material available at https://doi.org/10.1186/s10020-021-00361-9.

Additional file 1. Additional tables and figures.

Acknowledgements
Not applicable.

Authors' contributions
Designed research studies: RM, RB, PH, AD. Conducted experiments: RM, RB, JS, AD. Analyzed data: RM, RB, CB, ZY, JS, PH, WZ, AD. Wrote the manuscript: RM, ZY, CB, WZ, AD**.** All authors read and approved the final manuscript.

Funding
This work was funded by grants from the Lupus Research Alliance and the National Institutes of Health NIAMS R21 AR0765571-01 to AD.

Availability of data and materials
Data has been submitted to GEO with the following Accession Number: GSE131894.

Declarations

Ethics approval and consent to participate
Mouse studies were approved by the Feinstein Institutes IACUC committee.

Consent for publication
All authors consent to publication.

Competing interests
There are no competing interests.

Author details
[1]Institute for Molecular Medicine, Feinstein Institutes for Medical Research, 350 Community Drive, Manhasset, NY 11030, USA. [2]Department of Internal Medicine, Nephrology, University of Michigan, Ann Arbor, MI 48109, USA. [3]Department of Medicine, Mount Sinai Medical Center, One Gustave L. Levy Place, P.O. Box 1243, New York, NY 10029, USA.

Received: 24 March 2021 Accepted: 23 August 2021
Published online: 06 September 2021

References

Agarwal R, Light RP. GFR, proteinuria and circadian blood pressure. Nephrol Dial Transplant. 2009;24(8):2400–6.
Ansary TM, Nakano D, Nishiyama A. Diuretic effects of sodium glucose cotransporter 2 inhibitors and their influence on the renin-angiotensin system. Int J Mol Sci. 2019. https://doi.org/10.3390/ijms20030629.
Bankir L, Bochud M, Maillard M, Bovet P, Gabriel A, Burnier M. Nighttime blood pressure and nocturnal dipping are associated with daytime urinary sodium excretion in African subjects. Hypertension. 2008;51(4):891–8.
Bechtold DA, Gibbs JE, Loudon AS. Circadian dysfunction in disease. Trends Pharmacol Sci. 2010;31(5):191–8.
Berthier CC, Bethunaickan R, Gonzalez-Rivera T, Nair V, Ramanujam M, Zhang W, Bottinger EP, Segerer S, Lindenmeyer M, Cohen CD, et al. Cross-species transcriptional network analysis defines shared inflammatory responses in murine and human lupus nephritis. J Immunol. 2012;189(2):988–1001.
Bethunaickan R, Berthier CC, Zhang W, Kretzler M, Davidson A. Comparative transcriptional profiling of 3 murine models of SLE nephritis reveals both unique and shared regulatory networks. PLoS ONE. 2013;8(10):e77489.
Bethunaickan R, Berthier CC, Zhang W, Eksi R, Li HD, Guan Y, Kretzler M, Davidson A. Identification of stage-specific genes associated with lupus nephritis and response to remission induction in (NZB x NZW)F1 and NZM2410 mice. Arthritis Rheum. 2014;66(8):2246–58.
Bowles NP, Thosar SS, Herzig MX, Shea SA. Chronotherapy for hypertension. Curr Hypertens Rep. 2018;20(11):97.
Burnier M, Coltamai L, Maillard M, Bochud M. Renal sodium handling and nighttime blood pressure. Semin Nephrol. 2007;27(5):565–71.
Canpolat N, Kasapcopur O, Caliskan S, Gokalp S, Bor M, Tasdemir M, Sever L, Arisoy N. Ambulatory blood pressure and subclinical cardiovascular disease in patients with juvenile-onset systemic lupus erythematosus. Pediatr Nephrol. 2013;28(2):305–13.
Carriazo S, Ramos AM, Sanz AB, Sanchez-Niño MD, Kanbay M, Ortiz A. Chronodisruption: a poorly recognized feature of CKD. Toxins. 2020;12(3):151.
Cavadini G, Petrzilka S, Kohler P, Jud C, Tobler I, Birchler T, Fontana A. Circadian variation of blood pressure and the vascular response to asynchronous stress. Proc Natl Acad Sci USA. 2007;104(9):3450–5.
Curtis AM, Fagundes CT. Catabolic cytokines disrupt the circadian clock and the expression of pathway. Methods Mol Biol. 2015;23(11):1981–8.
Cuspidi C, Sala C, Tadic M, Gherbesi E, De Giorgi A, Grassi G, Mancia G. Clinical and prognostic significance of a reverse dipping pattern on ambulatory monitoring: an updated review. J Clin Hypertens. 2017;19(7):713–21.
Dinh QN, Drummond GR, Sobey CG, Chrissobolis S. Roles of inflammation, oxidative stress, and vascular dysfunction in hypertension. BioMed Res Int. 2014;2014:406960.
Doi M, Takahashi Y, Komatsu R, Yamazaki F, Yamada H, Haraguchi S, Emoto N, Okuno Y, Tsujimoto G, Kanematsu A, et al. Salt-sensitive hypertension in circadian clock-deficient Cry-null mice involves dysregulated adrenal Hsd3b6. Nat Med. 2010;16(1):67–74.
Douma LG, Gumz ML. Circadian clock-mediated regulation of blood pressure. Free Radic Biol Med. 2018;119:108–14.
Dyer AR, Martin GJ, Burton WN, Levin M, Stamler J. Blood pressure and diurnal variation in sodium, potassium, and water excretion. J Hum Hypertens. 1998;12(6):363–71.
Feng D, Lazar MA. Clocks, metabolism, and the epigenome. Mol Cell. 2012;47(2):158–67.
Firsov D, Bonny O. Circadian rhythms and the kidney. Nat Rev Nephrol. 2018;14(10):626–35.
Gachon F, Olela FF, Schaad O, Descombes P, Schibler U. The circadian PAR-domain basic leucine zipper transcription factors DBP, TEF, and HLF modulate basal and inducible xenobiotic detoxification. Cell Metab. 2006;4(1):25–36.
Grayson PC, Eddy S, Taroni JN, Lightfoot YL, Mariani L, Parikh H, Lindenmeyer MT, Ju W, Greene CS, Godfrey B, et al. Metabolic pathways and immunometabolism in rare kidney diseases. Ann Rheum Dis. 2018;77(8):1226–33.
Guan D, Xiong Y, Borck PC, Jang C, Doulias PT, Papazyan R, Fang B, Jiang C, Zhang Y, Briggs ER, et al. Diet-induced circadian enhancer remodeling synchronizes opposing hepatic lipid metabolic processes. Cell. 2018;174(4):831-42.e12.
Gumz ML. Molecular basis of circadian rhythmicity in renal physiology and pathophysiology. Exp Physiol. 2016;101(8):1025–9.
Guo B, Yang N, Borysiewicz E, Dudek M, Williams JL, Li JC, Maywood ES, Adamson A, Hastings MH, Bateman JF, et al. Circadian control of innate immunity in macrophages by miR-155 targeting Bmal1. Osteoarthritis Cartilage. 2015;112(23):7231–6.
Haimovich B, Calvano J, Haimovich AD, Calvano SE, Coyle SM, Lowry SF. A circadian clock in macrophages controls inflammatory immune responses. Crit Care Med. 2009;106(50):21407–12.
Hermida RC, Mojón A, Fernández JR. Bedtime hypertension chronotherapy best reduces cardiovascular disease risk as documented by MAPEC and Hygia Chronotherapy outcomes trials. Chronobiol Int. 2020;37(5):731–8.
Hoffman JF, Fan AX, Neuendorf EH, Vergara VB, Kalinich JF. Hydrophobic sand versus metabolic cages: a comparison of urine collection methods for rats (Rattus norvegicus). JAALAS. 2018;57(1):51–7.

Honma S. The mammalian circadian system: a hierarchical multi-oscillator structure for generating circadian rhythm. J Physiol Sci. 2018;68(3):207–19.
Johnson WE, Li C, Rabinovic A. Adjusting batch effects in microarray expression data using empirical Bayes methods. Biostatistics. 2007;8(1):118–27.
Johnston JG, Pollock DM. Circadian regulation of renal function. Free Radic Biol Med. 2018;119:93–107.
Kang HM, Ahn SH, Choi P, Ko YA, Han SH, Chinga F, Park AS, Tao J, Sharma K, Pullman J, et al. Defective fatty acid oxidation in renal tubular epithelial cells has a key role in kidney fibrosis development. Nat Med. 2015;21(1):37–46.
Koo H, Lee SG, Kim JH. Evaluation of random urine sodium and potassium compensated by creatinine as possible alternative markers for 24 hours urinary sodium and potassium excretion. Ann Lab Med. 2015;35(2):238–41.
Kyriacou CP, Hastings MH. Circadian clocks: genes, sleep, and cognition. Trends Cogn Sci. 2010;14(6):259–67.
Lamia KA, Storch KF, Weitz CJ. Physiological significance of a peripheral tissue circadian clock. Proc Natl Acad Sci USA. 2008;105(39):15172–7.
Lan R, Geng H, Singha PK, Saikumar P, Bottinger EP, Weinberg JM, Venkatachalam MA. Mitochondrial pathology and glycolytic shift during proximal tubule atrophy after ischemic AKI. J Am Soc Nephrol. 2016;27(11):3356–67.
Lee SG, Lee W, Kwon OH, Kim JH. Association of urinary sodium/creatinine ratio and urinary sodium/specific gravity unit ratio with blood pressure and hypertension: KNHANES 2009–2010. Clin Chim Acta. 2013;424:168–73.
Levi F, Schibler U. Circadian rhythms: mechanisms and therapeutic implications. Annu Rev Pharmacol Toxicol. 2007;47:593–628.
Li H, Durbin R. Fast and accurate short read alignment with Burrows-Wheeler transform. Bioinformatics. 2009;25(14):1754–60.
Lunt SY, Heiden Vander MG. Aerobic glycolysis: meeting the metabolic requirements of cell proliferation. Annu Rev Cell Dev Biol. 2011;27:441–64.
Makrides V, Camargo SM, Verrey F. Transport of amino acids in the kidney. Compr Physiol. 2014;4(1):367–403.
Mann M, Waz W, Poupoulos J, Kadle R, Korn A, Vaughan R, Borowitz D. Urinary sodium to creatinine ratio in healthy infants. Clin Pediatr. 2012;51(9):852–5.
Mohawk JA, Green CB, Takahashi JS. Central and peripheral circadian clocks in mammals. Ann Rev Neurosci. 2012;35:445–62.
Moškon M. CosinorPy: a python package for cosinor-based rhythmometry. BMC Bioinformatics. 2020;21(1):485.
Munn E, Bunning M, Prada S, Bohlen M, Crabbe JC, Wahlsten D. Reversed light-dark cycle and cage enrichment effects on ethanol-induced deficits in motor coordination assessed in inbred mouse strains with a compact battery of refined tests. Behav Brain Res. 2011;224(2):259–71.
Myung J, Wu MY, Lee CY, Rahim AR, Truong VH, Wu D, Piggins HD, Wu MS. The kidney clock contributes to timekeeping by the master circadian Clock. Int J Mol Sci. 2019. https://doi.org/10.3390/ijms20112765.
Nikolaeva S, Pradervand S, Centeno G, Zavadova V, Tokonami N, Maillard M, Bonny O, Firsov D. The circadian clock modulates renal sodium handling. J Am Soc Nephrol. 2012;23(6):1019–26.
Palmieri F. Mitochondrial transporters of the SLC25 family and associated diseases: a review. J Inherit Metab Dis. 2014;37(4):565–75.
Panda S, Antoch MP, Miller BH, Su AI, Schook AB, Straume M, Schultz PG, Kay SA, Takahashi JS, Hogenesch JB. Coordinated transcription of key pathways in the mouse by the circadian clock. Cell. 2002;109(3):307–20.
Pariollaud M, Gibbs JE, Hopwood TW, Brown S, Begley NM, Vonslow R, Poolman T, Guo B, Saer B, Jones DH, et al. Nuclear receptor subfamily 1 group D member 1 regulates circadian activity of nlrp3 inflammasome to reduce the severity of fulminant hepatitis in Mice. J Clin Invest. 2018. https://doi.org/10.1053/j.gastro.2017.12.019.
Pourcet B, Zecchin M, Ferri L, Beauchamp J, Sitaula S, Billon C, Delhaye S, Vanhoutte J, Mayeuf-Louchart A, Thorel Q, et al. The circadian PER2 enhancer nobiletin reverses the deleterious effects of midazolam in myocardial ischemia and reperfusion injury. Gastroenterology. 2018;24(28):3376–83.
Ramanujam M, Wang X, Huang W, Liu Z, Schiffer L, Tao H, Frank D, Rice J, Diamond B, Yu KO, et al. Similarities and differences between selective and nonselective BAFF blockade in murine SLE. J Clin Investig. 2006;116(3):724–34.
Rao MS, Van Vleet TR, Ciurlionis R, Buck WR, Mittelstadt SW, Blomme EAG, Liguori MJ. Comparison of RNA-seq and microarray gene expression platforms for the toxicogenomic evaluation of liver from short-term rat toxicity studies. Front Genet. 2018;9:636.
Reddy AB, O'Neill JS. Healthy clocks, healthy body, healthy mind. Trends Cell Biol. 2010;20(1):36–44.
Richards J, Cheng KY, All S, Skopis G, Jeffers L, Lynch IJ, Wingo CS, Gumz ML. A role for the circadian clock protein Per1 in the regulation of aldosterone levels and renal Na+ retention. Am J Physiol Renal Physiol. 2013;305(12):F1697–704.
Sabio JM, Martinez-Bordonado J, Sánchez-Berná I, Vargas-Hitos JA, Mediavilla JD, Navarrete-Navarrete N, Zamora-Pasadas M, Ruíz ME, Jiménez-Alonso J. Nighttime blood pressure patterns and subclinical atherosclerosis in women with systemic lupus erythematosus. J Rheumatol. 2015;42(12):2310–7.
Saifur Rohman M, Emoto N, Nonaka H, Okura R, Nishimura M, Yagita K, van der Horst GT, Matsuo M, Okamura H, Yokoyama M. Circadian clock genes directly regulate expression of the Na(+)/H(+) exchanger NHE3 in the kidney. Kidney Int. 2005;67(4):1410–9.
Sato F, Otsuka T, Kohsaka A, Le HT, Bhawal UK, Muragaki Y. Smad3 suppresses epithelial cell migration and proliferation via the clock gene Dec1, which negatively regulates the expression of clock genes Dec2 and Per1. Am J Pathol. 2019;189(4):773–83.
Savoia C, Schiffrin EL. Inflammation in hypertension. Curr Opin Nephrol Hypertens. 2006;15(2):152–8.
Schiffer L, Sinha J, Wang X, Huang W, von Gersdorff G, Schiffer M, Madaio MP, Davidson A. Short term administration of costimulatory blockade and cyclophosphamide induces remission of systemic lupus erythematosus nephritis in NZB/W F1 mice by a mechanism downstream of renal immune complex deposition. J Immuno. 2003;171(1):489–97.
Schiffer L, Bethunaickan R, Ramanujam M, Huang W, Schiffer M, Tao H, Madaio MP, Bottinger EP, Davidson A. Activated renal macrophages are markers of disease onset and disease remission in lupus nephritis. J Immuno. 2008;180(3):1938–47.
Smith JA, Stallons LJ, Schnellmann RG. Renal cortical hexokinase and pentose phosphate pathway activation through the EGFR/Akt signaling pathway in endotoxin-induced acute kidney injury. Am J Physiol Renal Physiol. 2014;307(4):F435–44.
Solocinski K, Holzworth M, Wen X, Cheng KY, Lynch IJ, Cain BD, Wingo CS, Gumz ML. Desoxycorticosterone pivalate-salt treatment leads to non-dipping hypertension in Per1 knockout mice. Acta Physiol (oxf). 2017;220(1):72–82.
Stow LR, Gumz ML. The circadian clock in the kidney. J Am Soc Nephrol. 2011;22(4):598–604.
Stujanna EN, Murakoshi N, Tajiri K, Xu D, Kimura T, Qin R, Feng D, Yonebayashi S, Ogura Y, Yamagami F, et al. Rev-erb agonist improves adverse cardiac remodeling and survival in myocardial infarction through an anti-inflammatory mechanism. PLoS ONE. 2017;12(12):e0189330.
Supek F, Bosnjak M, Skunca N, Smuc T. REVIGO summarizes and visualizes long lists of gene ontology terms. PLoS ONE. 2011;6(7):e21800.
Tadic M, Cuspidi C, Pencic B, Mancia G, Grassi G, Kocijancic V, Quarti-Trevano F, Celic V. Impact of different dipping patterns on left atrial function in hypertension. J Hypertens. 2020a;38(11):2245–51.
Tadic M, Cuspidi C, Celic V, Petrovic O, Pencic B, Mancia G, Grassi G, Ivanovic B. The prognostic importance of right ventricular remodeling and the circadian blood pressure pattern on the long-term cardiovascular outcome. J Hypertens. 2020b;38(8):1525–30.
Thaben PF, Westermark PO. Detecting rhythms in time series with RAIN. J Biol Rhythms. 2014;29(6):391–400.
Wang S. REV-ERBalpha integrates colon clock with experimental colitis through regulation of NF-kappaB/NLRP3 axis. Nat Commun. 2018;9(1):4246.
Zhang R, Lahens NF, Ballance HI, Hughes ME, Hogenesch JB. A circadian gene expression atlas in mammals: implications for biology and medicine. Proc Natl Acad Sci USA. 2014;111(45):16219–24.
Zhao S, Fung-Leung WP, Bittner A, Ngo K, Liu X. Comparison of RNA-Seq and microarray in transcriptome profiling of activated T cells. PLoS ONE. 2014;9(1):e78644.
Zhao M, Xing H, Chen M, Dong D, Wu B. Circadian clock-controlled drug metabolism and transport. Xenobiotica. 2020;50(5):495–505.

Publisher's Note

SUPPLEMENTARY FIGURES AND TABLES

Supplementary Figure 1: A. Clustering of 15 samples with both microarray and RNA sequencing data before normalization; **B.** Clustering of 15 samples with both microarray and RNA sequencing data after median centering, quantile normalization and batch correction. The normalized data were segregated by the samples instead of experimental approaches; **C.** Clustering of all samples before normalization; **D.** Clustering of all samples with microarray and/or sequencing data after median centering, quantile normalization and batch correction shows clear separation between young and nephritic mice and between NZB/W and C57BL/6 strains. **E.** Correlation of microarray with RNASeq data for the 15 samples that were analyzed on both platforms.

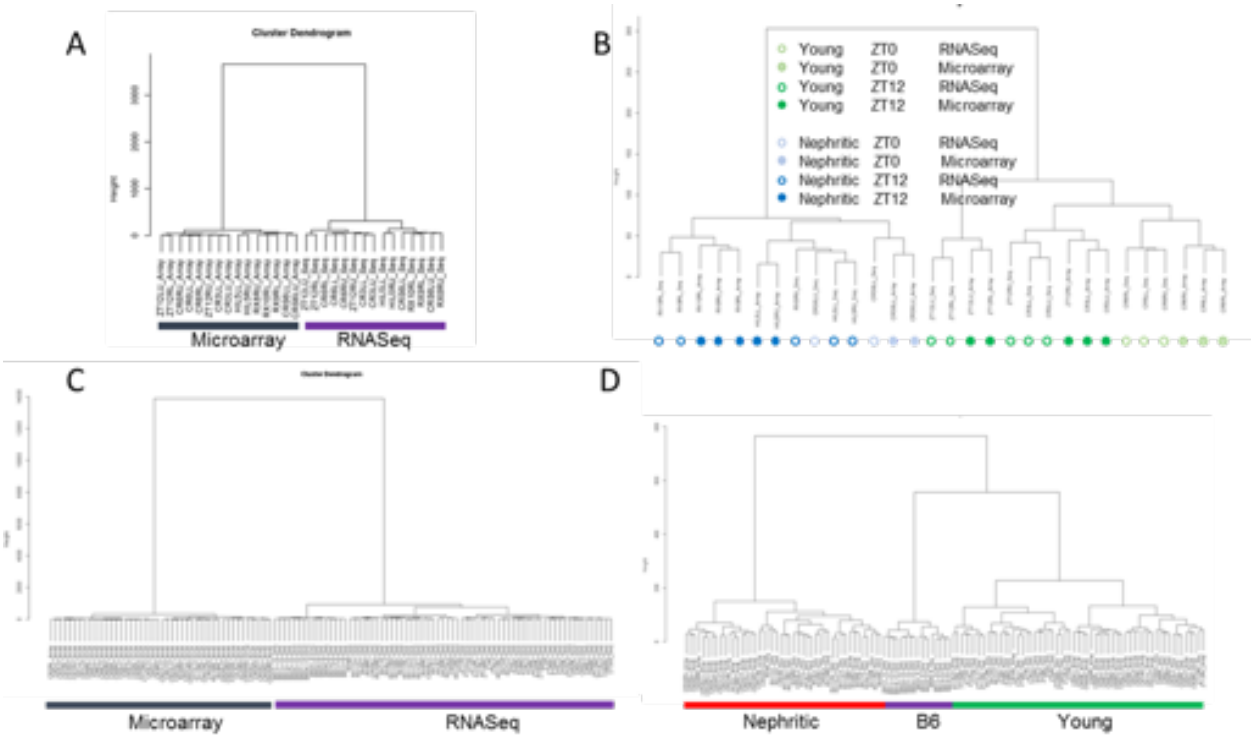

E

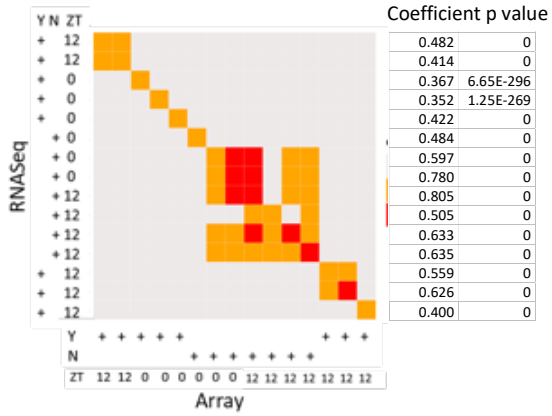

Coefficient p value

0.482	0
0.414	0
0.367	6.65E-296
0.352	1.25E-269
0.422	0
0.484	0
0.597	0
0.780	0
0.805	0
0.505	0
0.633	0
0.635	0
0.559	0
0.626	0
0.400	0

Supplementary Figure 2: **A:** Heat maps of genes that passed the RAIN test for circadian rhythm from young (upper panel) and nephritic (lower panel) NZB/W kidneys show the time of peak expression of each set of genes. Normalized data are shown and where samples were repeated only the sample analyzed by microarray analysis is shown. **B, C**: Expression of representative inflammatory genes (B) and genes reflecting injury of renal stromal cells (C) in young (grey symbols) and nephritic mice (black circles) and aged mice with induced remission (grey squares) confirm the clinical status of the mice. Statistics performed using Kruskal Wallis ANOVA followed by adjustment for multiple comparisons using Dunn's test. * $p<0.05$: ** $p<0.01$, *** $p<0.001$, **** $p<0.0001$.

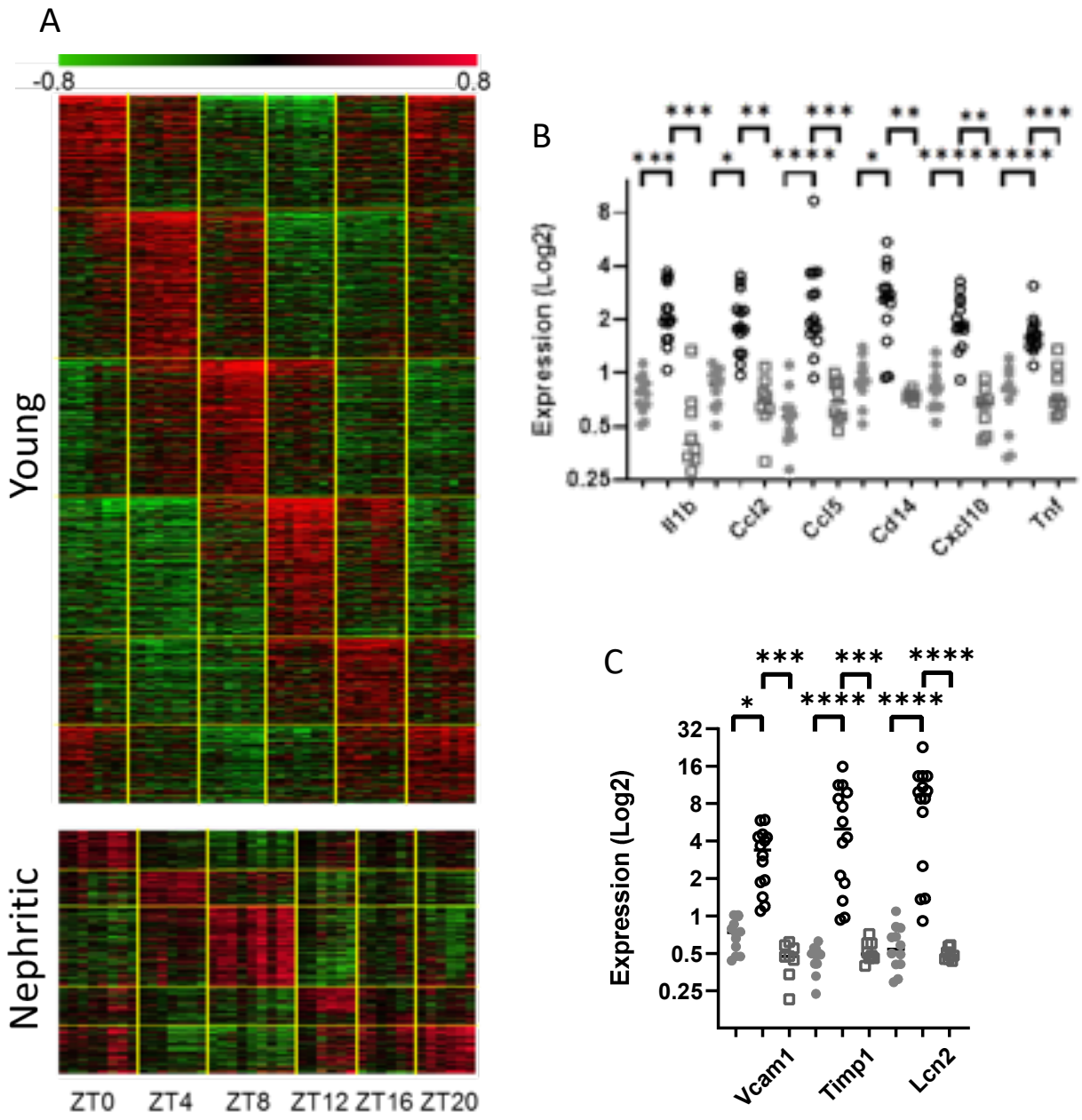

Supplementary Figure 3: A. PCR confirmation of a subset of genes, including several master transcriptional regulators of circadian rhythm, from young (black) and nephritic (grey) NZB/W kidneys. **B.** Heatmap of circadian genes in young and nephritic mice. Samples are the same as those shown in Figure 1. Each symbol represents an individual mouse. **C.** Sleep-wake cycles in young and nephritic mice observed over a 24 hour period. Data is displayed as the proportion of the time that the mice were active in each 10 minute-interval where 1=100%. D: Analysis of percent active time during the light and dark cycles. Statistics performed using Kruskal Wallis ANOVA followed by adjustment for multiple comparisons using Dunn's test. **** $p<0.0001$.

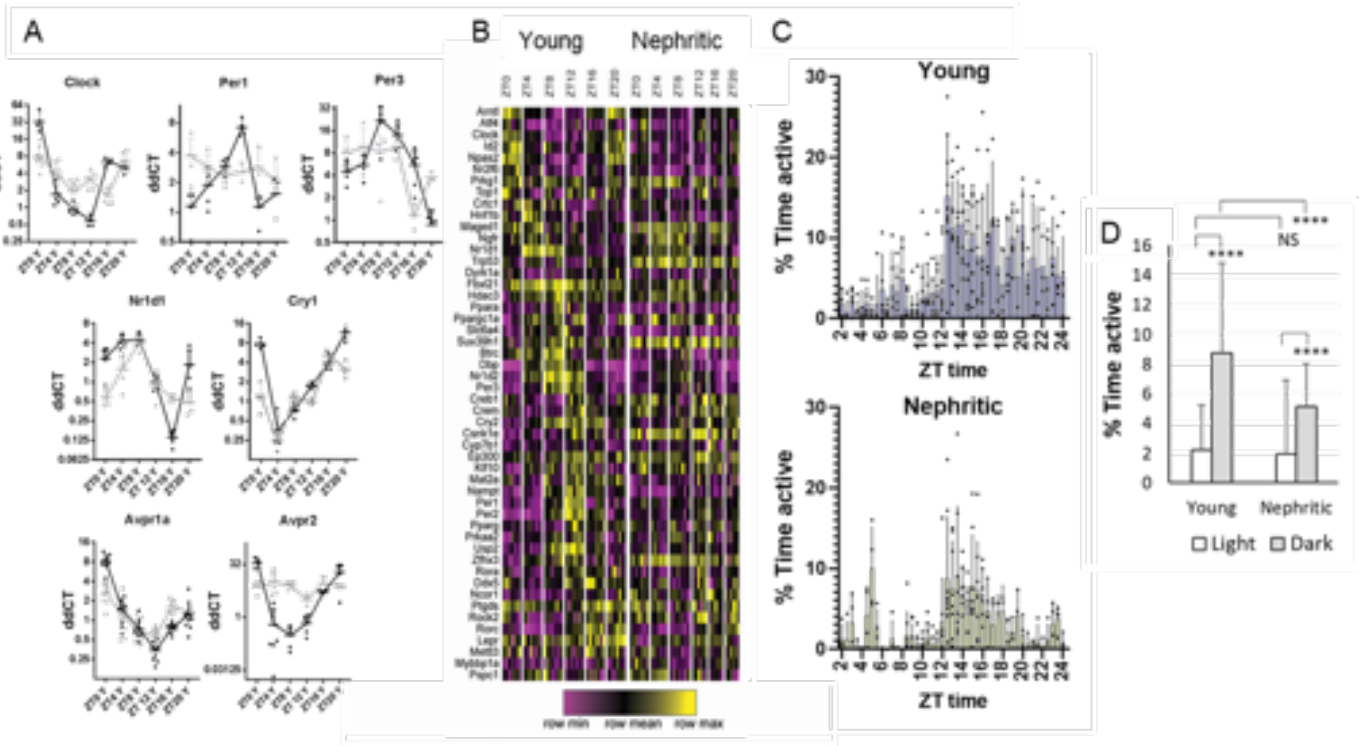

Supplementary Figure 4: REVIGO analyses of Genes passing the RAIN test for circadian rhythm in young (upper box in each panel) and nephritic (lower box in each panel) NZB/W kidneys at ZT0 (**A**), ZT4 (**B**), ZT8 (**C**), ZT12 (**D**), ZT16 (**E**) and ZT20 (**F**).

Supplementary Figure 4A: ZT0

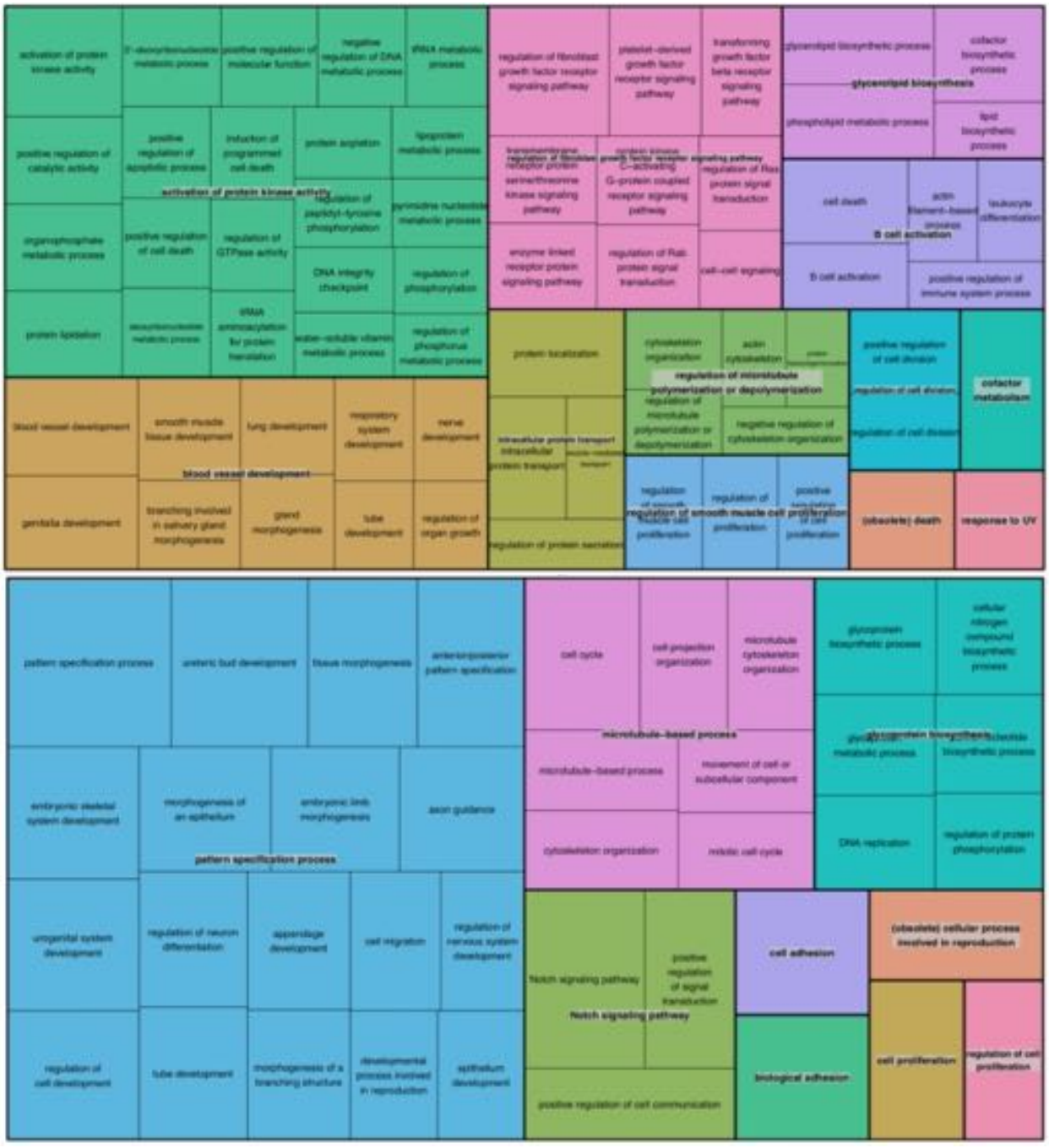

Supplementary Figure 4B: ZT4

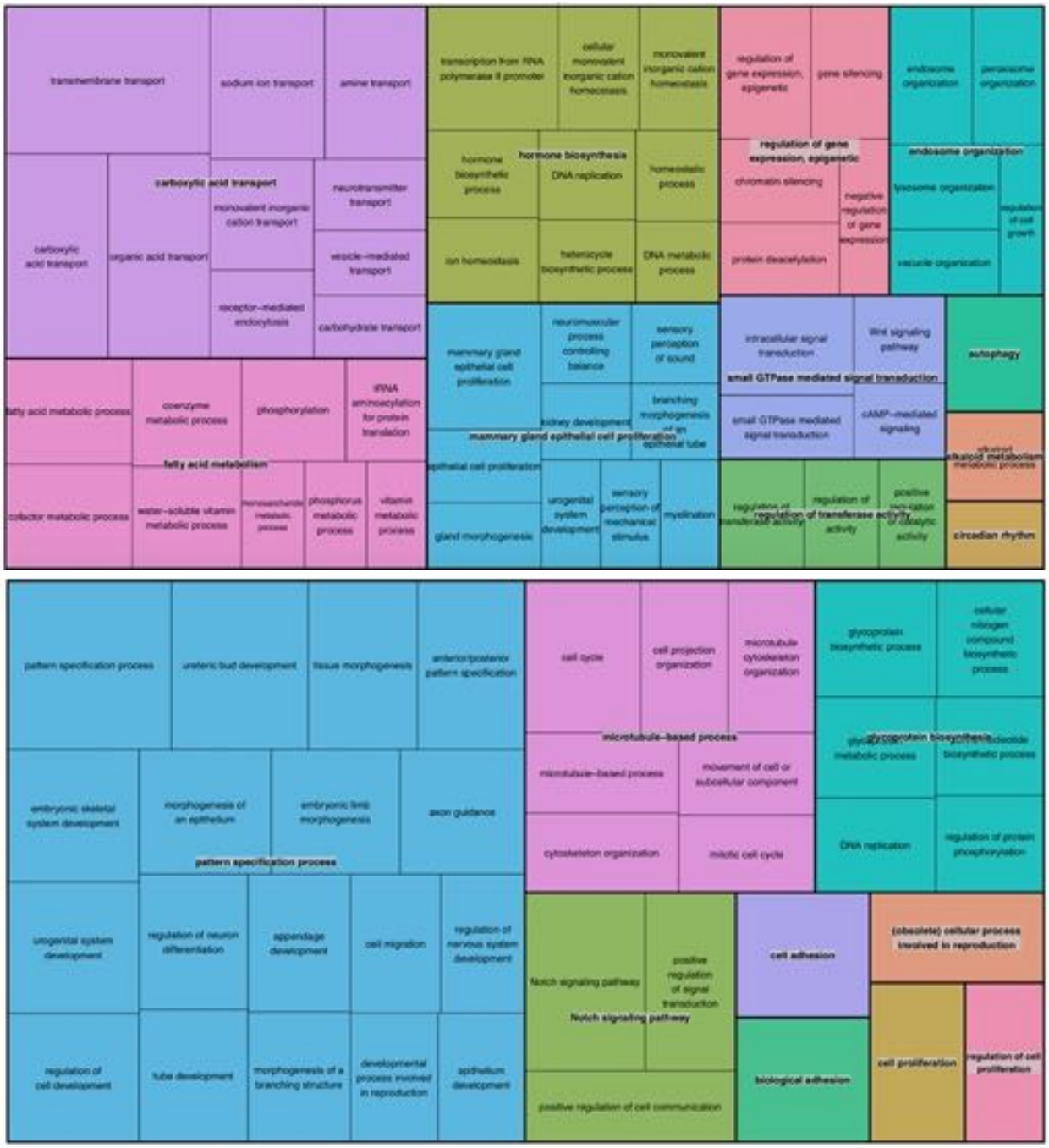

Supplementary Figure 4C: ZT8

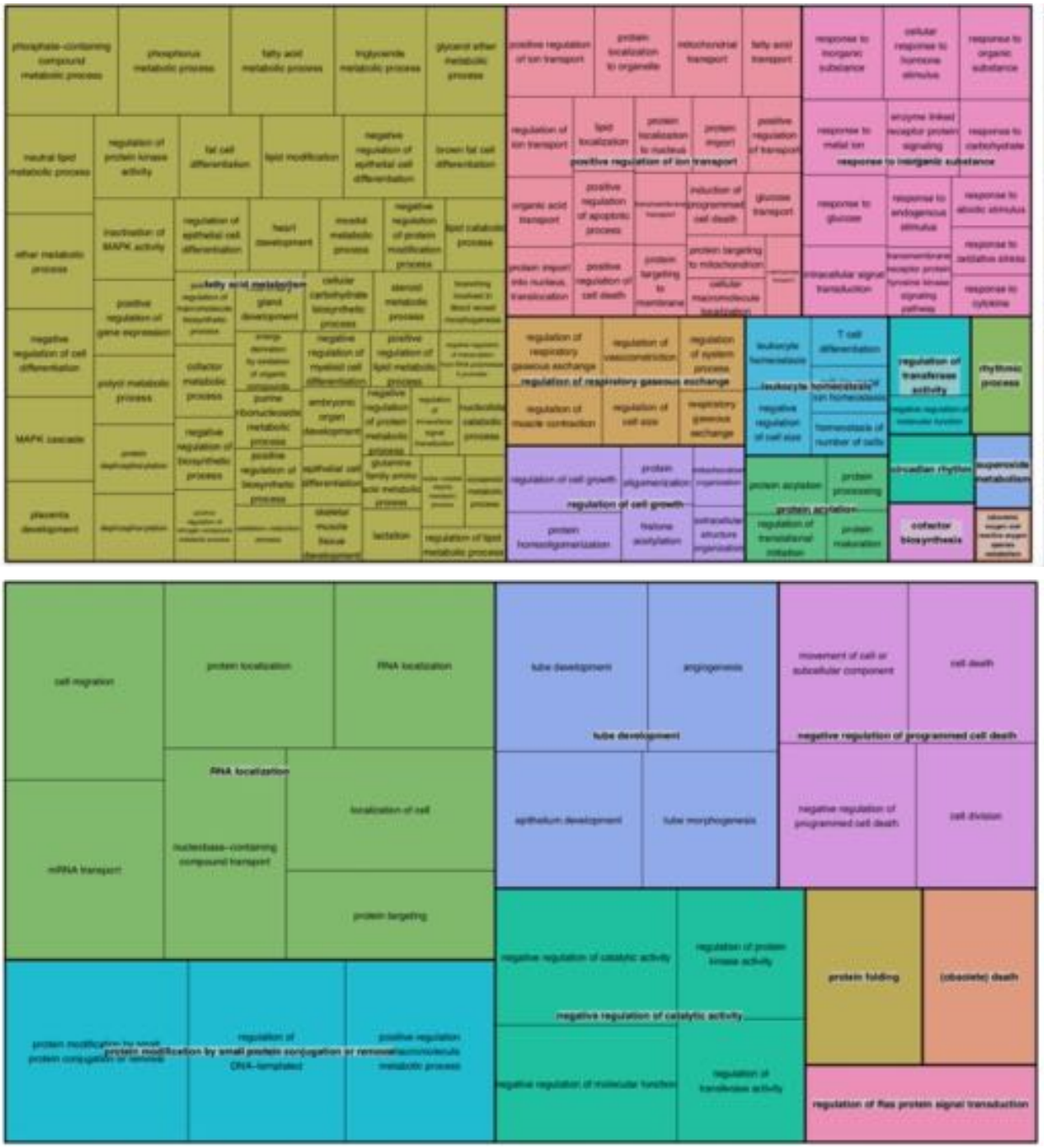

Supplementary Figure 4D: ZT12

Supplementary Figure 4E: ZT16

Supplementary Figure 4F: ZT20

Supplementary Figure 5: Urine sodium (A, B), potassium (C, D) and creatinine (E) in young (grey circles) and nephritic (black circles) NZB/W F1 mice. Each symbol represents an individual mouse. Statistics performed using Kruskal Wallis ANOVA followed by adjustment for multiple comparisons using Dunn's test. * $p<0.05$.

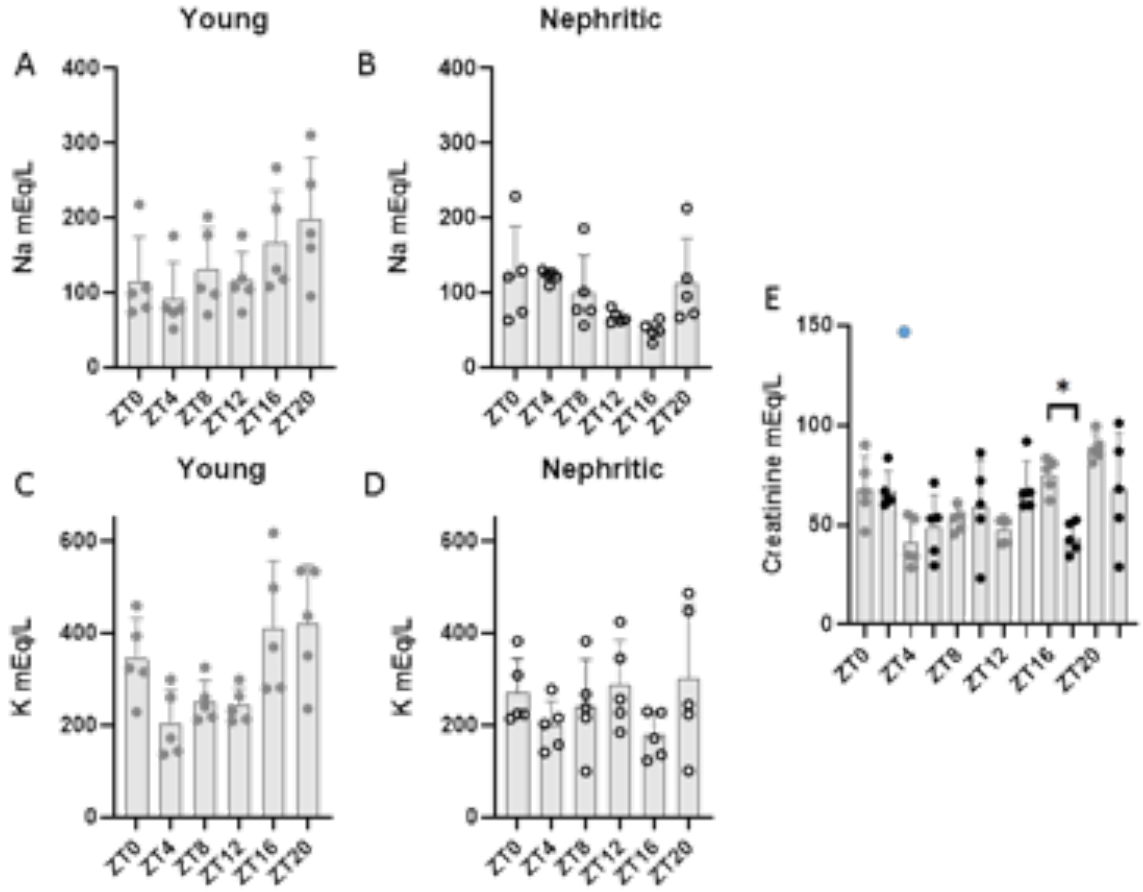

Supplementary Figure 6: Changes in serum glucose (**A, B**) and urine glucose (**C**) at the indicated ZT times in young (Y - grey) and nephritic (N – black circles) NZB/W mice.

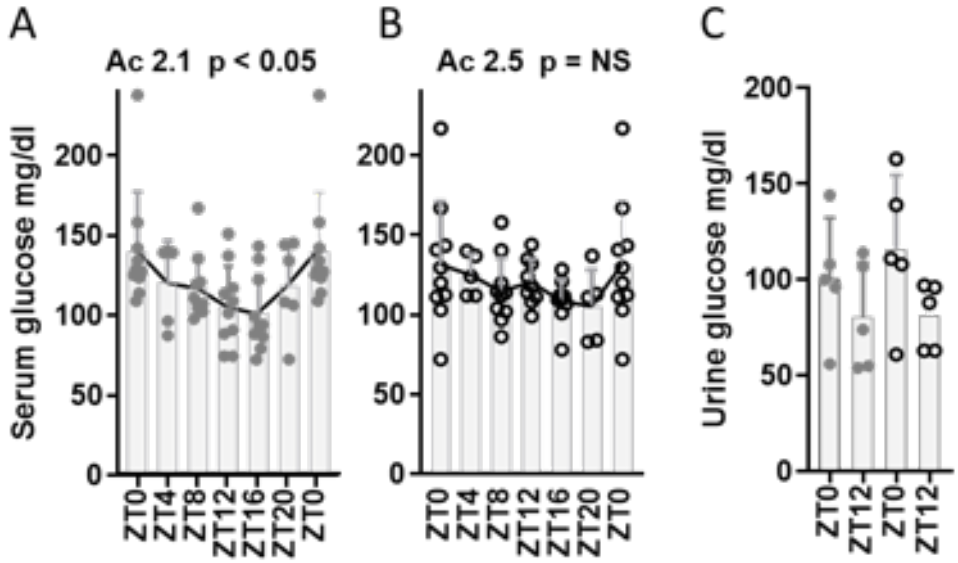

Supplementary Figure 7: Pathway analyses of circadian genes that corrected or did not correct after remission induction. A-C: Heatmaps of expression of genes related to circadian rhythm (**A**), fatty acid metabolism (**B**) and blood pressure regulation (**C**) from individual remission mice at ZT0 and ZT12 compared with young and nephritic mice. **D-G**. Major pathways identified by Ingenuity Pathway analysis that either corrected (green) or failed to correct (blue) after remission induction.

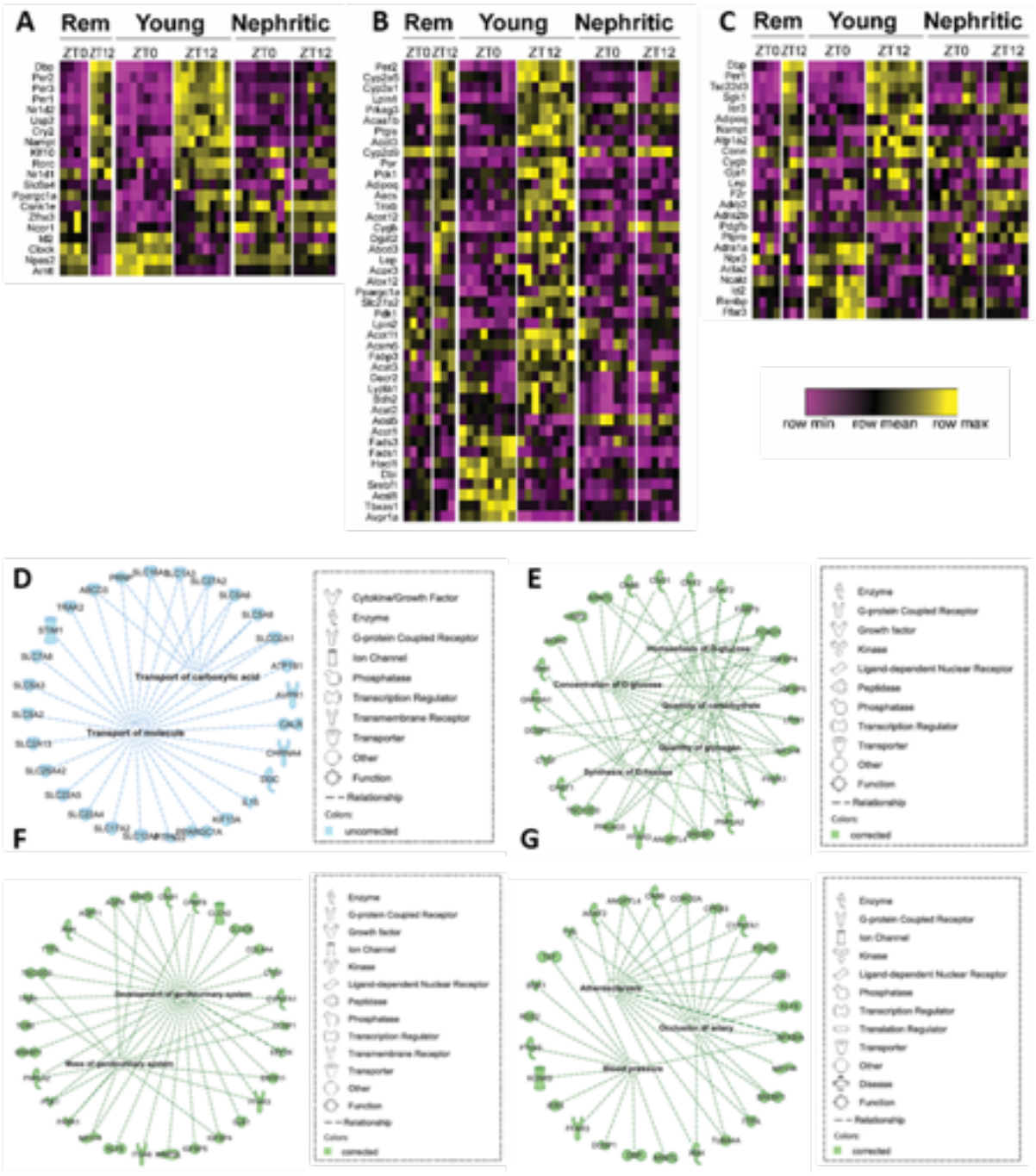

SUPPLEMENTARY TABLES

Supplementary Table 1: Samples used for gene profiling								
	Time	**Unique samples**	**Microarray**		**RNASeq**		**Both**	
			Set 1	**Set 2**	**Set 1**	**Set 2**	**Set 1**	**Set 2**
NZB/W young	ZT0	8	4		3	4	3	
	ZT4	8	4			4		
	ZT8	8	4			4		
	ZT12	7	3	3	3	4	2	3
	ZT16	8	4			4		
	ZT20	8	4			4		
Total		**47**	**23**			**24**		
NZB/W Nephritic	ZT0	7	3		3	4	2	
	ZT4	7	3			4		
	ZT8	9	5			4		
	ZT12	6	2	3	2	4	2	3
	ZT16	6	3			3		
	ZT20	6	3			3		
Total		**41**	**19**	**3**	**5**	**22**		
C57BL/6 8 weeks	ZT0	4				4		
	ZT12	4				4		
C57BL/6 36 weeks	ZT0	4				4		
	ZT12	4				4		
Total		**16**				**16**		
NZB/W Remission	ZT0	3				3		
	ZT12	4				4		
Total		**7**				**7**		

Supplementary Table 2: List of diurnally regulated genes involved in key metabolic and homeostatic functions

Category	Symbol	RefSeq	Name	UniGene_ID
Blood Pressure	Avpr1a	NM_016847	arginine vasopressin receptor 1A	Mm.4351
Blood Pressure	Ncald	NM_001170867	neurocalcin delta	Mm.283370
Blood Pressure	Adra1a	NM_013461	adrenergic receptor, alpha 1a	Mm.57064
Blood Pressure	Npr3	NM_008728	natriuretic peptide receptor 3	Mm.25259
Blood Pressure	Renbp	NM_001164704	renin binding protein	Mm.236969
Blood Pressure	Id2	NM_010496	inhibitor of DNA binding 2	Mm.34871
Blood Pressure	Ramp2	NM_019444	receptor (calcitonin) activity modifying protein 2	Mm.260698
Blood Pressure	P2rx1	NM_008771	purinergic receptor P2X, ligand-gated ion channel, 1	Mm.25722
Blood Pressure	Hsd11b2	NM_008289	hydroxysteroid 11-beta dehydrogenase 2	Mm.5079
Blood Pressure	Kl	NM_013823	klotho	Mm.6500
Blood Pressure	Kcnj1	NM_001168354	potassium inwardly-rectifying channel, subfamily J, member 1	Mm.390168
Blood Pressure	Ffar3	NM_001033316	free fatty acid receptor 3	Mm.291167
Blood Pressure	Pdgfb	NM_011057	platelet derived growth factor, B polypeptide	Mm.144089
Blood Pressure	Ptpro	NM_011216	protein tyrosine phosphatase, receptor type, O	Mm.186361
Blood Pressure	Sucnr1	NM_032400	succinate receptor 1	Mm.125110
Blood Pressure	Ang	NM_001161731	angiogenin, ribonuclease, RNase A family, 5	Mm.202665
Blood Pressure	Eng	NM_007932	endoglin	Mm.225297
Blood Pressure	Ece1	NM_199307	endothelin converting enzyme 1	Mm.401062
Blood Pressure	P2rx1	NM_008771	purinergic receptor P2X, ligand-gated ion channel, 1	Mm.25722
Blood Pressure	Smtn	NM_001284428	smoothelin	Mm.188516
Blood Pressure	Agtr1a	NM_177322	angiotensin II receptor, type 1a	Mm.35062
Blood Pressure	Adrb2	NM_007420	adrenergic receptor, beta 2	Mm.5598
Blood Pressure	Scnn1b	NM_011325	sodium channel, nonvoltage-gated 1 beta	Mm.7709
Blood Pressure	Ace2	NM_027286	angiotensin I converting enzyme (peptidyl-dipeptidase A) 2	Mm.13451
Blood Pressure	Add1	NM_001331087	adducin 1 (alpha)	Mm.289106

Blood Pressure	Ppara	NM_001113418	peroxisome proliferator activated receptor alpha	Mm.212789
Blood Pressure	Sucnr1	NM_032400	succinate receptor 1	Mm.125110
Blood Pressure	Dbp	NM_016974	D site albumin promoter binding protein	Mm.24222
Blood Pressure	Tsc22d3	NM_010286	TSC22 domain family, member 3	Mm.22216
Blood Pressure	Sgk1	NM_001161848	serum/glucocorticoid regulated kinase 1	Mm.28405
Blood Pressure	Nampt	NM_021524	nicotinamide phosphoribosyltransferase	Mm.202727
Blood Pressure	Prcp	NM_028243	prolylcarboxypeptidase (angiotensinase C)	Mm.389969
Blood Pressure	Per1	NM_011065	period circadian clock 1	Mm.7373
Blood Pressure	Cygb	NM_030206	cytoglobin	Mm.34598
Blood Pressure	Gja1	NM_010288	gap junction protein, alpha 1	Mm.378921
Blood Pressure	Pparg	NM_001308352	peroxisome proliferator activated receptor gamma	Mm.3020
Blood Pressure	Mecp2	NM_010788	methyl CpG binding protein 2	Mm.131408
Blood Pressure	Nedd4l	NM_031881	neural precursor cell expressed, developmentally down-regulated gene 4-like	Mm.98668
Blood Pressure	Adra2b	NM_009633	adrenergic receptor, alpha 2b	Mm.347390
Blood Pressure	Ier3	NM_133662	immediate early response 3	Mm.25613
Blood Pressure	Corin	NM_001122756	corin	Mm.332425
Blood Pressure	Aoc3	NM_009675	amine oxidase, copper containing 3	Mm.67281
Blood Pressure	Atp1a2	NM_178405	ATPase, Na+/K+ transporting, alpha 2 polypeptide	Mm.207432
Blood Pressure	Adipoq	NM_009605	adiponectin, C1Q and collagen domain containing	Mm.3969
Blood Pressure	F2r	NM_010169	coagulation factor II (thrombin) receptor	Mm.24816
Blood Pressure	Klk1	NM_001320331	kallikrein 1	Mm.142722
Blood Pressure	Lep	NM_008493	leptin	Mm.277072
Blood Pressure	G6pdx	NM_008062	glucose-6-phosphate dehydrogenase X-linked	Mm.27210
Blood Pressure	Gnas	NM_001077510	GNAS (guanine nucleotide binding protein, alpha stimulating) complex locus	Mm.125770
Blood Pressure	Hsd11b1	NM_008288	hydroxysteroid 11-beta dehydrogenase 1	Mm.28328

Blood Pressure	Sod2	NM_013671	superoxide dismutase 2, mitochondrial	Mm.290876
Blood Pressure	Npy1r	NM_010934	neuropeptide Y receptor Y1	Mm.5112
Blood Pressure	Acta2	NM_007392	actin, alpha 2, smooth muscle, aorta	Mm.213025
Blood Pressure	Ephx2	NM_001271403	epoxide hydrolase 2, cytoplasmic	Mm.15295
Blood Pressure	Nr2f2	NM_183261	nuclear receptor subfamily 2, group F, member 2	Mm.158143
Blood Pressure	Adra1a	NM_013461	adrenergic receptor, alpha 1a	Mm.57064
Blood Pressure	Lep	NM_008493	leptin	Mm.277072
Blood Pressure	Sgk1	NM_001161848	serum/glucocorticoid regulated kinase 1	Mm.28405
Blood Pressure	Avpr1a	NM_016847	arginine vasopressin receptor 1A	Mm.4351
Blood Pressure	Tsc22d3	NM_010286	TSC22 domain family, member 3	Mm.22216
Blood Pressure	Rasl10b	NM_001013386	RAS-like, family 10, member B	Mm.66275
Blood Pressure	Cyp3a11	NM_007818	cytochrome P450, family 3, subfamily a, polypeptide 11	Mm.332844
Circadian Rhythm	Npas2	NM_008719	neuronal PAS domain protein 2	Mm.2380
Circadian Rhythm	Clock	NM_001289826	circadian locomotor output cycles kaput	Mm.3552
Circadian Rhythm	Arntl	NM_007489	aryl hydrocarbon receptor nuclear translocator-like	Mm.33970
Circadian Rhythm	Nr2f6	NM_010150	nuclear receptor subfamily 2, group F, member 6	Mm.28989
Circadian Rhythm	Id2	NM_010496	inhibitor of DNA binding 2	Mm.34871
Circadian Rhythm	Atf4	NM_009716	activating transcription factor 4	Mm.641
Circadian Rhythm	Prkg1	NM_011160	protein kinase, cGMP-dependent, type I	Mm.381170
Circadian Rhythm	Top1	NM_009408	topoisomerase (DNA) I	Mm.217233
Circadian Rhythm	Nr1d1	NM_145434	nuclear receptor subfamily 1, group D, member 1	Mm.390397
Circadian Rhythm	Maged1	NM_019791	melanoma antigen, family D, 1	Mm.27578
Circadian Rhythm	Hnf1b	NM_001291268	HNF1 homeobox B	Mm.7226
Circadian Rhythm	Ngfr	NM_033217	nerve growth factor receptor (TNFR superfamily, member 16)	Mm.283893
Circadian Rhythm	Crtc1	NM_001004062	CREB regulated transcription coactivator 1	Mm.227767

Circadian Rhythm	Trp53	NM_001127233	transformation related protein 53	Mm.222
Circadian Rhythm	Pspc1	NM_025682	paraspeckle protein 1	Mm.20129
Circadian Rhythm	Slc6a4	NM_010484	solute carrier family 6 (neurotransmitter transporter, serotonin), member 4	Mm.300318
Circadian Rhythm	Fbxl21	NM_178674	F-box and leucine-rich repeat protein 21	Mm.233904
Circadian Rhythm	Hdac3	NM_010411	histone deacetylase 3	Mm.20521
Circadian Rhythm	Ppara	NM_001113418	peroxisome proliferator activated receptor alpha	Mm.212789
Circadian Rhythm	Suv39h1	NM_011514	suppressor of variegation 3-9 homolog 1 (Drosophila)	Mm.9244
Circadian Rhythm	Ppargc1a	NR_132764	peroxisome proliferative activated receptor, gamma, coactivator 1 alpha	Mm.259072
Circadian Rhythm	Nr1d1	NM_145434	nuclear receptor subfamily 1, group D, member 1	Mm.390397
Circadian Rhythm	Nr1d2	NM_011584	nuclear receptor subfamily 1, group D, member 2	Mm.26587
Circadian Rhythm	Per3	NM_011067	period circadian clock 3	Mm.121361
Circadian Rhythm	Dbp	NM_016974	D site albumin promoter binding protein	Mm.24222
Circadian Rhythm	Btrc	NM_001286466	beta-transducin repeat containing protein	Mm.119717
Circadian Rhythm	Nampt	NM_021524	nicotinamide phosphoribosyltransferase	Mm.202727
Circadian Rhythm	Per2	NM_011066	period circadian clock 2	Mm.482463
Circadian Rhythm	Usp2	NM_198092	ubiquitin specific peptidase 2	Mm.272770
Circadian Rhythm	Cry2	NM_009963	cryptochrome 2 (photolyase-like)	Mm.254181
Circadian Rhythm	Csnk1e	NM_001289899	casein kinase 1, epsilon	Mm.30199
Circadian Rhythm	Per1	NM_011065	period circadian clock 1	Mm.7373
Circadian Rhythm	Klf10	NM_013692	Kruppel-like factor 10	Mm.4292
Circadian Rhythm	Crem	NM_001110854	cAMP responsive element modulator	Mm.5244

Circadian Rhythm	Pparg	NM_001308352	peroxisome proliferator activated receptor gamma	Mm.3020
Circadian Rhythm	Zfhx3	NM_007496	zinc finger homeobox 3	Mm.416972
Circadian Rhythm	Ep300	NM_177821	E1A binding protein p300	Mm.258397
Circadian Rhythm	Prkaa2	NM_178143	protein kinase, AMP-activated, alpha 2 catalytic subunit	Mm.48638
Circadian Rhythm	Mat2a	NM_145569	methionine adenosyltransferase II, alpha	Mm.29815
Circadian Rhythm	Cyp7b1	NM_007825	cytochrome P450, family 7, subfamily b, polypeptide 1	Mm.316000
Circadian Rhythm	Creb1	NM_001037726	cAMP responsive element binding protein 1	Mm.422634
Circadian Rhythm	Lepr	NM_001122899	leptin receptor	Mm.259282
Circadian Rhythm	Clock	NM_001289826	circadian locomotor output cycles kaput	Mm.3552
Circadian Rhythm	Rock2	NM_009072	Rho-associated coiled-coil containing protein kinase 2	Mm.276024
Circadian Rhythm	Rora	NM_013646	RAR-related orphan receptor alpha	Mm.378450
Circadian Rhythm	Rorc	NM_011281	RAR-related orphan receptor gamma	Mm.4372
Circadian Rhythm	Ddx5	NM_007840	DEAD (Asp-Glu-Ala-Asp) box polypeptide 5	Mm.491096
Circadian Rhythm	Ncor1	NM_011308	nuclear receptor co-repressor 1	Mm.271814
Circadian Rhythm	Ptgds	NM_008963	prostaglandin D2 synthase (brain)	Mm.1008
Circadian Rhythm	Rock2	NM_009072	Rho-associated coiled-coil containing protein kinase 2	Mm.276024
Circadian Rhythm	Dyrk1a	NM_007890	dual-specificity tyrosine-(Y)-phosphorylation regulated kinase 1a	Mm.310973
Circadian Rhythm	Rorc	NM_011281	RAR-related orphan receptor gamma	Mm.4372
Circadian Rhythm	Arntl	NM_007489	aryl hydrocarbon receptor nuclear translocator-like	Mm.33970
Circadian Rhythm	Npas2	NM_008719	neuronal PAS domain protein 2	Mm.2380
Circadian Rhythm	Mybbp1a	NM_016776	MYB binding protein (P160) 1a	Mm.147946

Circadian Rhythm	Mettl3	NM_019721	methyltransferase like 3	Mm.271759
Fatty Acid	Avpr1a	NM_016847	arginine vasopressin receptor 1A	Mm.4351
Fatty Acid	Acsl1	NM_007981	acyl-CoA synthetase long-chain family member 1	Mm.210323
Fatty Acid	Tbxas1	NM_011539	thromboxane A synthase 1, platelet	Mm.4054
Fatty Acid	Dbi	NM_007830	diazepam binding inhibitor	Mm.2785
Fatty Acid	Fads3	NM_021890	fatty acid desaturase 3	Mm.253875
Fatty Acid	Hacl1	NM_019975	2-hydroxyacyl-CoA lyase 1	Mm.38887
Fatty Acid	Sgpl1	NM_001316673	sphingosine phosphate lyase 1	Mm.412319
Fatty Acid	Prkaca	NM_001277898	protein kinase, cAMP dependent, catalytic, alpha	Mm.19111
Fatty Acid	Prkab2	NM_182997	protein kinase, AMP-activated, beta 2 non-catalytic subunit	Mm.31175
Fatty Acid	C1qtnf2	NM_026979	C1q and tumor necrosis factor related protein 2	Mm.390374
Fatty Acid	Acsl5	NM_027976	acyl-CoA synthetase long-chain family member 5	Mm.292056
Fatty Acid	Acss1	NM_080575	acyl-CoA synthetase short-chain family member 1	Mm.7044
Fatty Acid	Srebf2	NM_033218	sterol regulatory element binding factor 2	Mm.9002
Fatty Acid	Eif6	NM_010579	eukaryotic translation initiation factor 6	Mm.271674
Fatty Acid	Prkab1	NM_031869	protein kinase, AMP-activated, beta 1 non-catalytic subunit	Mm.458152
Fatty Acid	Ptges	NM_022415	prostaglandin E synthase	Mm.28768
Fatty Acid	Alkbh7	NM_025538	alkB homolog 7	Mm.196150
Fatty Acid	Lias	NM_001310612	lipoic acid synthetase	Mm.195776
Fatty Acid	Ggt5	NM_011820	gamma-glutamyltransferase 5	Mm.257927
Fatty Acid	Degs1	NM_007853	delta(4)-desaturase, sphingolipid 1	Mm.29648
Fatty Acid	Acaa1a	NM_130864	acetyl-Coenzyme A acyltransferase 1A	Mm.205266
Fatty Acid	Acsm5	NM_178758	acyl-CoA synthetase medium-chain family member 5	Mm.185183
Fatty Acid	Fabp3	NM_010174	fatty acid binding protein 3, muscle and heart	Mm.388886
Fatty Acid	Mapk14	NM_001168508	mitogen-activated protein kinase 14	Mm.311337

Fatty Acid	Cyp2s1	NM_028775	cytochrome P450, family 2, subfamily s, polypeptide 1	Mm.275188
Fatty Acid	Acot3	NM_134246	acyl-CoA thioesterase 3	Mm.202331
Fatty Acid	Prkag2	NM_001170556	protein kinase, AMP-activated, gamma 2 non-catalytic subunit	Mm.33649
Fatty Acid	Mlycd	NM_019966	malonyl-CoA decarboxylase	Mm.423037
Fatty Acid	Acot12	NM_028790	acyl-CoA thioesterase 12	Mm.275963
Fatty Acid	Bdh2	NM_027208	3-hydroxybutyrate dehydrogenase, type 2	Mm.45121
Fatty Acid	Cryl1	NM_030004	crystallin, lambda 1	Mm.25539
Fatty Acid	Prkacb	NM_001164198	protein kinase, cAMP dependent, catalytic, beta	Mm.16766
Fatty Acid	Nr1h2	NM_001285518	nuclear receptor subfamily 1, group H, member 2	Mm.968
Fatty Acid	Erlin1	NM_145502	ER lipid raft associated 1	Mm.279865
Fatty Acid	Ppara	NM_001113418	peroxisome proliferator activated receptor alpha	Mm.212789
Fatty Acid	Ppargc1a	NR_132764	peroxisome proliferative activated receptor, gamma, coactivator 1 alpha	Mm.259072
Fatty Acid	Pdk2	NM_133667	pyruvate dehydrogenase kinase, isoenzyme 2	Mm.29768
Fatty Acid	Fads1	NM_146094	fatty acid desaturase 1	Mm.30158
Fatty Acid	Degs1	NM_007853	delta(4)-desaturase, sphingolipid 1	Mm.29648
Fatty Acid	Tbxas1	NM_011539	thromboxane A synthase 1, platelet	Mm.4054
Fatty Acid	Fabp5	NM_001272097	fatty acid binding protein 5, epidermal	Mm.741
Fatty Acid	Thnsl2	NM_001033929	threonine synthase-like 2 (bacterial)	Mm.37547
Fatty Acid	Slc27a5	NM_009512	solute carrier family 27 (fatty acid transporter), member 5	Mm.10984
Fatty Acid	Cyp2c70	NM_145499	cytochrome P450, family 2, subfamily c, polypeptide 70	Mm.29119
Fatty Acid	Apoa2	NR_131173	apolipoprotein A-II	Mm.389209
Fatty Acid	Per2	NM_011066	period circadian clock 2	Mm.482463
Fatty Acid	Por	NM_008898	P450 (cytochrome) oxidoreductase	Mm.3863
Fatty Acid	Cyp2e1	NM_021282	cytochrome P450, family 2, subfamily e, polypeptide 1	Mm.21758
Fatty Acid	Cpt2	NM_009949	carnitine palmitoyltransferase 2	Mm.307620
Fatty Acid	Lpin1	NM_015763	lipin 1	Mm.153625

Fatty Acid	Dgat2	NM_026384	diacylglycerol O-acyltransferase 2	Mm.180189
Fatty Acid	Abcd3	NM_008991	ATP-binding cassette, sub-family D (ALD), member 3	Mm.399042
Fatty Acid	Acnat2	NM_145368	acyl-coenzyme A amino acid N-acyltransferase 2	Mm.35071
Fatty Acid	Aacs	NM_030210	acetoacetyl-CoA synthetase	Mm.431573
Fatty Acid	Tnxb	NM_031176	tenascin XB	Mm.290527
Fatty Acid	Cygb	NM_030206	cytoglobin	Mm.34598
Fatty Acid	Prkag3	NM_153744	protein kinase, AMP-activated, gamma 3 non-catatlytic subunit	Mm.166501
Fatty Acid	Pparg	NM_001308352	peroxisome proliferator activated receptor gamma	Mm.3020
Fatty Acid	Pdk1	NM_172665	pyruvate dehydrogenase kinase, isoenzyme 1	Mm.34411
Fatty Acid	Adipor2	NM_197985	adiponectin receptor 2	Mm.291826
Fatty Acid	Ptgis	NM_008968	prostaglandin I2 (prostacyclin) synthase	Mm.2339
Fatty Acid	Pck1	NM_011044	phosphoenolpyruvate carboxykinase 1, cytosolic	Mm.266867
Fatty Acid	Acaa1b	NM_146230	acetyl-Coenzyme A acyltransferase 1B	Mm.379402
Fatty Acid	Slc27a2	NM_011978	solute carrier family 27 (fatty acid transporter), member 2	Mm.290044
Fatty Acid	Lpin3	NM_022883	lipin 3	Mm.292111
Fatty Acid	Decr2	NM_011933	2-4-dienoyl-Coenzyme A reductase 2, peroxisomal	Mm.292869
Fatty Acid	Hsd17b4	NM_008292	hydroxysteroid (17-beta) dehydrogenase 4	Mm.277857
Fatty Acid	Pnpla8	NM_026164	patatin-like phospholipase domain containing 8	Mm.54126
Fatty Acid	Decr1	NM_026172	2,4-dienoyl CoA reductase 1, mitochondrial	Mm.393293
Fatty Acid	Lpin2	NM_001164885	lipin 2	Mm.227924
Fatty Acid	Asah2	NM_018830	N-acylsphingosine amidohydrolase 2	Mm.491229
Fatty Acid	Acat2	NM_009338	acetyl-Coenzyme A acetyltransferase 2	Mm.439711
Fatty Acid	Prkaa2	NM_178143	protein kinase, AMP-activated, alpha 2 catalytic subunit	Mm.48638
Fatty Acid	Alox12	NM_001331118	arachidonate 12-lipoxygenase	Mm.12286
Fatty Acid	Acot11	NM_001347159	acyl-CoA thioesterase 11	Mm.222956

Fatty Acid	Adipoq	NM_009605	adiponectin, C1Q and collagen domain containing	Mm.3969
Fatty Acid	Cav1	NM_007616	caveolin 1, caveolae protein	Mm.28278
Fatty Acid	Sesn2	NM_144907	sestrin 2	Mm.23608
Fatty Acid	Acox3	NM_030721	acyl-Coenzyme A oxidase 3, pristanoyl	Mm.291503
Fatty Acid	Cyp2a5	NM_007812	cytochrome P450, family 2, subfamily a, polypeptide 5	Mm.389848
Fatty Acid	Slc45a3	NM_145977	solute carrier family 45, member 3	Mm.200307
Fatty Acid	Acat3	NM_153151	acetyl-Coenzyme A acetyltransferase 3	Mm.490312
Fatty Acid	Nr1h3	NM_013839	nuclear receptor subfamily 1, group H, member 3	Mm.22690
Fatty Acid	Elovl5	NM_134255	ELOVL family member 5, elongation of long chain fatty acids (yeast)	Mm.430736
Fatty Acid	Srebf1	NM_011480	sterol regulatory element binding transcription factor 1	Mm.278701
Fatty Acid	Lep	NM_008493	leptin	Mm.277072
Fatty Acid	Them4	NM_029431	thioesterase superfamily member 4	Mm.45092
Fatty Acid	Crat	NM_007760	carnitine acetyltransferase	Mm.20396
Fatty Acid	Cyp2d9	NM_010006	cytochrome P450, family 2, subfamily d, polypeptide 9	Mm.226708
Fatty Acid	Lypla1	NM_008866	lysophospholipase 1	Mm.299955
Fatty Acid	Ptgds	NM_008963	prostaglandin D2 synthase (brain)	Mm.1008
Fatty Acid	Acsl4	NM_001033600	acyl-CoA synthetase long-chain family member 4	Mm.391337
Fatty Acid	Ivd	NM_019826	isovaleryl coenzyme A dehydrogenase	Mm.6635
Fatty Acid	Acadl	NM_007381	acyl-Coenzyme A dehydrogenase, long-chain	Mm.2445
Fatty Acid	Pank2	NM_153501	pantothenate kinase 2	Mm.101264
Fatty Acid	Abcd2	NM_011994	ATP-binding cassette, sub-family D (ALD), member 2	Mm.295456
Fatty Acid	Acot1	NM_012006	acyl-CoA thioesterase 1	Mm.1978
Fatty Acid	Elovl7	NM_029001	ELOVL family member 7, elongation of long chain fatty acids (yeast)	Mm.286127
Fatty Acid	Faah	NM_010173	fatty acid amide hydrolase	Mm.256025
Fatty Acid	Acsl3	NM_001136222	acyl-CoA synthetase long-chain family member 3	Mm.276016

Fatty Acid	Ephx2	NM_001271403	epoxide hydrolase 2, cytoplasmic	Mm.15295
Fatty Acid	Acnat2	NM_145368	acyl-coenzyme A amino acid N-acyltransferase 2	Mm.35071
Fatty Acid	Ankrd23	NM_153502	ankyrin repeat domain 23	Mm.41421
Fatty Acid	Lep	NM_008493	leptin	Mm.277072
Fatty Acid	Acsm3	NM_212442	acyl-CoA synthetase medium-chain family member 3	Mm.334199
Fatty Acid	Adipor2	NM_197985	adiponectin receptor 2	Mm.291826
Fatty Acid	Avpr1a	NM_016847	arginine vasopressin receptor 1A	Mm.4351
Fatty Acid	Acat3	NM_153151	acetyl-Coenzyme A acetyltransferase 3	Mm.490312
Fatty Acid	Acox1	NM_015729	acyl-Coenzyme A oxidase 1, palmitoyl	Mm.356689
Fatty Acid	Srebf1	NM_011480	sterol regulatory element binding transcription factor 1	Mm.278701
Fatty Acid	Prkag3	NM_153744	protein kinase, AMP-activated, gamma 3 non-catatlytic subunit	Mm.166501
Fatty Acid	Cyp4a31	NM_001252539	cytochrome P450, family 4, subfamily a, polypeptide 31	Mm.482086
Fatty Acid	Scd2	NM_009128	stearoyl-Coenzyme A desaturase 2	Mm.487021
Glycolysis	Idh1	NM_010497	isocitrate dehydrogenase 1 (NADP+), soluble	Mm.9925
Glycolysis	Pgam1	NM_023418	phosphoglycerate mutase 1	Mm.16783
Glycolysis	Igfbp5	NM_010518	insulin-like growth factor binding protein 5	Mm.405761
Glycolysis	Tnf	NM_001278601	tumor necrosis factor	Mm.1293
Glycolysis	Atf4	NM_009716	activating transcription factor 4	Mm.641
Glycolysis	Sirt6	NM_001163430	sirtuin 6	Mm.25643
Glycolysis	Gale	NM_178389	galactose-4-epimerase, UDP	Mm.247946
Glycolysis	Nr1d1	NM_145434	nuclear receptor subfamily 1, group D, member 1	Mm.390397
Glycolysis	C1qtnf2	NM_026979	C1q and tumor necrosis factor related protein 2	Mm.390374
Glycolysis	Lcmt1	NM_025304	leucine carboxyl methyltransferase 1	Mm.260527
Glycolysis	Arpp19	NM_001142655	cAMP-regulated phosphoprotein 19	Mm.247837
Glycolysis	Oma1	NM_025909	OMA1 zinc metallopeptidase	Mm.30021
Glycolysis	Eif6	NM_010579	eukaryotic translation initiation factor 6	Mm.271674
Glycolysis	Galk1	NM_016905	galactokinase 1	Mm.2820

Glycolysis	Tcf7l2	NM_001331144	transcription factor 7 like 2, T cell specific, HMG box	Mm.139815
Glycolysis	Ldha	NM_010699	lactate dehydrogenase A	Mm.29324
Glycolysis	Dcxr	NM_001347608	dicarbonyl L-xylulose reductase	Mm.231091
Glycolysis	Src	NM_009271	Rous sarcoma oncogene	Mm.22845
Glycolysis	Trp53	NM_001127233	transformation related protein 53	Mm.222
Glycolysis	Igfbp3	NM_008343	insulin-like growth factor binding protein 3	Mm.29254
Glycolysis	C1qtnf1	NM_001204129	C1q and tumor necrosis factor related protein 1	Mm.23845
Glycolysis	Mapk14	NM_001168508	mitogen-activated protein kinase 14	Mm.311337
Glycolysis	Prkag2	NM_001170556	protein kinase, AMP-activated, gamma 2 non-catalytic subunit	Mm.33649
Glycolysis	Mlycd	NM_019966	malonyl-CoA decarboxylase	Mm.423037
Glycolysis	Slc35b4	NM_021435	solute carrier family 35, member B4	Mm.245527
Glycolysis	Ugp2	NM_139297	UDP-glucose pyrophosphorylase 2	Mm.28877
Glycolysis	H6pd	NM_173371	hexose-6-phosphate dehydrogenase (glucose 1-dehydrogenase)	Mm.22183
Glycolysis	Galt	NM_001302511	galactose-1-phosphate uridyl transferase	Mm.439669
Glycolysis	Pfkm	NM_001163487	phosphofructokinase, muscle	Mm.272582
Glycolysis	Rpia	NM_009075	ribose 5-phosphate isomerase A	Mm.17905
Glycolysis	Ganc	NM_172672	glucosidase, alpha; neutral C	Mm.38851
Glycolysis	Ppara	NM_001113418	peroxisome proliferator activated receptor alpha	Mm.212789
Glycolysis	Ppargc1a	NR_132764	peroxisome proliferative activated receptor, gamma, coactivator 1 alpha	Mm.259072
Glycolysis	Pdk2	NM_133667	pyruvate dehydrogenase kinase, isoenzyme 2	Mm.29768
Glycolysis	Inpp5k	NM_008916	inositol polyphosphate 5-phosphatase K	Mm.1458
Glycolysis	Nr1d1	NM_145434	nuclear receptor subfamily 1, group D, member 1	Mm.390397
Glycolysis	Fabp5	NM_001272097	fatty acid binding protein 5, epidermal	Mm.741
Glycolysis	Mst1	NM_008243	macrophage stimulating 1 (hepatocyte growth factor-like)	Mm.8369
Glycolysis	Per2	NM_011066	period circadian clock 2	Mm.482463

Glycolysis	Dgat2	NM_026384	diacylglycerol O-acyltransferase 2	Mm.180189
Glycolysis	Igfbp4	NM_010517	insulin-like growth factor binding protein 4	Mm.233799
Glycolysis	Prkag3	NM_153744	protein kinase, AMP-activated, gamma 3 non-catatlytic subunit	Mm.166501
Glycolysis	Esrrb	NM_011934	estrogen related receptor, beta	Mm.235550
Glycolysis	Pdk1	NM_172665	pyruvate dehydrogenase kinase, isoenzyme 1	Mm.34411
Glycolysis	Dlat	NM_145614	dihydrolipoamide S-acetyltransferase (E2 component of pyruvate dehydrogenase complex)	Mm.285076
Glycolysis	Entpd5	NM_001286049	ectonucleoside triphosphate diphosphohydrolase 5	Mm.10211
Glycolysis	Pck1	NM_011044	phosphoenolpyruvate carboxykinase 1, cytosolic	Mm.266867
Glycolysis	Zbtb7a	NM_010731	zinc finger and BTB domain containing 7a	Mm.20920
Glycolysis	Ier3	NM_133662	immediate early response 3	Mm.25613
Glycolysis	Gys1	NM_030678	glycogen synthase 1, muscle	Mm.275654
Glycolysis	Prkaa2	NM_178143	protein kinase, AMP-activated, alpha 2 catalytic subunit	Mm.48638
Glycolysis	Adipoq	NM_009605	adiponectin, C1Q and collagen domain containing	Mm.3969
Glycolysis	Idh3a	NM_029573	isocitrate dehydrogenase 3 (NAD+) alpha	Mm.279195
Glycolysis	Foxo1	NM_019739	forkhead box O1	Mm.29891
Glycolysis	Sesn2	NM_144907	sestrin 2	Mm.23608
Glycolysis	Lepr	NM_001122899	leptin receptor	Mm.259282
Glycolysis	Nr3c1	NM_008173	nuclear receptor subfamily 3, group C, member 1	Mm.129481
Glycolysis	Rora	NM_013646	RAR-related orphan receptor alpha	Mm.378450
Glycolysis	Rorc	NM_011281	RAR-related orphan receptor gamma	Mm.4372
Glycolysis	Slc45a3	NM_145977	solute carrier family 45, member 3	Mm.200307
Glycolysis	G6pc	NM_008061	glucose-6-phosphatase, catalytic	Mm.18064
Glycolysis	Ncor1	NM_011308	nuclear receptor co-repressor 1	Mm.271814
Glycolysis	Lep	NM_008493	leptin	Mm.277072
Glycolysis	Kat2a	NM_020004	K(lysine) acetyltransferase 2A	Mm.218837
Glycolysis	G6pdx	NM_008062	glucose-6-phosphate dehydrogenase X-linked	Mm.27210

Glycolysis	Cbr2	NM_007621	carbonyl reductase 2	Mm.21454
Glycolysis	Igfbp4	NM_010517	insulin-like growth factor binding protein 4	Mm.233799
Glycolysis	Npy1r	NM_010934	neuropeptide Y receptor Y1	Mm.5112
Glycolysis	Pfkp	NM_001291071	phosphofructokinase, platelet	Mm.273874
Glycolysis	Gale	NM_178389	galactose-4-epimerase, UDP	Mm.247946
Glycolysis	Prps2	NM_026662	phosphoribosyl pyrophosphate synthetase 2	Mm.272955
Glycolysis	Pgm5	NM_175013	phosphoglucomutase 5	Mm.105222
Glycolysis	Rorc	NM_011281	RAR-related orphan receptor gamma	Mm.4372
Glycolysis	Lep	NM_008493	leptin	Mm.277072
Glycolysis	Rbp4	NM_001159487	retinol binding protein 4, plasma	Mm.2605
Glycolysis	Prkag3	NM_153744	protein kinase, AMP-activated, gamma 3 non-catatlytic subunit	Mm.166501
Ox phphos/mit	Bid	NM_007544	BH3 interacting domain death agonist	Mm.235081
Ox phphos/mit	Cox6a1	NM_007748	cytochrome c oxidase subunit VIa polypeptide 1	Mm.43415
Ox phphos/mit	Msh2	NM_008628	mutS homolog 2	Mm.4619
Ox phphos/mit	Pde2a	NM_001243758	phosphodiesterase 2A, cGMP-stimulated	Mm.247564
Ox phphos/mit	Slc25a33	NM_027460	solute carrier family 25, member 33	Mm.41877
Ox phphos/mit	Ndufs4	NM_010887	NADH dehydrogenase (ubiquinone) Fe-S protein 4	Mm.253142
Ox phphos/mit	Mecp2	NM_010788	methyl CpG binding protein 2	Mm.131408
Ox phphos/mit	Foxred1	NM_001291448	FAD-dependent oxidoreductase domain containing 1	Mm.138512
Ox phphos/mit	Foxred1	NM_001291448	FAD-dependent oxidoreductase domain containing 1	Mm.138512
Transporter	Slc7a8	NM_016972	solute carrier family 7 (cationic amino acid transporter, y+ system), member 8	Mm.276831
Transporter	Slc22a12	NM_009203	solute carrier family 22 (organic anion/cation transporter), member 12	Mm.391146
Transporter	Slc22a12	NM_009203	solute carrier family 22 (organic anion/cation transporter), member 12	Mm.391146

Transporter	Slc25a15	NM_181325	solute carrier family 25 (mitochondrial carrier ornithine transporter), member 15	Mm.200907
Transporter	Slc3a2	NM_001161413	solute carrier family 3 (activators of dibasic and neutral amino acid transport), member 2	Mm.4114
Transporter	Aqp8	NM_001109045	aquaporin 8	Mm.273175
Transporter	Slc24a3	NM_053195	solute carrier family 24 (sodium/potassium/calcium exchanger), member 3	Mm.217171
Transporter	Slc16a10	NM_028247	solute carrier family 16 (monocarboxylic acid transporters), member 10	Mm.186778
Transporter	Slc5a2	NM_133254	solute carrier family 5 (sodium/glucose cotransporter), member 2	Mm.38870
Transporter	Slc31a2	NM_025286	solute carrier family 31, member 2	Mm.292539
Transporter	Slc16a1	NM_009196	solute carrier family 16 (monocarboxylic acid transporters), member 1	Mm.9086
Transporter	Slc4a1ap	NM_009206	solute carrier family 4 (anion exchanger), member 1, adaptor protein	Mm.352407
Transporter	Slc35f1	NM_178675	solute carrier family 35, member F1	Mm.338690
Transporter	Slc35a3	NM_144902	solute carrier family 35 (UDP-N-acetylglucosamine (UDP-GlcNAc) transporter), member 3	Mm.190758
Transporter	Slc22a17	NM_021551	solute carrier family 22 (organic cation transporter), member 17	Mm.27435
Transporter	Slc25a19	NM_001252395	solute carrier family 25 (mitochondrial thiamine pyrophosphate carrier), member 19	Mm.383426
Transporter	Slc29a3	NM_023596	solute carrier family 29 (nucleoside transporters), member 3	Mm.284462
Transporter	Slc34a3	NM_080854	solute carrier family 34 (sodium phosphate), member 3	Mm.346652
Transporter	Slc35c2	NM_001252575	solute carrier family 35, member C2	Mm.21184
Transporter	Slc15a3	NM_023044	solute carrier family 15, member 3	Mm.27387

Transporter	Slc7a7	NM_011405	solute carrier family 7 (cationic amino acid transporter, y+ system), member 7	Mm.142455
Transporter	Slc41a3	NM_027868	solute carrier family 41, member 3	Mm.272633
Transporter	Slc2a6	NM_172659	solute carrier family 2 (facilitated glucose transporter), member 6	Mm.41203
Transporter	Slc5a11	NM_146198	solute carrier family 5 (sodium/glucose cotransporter), member 11	Mm.211838
Transporter	Slc31a1	NM_175090	solute carrier family 31, member 1	Mm.248637
Transporter	Slc35b3	NM_134060	solute carrier family 35, member B3	Mm.255506
Transporter	Slc22a18	NM_001042760	solute carrier family 22 (organic cation transporter), member 18	Mm.271740
Transporter	Slc26a6	NM_134420	solute carrier family 26, member 6	Mm.45201
Transporter	Slc26a6	NM_134420	solute carrier family 26, member 6	Mm.45201
Transporter	Slc39a8	NM_001135150	solute carrier family 39 (metal ion transporter), member 8	Mm.30239
Transporter	Slc22a12	NM_009203	solute carrier family 22 (organic anion/cation transporter), member 12	Mm.391146
Transporter	Slc22a12	NM_009203	solute carrier family 22 (organic anion/cation transporter), member 12	Mm.391146
Transporter	Slc35f3	NM_175434	solute carrier family 35, member F3	Mm.405238
Transporter	Slc22a4	NM_001330304	solute carrier family 22 (organic cation transporter), member 4	Mm.274590
Transporter	Slc25a33	NM_027460	solute carrier family 25, member 33	Mm.41877
Transporter	Slc12a7	NM_011390	solute carrier family 12, member 7	Mm.275800
Transporter	Slc13a2	NM_022411	solute carrier family 13 (sodium-dependent dicarboxylate transporter), member 2	Mm.274058
Transporter	Slc25a42	NM_001007570	solute carrier family 25, member 42	Mm.185413
Transporter	Slc6a19	NM_028878	solute carrier family 6 (neurotransmitter transporter), member 19	Mm.271635
Transporter	Slc9a3r1	NM_012030	solute carrier family 9 (sodium/hydrogen exchanger), member 3 regulator 1	Mm.27842

Transporter	Slc6a9	NM_008135	solute carrier family 6 (neurotransmitter transporter, glycine), member 9	Mm.244549
Transporter	Slc46a1	NM_026740	solute carrier family 46, member 1	Mm.131618
Transporter	Slc26a1	NM_001310691	solute carrier family 26 (sulfate transporter), member 1	Mm.440571
Transporter	Slc25a10	NM_013770	solute carrier family 25 (mitochondrial carrier, dicarboxylate transporter), member 10	Mm.3991
Transporter	Slc26a6	NM_134420	solute carrier family 26, member 6	Mm.45201
Transporter	Slc26a6	NM_134420	solute carrier family 26, member 6	Mm.45201
Transporter	Aqp11	NM_175105	aquaporin 11	Mm.29756
Transporter	Slc6a4	NM_010484	solute carrier family 6 (neurotransmitter transporter, serotonin), member 4	Mm.300318
Transporter	Slc25a37	NM_026331	solute carrier family 25, member 37	Mm.293635
Transporter	Slc5a9	NM_145551	solute carrier family 5 (sodium/glucose cotransporter), member 9	Mm.26630
Transporter	Slc35b4	NM_021435	solute carrier family 35, member B4	Mm.245527
Transporter	Slc25a26	NM_026255	solute carrier family 25 (mitochondrial carrier, phosphate carrier), member 26	Mm.280725
Transporter	Aqp3	NM_016689	aquaporin 3	Mm.34043
Transporter	Slc5a1	NM_019810	solute carrier family 5 (sodium/glucose cotransporter), member 1	Mm.25237
Transporter	Slc30a9	NM_178651	solute carrier family 30 (zinc transporter), member 9	Mm.234455
Transporter	Slc17a5	NM_172773	solute carrier family 17 (anion/sugar transporter), member 5	Mm.46932
Transporter	Slc7a9	NM_021291	solute carrier family 7 (cationic amino acid transporter, y+ system), member 9	Mm.45874
Transporter	Slc25a44	NM_001145876	solute carrier family 25, member 44	Mm.301740

Transporter	Slc28a1	NM_001004184	solute carrier family 28 (sodium-coupled nucleoside transporter), member 1	Mm.389909
Transporter	Slc35e4	NM_153142	solute carrier family 35, member E4	Mm.171514
Transporter	Slc6a20b	NM_011731	solute carrier family 6 (neurotransmitter transporter), member 20B	Mm.41963
Transporter	Slc25a11	NM_024211	solute carrier family 25 (mitochondrial carrier oxoglutarate carrier), member 11	Mm.296082
Transporter	Slc38a10	NM_001164802	solute carrier family 38, member 10	Mm.253403
Transporter	Slc27a5	NM_009512	solute carrier family 27 (fatty acid transporter), member 5	Mm.10984
Transporter	Slc25a46	NM_026165	solute carrier family 25, member 46	Mm.23896
Transporter	Slc5a6	NM_177870	solute carrier family 5 (sodium-dependent vitamin transporter), member 6	Mm.205463
Transporter	Slc7a4	NM_144852	solute carrier family 7 (cationic amino acid transporter, y+ system), member 4	Mm.298878
Transporter	Slc17a4	NM_177016	solute carrier family 17 (sodium phosphate), member 4	Mm.97959
Transporter	Slc12a6	NM_133648	solute carrier family 12, member 6	Mm.491155
Transporter	Slc46a3	NM_027872	solute carrier family 46, member 3	Mm.153218
Transporter	Slc16a9	NM_025807	solute carrier family 16 (monocarboxylic acid transporters), member 9	Mm.19325
Transporter	Slc25a20	NM_020520	solute carrier family 25 (mitochondrial carnitine/acylcarnitine translocase), member 20	Mm.29666
Transporter	Slc22a5	NM_011396	solute carrier family 22 (organic cation transporter), member 5	Mm.42253
Transporter	Slc25a34	NM_001013780	solute carrier family 25, member 34	Mm.295682
Transporter	Slc27a2	NM_011978	solute carrier family 27 (fatty acid transporter), member 2	Mm.290044
Transporter	Slc17a2	NM_144836	solute carrier family 17 (sodium phosphate), member 2	Mm.24030

Transporter	Slc5a8	NM_145423	solute carrier family 5 (iodide transporter), member 8	Mm.77381
Transporter	Slc1a3	NM_148938	solute carrier family 1 (glial high affinity glutamate transporter), member 3	Mm.204834
Transporter	Slc37a4	NM_001293631	solute carrier family 37 (glucose-6-phosphate transporter), member 4	Mm.30087
Transporter	Slc2a13	NM_001033633	solute carrier family 2 (facilitated glucose transporter), member 13	Mm.360596
Transporter	Slc35e3	NM_029875	solute carrier family 35, member E3	Mm.256753
Transporter	Slco2a1	NM_033314	solute carrier organic anion transporter family, member 2a1	Mm.207106
Transporter	Slc7a2	NM_007514	solute carrier family 7 (cationic amino acid transporter, y+ system), member 2	Mm.4676
Transporter	Slc25a13	NM_001177572	solute carrier family 25 (mitochondrial carrier, adenine nucleotide translocator), member 13	Mm.24513
Transporter	Slc16a14	NM_027921	solute carrier family 16 (monocarboxylic acid transporters), member 14	Mm.158754
Transporter	Slc5a3	NM_017391	solute carrier family 5 (inositol transporters), member 3	Mm.217354
Transporter	Slc25a25	NM_001164358	solute carrier family 25 (mitochondrial carrier, phosphate carrier), member 25	Mm.37395
Transporter	Slc15a4	NM_133895	solute carrier family 15, member 4	Mm.28506
Transporter	Slc44a1	NM_133891	solute carrier family 44, member 1	Mm.482207
Transporter	Slco3a1	NM_023908	solute carrier organic anion transporter family, member 3a1	Mm.425467
Transporter	Slc2a1	NM_011400	solute carrier family 2 (facilitated glucose transporter), member 1	Mm.21002
Transporter	Slc45a3	NM_145977	solute carrier family 45, member 3	Mm.200307
Transporter	Slc6a6	NM_009320	solute carrier family 6 (neurotransmitter transporter, taurine), member 6	Mm.395650
Transporter	Slc25a35	NM_028048	solute carrier family 25, member 35	Mm.298622
Transporter	Slc17a1	NR_121611	solute carrier family 17 (sodium phosphate), member 1	Mm.2656

Transporter	Slc22a13	NM_133980	solute carrier family 22 (organic cation transporter), member 13	Mm.38775
Transporter	Slc6a15	NM_175328	solute carrier family 6 (neurotransmitter transporter), member 15	Mm.458408
Transporter	Slc22a7	NM_144856	solute carrier family 22 (organic anion transporter), member 7	Mm.387538
Transporter	Slc9a3r2	NM_023449	solute carrier family 9 (sodium/hydrogen exchanger), member 3 regulator 2	Mm.21587
Transporter	Slc19a3	NM_030556	solute carrier family 19, member 3	Mm.261542
Transporter	Slc35f2	NM_028060	solute carrier family 35, member F2	Mm.26159
Transporter	Slc35b1	NM_016752	solute carrier family 35, member B1	Mm.4593
Transporter	Slc15a2	NM_021301	solute carrier family 15 (H+/peptide transporter), member 2	Mm.281804
Transporter	Slc10a3	NM_001256104	solute carrier family 10 (sodium/bile acid cotransporter family), member 3	Mm.19931
Transporter	Slc6a12	NM_133661	solute carrier family 6 (neurotransmitter transporter, betaine/GABA), member 12	Mm.274506
Transporter	Slc11a2	NM_008732	solute carrier family 11 (proton-coupled divalent metal ion transporters), member 2	Mm.234608
Transporter	Slc25a38	NM_144793	solute carrier family 25, member 38	Mm.236656

Supplementary Table 3: List of transporters belonging to the Slc family				
Name	**Transport**	**Slc family**	**Young ANOVA Padj**	**Nephritic ANOVA Padj**
Slc15a2	small peptides	Proton oligopeptide cotransporter	**0.017**	0.99
Slc15a3	peptides/histidine	Proton oligopeptide cotransporter	**0.008**	0.46
Slc16a10	aromatic amino acids	Monocarboxylate transporter	**0.000**	0.39
Slc1a3	neutral amino acids	High-affinity glutamate and neutral amino acid transporter	**0.001**	0.41
Slc3a2	neutral amino acids - colocalizes with Slc7a8	Heavy subunits of the heteromeric amino acid transporters	**0.000**	0.57
Slc6a15	neutral amino acids	Sodium- and chloride-dependent neurotransmitter transporter	**0.002**	0.24
Slc6a19	neutral amino acids	Sodium- and chloride-dependent neurotransmitter transporter	**0.000**	0.11
Slc6a20b	proline, sarcosine	Sodium- and chloride-dependent neurotransmitter transporter	**0.027**	0.61
Slc6a6	taurine	Sodium- and chloride-dependent neurotransmitter transporter	**0.002**	0.11
Slc6a9	glycine	Sodium- and chloride-dependent neurotransmitter transporter	**0.003**	0.45
Slc7a2	cationic amino acids	Cationic amino acid transporter/glycoprotein-associated	**0.037**	0.65
Slc7a4	cationic amino acids	Cationic amino acid transporter/glycoprotein-associated	**0.001**	**0.01**
Slc7a7	cationic amino acids	Cationic amino acid transporter/glycoprotein-associated	**0.002**	0.56
Slc7a8	neutral amino acids	Cationic amino acid transporter/glycoprotein-associated	**0.000**	0.10
Slc7a9	cationic amino acids	Cationic amino acid transporter/glycoprotein-associated	**0.033**	0.41
Slc6a4	serotonin	Sodium- and chloride-dependent neurotransmitter transporter	**0.001**	0.22
Slc6a12	GABA, betaine	Sodium- and chloride-dependent neurotransmitter transporter	**0.008**	0.18
Slc16a1	GABA	Monocarboxylate transporter	**0.006**	0.13
Slc12a6	Cl	Electroneutral cation-coupled Cl cotransporter	**0.000**	0.41
Slc12a7	Cl	Electroneutral cation-coupled Cl cotransporter	**0.000**	**0.05**
Slc17a2	PO4	Vesicular glutamate transporter	**0.001**	0.43
Slc17a4	Na/PO4	Vesicular glutamate transporter	**0.005**	**0.02**
Slc24a3	Na/K/Ca	Na+/(Ca2+-K+) exchanger	**0.002**	0.09
Slc34a3	Na/PO4	Type II Na+-phosphate cotransporter	**0.000**	0.19

Slc4a1ap	anions	Bicarbonate transporter	**0.023**	0.10
Slc9a3r1	Na/H	Na+/H+ exchanger	**0.000**	0.38
Slc9a3r2	Na/H	Na+/H+ exchanger	**0.006**	0.04
Slc2a1	glucose, galactose, mannose, glucosamine Glut1	Facilitative GLUT transporter	**0.000**	0.18
Slc2a6	glucose, galactose, fructose, mannose, glucosamine Glut 6	Facilitative GLUT transporter	**0.022**	0.29
Slc2a13	H/myoinositol	Facilitative GLUT transporter	**0.000**	0.08
Slc45a3	sucrose, glucose, fructose	H+/sugar cotransporter	**0.000**	0.14
Slc5a1	glucose galactose SGLT1	Sodium glucose cotransporter	**0.017**	0.08
Slc5a2	glucose SGLT2	Sodium glucose cotransporter	**0.024**	0.84
Slc5a3	glucose myoinositol	Sodium glucose cotransporter	**0.017**	0.72
Slc5a9	mannose, fructose, glucose	Sodium glucose cotransporter	**0.006**	0.36
Slc5a11	myoinositol	Sodium glucose cotransporter	**0.040**	0.24
Slc17a5	sialic acid, other acidic sugars	Vesicular glutamate transporter	**0.035**	0.08
Slc22a4	Na/carnitine low affinity	Organic cation/anion/zwitterion	**0.000**	0.18
Slc22a5	Na/carnitine high affinity	Organic cation/anion/zwitterion	**0.000**	0.94
Slc27a2	fatty acid	Fatty acid transporter	**0.003**	0.41
Slc5a8	short chain fatty acids	Sodium glucose cotransporter	**0.000**	0.61
Slc19a3	thiamine	Folate/thiamine transporter	**0.000**	0.47
Slc46a1	folate, heme	Folate transporter	**0.001**	0.23
Slc5a6	pantothenate, biotin, lipoate	Sodium glucose cotransporter	**0.000**	**0.02**
Slc30a9	Zn Cd Mg	Zinc efflux	**0.007**	0.06
Slc31a1	Cu	Copper transporter	**0.019**	0.46
Slc31a2	Cu	Copper transporter	**0.001**	0.68
Slc41a3	Mg	MgtE-like magnesium transporter	**0.013**	0.36
Slc28a1	nucleoside	Na+-coupled nucleoside transport	**0.038**	0.51
Slc29a3	nucleoside	Facilitative nucleoside transporter	**0.000**	0.32
Slc35b1	nucleoside	Nucleoside sugar	**0.014**	**0.05**
Slc35b3	nucleoside	Nucleoside sugar	**0.013**	0.53
Slc35b4	nucleoside	Nucleoside sugar	**0.010**	0.38

Slc35c2	nucleoside	Nucleoside sugar	**0.000**	0.11
Slc35e3	nucleoside	Nucleoside sugar	**0.004**	0.14
Slc35e4	nucleoside	Nucleoside sugar	**0.044**	0.18
Slc35f1	nucleoside	Nucleoside sugar	**0.047**	0.28
Slc35f2	nucleoside	Nucleoside sugar	**0.001**	0.51
Slc35f3	nucleoside	Nucleoside sugar	**0.037**	**0.01**
Slc13a2	dicarboxylates	Human Na+-sulfate/carboxylate cotransporter	**0.000**	0.16
Slc16a14	monocarboxylates	Monocarboxylate transporter	**0.001**	0.16
Slc16a9	monocarboxylates	Monocarboxylate transporter	**0.000**	0.63
Slc26a1	monocarboxylates	Multifunctional anion exchanger	**0.000**	0.40
Slc26a6	monocarboxylates	Multifunctional anion exchanger	**0.000**	**0.01**
Slc25a10	dicarboxylates	Mitochondrial carrier	**0.003**	0.10
Slc25a13	aspartate, glutamate	Mitochondrial carrier	**0.019**	0.11
Slc25a15	ornithine	Mitochondrial carrier	**0.000**	0.66
Slc25a19	nucleosides	Mitochondrial carrier	**0.004**	**0.05**
Slc25a20	acylcarnitines	Mitochondrial carrier	**0.000**	0.07
Slc25a25	nucleosides	Mitochondrial carrier	**0.044**	0.35
Slc25a26	S-adenosyl-methionine, S-adenosyl-homocysteine	Mitochondrial carrier	**0.031**	0.52
Slc25a33	pyrimidines	Mitochondrial carrier	**0.000**	0.40
Slc25a34	unknown	Mitochondrial carrier	**0.000**	0.37
Slc25a35	unknown	Mitochondrial carrier	**0.000**	0.10
Slc25a37	Fe	Mitochondrial carrier	**0.002**	0.37
Slc25a42	nucleosides	Mitochondrial carrier	**0.000**	0.44
Slc25a44	unknown	Mitochondrial carrier	**0.025**	0.69
Slc17a1	organic anions/PO4/Cl	Vesicular glutamate transporter	**0.026**	0.91
Slc22a12	urate URAT1	Organic cation/anion/zwitterion	**0.000**	**0.05**
Slc22a13	urate organic anions OAT10	Organic cation/anion/zwitterion	**0.046**	0.68
Slc22a18	organic anions	Organic cation/anion/zwitterion	**0.036**	0.91
Slc22a7	organic anions OAT2	Organic cation/anion/zwitterion	**0.030**	0.20
Slc10a3	unknown	Sodium bile salt cotransport	**0.034**	0.23
Slc37a4	unknown	Sugar-phosphate/phosphate exchanger	**0.033**	0.44
Slc46a3	?lysosomal	Folate transporter	**0.000**	0.16
Slc15a4	peptides/histidine	Proton oligopeptide cotransporter	0.146	**0.05**
Slc27a5	bile acids	Fatty acid transporter	0.585	**0.05**
Slc44a1	choline	Choline-like transporter	0.263	**0.05**
Slc11a2	Fe	Proton-coupled metal ion transporter	0.405	**0.04**

Slc39a8	Zn Cd Mg	Metal ion transporter	0.149	**0.03**
Slc35a3	nucleoside	Nucleoside sugar	0.292	**0.04**
Slc25a11	oxoglutarate, malate	Mitochondrial carrier	0.283	**0.01**
Slc25a38	?glycine	Mitochondrial carrier	0.051	**0.04**
Slc25a46	unknown	Mitochondrial carrier	0.582	**0.02**
Slc22a17	unknown	Organic cation/anion/zwitterion	0.148	**0.05**
Slc38a10	unknown	System A and System N sodium-coupled neutral amino acid transporter	0.632	**0.01**

Supplementary Table 4: List of 320 diurnally regulated genes corrected by ≥50% and not corrected by remission induction

	A. Mean Normalized Expression (RNASeq)								
Corrected	**Remission**			**Young**			**Nephritic**		
Symbol	**ZT0**	**ZT12**	***Ratio ZT0:ZT12***	**ZT0**	**ZT12**	***Ratio ZT0:ZT12***	**ZT0**	**ZT12**	***Ratio ZT0:ZT12***
4930550C14Rik	1.13	0.73	*1.55*	1.30	0.76	*1.72*	1.14	0.89	*1.28*
Acaa1b	0.86	1.43	*0.60*	0.77	1.61	*0.48*	0.91	0.90	*1.02*
Acat3	0.82	1.29	*0.63*	0.90	1.14	*0.79*	1.22	1.02	*1.20*
Acot3	0.88	1.23	*0.71*	1.00	1.96	*0.51*	0.69	0.61	*1.13*
Acox3	0.85	1.32	*0.64*	0.86	1.29	*0.67*	0.89	0.89	*1.00*
Aifm2	0.95	1.25	*0.76*	0.93	1.36	*0.69*	0.97	0.87	*1.12*
Ak5	1.40	0.91	*1.55*	1.22	0.85	*1.44*	1.05	0.92	*1.14*
Akr1c19	0.83	1.19	*0.70*	0.60	1.01	*0.59*	1.09	1.14	*0.96*
Alas1	1.17	1.66	*0.71*	0.97	1.95	*0.50*	1.09	1.16	*0.94*
Amt	1.32	0.90	*1.48*	1.35	0.95	*1.42*	0.99	0.91	*1.09*
Angptl4	0.32	2.47	*0.13*	0.35	1.72	*0.20*	1.18	1.81	*0.65*
Ankrd12	0.83	1.10	*0.75*	0.81	1.18	*0.69*	1.09	1.11	*0.98*
Aqp11	0.86	1.07	*0.80*	0.98	1.24	*0.79*	0.70	0.70	*1.00*
Aqp8	1.36	0.29	*4.73*	2.21	0.71	*3.10*	0.96	0.47	*2.04*
Arhgef3	0.93	1.27	*0.73*	0.79	1.17	*0.68*	1.08	1.11	*0.98*
Arntl	1.88	0.14	*13.73*	3.92	0.33	*11.73*	1.04	0.76	*1.38*
Avpi1	0.94	1.15	*0.82*	0.88	1.15	*0.77*	0.97	0.85	*1.15*
Azin1	0.96	1.11	*0.87*	0.91	1.19	*0.76*	0.96	0.98	*0.97*
Blvrb	0.88	1.18	*0.75*	0.83	1.21	*0.69*	0.94	0.91	*1.03*
Car5b	1.16	0.81	*1.43*	1.64	0.98	*1.67*	1.13	0.98	*1.15*
Cdc42ep4	0.86	1.21	*0.71*	0.82	1.12	*0.74*	1.13	1.09	*1.04*
Cdkl1	1.15	0.60	*1.91*	1.43	0.86	*1.67*	0.94	0.80	*1.17*
Cdo1	0.78	1.26	*0.62*	0.80	1.09	*0.73*	1.01	0.96	*1.05*
Chst1	0.75	1.44	*0.52*	0.69	1.27	*0.55*	0.96	1.11	*0.86*
Chst8	0.86	1.06	*0.80*	0.74	1.15	*0.64*	0.90	0.87	*1.03*
Cited4	0.89	1.73	*0.52*	0.97	1.57	*0.62*	1.13	1.06	*1.06*
Ckb	1.34	0.78	*1.73*	1.09	0.73	*1.49*	1.01	0.87	*1.16*

Clcn2	0.87	1.18	*0.74*	0.85	1.44	*0.59*	0.93	0.93	*1.00*
Cldn10	1.41	0.84	*1.68*	1.41	0.91	*1.55*	0.75	0.79	*0.94*
Clec2d	0.67	1.40	*0.48*	0.83	1.25	*0.66*	1.10	1.03	*1.07*
Clock	1.29	0.79	*1.62*	1.27	0.81	*1.57*	1.08	1.14	*0.94*
Clpx	1.31	0.91	*1.44*	1.78	0.93	*1.91*	0.86	0.90	*0.96*
Clstn3	0.66	1.40	*0.48*	0.83	1.45	*0.57*	1.00	0.81	*1.24*
Cmc1	0.80	1.09	*0.73*	0.89	1.15	*0.78*	0.98	0.95	*1.03*
Col27a1	0.51	1.00	*0.51*	0.94	1.70	*0.55*	0.92	1.13	*0.82*
Col4a4	1.22	0.79	*1.55*	1.23	0.89	*1.38*	0.96	0.87	*1.10*
Coq10b	0.82	1.57	*0.52*	0.85	2.11	*0.40*	0.86	1.16	*0.75*
Coro2a	0.72	1.26	*0.57*	0.82	1.12	*0.73*	1.05	1.09	*0.96*
Cpeb3	0.78	1.30	*0.60*	0.78	1.23	*0.63*	0.82	1.00	*0.81*
Cpt2	0.92	1.31	*0.70*	0.76	1.21	*0.63*	0.87	1.01	*0.86*
Creb3l1	1.19	0.63	*1.88*	1.32	0.80	*1.65*	1.08	0.87	*1.23*
Cry2	0.63	1.34	*0.47*	0.66	1.44	*0.45*	0.77	0.95	*0.81*
Csnk1g3	0.92	1.21	*0.76*	0.84	1.25	*0.67*	0.86	1.00	*0.86*
Ctgf	0.57	1.56	*0.36*	0.59	1.41	*0.42*	1.23	1.79	*0.69*
Cygb	0.75	1.50	*0.50*	0.54	0.87	*0.62*	1.23	1.54	*0.80*
Cyp27a1	0.76	1.24	*0.61*	0.86	1.29	*0.67*	0.93	0.97	*0.95*
Cyp2a5	0.47	2.02	*0.23*	0.73	2.30	*0.32*	0.53	0.75	*0.70*
Cyp2e1	0.80	2.48	*0.32*	0.70	2.10	*0.33*	0.93	0.86	*1.08*
D930015E06Rik	0.76	1.13	*0.67*	0.70	1.02	*0.68*	1.03	1.12	*0.92*
Dbp	0.57	12.60	*0.04*	0.25	5.98	*0.04*	0.58	1.03	*0.57*
Dcun1d3	0.99	1.22	*0.81*	0.97	1.30	*0.75*	1.03	1.02	*1.01*
Ddit4l	1.31	0.57	*2.31*	1.41	0.65	*2.18*	1.22	1.07	*1.14*
Dgat2	0.77	1.41	*0.55*	0.95	1.52	*0.62*	0.77	0.85	*0.91*
Dhrs7	0.88	1.24	*0.71*	0.92	1.24	*0.74*	0.94	1.00	*0.94*
Dleu7	1.55	0.68	*2.28*	1.71	0.87	*1.97*	0.91	0.87	*1.04*
Dnase1	0.75	1.24	*0.60*	0.99	1.48	*0.67*	0.52	0.36	*1.46*
Dusp1	0.86	1.84	*0.47*	1.02	2.56	*0.40*	0.95	1.03	*0.92*
Dusp14	1.17	0.78	*1.50*	1.44	0.96	*1.50*	1.03	0.92	*1.12*
Dusp7	0.98	1.55	*0.63*	0.82	1.56	*0.53*	1.23	1.10	*1.12*
Eef2k	0.86	1.06	*0.81*	0.81	1.11	*0.74*	0.97	1.00	*0.97*
Efhd1	1.38	0.77	*1.80*	1.49	0.83	*1.78*	1.09	0.85	*1.29*
Eif4ebp3	0.74	1.26	*0.58*	0.92	1.23	*0.75*	0.97	0.90	*1.07*
Ephx1	0.87	1.27	*0.69*	0.71	1.35	*0.52*	0.90	1.08	*0.84*
Errfi1	0.79	1.35	*0.58*	1.11	1.77	*0.63*	0.97	1.07	*0.91*
Fabp3	0.99	1.14	*0.87*	0.90	1.14	*0.79*	0.85	0.72	*1.17*
Fam102a	0.90	1.22	*0.74*	0.90	1.14	*0.79*	1.14	1.15	*1.00*
Fam163a	1.86	0.58	*3.21*	1.64	0.79	*2.07*	1.00	0.69	*1.45*
Fermt1	1.29	0.73	*1.77*	1.18	0.80	*1.48*	1.13	1.05	*1.08*

Ffar3	0.98	0.46	*2.12*	1.91	1.00	*1.92*	1.01	0.86	*1.18*
Fkbp5	0.56	2.74	*0.20*	0.59	2.28	*0.26*	0.94	1.78	*0.53*
Fmnl1	0.72	1.49	*0.49*	0.79	1.49	*0.53*	0.94	0.91	*1.04*
Foxo1	0.91	1.41	*0.64*	1.05	1.39	*0.75*	1.03	1.05	*0.98*
Gja1	0.72	1.32	*0.54*	1.02	1.61	*0.63*	0.88	0.81	*1.09*
Gldc	0.92	2.44	*0.38*	1.19	2.46	*0.49*	0.89	1.05	*0.85*
Glul	0.89	1.60	*0.56*	0.86	1.73	*0.50*	0.96	1.02	*0.94*
Gnpda1	1.08	0.84	*1.29*	1.55	1.01	*1.54*	0.96	1.00	*0.96*
Grasp	0.77	1.28	*0.60*	0.82	1.29	*0.64*	1.05	1.14	*0.92*
Gstt2	0.82	1.23	*0.67*	0.74	1.29	*0.58*	0.90	0.95	*0.94*
Gypc	0.94	1.27	*0.74*	0.98	1.71	*0.57*	0.74	0.79	*0.93*
Herpud1	0.68	1.94	*0.35*	0.78	2.16	*0.36*	0.95	1.31	*0.73*
Hn1l	1.19	0.65	*1.83*	1.31	0.62	*2.12*	1.22	0.98	*1.25*
Hspb6	0.84	1.17	*0.72*	0.77	1.11	*0.70*	0.93	0.94	*0.99*
Idh1	1.07	0.74	*1.45*	1.46	0.87	*1.68*	1.04	0.97	*1.06*
Ier3	0.75	1.28	*0.59*	0.78	1.69	*0.46*	1.14	1.45	*0.78*
Ifrd2	0.91	1.34	*0.68*	0.93	1.21	*0.77*	0.92	0.91	*1.01*
Igfbp4	0.73	1.39	*0.52*	0.77	1.30	*0.59*	0.90	1.05	*0.86*
Igfbp5	1.59	0.60	*2.67*	1.23	0.88	*1.39*	0.72	0.70	*1.02*
Il17f	2.07	0.68	*3.02*	2.21	1.19	*1.86*	0.57	0.84	*0.68*
Il17rb	0.88	1.08	*0.81*	0.78	1.14	*0.69*	1.16	1.04	*1.11*
Immp2l	0.80	1.33	*0.60*	0.94	1.32	*0.71*	0.91	0.84	*1.09*
Insc	2.01	0.40	*5.03*	2.71	0.61	*4.46*	1.37	0.64	*2.15*
Itga6	1.14	0.65	*1.75*	1.38	0.72	*1.91*	0.99	1.09	*0.90*
Itgb6	1.50	0.68	*2.21*	1.50	0.72	*2.09*	0.94	0.84	*1.12*
Itprip	0.84	1.44	*0.58*	0.78	1.26	*0.62*	1.11	1.18	*0.94*
Kcnj15	0.92	1.08	*0.85*	0.93	1.25	*0.74*	0.93	0.97	*0.96*
Kcnk5	0.81	1.96	*0.41*	1.01	2.07	*0.49*	1.21	1.34	*0.90*
Kif27	1.06	0.78	*1.37*	1.55	1.00	*1.54*	1.01	0.87	*1.16*
Klf10	0.77	1.12	*0.68*	0.63	1.18	*0.53*	1.14	1.07	*1.06*
Klf13	0.79	1.48	*0.53*	0.66	1.25	*0.52*	1.03	1.10	*0.94*
Klf6	0.89	1.29	*0.69*	0.67	1.05	*0.64*	1.58	1.74	*0.91*
Klf9	0.91	1.42	*0.64*	0.79	1.52	*0.52*	0.89	1.06	*0.84*
Klhl21	0.94	1.17	*0.81*	0.90	1.32	*0.68*	1.09	1.14	*0.96*
Lama1	1.05	0.83	*1.26*	1.06	0.75	*1.41*	1.07	0.99	*1.08*
Ldoc1l	1.39	0.61	*2.26*	1.60	0.53	*3.00*	1.14	0.81	*1.39*
Leo1	1.24	0.66	*1.88*	1.34	0.76	*1.75*	1.14	1.00	*1.14*
Lonrf1	1.01	1.42	*0.71*	0.93	1.52	*0.61*	0.89	1.06	*0.84*
Lpin1	0.77	2.21	*0.35*	0.85	2.43	*0.35*	0.91	0.89	*1.02*
Lrrc40	0.89	1.11	*0.80*	0.89	1.16	*0.77*	0.88	0.92	*0.96*
Lyrm1	0.86	1.06	*0.81*	1.00	1.37	*0.73*	0.86	0.86	*1.00*

Map3k6	0.67	1.88	*0.35*	0.71	1.85	*0.38*	1.20	1.40	*0.86*
Mbd1	0.91	1.40	*0.65*	0.88	1.26	*0.70*	0.98	1.04	*0.94*
Mknk2	0.92	1.35	*0.68*	0.82	1.32	*0.62*	1.12	1.13	*0.99*
Mpp4	0.59	1.27	*0.47*	0.92	1.62	*0.57*	0.78	0.94	*0.83*
Mreg	0.75	1.52	*0.49*	0.97	1.36	*0.71*	0.87	0.97	*0.90*
Myo9a	1.01	0.79	*1.28*	1.13	0.82	*1.38*	1.11	1.18	*0.94*
Nampt	0.88	1.31	*0.67*	0.81	1.54	*0.53*	0.83	0.94	*0.88*
Nat2	0.79	1.68	*0.47*	0.94	1.83	*0.51*	0.91	0.93	*0.98*
Ncald	1.18	0.87	*1.35*	1.32	0.92	*1.43*	0.89	0.87	*1.03*
Nfkbia	0.85	1.62	*0.52*	0.71	1.38	*0.51*	1.27	1.34	*0.95*
Nid2	1.11	0.78	*1.42*	1.29	0.85	*1.51*	0.92	1.05	*0.87*
Npas2	1.02	0.10	*10.11*	2.92	0.37	*7.92*	1.35	0.57	*2.37*
Nr1d1	0.90	1.15	*0.79*	0.64	1.03	*0.62*	0.82	0.74	*1.12*
Nr1d2	0.73	1.88	*0.39*	0.61	2.34	*0.26*	0.77	1.16	*0.67*
Nr1h4	0.86	1.22	*0.70*	0.89	1.46	*0.61*	0.81	0.84	*0.96*
Nrg4	0.67	1.39	*0.48*	0.87	1.56	*0.56*	0.83	0.91	*0.92*
Oplah	0.94	1.35	*0.70*	0.72	1.37	*0.53*	1.00	1.12	*0.89*
Osbpl9	0.88	1.55	*0.56*	0.89	1.69	*0.53*	0.91	1.19	*0.77*
Pank1	1.12	1.50	*0.75*	1.01	1.48	*0.68*	0.80	0.78	*1.02*
Paox	0.89	1.39	*0.64*	0.92	1.28	*0.72*	1.02	0.91	*1.13*
Paqr7	1.01	1.25	*0.81*	0.85	1.22	*0.70*	0.83	0.82	*1.01*
Pck1	0.79	1.63	*0.49*	1.15	2.19	*0.53*	0.72	0.76	*0.95*
Pdk1	0.96	1.19	*0.81*	0.85	1.18	*0.72*	0.84	0.91	*0.92*
Per1	0.45	1.94	*0.23*	0.59	3.11	*0.19*	1.09	1.35	*0.81*
Per2	0.43	2.46	*0.17*	0.36	3.30	*0.11*	0.79	1.52	*0.52*
Per3	0.53	1.87	*0.28*	0.49	2.85	*0.17*	0.69	1.24	*0.55*
Pex11a	0.98	1.39	*0.71*	0.82	1.25	*0.66*	1.02	1.11	*0.92*
Pik3ip1	0.77	1.25	*0.62*	0.82	1.25	*0.65*	0.98	1.04	*0.94*
Pim3	0.77	1.78	*0.43*	1.11	2.40	*0.46*	0.89	1.03	*0.86*
Plek2	0.91	1.25	*0.73*	1.07	1.63	*0.65*	0.89	0.87	*1.03*
Plk3	0.51	2.54	*0.20*	0.93	3.90	*0.24*	1.10	1.75	*0.63*
Pnpla2	0.79	1.27	*0.62*	0.85	1.37	*0.62*	1.02	0.97	*1.05*
Pnpla7	0.85	1.31	*0.65*	0.87	1.31	*0.66*	0.96	0.86	*1.12*
Podn	0.79	1.21	*0.65*	0.89	1.35	*0.66*	0.97	0.92	*1.05*
Ppm1h	1.11	0.69	*1.61*	1.20	0.74	*1.62*	1.14	0.95	*1.20*
Prkag3	0.56	1.80	*0.31*	0.66	1.45	*0.46*	1.05	1.27	*0.83*
Ptgis	0.78	1.54	*0.51*	0.75	1.53	*0.49*	0.97	1.09	*0.89*
Ptprd	1.01	1.08	*0.93*	0.98	1.35	*0.73*	0.87	0.75	*1.15*
Ptprk	1.10	0.82	*1.35*	1.32	0.95	*1.39*	0.97	0.96	*1.01*
Pxmp2	0.80	1.26	*0.63*	1.02	1.48	*0.69*	0.70	0.64	*1.09*
Rab43	0.90	1.28	*0.71*	0.80	1.14	*0.70*	0.98	1.02	*0.97*

Rab6b	0.90	1.28	*0.71*	0.59	0.98	*0.60*	1.08	1.24	*0.87*
Rabep2	0.78	0.98	*0.79*	0.87	1.16	*0.75*	1.06	1.02	*1.04*
Rasl11a	1.06	0.70	*1.52*	1.03	0.56	*1.86*	1.22	1.17	*1.04*
Rgs2	0.68	1.39	*0.49*	0.80	1.25	*0.64*	1.03	1.03	*1.00*
Ripk4	0.89	1.28	*0.70*	0.99	1.62	*0.61*	0.98	1.01	*0.97*
Rorc	0.77	1.81	*0.43*	0.93	1.71	*0.54*	0.90	1.18	*0.76*
Rtkn	0.83	1.24	*0.67*	0.86	1.38	*0.62*	0.99	0.98	*1.02*
Sema7a	0.74	1.30	*0.56*	0.70	1.22	*0.58*	1.05	1.41	*0.74*
Serpina7	1.27	0.42	*3.01*	1.77	0.78	*2.26*	1.72	1.05	*1.64*
Sgk1	0.84	2.59	*0.32*	1.06	3.23	*0.33*	1.30	1.60	*0.81*
Slc13a2	0.81	1.38	*0.59*	0.95	1.68	*0.56*	0.76	0.69	*1.10*
Slc22a12	1.54	0.85	*1.80*	1.55	0.69	*2.24*	0.89	0.65	*1.37*
Slc25a20	0.83	1.42	*0.58*	0.87	1.52	*0.57*	0.86	1.02	*0.84*
Slc25a33	0.84	1.67	*0.50*	0.95	1.75	*0.54*	0.94	0.96	*0.99*
Slc25a34	0.92	1.22	*0.75*	0.85	1.41	*0.60*	0.87	0.92	*0.94*
Slc46a3	0.86	1.56	*0.55*	0.85	1.86	*0.45*	0.72	0.91	*0.79*
Smarca2	0.92	1.22	*0.76*	0.91	1.22	*0.75*	0.86	0.90	*0.95*
Smpdl3b	0.91	1.75	*0.52*	0.59	0.98	*0.60*	2.36	2.48	*0.95*
Snrk	0.97	1.43	*0.68*	0.96	1.39	*0.69*	0.98	1.01	*0.97*
Spsb3	1.11	0.80	*1.38*	1.12	0.77	*1.45*	1.07	0.98	*1.09*
Srebf1	1.19	0.82	*1.45*	1.43	0.90	*1.59*	0.96	0.86	*1.12*
St5	1.03	0.78	*1.32*	1.10	0.72	*1.53*	1.09	0.98	*1.11*
St6galnac2	0.76	1.16	*0.66*	0.86	1.10	*0.78*	1.17	1.17	*1.00*
Stc2	1.22	0.80	*1.54*	0.93	0.60	*1.54*	1.60	1.32	*1.21*
Stk35	0.87	1.14	*0.77*	0.94	1.30	*0.73*	1.00	1.08	*0.92*
Stx18	1.29	0.83	*1.56*	1.53	0.89	*1.72*	1.19	0.92	*1.29*
Sult1a1	0.71	1.36	*0.52*	1.03	1.86	*0.55*	1.03	0.88	*1.17*
Sult1d1	1.01	1.17	*0.87*	0.94	1.24	*0.76*	0.99	1.00	*0.98*
Susd3	0.77	2.09	*0.37*	0.84	2.41	*0.35*	0.83	1.03	*0.80*
Syt12	0.65	1.20	*0.54*	0.83	1.05	*0.79*	1.12	1.14	*0.98*
Taf1d	0.82	0.98	*0.83*	0.91	1.18	*0.77*	1.14	1.00	*1.14*
Tchhl1	1.20	0.66	*1.83*	1.38	0.91	*1.51*	1.06	1.04	*1.01*
Tef	0.69	1.62	*0.43*	0.63	2.00	*0.32*	0.69	1.16	*0.59*
Tmem108	1.20	0.74	*1.63*	1.48	0.81	*1.82*	0.98	0.93	*1.05*
Tmem218	1.17	0.89	*1.31*	1.40	0.99	*1.42*	0.96	0.84	*1.13*
Tmem57	0.90	1.27	*0.71*	0.79	1.19	*0.67*	0.89	1.00	*0.88*
Tnfrsf21	0.87	1.70	*0.51*	0.77	1.96	*0.40*	0.95	1.20	*0.80*
Tnnc1	0.76	1.62	*0.47*	0.68	1.98	*0.34*	0.93	1.26	*0.74*
Tnxb	0.86	1.29	*0.67*	0.71	1.28	*0.56*	0.83	0.95	*0.87*
Tob2	0.86	2.19	*0.39*	0.67	1.66	*0.40*	1.40	1.31	*1.07*
Trib1	0.86	1.33	*0.65*	0.75	1.21	*0.62*	1.15	1.02	*1.12*

Tsc22d3	0.74	2.85	*0.26*	0.85	2.81	*0.30*	1.12	1.47	*0.76*
Tsku	0.71	1.98	*0.36*	0.67	1.35	*0.49*	0.96	1.11	*0.86*
Tspan14	1.16	0.92	*1.26*	1.25	0.93	*1.35*	1.01	0.98	*1.03*
Tspan4	0.70	1.54	*0.45*	0.76	1.33	*0.57*	0.93	1.11	*0.84*
Ttn	1.34	0.72	*1.85*	1.38	0.98	*1.42*	0.99	1.11	*0.90*
Ttpa	0.91	1.60	*0.57*	0.85	1.22	*0.70*	1.00	1.05	*0.95*
Tuba4a	1.21	0.84	*1.44*	1.24	0.92	*1.35*	1.03	0.98	*1.05*
Tut1	0.85	1.19	*0.71*	0.93	1.24	*0.75*	1.02	0.99	*1.03*
Unc5c	1.37	0.75	*1.84*	1.37	0.84	*1.63*	1.03	0.87	*1.18*
Upp2	0.83	1.99	*0.42*	0.87	2.04	*0.42*	0.76	0.98	*0.78*
Usp2	0.73	2.30	*0.32*	0.72	2.33	*0.31*	0.98	1.07	*0.91*
Vasn	0.85	1.28	*0.66*	0.92	1.47	*0.63*	1.12	1.21	*0.92*
Wnt5b	0.83	1.61	*0.52*	0.94	2.01	*0.47*	0.79	0.88	*0.90*
Xdh	0.84	1.30	*0.65*	0.73	1.22	*0.60*	1.02	1.15	*0.89*
Not corrected									
Symbol									
4930404N11Rik	*0.70*	*1.08*	*0.65*	*1.24*	*0.88*	*1.41*	*0.99*	*0.97*	*1.02*
Aacs	*1.12*	*1.42*	*0.79*	*1.10*	*1.98*	*0.55*	*0.69*	*0.80*	*0.86*
Abcd3	*0.95*	*1.21*	*0.79*	*0.79*	*1.24*	*0.64*	*0.90*	*0.98*	*0.92*
Acot11	*1.04*	*1.05*	*0.99*	*0.92*	*1.21*	*0.76*	*0.90*	*0.87*	*1.02*
Acot12	*1.15*	*1.33*	*0.86*	*0.88*	*1.48*	*0.60*	*0.81*	*0.84*	*0.96*
Acsm5	*0.98*	*1.02*	*0.96*	*1.05*	*1.35*	*0.78*	*0.79*	*0.74*	*1.07*
Acvr2b	*0.87*	*1.03*	*0.85*	*0.61*	*1.77*	*0.34*	*0.93*	*1.09*	*0.85*
Alox12	*1.00*	*1.02*	*0.98*	*0.95*	*1.41*	*0.67*	*0.95*	*1.03*	*0.92*
Asah2	*1.21*	*1.01*	*1.20*	*0.80*	*1.11*	*0.72*	*0.96*	*0.91*	*1.05*
Atp1b1	*1.11*	*1.00*	*1.11*	*0.81*	*1.11*	*0.73*	*1.01*	*0.98*	*1.04*
Avpr1a	*1.29*	*0.69*	*1.85*	*1.81*	*0.56*	*3.22*	*1.10*	*0.85*	*1.30*
BC022687	*1.10*	*0.81*	*1.35*	*1.60*	*0.68*	*2.36*	*0.98*	*0.79*	*1.23*
Calr	*1.13*	*0.80*	*1.41*	*1.52*	*0.82*	*1.87*	*1.23*	*1.05*	*1.17*
Cd300lg	*1.03*	*1.27*	*0.81*	*0.81*	*1.46*	*0.55*	*0.66*	*0.65*	*1.01*
Cdkn1a	*0.86*	*1.52*	*0.56*	*1.05*	*0.56*	*1.88*	*1.88*	*1.68*	*1.12*
Cdr2	*1.13*	*1.38*	*0.82*	*1.01*	*1.42*	*0.71*	*1.05*	*1.14*	*0.92*
Chrna4	*0.96*	*0.75*	*1.27*	*1.87*	*0.77*	*2.44*	*0.83*	*0.78*	*1.06*
Corin	*1.19*	*0.41*	*2.89*	*0.85*	*1.48*	*0.57*	*0.65*	*0.81*	*0.80*
Csdc2	*1.06*	*0.83*	*1.28*	*1.33*	*0.89*	*1.49*	*1.15*	*0.97*	*1.18*
Ctps	*0.97*	*1.12*	*0.87*	*0.76*	*1.07*	*0.71*	*1.20*	*1.23*	*0.98*
D630023F18Rik	*1.15*	*0.87*	*1.33*	*1.84*	*0.69*	*2.69*	*1.03*	*0.77*	*1.33*
Ddc	*1.81*	*0.75*	*2.42*	*3.04*	*0.69*	*4.39*	*1.06*	*0.69*	*1.53*
Defb1	*1.17*	*0.93*	*1.26*	*1.60*	*0.95*	*1.69*	*0.90*	*0.76*	*1.18*
Dlat	*1.16*	*1.06*	*1.09*	*0.85*	*1.16*	*0.73*	*0.93*	*0.89*	*1.05*

Dnajc6	*1.30*	*0.99*	*1.31*	*0.86*	*1.72*	*0.50*	*0.68*	*0.72*	*0.94*
Dtx4	*0.92*	*0.67*	*1.37*	*1.29*	*0.43*	*3.02*	*1.44*	*1.11*	*1.29*
Elfn1	*1.83*	*0.97*	*1.89*	*0.78*	*1.31*	*0.59*	*1.05*	*0.76*	*1.38*
Enox1	*1.17*	*1.12*	*1.04*	*1.01*	*1.56*	*0.65*	*1.06*	*1.27*	*0.84*
Entpd5	*1.08*	*1.05*	*1.03*	*0.81*	*1.23*	*0.65*	*0.80*	*0.93*	*0.86*
Esrrb	*1.31*	*1.13*	*1.16*	*0.89*	*1.42*	*0.63*	*0.91*	*0.89*	*1.02*
Ethe1	*1.21*	*0.70*	*1.72*	*2.23*	*0.41*	*5.49*	*1.25*	*0.83*	*1.51*
G0s2	*0.91*	*1.30*	*0.70*	*1.52*	*1.05*	*1.45*	*0.85*	*0.77*	*1.11*
Gdpd2	*0.60*	*1.01*	*0.60*	*1.25*	*0.78*	*1.61*	*1.23*	*1.01*	*1.22*
Gfpt2	*1.18*	*0.87*	*1.36*	*1.30*	*0.85*	*1.52*	*1.04*	*0.87*	*1.20*
Il15	*0.91*	*1.00*	*0.91*	*0.91*	*1.49*	*0.61*	*0.74*	*0.91*	*0.81*
Kcnab2	*1.00*	*1.25*	*0.80*	*1.14*	*0.77*	*1.47*	*1.19*	*1.09*	*1.09*
Kif13a	*1.17*	*1.08*	*1.09*	*0.88*	*1.22*	*0.72*	*1.00*	*1.01*	*0.99*
Klf1	*0.93*	*0.96*	*0.97*	*1.03*	*1.61*	*0.64*	*0.81*	*0.80*	*1.01*
Lgmn	*0.87*	*1.12*	*0.77*	*1.20*	*0.85*	*1.41*	*1.06*	*1.11*	*0.95*
Lhfpl2	*1.03*	*0.75*	*1.37*	*1.18*	*0.66*	*1.78*	*1.29*	*1.19*	*1.08*
Lpin2	*1.27*	*0.92*	*1.37*	*0.76*	*1.02*	*0.75*	*1.12*	*1.12*	*1.00*
Lrig3	*1.06*	*1.00*	*1.06*	*0.84*	*1.18*	*0.71*	*0.98*	*1.04*	*0.94*
Masp2	*1.24*	*0.78*	*1.59*	*0.91*	*1.44*	*0.64*	*1.03*	*0.85*	*1.21*
Mif4gd	*1.11*	*0.84*	*1.32*	*1.33*	*0.84*	*1.58*	*1.08*	*0.96*	*1.13*
Mmp15	*1.09*	*0.76*	*1.43*	*1.12*	*0.60*	*1.85*	*1.22*	*1.05*	*1.16*
Mpp5	*1.08*	*1.14*	*0.95*	*0.85*	*1.13*	*0.75*	*0.96*	*0.99*	*0.97*
Mpv17l	*1.32*	*1.04*	*1.26*	*0.94*	*1.67*	*0.56*	*0.77*	*0.90*	*0.86*
Mtss1	*0.94*	*1.10*	*0.85*	*0.91*	*1.35*	*0.67*	*0.95*	*1.03*	*0.92*
Narf	*0.94*	*1.11*	*0.85*	*0.76*	*1.15*	*0.66*	*0.90*	*0.96*	*0.94*
Neu2	*1.05*	*1.19*	*0.89*	*0.75*	*1.27*	*0.59*	*0.79*	*0.88*	*0.90*
Nfib	*0.91*	*1.06*	*0.85*	*0.91*	*1.27*	*0.72*	*0.85*	*0.94*	*0.91*
Ngef	*0.94*	*1.17*	*0.80*	*0.88*	*1.42*	*0.62*	*0.82*	*0.84*	*0.98*
Notch4	*0.95*	*0.99*	*0.96*	*0.85*	*1.13*	*0.76*	*0.98*	*1.02*	*0.96*
Nphs2	*1.27*	*0.88*	*1.44*	*1.63*	*0.77*	*2.12*	*1.12*	*1.14*	*0.99*
Nudt19	*1.40*	*1.93*	*0.73*	*0.98*	*2.24*	*0.44*	*0.49*	*0.67*	*0.74*
Osr2	*1.05*	*0.78*	*1.35*	*1.67*	*1.05*	*1.59*	*0.99*	*0.80*	*1.23*
P2ry14	*0.88*	*1.00*	*0.88*	*0.69*	*1.21*	*0.57*	*0.97*	*1.15*	*0.84*
Pcdh17	*1.02*	*0.94*	*1.09*	*0.73*	*1.32*	*0.55*	*0.72*	*0.80*	*0.90*
Pcgf5	*1.11*	*1.21*	*0.92*	*0.87*	*1.29*	*0.67*	*0.97*	*1.05*	*0.93*
Pcsk9	*1.18*	*0.86*	*1.37*	*2.93*	*0.90*	*3.25*	*1.03*	*0.73*	*1.42*
Polg2	*1.01*	*1.07*	*0.94*	*0.96*	*1.35*	*0.71*	*0.79*	*0.79*	*1.01*
Por	*1.07*	*1.21*	*0.88*	*0.88*	*1.69*	*0.52*	*0.78*	*0.90*	*0.87*
Ppargc1a	*1.10*	*0.93*	*1.18*	*0.74*	*1.09*	*0.68*	*0.97*	*1.00*	*0.98*
Ppp1r9a	*1.00*	*0.78*	*1.28*	*0.90*	*1.15*	*0.78*	*0.93*	*0.93*	*0.99*
Ppp2r5e	*0.99*	*1.15*	*0.86*	*0.87*	*1.17*	*0.74*	*0.99*	*1.03*	*0.96*

Ppp3cc	1.03	1.19	0.86	0.89	1.30	0.68	0.91	0.93	0.97
Prmt2	1.16	0.90	1.29	1.13	0.71	1.61	1.15	1.09	1.06
Prnp	0.93	1.38	0.67	0.77	1.55	0.49	0.93	1.19	0.77
Ptpn22	0.68	1.31	0.51	0.99	0.61	1.60	1.21	1.42	0.85
Rsad1	0.98	1.07	0.92	0.84	1.17	0.72	0.97	0.91	1.06
Rxrg	1.42	0.97	1.45	1.75	0.83	2.11	1.00	0.64	1.57
Sall2	1.04	0.79	1.31	1.62	0.81	1.99	1.03	0.82	1.26
Sdc3	0.89	1.07	0.84	0.62	1.05	0.59	1.02	1.28	0.80
Sema3f	1.00	1.09	0.92	0.74	0.95	0.78	1.17	1.19	0.98
Slc12a6	0.85	1.15	0.74	0.78	1.73	0.45	0.85	1.05	0.81
Slc16a1	1.23	0.85	1.44	1.74	0.86	2.03	1.14	0.99	1.15
Slc16a9	0.87	1.41	0.61	0.67	1.94	0.34	0.66	0.94	0.70
Slc17a2	1.17	0.81	1.45	1.10	2.24	0.49	0.62	0.48	1.30
Slc1a3	1.10	1.16	0.95	0.83	1.40	0.59	0.89	1.05	0.85
Slc22a4	0.96	1.19	0.81	0.89	1.50	0.59	0.71	0.83	0.85
Slc22a5	0.98	1.25	0.78	0.83	1.41	0.59	0.84	0.95	0.88
Slc25a35	1.04	0.98	1.06	0.97	1.24	0.78	0.88	0.86	1.02
Slc25a42	0.89	1.43	0.62	0.76	1.70	0.45	0.84	1.09	0.77
Slc27a2	1.19	1.05	1.14	0.88	1.26	0.70	0.83	0.91	0.92
Slc2a13	1.74	0.99	1.75	0.91	1.83	0.50	0.79	0.87	0.90
Slc5a2	0.78	1.18	0.66	1.96	1.08	1.82	0.95	0.84	1.13
Slc5a3	1.69	1.06	1.60	0.80	1.14	0.70	1.26	1.09	1.16
Slc5a6	1.16	1.22	0.95	0.91	2.02	0.45	0.66	0.62	1.06
Slc5a8	1.29	1.66	0.77	0.85	2.08	0.41	0.79	0.85	0.93
Slc7a8	1.23	0.86	1.43	2.24	0.73	3.05	1.14	0.79	1.45
Slco2a1	1.03	1.09	0.95	0.91	1.26	0.72	0.97	0.98	0.99
Slit2	0.98	1.34	0.73	0.90	1.60	0.56	0.83	0.93	0.90
Spsb4	1.25	0.87	1.43	1.50	0.78	1.92	1.10	0.93	1.18
Srd5a1	0.95	1.07	0.89	0.77	1.04	0.73	1.10	1.19	0.92
Stim1	1.06	1.21	0.87	0.81	1.28	0.64	1.00	1.04	0.97
Stk32b	1.07	1.26	0.85	0.95	1.53	0.62	0.92	0.99	0.93
Stxbp4	1.09	0.90	1.21	0.84	1.46	0.57	0.94	1.05	0.90
Sult1c2	1.18	0.90	1.31	1.40	0.91	1.54	0.97	0.81	1.20
Sumo3	1.15	0.86	1.34	1.36	0.81	1.68	1.08	0.94	1.14
Sypl2	0.91	1.26	0.72	0.93	1.67	0.55	0.75	0.97	0.77
Tbxas1	1.07	0.70	1.52	2.28	0.94	2.44	0.90	0.68	1.33
Timm8a1	0.98	1.08	0.91	0.90	1.26	0.71	0.84	0.91	0.92
Tmem45b	0.88	1.06	0.83	0.88	1.24	0.72	0.89	0.97	0.93
Tmem53	1.07	0.84	1.27	1.50	0.95	1.57	0.95	0.80	1.19
Tppp	1.03	1.17	0.88	1.06	1.52	0.70	0.79	0.84	0.93
Trak2	1.18	1.02	1.16	0.88	1.20	0.74	0.92	0.97	0.94

Trp53bp2	*1.07*	*1.13*	*0.95*	*0.88*	*1.30*	*0.67*	*0.99*	*0.94*	*1.05*
Ttc22	*1.06*	*0.66*	*1.61*	*1.36*	*0.70*	*1.96*	*1.11*	*0.86*	*1.29*
Vps37d	*0.98*	*0.70*	*1.39*	*1.22*	*0.63*	*1.94*	*1.10*	*0.72*	*1.52*
Wsb1	*0.95*	*0.60*	*1.58*	*1.71*	*0.64*	*2.65*	*1.17*	*1.11*	*1.06*
Yaf2	*1.17*	*1.12*	*1.05*	*0.88*	*1.15*	*0.76*	*0.91*	*0.95*	*0.97*
Zbtb7a	*1.12*	*1.03*	*1.09*	*0.83*	*1.16*	*0.71*	*1.16*	*1.22*	*0.95*
Zc3h6	*0.98*	*0.97*	*1.01*	*0.84*	*1.08*	*0.78*	*0.83*	*0.83*	*1.00*
Zfp612	*0.86*	*0.88*	*0.98*	*0.85*	*1.14*	*0.74*	*1.00*	*1.07*	*0.93*
Zhx3	*1.31*	*1.22*	*1.08*	*0.89*	*1.52*	*0.59*	*1.11*	*1.26*	*0.88*

Supplementary Table 5: Pathway analysis of 320 diurnally regulated genes corrected and not corrected by remission induction				
Corrected by remission induction				
Categories	**Diseases or Functions Annotation**	**Molecules**	**p-value**	**# Molecules**
Behavior,Nervous System Development and Function	Circadian rhythm	ARNTL,CLOCK,CRY2,DBP,KLF10,NAMPT,NPAS2,NR1D1,NR1D2,PER1,PER2,PER3,SREBF1	6.52E-11	13
Cancer,Organismal Injury and Abnormalities	Cancer,Organismal Injury and Abnormalities	ACAT2,ACOT1,ACOX3,AIFM2,AK5,ALAS1,AMT,ANGPTL4,ANKRD12,AQP8,ARHGEF3,ARNTL,AZIN1,BLVRB,C11orf65,CA5B,CDC42EP4,CDKL1,CDO1,CHST1,CHST8,CITED4,CKB,CLCN2,CLDN10,CLOCK,CLPX,CLSTN3,COL27A1,COL4A4,COQ10B,CORO2A,CPEB3,CPT2,CREB3L1,CRY2,CSNK1G3,CTGF,CYGB,CYP27A1,CYP2A6 (includes others),P2E1,DBP,DCUN1D3,DGAT2,DHRS7,DLEU7,DNASE1,DUSP1,DUSP7,EEF2K,EFHD1,EIF4EBP3,EPHX1,ERRFI1,FABP3,FAM102A,FAM163A,FERMT1,FFAR3,FKBP5,FOXO1,GJA1,GLDC,GLUL,GNPDA1,GRASP,GSTT2/GSTT2B,GYPC,HERPUD1,HSPB6,IDH1,IER3,IFRD2,IGFBP4,IGFBP5,IL17F,IL17RB,IMMP2L,INSC,ITGA6,ITGB6,ITPRIP,KCNJ15,KCNK5,KIF27,KLF10,KLF13,KLF6,KLF9,KLHL21,LAMA1,LEO1,LONRF1,LPIN1,LRRC40,LYRM1,MAP3K6,MBD1,MKNK2,MPP4,MREG,MYO9A,NAMPT,NAT1,NCALD,NFKBIA,NID2,NPAS2,NR1D1,NR1D2,NR1H4,OSBPL9,PANK1,PAOX,PAQR7,PCK1,PDK1,PER1,PER2,PER3,PEX11A,PIK3IP1,PIM3,PLEK2,PLK3,PNPLA2,PNPLA7,PODN,PPM1H,PRKAG3,PTGIS,PTPRK,PXMP2,RAB43,RAB6B,RABEP2,RASL11A,RGS2,RIPK4,RORC,RTKN,SEMA7A,SERPINA7,SGK1,SLC13A2,SLC22A12,SLC25A20,SLC25A33,SLC25A34,SLC46A3,SMARCA2,SMPDL3B,SNRK,SPSB3,SREBF1,ST5,ST6GALNAC2,STC2,STK35,STX18,SUS	6.62E-08	185

Cancer,Organismal Injury and Abnormalities	Cancer,Organismal Injury and Abnormalities	ACAT2,ACOT1,ACOX3,AIFM2,AK5,ALAS1,AMT,ANGPTL4,ANKRD12,AQP8,ARHGEF3,ARNTL,AZIN1,BLVRB,C11orf65,CA5B,CDC42EP4,CDKL1,CDO1,CHST1,CHST8,CITED4,CKB,CLCN2,CLDN10,CLOCK,CLPX,CLSTN3,COL27A1,COL4A4,COQ10B,CORO2A,CPEB3,CPT2,CREB3L1,CRY2,CSNK1G3,CTGF,CYGB,CYP27A1,CYP2A6 (includes others),P2E1,DBP,DCUN1D3,DGAT2,DHRS7,DLEU7,DNASE1,DUSP1,DUSP7,EEF2K,EFHD1,EIF4EBP3,EPHX1,ERRFI1,FABP3,FAM102A,FAM163A,FERMT1,FFAR3,FKBP5,FOXO1,GJA1,GLDC,GLUL,GNPDA1,GRASP,GSTT2/GSTT2B,GYPC,HERPUD1,HSPB6,IDH1,IER3,IFRD2,IGFBP4,IGFBP5,IL17F,IL17RB,IMMP2L,INSC,ITGA6,ITGB6,ITPRIP,KCNJ15,KCNK5,KIF27,KLF10,KLF13,KLF6,KLF9,KLHL21,LAMA1,LEO1,LONRF1,LPIN1,LRRC40,LYRM1,MAP3K6,MBD1,MKNK2,MPP4,MREG,MYO9A,NAMPT,NAT1,NCALD,NFKBIA,NID2,NPAS2,NR1D1,NR1D2,NR1H4,OSBPL9,PANK1,PAOX,PAQR7,PCK1,PDK1,PER1,PER2,PER3,PEX11A,PIK3IP1,PIM3,PLEK2,PLK3,PNPLA2,PNPLA7,PODN,PPM1H,PRKAG3,PTGIS,PTPRK,PXMP2,RAB43,RAB6B,RABEP2,RASL11A,RGS2,RIPK4,RORC,RTKN,SEMA7A,SERPINA7,SGK1,SLC13A2,SLC22A12,SLC25A20,SLC25A33,SLC25A34,SLC46A3,SMARCA2,SMPDL3B,SNRK,SPSB3,SREBF1,ST5,ST6GALNAC2,STC2,STK35,STX18,SUSD3,SYT12,TAF1D,TCHHL1,TEF,TMEM108,TNFRSF21,TNXB,TOB2,TRIB1,TSC22D3,TSKU,TSPAN14,TSPAN4,TTN,TTPA,TUBA4A,TUT1,UNC5C,UPP2,USP2,VASN,WNT5B,XDH	6.62E-08	185
Carbohydrate Metabolism,Small Molecule Biochemistry	Synthesis of D-hexose	FOXO1,GNPDA1,IDH1,NR1H4,PCK1,RORC,SREBF1,USP2	4.97E-06	8

Carbohydrate Metabolism,Molecular Transport	Quantity of glycogen	DGAT2,DUSP1,FABP3,FOXO1,NR1H4,PCK1,PNPLA2,PRKAG3	9.15E-06	8
Carbohydrate Metabolism,Molecular Transport,Small Molecule Biochemistry	Concentration of D-glucose	ARNTL,CA5B,CDO1,CRY2,DGAT2,FABP3,FOXO1,IGFBP4,IGFBP5,LPIN1,NR1H4,PANK1,PCK1,PNPLA2,SREBF1	1.64E-05	15
Carbohydrate Metabolism,Cellular Function and Maintenance,Small Molecule Biochemistry	Homeostasis of D-glucose	ANGPTL4,ARNTL,CRY2,FFAR3,FOXO1,IGFBP4,IGFBP5,NR1H4,PCK1,PRKAG3,TSC22D3	4.82E-05	11
Carbohydrate Metabolism	Quantity of carbohydrate	ARNTL,CA5B,CDO1,CHST1,CRY2,CTGF,DGAT2,DUSP1,FABP3,FOXO1,IGFBP4,IGFBP5,LPIN1,NR1H4,PANK1,PCK1,PNPLA2,PRKAG3,SREBF1	6.66E-05	19
Cell Death and Survival	Apoptosis	AIFM2,ANGPTL4,AQP11,ARHGEF3,CLCN2,COL4A4,CTGF,CYGB,CYP2E1,DCUN1D3,DLEU7,DNASE1,DUSP1,EEF2K,EPHX1,ERRFI1,FFAR3,FKBP5,FOXO1,GJA1,HERPUD1,HSPB6,IER3,IGFBP4,IGFBP5,IL17RB,ITGA6,KLF10,KLF13,KLF6,KLF9,LAMA1,NAMPT,NFKBIA,NR1D1,NR1H4,NRG4,PDK1,PER1,PIK3IP1,PIM3,PLK3,PNPLA2,PTGIS,RORC,RTKN,SEMA7A,SGK1,SMARCA2,SNRK,SREBF1,STK35,TNFRSF21,TRIB1,TSC22D3,TTN,TTPA,UNC5C,USP2,VASN,XDH	2.86E-05	61
Cell Death and Survival,Organismal Injury and Abnormalities	Necrosis of epithelial tissue	CYGB,CYP2E1,EEF2K,FOXO1,IER3,IGFBP5,ITGA6,KLF10,NAMPT,NFKBIA,NR1H4,NRG4,PLK3,PTGIS,SEMA7A,SGK1,STK35,TNFRSF21,USP2,VASN,XDH	3.41E-05	21

Cell Death and Survival	Necrosis	AQP11,ARHGEF3,AVPI1,Clec2d (includes others),CLOCK,CREB3L1,CTGF,CYGB,CYP2E1,DLEU7,DNASE1,DUSP1,EEF2K,EPHX1,FABP3,FKBP5,FOXO1,GJA1,HERPUD1,HSPB6,IER3,IGFBP4,IGFBP5,IL17RB,ITGA6,ITPRIP,KLF10,KLF13,KLF6,KLF9,MBD1,NAMPT,NFKBIA,NR1D1,NR1H4,NRG4,PDK1,PER1,PEX11A,PIK3IP1,PIM3,PLK3,PNPLA2,PTGIS,RORC,RTKN,SEMA7A,SGK1,SNRK,SREBF1,STK35,TNFRSF21,TRIB1,TSC22D3,TTN,TTPA,UNC5C,USP2,VASN,XDH	7.05E-05	60
Lipid Metabolism,Molecular Transport,Small Molecule Biochemistry	Concentration of triacylglycerol	ACAT2,ANGPTL4,AQP8,ARNTL,CYP27A1,DGAT2,DUSP1,FFAR3,FOXO1,IDH1,LPIN1,NAMPT,NR1H4,PANK1,PCK1,PEX11A,PNPLA2,SNRK,SREBF1,TRIB1,XDH	6.42E-10	21
Lipid Metabolism,Molecular Transport,Small Molecule Biochemistry	Concentration of fatty acid	ANGPTL4,ARNTL,CYP27A1,CYP2E1,DGAT2,DUSP1,FABP3,FOXO1,IDH1,LPIN1,NR1H4,PANK1,PCK1,PEX11A,PNPLA2,PTGIS,SNRK,SREBF1,XDH	2.37E-09	19
Metabolic Disease,Organismal Injury and Abnormalities	Abnormal metabolism	ACAT2,ANGPTL4,ARNTL,CPT2,CTGF,FOXO1,IDH1,IGFBP4,IGFBP5,ITGB6,LPIN1,NR1H4,PANK1,PCK1,PNPLA2,SLC25A20,SREBF1,TNFRSF21,TRIB1	2.11E-07	19
Lipid Metabolism,Molecular Transport,Small Molecule Biochemistry	Concentration of lipid	ACAT2,ANGPTL4,AQP8,ARNTL,CHST8,CLOCK,CRY2,CYP27A1,CYP2E1,DGAT2,DUSP1,FABP3,FFAR3,FOXO1,IDH1,LPIN1,NAMPT,NR1H4,PANK1,PCK1,PEX11A,PNPLA2,PTGIS,SGK1,SNRK,SREBF1,TRIB1,TSC22D3,TTPA,XDH	4.85E-07	30
Lipid Metabolism,Small Molecule Biochemistry	Homeostasis of lipid	ANGPTL4,ARNTL,CYP27A1,DGAT2,FABP3,NR1D1,NR1D2,NR1H4,PNPLA2,SREBF1,TTPA,XDH	3.53E-06	12
Lipid Metabolism,Small Molecule Biochemistry	Metabolism of acylglycerol	CYP2E1,DGAT2,EPHX1,FABP3,FOXO1,LPIN1,PNPLA2,RGS2,SREBF1,TNXB	3.98E-06	10
Lipid Metabolism,Molecular Transport,Small Molecule	Accumulation of triacylglycerol	ACAT2,FOXO1,LPIN1,NR1H4,PNPLA2,PRKAG3,SREBF1	9.29E-05	7

Biochemistry				
Organ Morphology,Organismal Development	Mass of genitourinary system	AQP8,ARNTL,CHST8,CYP27A1,DUSP1,ERRFI1,FFAR3,IGFBP4,NR1H4,PANK1,PCK1,PNPLA2,TRIB1,TSC22D3	2.57E-05	14
Organismal Development	Development of genitourinary system	AQP11,AQP8,ARNTL,CDO1,CHST8,CLCN2,CLOCK,COL4A4,CTGF,CYP27A1,DUSP1,EEF2K,ERRFI1,FFAR3,GJA1,IGFBP4,IGFBP5,IMMP2L,ITGA6,KLF6,NR1H4,PANK1,PCK1,PNPLA2,SREBF1,TOB2,TRIB1,TSC22D3,TTPA,XDH	2.01E-05	30
Cardiovascular System Development and Function,Hematological System Development and Function	Blood pressure	ARNTL,DBP,DUSP1,FFAR3,IER3,KCNK5,NFKBIA,PTGIS,RGS2,SGK1,TEF,TTN	0.00029	12
Cardiovascular Disease,Organismal Injury and Abnormalities	Atherosclerosis	ACAT2,ANGPTL4,CA5B,CORO2A,CPEB3,CYP27A1,FOXO1,GJA1,KLF6,NFKBIA,NR1H4,SREBF1,TTPA,TUBA4A,XDH	0.0013	15
Cardiovascular Disease,Organismal Injury and Abnormalities	Occlusion of artery	ACAT2,ANGPTL4,CA5B,CORO2A,CPEB3,CYP27A1,FOXO1,GJA1,KLF6,NFKBIA,NR1H4,SREBF1,TTN,TTPA,TUBA4A,XDH	0.0017	16
Not corrected by remission induction				
Categories	**Diseases or Functions Annotation**	**Molecules**	**p-value**	**# Molecules**

Cancer,Organismal Injury and Abnormalities	Cancer,Organismal Injury and Abnormalities	AACS,ABCD3,ACOT11,ACOT12,ACSM5,ACVR2B,ALOX12,ASAH2,ATP1B1,AVPR1A,C19orf71,CALR,CD300LG,CDKN1A,CDR2,CHRNA4,CLBA1,CORIN,CSDC2,CTPS1,DDC,DLAT,DNAJC6,DTX4,ELFN1,ENOX1,ENTPD5,ESRRB,ETHE1,G0S2,GDPD2,GFPT2,IL15,KCNAB2,KIF13A,KLF1,LGMN,LHFPL2,LPIN2,LRIG3,MASP2,MIF4GD,MMP15,MPP5,MPV17L,MTSS1,NARF,NEU2,NFIB,NGEF,NOTCH4,NPHS2,NUDT19,OSR2,P2RY14,PCDH17,PCGF5,PCSK9,POLG2,POR,PPARGC1A,PPP1R9A,PPP2R5E,PPP3CC,PRMT2,PRNP,PTPN22,RSAD1,RXRG,SALL2,SDC3,SEMA3F,SLC12A6,SLC16A1,SLC16A9,SLC17A2,SLC1A3,SLC22A4,SLC22A5,SLC25A35,SLC25A42,SLC27A2,SLC2A13,SLC5A2,SLC5A3,SLC5A6,SLC5A8,SLC7A8,SLCO2A1,SLIT2,SPSB4,SRD5A1,STIM1,STK32B,STXBP4,SULT1C2,SUMO3,SYPL2,TBXAS1,TIMM8A,TMEM45B,TMEM53,TP53BP2,TPPP,TRAK2,TTC22,VPS37D,WSB1,ZBTB7A,ZC3H6,ZHX3,ZNF23	9.69E-11	112
Lipid Metabolism,Small Molecule Biochemistry	Fatty acid metabolism	AACS,ABCD3,ACOT11,ACOT12,ALOX12,ASAH2,AVPR1A,DLAT,IL15,NUDT19,POR,PPARGC1A,PRNP,SLC16A1,SLC1A3,SLC22A5,SLC27A2,SLCO2A1,STIM1,TBXAS1	7.77E-09	20
Energy Production,Lipid Metabolism,Small Molecule Biochemistry	Oxidation of lipid	ABCD3,ACOT11,ALOX12,G0S2,IL15,POR,PPARGC1A,SLC22A5,SLC27A2,SLCO2A1	1.47E-06	10
Lipid Metabolism,Molecular Transport,Small Molecule Biochemistry	Concentration of lipid	ACOT11,ALOX12,ASAH2,AVPR1A,CDKN1A,ENTPD5,G0S2,NEU2,PCSK9,POR,PPARGC1A,PRNP,RXRG,SLC5A3,SLCO2A1,SRD5A1	0.000451	16
Lipid Metabolism,Small Molecule Biochemistry	Synthesis of lipid	ABCD3,ALOX12,ASAH2,AVPR1A,DLAT,IL15,LPIN2,POR,PPARGC1A,PRNP,SLC1A3,SLC27A2,SRD5A1,STIM1,TBXAS1	0.00107	15
Molecular Transport	Transport of carboxylic acid	ABCD3,PRNP,SLC16A1,SLC1A3,SLC27A2,SLC5A6,SLC5A8,SLCO2A1	3.13E-07	8

Molecular Transport	Transport of molecule	ABCD3,ATP1B1,AVPR1A,CALR,CHRNA4,DDC,IL15,KIF13A,PPARGC1A,PRNP,PTPN22,SLC12A6,SLC16A1,SLC17A2,SLC1A3,SLC22A4,SLC22A5,SLC25A42,SLC27A2,SLC2A13,SLC5A2,SLC5A3,SLC5A6,SLC5A8,SLC7A8,SLCO2A1,STIM1,TRAK2	3.21E-05	28
Organismal Survival	Organismal death	ACVR2B,ALOX12,ATP1B1,CALR,CDKN1A,CHRNA4,Defb1,DNAJC6,ESRRB,ETHE1,IL15,KCNAB2,KLF1,MIF4GD,MMP15,MTSS1,NFIB,NOTCH4,NPHS2,POLG2,POR,PPARGC1A,PPP1R9A,PRNP,SALL2,SLC1A3,SLC22A4,SLC22A5,SLC5A3,SLCO2A1,SLIT2,STIM1,SUMO3,TP53BP2,ZBTB7A	0.000197	35
Cell Death and Survival	Apoptosis of tumor cell lines	ACSM5,ACVR2B,ALOX12,CALR,CDKN1A,ENTPD5,ETHE1,G0S2,IL15,NEU2,NFIB,NOTCH4,PPARGC1A,PRNP,PTPN22,SALL2,SEMA3F,SLC5A8,STIM1,SUMO3,TP53BP2,WSB1	0.000274	22

frontiers in Neurology

ORIGINAL RESEARCH
published: 13 October 2021
doi: 10.3389/fneur.2021.721108

Contributions of Sex Chromosomes and Gonadal Hormones to the Male Bias in a Maternal Antibody-Induced Model of Autism Spectrum Disorder

Adriana Gata-Garcia[1,2], *Amit Porat*[3], *Lior Brimberg*[1], *Bruce T. Volpe*[1], *Patricio T. Huerta*[2,4] *and Betty Diamond*[1,2*]

[1] Center for Autoimmune, Musculoskeletal and Hematopoietic Diseases, Institute of Molecular Medicine, Feinstein Institutes for Medical Research, Northwell Health, Manhasset, NY, United States, [2] Donald and Barbara Zucker School of Medicine at Hofstra/Northwell, Hempstead, NY, United States, [3] Elmezzi Graduate School of Molecular Medicine, Feinstein Institutes for Medical Research, Northwell Health, Manhasset, NY, United States, [4] Laboratory of Immune and Neural Networks, Institute of Molecular Medicine, Feinstein Institutes for Medical Research, Northwell Health, Manhasset, NY, United States

OPEN ACCESS

Edited by:
Serge Nataf,
Université Claude Bernard Lyon 1, France

Reviewed by:
Vincent Russel Harley,
Hudson Institute of Medical Research, Australia
Cristina A. Ghiani,
University of California, Los Angeles, United States
Michael Q. Steinman,
Consultant, San Diego, United States

***Correspondence:**
Betty Diamond
bdiamond@northwell.edu

Specialty section:
This article was submitted to Multiple Sclerosis and Neuroimmunology, a section of the journal Frontiers in Neurology

Received: 06 June 2021
Accepted: 14 September 2021
Published: 13 October 2021

Citation:
Gata-Garcia A, Porat A, Brimberg L, Volpe BT, Huerta PT and Diamond B (2021) Contributions of Sex Chromosomes and Gonadal Hormones to the Male Bias in a Maternal Antibody-Induced Model of Autism Spectrum Disorder. Front. Neurol. 12:721108. doi: 10.3389/fneur.2021.721108

Autism Spectrum Disorder (ASD) is a group of neurodevelopmental conditions that is four times more commonly diagnosed in males than females. While susceptibility genes located in the sex chromosomes have been identified in ASD, it is unclear whether they are sufficient to explain the male bias or whether gonadal hormones also play a key role. We evaluated the sex chromosomal and hormonal influences on the male bias in a murine model of ASD, in which mice are exposed *in utero* to a maternal antibody reactive to contactin-associated protein-like 2 (Caspr2), which was originally cloned from a mother of a child with ASD (termed C6 mice henceforth). In this model, only male mice are affected**.** We used the four-core-genotypes (FCG) model in which the *Sry* gene is deleted from the Y chromosome (Y^-) and inserted into autosome 3 (*TgSry*). Thus, by combining the C6 and FCG models, we were able to differentiate the contributions of sex chromosomes and gonadal hormones to the development of fetal brain and adult behavioral phenotypes. We show that the presence of the Y chromosome, or lack of two X chromosomes, irrespective of gonadal sex, increased the susceptibility to C6-induced phenotypes including the abnormal growth of the developing fetal cerebral cortex, as well as a behavioral pattern of decreased open-field exploration in adult mice. Our results indicate that sex chromosomes are the main determinant of the male bias in the maternal C6-induced model of ASD. The less dominant hormonal effect may be due to modulation by sex chromosome genes of factors involved in gonadal hormone pathways in the brain.

Keywords: autism spectrum disorder, male bias, sex chromosome, gonadal hormones, four core genotypes, SRY gene, maternal antibody

INTRODUCTION

Autism Spectrum Disorder (ASD) is a group of neurodevelopmental conditions that manifest early in childhood. ASD is characterized by varying degrees of impairment in social interaction and communication, and by restricted interests and repetitive behaviors (DSM-V). In the U.S., about 1 in 59 children was diagnosed with ASD in 2014 (1). Both genetic and environmental factors

contribute to the etiology of ASD [reviewed in (2)]. A recent study estimated the heritability of ASD to be 80% (3). However, environmental factors, especially those present during critical periods of prenatal and perinatal brain development, play an essential role in modulating the risk to develop ASD and may account, in part, for the phenotypic variability observed (2).

ASD is four times more frequently diagnosed in males than in females (1). A strong male preponderance is not unique to ASD; other neuropsychiatric conditions, especially those diagnosed earlier in life, also show a male sex bias [reviewed in (4)]. Conversely, neuropsychiatric conditions with a female predominance, including anorexia nervosa and internalizing disorders such as depression and anxiety, present during puberty or later in life [reviewed in (4–6)]. Identifying factors that contribute to neuropsychiatric syndrome susceptibility in either males or females will increase our understanding of brain development and the pathogenesis of these conditions while also providing a foundation for the discovery of new treatments.

Maternal brain-reactive antibodies and gonadal hormones include some of the environmental factors *in utero* that may contribute to ASD risk and its sex bias. This study evaluated the role of gonadal hormones and sex chromosomes in the male bias we observed in a maternal antibody-induced mouse model of ASD (7). In this model, mice were exposed *in utero* to C6, a monoclonal antibody reactive to contactin-associated protein-like 2 (Caspr2) cloned from a mother of a child with ASD, or to an isotype matched control antibody, B1. Caspr2 is a cell-adhesion molecule expressed by neurons (8, 9). Rare and common variants of *CNTNAP2*, the gene encoding Caspr2, have been linked to an increased risk of ASD or ASD-related phenotypes including language delay and developmental language disorders (10–20). *In utero* exposure to C6, but not to B1, leads to thinning of the cortical plate (CP), impaired social interactions, and increased repetitive behaviors in male offspring only in C57BL/6 mice (7). Here, we used the four-core-genotypes (FCG) mouse model to isolate gonadal hormone from sex chromosome contributions to the male bias observed (21). The FCG model allows for the dissociation of gonadal development from sex chromosome complement through the deletion of the *Sry* gene from the Y chromosome (referred to as Y^-) and the insertion of the *Sry* transgene into autosome 3 (*TgSry*), leading to the development of mice with four genotypes: *XY*$^-$ *TgSry*, *XX TgSry*, *XY*$^-$, and *XX* (21, 22), with the first two having and the second two lacking male hormone synthesis *in utero*. Our results demonstrate that the male bias of thinner CP seen during fetal development is driven by sex chromosome differences. Furthermore, we found that, in this strain of mice, *in utero* exposure to C6 antibody causes increased sustained anxiety-like behavior which may also be sex chromosome dependent.

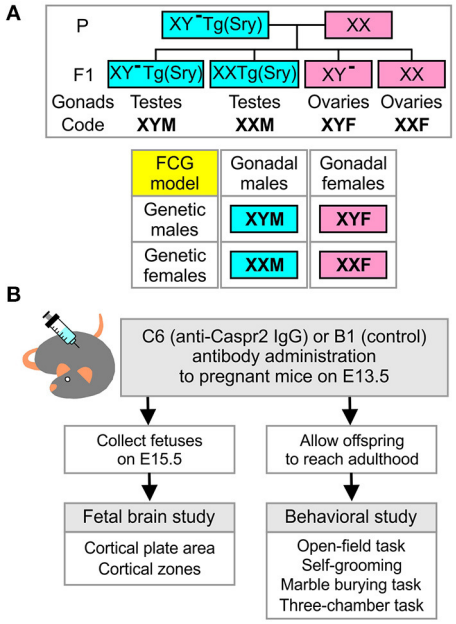

FIGURE 1 | Four-core-genotypes model, combined with *in utero* exposure to C6, to study maternal antibody-induced model of ASD. **(A)** Description of the four-core-genotypes (FCG) model in which a C57Bl/6J female mouse (XX) is mated with a XY^-(*Sry*) male mouse (XYM) to generate offspring in which gonadal and chromosomal contributions can be separately studied. **(B)** Description of the experimental plan for the fetal brain and behavioral studies.

MATERIALS AND METHODS

Ethical Statement

All animal experimentation was performed in accordance with the National Institutes of Health (NIH) Guidelines, under protocols approved by the Institutional Animal Care and Use Committee (IACUC) of the Feinstein Institutes for Medical Research.

In vitro Antibody Production

As described previously (7), human embryonic kidney fibroblast 293T cells (HEK-293T, ATCC CRL 11268^{TM}) were split into culture dishes (100 × 20 mm) in high glucose DMEM (HyClone, GE Healthcare), supplemented with heat inactivated fetal bovine serum (FBS, 10%), glutamine (1%) and penicillin-streptomycin (1%, HyClone, GE Healthcare). After 16–24 h, at 70–80% confluence, the medium was replaced with SFM4Transfx-293 (Hyclone, GE Healthcare) supplemented with 10% FBS, 1% glutamine and 1% penicillin-streptomycin (HyClone, GE Healthcare). Cells were co-transfected 8 h later, using Lipofectamine LTX Reagent (Invitrogen), with IgH and IgL encoding plasmids (5 μg). Supernatants were collected after 7 days, and the antibodies were purified on protein G-sepharose beads (GE Healthcare, Life Technologies). Glycine buffer (0.1 M, pH 3.5) and Tris-HCl (1 M, pH 8) were used for antibody elution and pH neutralization, respectively. Purified antibody was dialyzed in PBS and its concentration was determined by Nanodrop. Antibody integrity was assessed on NuPAGE 4–12% BisTris gels (Invitrogen) stained with Coomassie blue.

Timed Pregnancies and Antibody Administration

C57BL/6 female mice and *XY*$^-$ *TgSry* male mice (6–10 weeks old) obtained from the Jackson Laboratory were used for timed

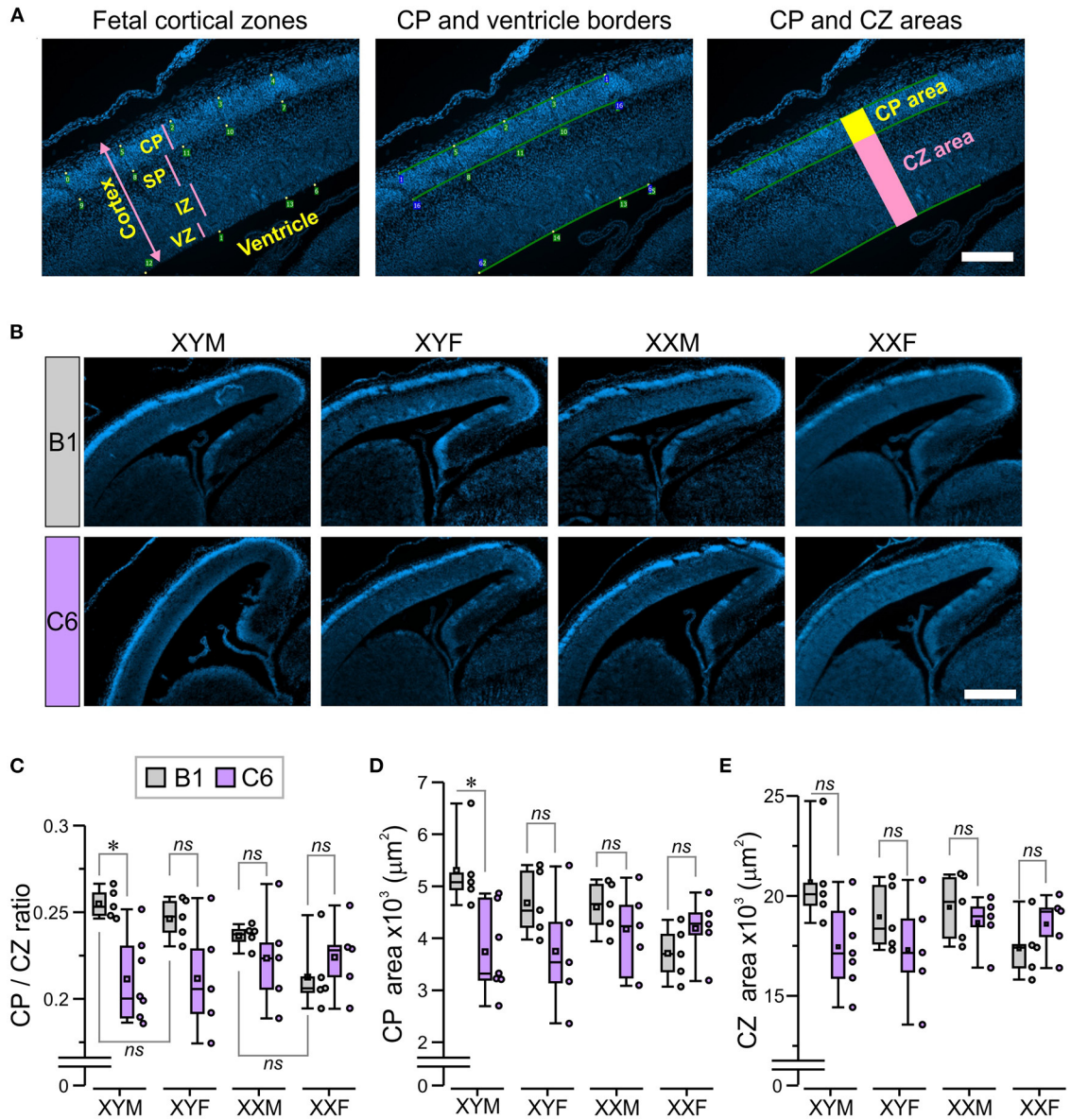

FIGURE 2 | The presence of the Y chromosome predisposes fetuses to develop a smaller cortical plate due to C6 exposure *in utero*. We established mating pairs between wild type C57Bl/6J female and XYM male mice. This mating scheme produced offspring with four genotypes, whose gonadal development was independent of sex chromosome complement. Offspring from 5 to 7 litters for each antibody were analyzed, with no more than two offspring per genotype selected from each litter. **(A)** The micrographs describe the technique for measuring the cortical plate (CP) area and the CZ area, which included the subplate (SP), intermediate zone (IZ), and ventricular zone (VZ; as explained in detail in the Methods. Scale = 100 µm. **(B)** The panels show staining with DAPI, which was used to identify the CP in E15.5 fetuses. Scale = 400 µm. **(C–E)** Box-and-whisker plots represent median and Q1–Q3 quartiles (whiskers are 10–90 range). Dots represent individual measurements. **(C)** Quantification of CP/CZ ratio shows that C6-exposed XYM fetuses had a smaller ratio relative to their respective B1-exposed controls. **(D)** Measurement of the CP area. Compared to their B1 control fetuses, C6-XYM fetuses had a significantly smaller CP area. **(E)** Measurement of the CZ area. There were no significant differences in the cortical area between C6 and B1 exposed mice irrespective of genotype; 2-way ANOVA with Tukey test was used for statistical comparisons. See **Table 1** and **Supplementary Table 1** for details of statistical testing; *ns*, non-significant; $^*P < 0.05$.

pregnancies. In detail, two wild type females and one *XY*$^-$ *TgSry* male mouse were housed together for 15 h starting at the beginning of the dark cycle. The male was removed after 15 h. This mating scheme produced offspring with the genotypes *XY*$^-$ *TgSry* (termed XYM henceforth), *XX TgSry* (termed XXM), *XY*$^-$ (termed XYF), and *XX* (termed XXF) (**Figure 1A**). Embryonic age was determined by the time of male mouse removal which was defined as embryonic day E0.5. Pregnant females were randomly assigned to receive either C6 (anti-Caspr2 IgG, 200 µg) or B1 (control IgG, 200 µg) by retro-orbital sinus injection

under light isoflurane anesthesia on E13.5. Subsequently, E15.5 embryos were harvested, genotyped, and processed for brain histology (**Figure 1B**). In the fetal analysis, 5–7 litters per antibody were included. No more than two fetuses per genotype were selected from each litter for analysis. When two mice were derived from the same litter, the average score was used. A subgroup of pregnancies was assigned for offspring behavior assessment and allowed to reach full term (**Figure 1B**). Adult mice from each of the four core genotypes (FCG) were obtained from eight litters for C6 and six litters for B1.

Fetal Processing for Brain Histological Analysis

Fetuses were fixed with a 4% paraformaldehyde, 4% sucrose solution for 4 h, at 4°C. They were then cryoprotected at 4°C with a gradual increase in sucrose (45 min in 10% sucrose, 1 h in 20% sucrose, and overnight in 30% sucrose). Fetuses were then submerged in a 1:1 solution of 30% sucrose and OCT compound (Fisher Scientific, Pittsburg, PA, USA) for 1 h at room temperature (RT) and transferred to a cryomold with OCT and frozen on dry ice. Samples were kept at −80°C until cut. Whole embryos were mounted and cut with a Cryostat (Leica, Billerica, MA, USA) and all sections (14 μm) were collected and mounted on gelatin-coated slides. The sampling strategy ensured that sagittal sections 8 and 9, according to the Prenatal Mouse Brain Atlas [(23), p. 295–7], were included. Sections were stored at −80°C until stained.

Fetal Brain Immunohistochemistry

Sections were thawed for 25 min and rinsed once with 1× PBS at RT. For antigen retrieval, sections were heated in 10 mM Sodium Citrate Buffer for 10 min at 95°C and cooled to RT with two rinses of 1× PBS. Blocking was done for 1 h, at RT, with a blocking buffer containing 1× PBS/0.1% Triton X-100/3% normal goat serum/2.5% bovine serum albumin (BSA). Sections were then incubated with anti-nestin antibody (MAB353, Millipore, Wetzlar, Germany), at 1:400 dilution in 1× PBS/0.1% Triton X-100/5% BSA, overnight at 4°C. After washing with 1× PBS/0.1% Tween20, Alexa Fluor 488 goat anti-mouse IgG (A11001, Life Technologies), at 1:400 dilution in 1× PBS with 0.2% BSA, was used to detect antibody binding (45 min incubation at RT). Secondary antibody was washed off with 1× PBS/0.1% Tween20, and sections were stained with DAPI (Life Technologies) for 7 min at RT. Sections were washed with 1× PBS, and coverslipped with Dako Fluorescence Mounting Medium (Dako North America Inc.). Images were obtained with Axio-Imager (Z-1, Zen3.1, Zeiss, Peabody, MA, USA).

Analysis of Cortical Plate and Cortical Zones

The cortical plate (CP) was identified as the highly DAPI-dense band of cells, most distal from the ventricle. This was confirmed on the alternate slides, stained with nestin, which was absent in this region (24). Microscope images (10×) of fetal sections stained with DAPI were digitally analyzed using a program that generated orthogonal lines so that a 2-D cortical region was isolated for measurement (**Figure 2A**). The program allowed the placement of points along the borders of the CP and the ventricle, which were defined using the zoom function (Pyramid, Axiophot2.1, Zen 3.1, Zeiss), and the software joined the points. The CP area was measured as the region contained within the superior and inferior borders of the appropriately joined points and the orthogonal lines (**Figure 2A**). Next, the region containing the subplate (SP), intermediate zone (IZ), and ventricular zone (VZ) was measured, and defined as the 'cortical zones' (CZ) area (**Figure 2A**); the marginal zone was not included in the CZ area. The CP/CZ ratio was calculated by dividing the two areas, followed by repeated sampling (20–30×) throughout the length of the defined CP within the section. Additionally, the VZ was defined by the presence of spindle-shaped cells on the edge of the tissue and bright DAPI stain, the IZ was distinguished as the densely-packed DAPI-stained cells (dorsal to VZ), whereas the SP was defined as the sparsely-packed region located dorsal to IZ and ventral to the DAPI-dense CP (**Figure 2A**). We evaluated 1–3 alternate sections per fetal brain with the CP area, CZ area, CP/CZ ratio, as well as the SP, IZ, and VZ areas being averaged for the entire section. The mean values were used for statistical comparisons across groups. The investigator that performed the CP analysis was blinded to both genotype and antibody exposure. A separate investigator performed the statistical analysis.

Behavioral Assessments

FCG mice exposed to C6 or B1 IgG *in utero* were housed under a reversed dark (9:00–21:00) and light (21:00–9:00) cycle, with *ad libitum* access to food and water. All manipulations were conducted during the dark phase, at least 1 h after turning lights off, and male and female mice were assessed on different days. Prior to behavioral assessments, mice were handled three times, for 15 min each, on separate days. At 6–11 weeks of age, mice underwent an observational screen, which we have described in detail previously (24), to assess muscle and spinal, spinocerebellar, sensory, neuropsychiatric, and autonomic functions (**Table 2**). Behavioral assessments were performed at 14–26 weeks of age and included the open-field task (14–15 weeks of age), followed by the marble burying task (17–20 weeks of age), and finally the three-chamber task (22–26 weeks of age). Experiments were conducted and analyzed according to randomly assigned cage numbers which did not indicate mouse genotype or antibody exposure. The investigator was blinded to both genotype and antibody exposure.

Open-Field Task

This task was used to examine locomotor activity, habituation to a novel chamber, and anxiety-like behavior by placing the mice in the center of a square arena (40 × 40 cm^2) with gray walls (35 cm high) and allowing them to freely explore the chamber during two sessions (10 min each) separated by 24 h. The sessions were recorded with a centrally placed video camera directly above the arena which fed the signal to the tracking software (EthoVision XT 14.0, Noldus, Attleboro, MA, USA) used for automated analysis of animal behaviors including distance traveled, velocity, time spent moving, time spent in the center of the arena (18.9 × 18.9 cm^2), and self-grooming. We used customized settings,

TABLE 1 | Statistical analysis for the parameters presented in the figures.

Figure	Groups	mean ± SEM	Interactions	Statistic	*P*-value
Figure 2C	**CP/CZ ratio**		**2Way-ANOVA followed by Tukey test**		
	B1-XYM	0.255 ± 0.003	B1-XYM vs. C6-XYM	$q = 4.892$	0.029
	C6-XYM	0.211 ± 0.009	B1-XYF vs. C6-XYF	$q = 3.565$	0.22
	B1-XYF	0.246 ± 0.005	B1-XXM vs. C6-XXM	$q = 1.38$	0.97
	C6-XYF	0.212 ± 0.015	B1-XXF vs. C6-XXF	$q = 1.096$	0.99
	B1-XXM	0.237 ± 0.003	B1-XYM vs. B1-XYF	$q = 0.907$	0.99
	C6-XXM	0.223 ± 0.013	B1-XXM vs. B1-XXF	$q = 2.392$	0.692
	B1-XXF	0.213 ± 0.009			
	C6-XXF	0.224 ± 0.009			
Figure 2D	**CP area (μm^2)**		**2Way-ANOVA followed by Tukey test**		
	B1-XYM	5,307.87 ± 341.59	B1-XYM vs. C6-XYM	$q = 4.987$	0.024
	C6-XYM	3,735.62 ± 317.91	B1-XYF vs. C6-XYF	$q = 2.74$	0.53
	B1-XYF	4,690.79 ± 287.51	B1-XXM vs. C6-XXM	$q = 1.24$	0.98
	C6-XYF	3,757.42 ± 516.34	B1-XXF vs. C6-XXF	$q = 1.384$	0.97
	B1-XXM	4,611.52 ± 221.75			
	C6-XXM	4,189.88 ± 354.11			
	B1-XXF	3,718.58 ± 231.27			
	C6-XXF	4,190.05 ± 282.18			
Figure 2E	**CZ area (μm^2)**		**2Way-ANOVA followed by Tukey test**		
	B1-XYM	20,736.68 ± 1,049.35	B1-XYM vs. C6-XYM	$q = 4.146$	0.097
	C6-XYM	17,444.57 ± 789.28	B1-XYF vs. C6-XYF	$q = 1.899$	0.875
	B1-XYF	18,955.79 ± 754.52	B1-XXM vs. C6-XXM	$q = 0.909$	0.99
	C6-XYF	17,326.93 ± 1,216.2	B1-XXF vs. C6-XXF	$q = 1.4$	0.972
	B1-XXM	19,433.69 ± 752.77			
	C6-XXM	18,653.41 ± 605.75			
	B1-XXF	17,394.5 ± 665.74			
	C6-XXF	18,595.52 ± 645.57			
Figure 3B	**Open-field task: Mean time-in-center (s)**		**2Way-RMANOVA followed by Bonferroni test**		
	B1-XYM-S1	0.937 ± 0.054	S1: B1-XYM vs. C6-XYM	$F_{(15)} = 0.412$	0.686
	B1-XYM-S2	2.07 ± 0.094	S2: B1-XYM vs. C6-XYM	$F_{(15)} = 6.285$	1.462×10^{-5}
	C6-XYM-S1	0.902 ± 0.064	S1: B1-XYF vs. C6-XYF	$F_{(15)} = 1.61$	0.13
	C6-XYM-S2	1.148 ± 0.113	S2: B1-XYF vs. C6-XYF	$F_{(15)} = 9.384$	1.145×10^{-7}
	B1-XYF-S1	1.054 ± 6.97	S1: B1-XXM vs. C6-XXM	$F_{(15)} = 1.451$	0.164
	B1-XYF-S2	1.886 ± 0.094	S2: B1-XXM vs. C6-XXM	$F_{(15)} = 1.337$	0.198
	C6-XYF-S1	0.924 ± 0.052			
	C6-XYF-S2	0.731 ± 0.079			
	B1-XXM-S1	1.003 ± 0.101			
	B1-XXM-S2	1.674 ± 0.209			
	C6-XXM-S1	1.212 ± 0.101			
	C6-XXM-S2	2.069 ± 0.21			
Figure 3C	**OF task: total time-in center per subject (s)**		**3Way-ANOVA followed by Tukey test**		
	B1-XYM-S1	55.252 ± 6.12	B1-XYM-S2 vs. C6-XYM-S2	$q = 5.473$	0.01
	B1-XYM-S2	122.13 ± 16.23	B1-XYF-S2 vs. C6-XYF-S2	$q = 6.857$	2.886×10^{-4}
	C6-XYM-S1	53.222 ± 7.45	B1-XXM-S2 vs. C6-XXM-S2	$q = 2.591$	0.796
	C6-XYM-S2	67.736 ± 11.1	C6-XYM-S1 vs. C6-XYM-S2	$q = 1.346$	0.998
	B1-XYF-S1	62.188 ± 6.97	C6-XYF-S1 vs. C6-XYF-S2	$q = 1.265$	0.999
	B1-XYF-S2	111.26 ± 16.55			
	C6-XYF-S1	54.518 ± 2.07			
	C6-XYF-S2	43.113 ± 7.74			

(Continued)

TABLE 1 | Continued

Figure	Groups	mean ± SEM	Interactions	Statistic	*P*-value
	B1-XXM-S1	59.202 ± 4.88			
	B1-XXM-S2	98.728 ± 14.03			
	C6-XXM-S1	71.482 ± 6.92			
	C6-XXM-S2	122.103 ± 10.43			
Figure 3D	**OF task: time difference [S2–S1] (s)**		**2Way-ANOVA followed by Tukey test**		
	B1-XYM	66.878 ± 13.688	B1-XYM vs. C6-XYM	$q = 4.265$	0.004
	C6-XYM	14.514 ± 11.555	B1-XYF vs. C6-XYF	$q = 4.596$	0.024
	B1-XYF	49.075 ± 19.05	B1-XXM vs. C6-XXM	$q = 0.929$	0.98
	C6-XYF	−11.405 ± 7.832			
	B1-XXM	39.525 ± 13.415			
	C6-XXM	50.621 ± 9.999			
Figure 4A	**OF task: time moving (s)**		**3Way-ANOVA followed by Tukey test**		
	B1-XYM-S1	370.17 ± 31.7	B1-XYM-S2 vs. C6-XYM-S2	$q = 0.8455$	0.99
	B1-XYM-S2	271.42 ± 12.22	B1-XYF-S2 vs. C6-XYF-S2	$q = 0.138$	0.99
	C6-XYM-S1	381.39 ± 23.51	B1-XXM-S2 vs. C6-XXM-S2	$q = 0.811$	0.99
	C6-XYM-S2	261.71 ± 11.13			
	B1-XYF-S1	340.31 ± 40.05			
	B1-XYF-S2	260.00 ± 11.01			
	C6-XYF-S1	335.75 ± 25.64			
	C6-XYF-S2	200.14 ± 15.24			
	B1-XXM-S1	335.45 ± 27.99			
	B1-XXM-S2	279.01 ± 10.65			
	C6-XXM-S1	357.62 ± 37.1			
	C6-XXM-S2	287.37 ± 11.87			
Figure 4A	**OF task: distance (cm)**		**3Way-ANOVA followed by Tukey test**		
	B1-XYM-S1	4,379.025 ± 243.553	B1-XYM-S2 vs. C6-XYM-S2	$q = 0.588$	0.99
	B1-XYM-S2	2,774.775 ± 162.881	B1-XYF-S2 vs. C6-XYF-S2	$q = 3.531$	0.354
	C6-XYM-S1	4,471.654 ± 238.138	B1-XXM-S2 vs. C6-XXM-S2	$q = 1.588$	0.99
	C6-XYM-S2	2,656.923 ± 168.087			
	B1-XYF-S1	4,139.243 ± 290.059			
	B1-XYF-S2	3,025.794 ± 220.992			
	C6-XYF-S1	3,905.103 ± 139.724			
	C6-XYF-S2	2,342.452 ± 160.658			
	B1-XXM-S1	4,105.682 ± 196.187			
	B1-XXM-S2	3,143.498 ± 199.954			
	C6-XXM-S1	4,498.896 ± 209.671			
	C6-XXM-S2	3,114.608 ± 188.181			
Figure 4B	**Self-grooming Time (s)**		**2Way-ANOVA followed by Tukey test**		
	B1-XYM	10.384 ± 4.522	B1-XYM vs C6-XYM	$q = 0.419$	0.99
	C6-XYM	8.571 ± 3.557	B1-XYF vs. C6-XYF	$q = 1.755$	0.814
	B1-XYF	16.908 ± 6.947	B1-XXM vs. C6-XXM	$q = 0.557$	0.99
	C6-XYF	9.596 ± 2.884			
	B1-XXM	13.332 ± 3.282			
	C6-XXM	11.148 ± 3.664			
Figure 4C	**Marbles buried (#)**		**2Way-ANOVA followed by Tukey test**		
	B1-XYM	9.083 ± 1.104	B1-XYM vs. C6-XYM	$q = 0.321$	0.99
	C6-XYM	9.571 ± 2.202	B1-XYF vs. C6-XYF	$q = 0.476$	0.99
	B1-XYF	5.714 ± 1.392	B1-XXM vs. C6-XXM	$q = 0.719$	0.99
	C6-XYF	5 ± 1.115			
	B1-XXM	13.071 ± 1.344			
	C6-XXM	12.167 ± 1.342			

(Continued)

TABLE 1 | Continued

Figure	Groups	mean ± SEM	Interactions	Statistic	*P*-value
Figure 5B	**Three-Chamber task: social approach (s)**		**3Way-ANOVA followed by Tukey test**		
	B1-XYM-ms	52.992 ± 6.291	B1-ms vs. C6-ms	$q = 4.159$	0.02
	B1-XYM-ob	28.381 ± 3.58	B1-XYM-ms vs. B1-XYM-ob	$q = 4.332$	0.104
	C6-XYM-ms	58.071 ± 9.94	C6-XYM-ms vs. C6-XYM-ob	$q = 4.085$	0.159
	C6-XYM-ob	30.339 ± 4.103	B1-XYF-ms vs. B1-XYF-ob	$q = 8.578$	1.169×10^{-6}
	B1-XYF-ms	83.767 ± 11.282	C6-XYF-ms vs. C6-XYF-ob	$q = 13.857$	3.143×10^{-9}
	B1-XYF-ob	25.529 ± 4.122	B1-XXM-ms vs. B1-XXM-ob	$q = 10.212$	2.832×10^{-8}
	C6-XYF-ms	94.801 ± 6.046	C6-XXM-ms vs. C6-XXM-ob	$q = 14.96$	1.5×10^{-15}
	C6-XYF-ob	25.763 ± 3.026			
	B1-XXM-ms	77.182 ± 4.65			
	B1-XXM-ob	28.156 ± 2.292			
	C6-XXM-ms	102.583 ± 9.709			
	C6-XXM-ob	25.011 ± 2.041			
Figure 5C	**Three-Chamber task: discrimination ratio**		**2Way-ANOVA followed by Tukey test**		
	B1-XYM	0.295 ± 0.075	B1-XYM vs. C6-XYM	$q = 0.102$	0.99
	C6-XYM	0.287 ± 0.066	B1-XYF vs. C6-XYF	$q = 0.751$	0.99
	B1-XYF	0.453 ± 0.049	B1-XXM vs. C6-XXM	$q = 1.927$	0.748
	C6-XYF	0.565 ± 0.073			
	B1-XXM	0.51 ± 0.079			
	C6-XXM	0.562 ± 0.049			

Ab, antibody; CP, cortical plate; CZ, cortical zones (including the subplate, intermediate zone and ventricular zone); IZ, intermediate zone; ms, mouse-stimulus; ob, object; SP, subplate; S1, session 1; S2, session 2; VZ, ventricular zone.

within EthoVision, to detect only grooming bouts >2 s, thus reducing the detection of extra-short bouts.

Marble Burying Task

Repetitive behavior was examined with the marble burying task (25) in which mice were placed in the center of a square arena (40 × 40 cm^2, 35-cm wall height) containing 25 black glass marbles (1.2 cm diameter) placed on top of corn cob bedding (5 cm depth) in a 5 × 5 grid pattern arrangement. The mice freely explored the environment for 20 min and at the end of the session, the number of buried marbles (>50% of marble surface area covered by bedding material) was recorded.

Three-Chamber Task

This task was used to measure social approach, by placing the subject mouse in an apparatus (60 cm × 40 cm, 40-cm wall height) with clear plexiglass walls, which was subdivided into 3 chambers with sealable doors between chambers. A subject mouse was placed in the center chamber with the left and right chambers sealed off; the doors were opened, and the subject was allowed to explore the empty arena, with access to the 3 chambers, for 10 min. The subject mouse was then gently guided to the center chamber and access to the side chambers was sealed off. An age and sex matched (XYM or XXF) unfamiliar "mouse-stimulus" was placed in one of the side chambers, confined by a cylinder (diameter 9 cm, height 20 cm) with the bottom 5.5 cm perforated with holes (diameter, 0.5 cm). The cylinder was 3D-printed with clear methacrylate resin (FormLabs, Somerville, MA, USA). Each mouse-stimulus was acclimated to the cylinder for 10 min prior to the experiment. An identical but empty methacrylate cylinder was used as a novel object and placed in the second side chamber. The subject mouse was then allowed to explore the arena for 10 min, with access to the three chambers. The chamber used for the mouse-stimulus and the novel object were alternated between trials. The three-chambered apparatus and the methacrylate cylinders were cleaned prior to each trial with 70% ethanol followed by water and wiped dry. Video tracking software (Etovision XT 14.0) was used to obtain the total time spent interacting with the mouse-stimulus and with the novel object. A discrimination ratio was computed by the formula $(T_{MS}\text{-}T_O)/(T_{MS} + T_O)$, in which T_{MS} denotes the time near the mouse-stimulus and T_O denotes the time near the novel object.

Statistical Analysis

Most datasets were analyzed with two-way analysis of variance (ANOVA), with "genotype" (XYM, XXM, XYF and XXF) and "antibody" (C6 and B1) as factors, which was followed by *post-hoc* Tukey correction for multiple comparisons. For the open-field task, time series data were analyzed with 2-way repeated measures ANOVA (RMANOVA) followed by *post-hoc* Bonferroni correction. For the two sessions of the open-field task, data were analyzed with 3-way ANOVA (with genotype, antibody and sessions as factors) followed by Tukey correction for multiple comparisons. For the three-chamber task, 3-way ANOVA was also used, with genotype, antibody and "stimulus" (mouse-stimulus and object) as factors, followed by Tukey correction for multiple comparisons. The software Origin [Origin Pro

TABLE 2 | Five functions were evaluated in the observational screen.

Function	Variables
Muscle and spinal function	Abdominal tone, body position, body tone, contact righting, defecation, gait, grip strength, limb grasping, limb tone, pelvic elevation, positional passivity, righting reflex, spontaneous activity, tail elevation, trunk curl, urination, visual placing, wire maneuver
Spino-Cerebellar function	Abdominal tone, body position, body tone, contact righting, gait, grip strength, limb grasping, limb tone, pelvic elevation, righting reflex, tail elevation, trunk curl, visual placing
Sensory function	corneal reflex, gait, negative geotaxis, pinna reflex, righting reflex, toe pinch, transfer arousal, visual placing
Neuro-Psychiatric function	Aggressivity, body position, body tone, contact righting, fear (to human handler), irritability, latency to move, locomotion, negative geotaxis, positional passivity, righting reflex, spontaneous activity, startle response, transfer arousal, tremor, vocalizations, wire maneuver
Autonomic function	Defecation, heart rate, lacrimation, palpebral closure, piloerection, respiratory rate, salivation, skin color, startle response, tail elevation, urination

Groups	Mean ± SEM	Interactions	Statistic	*P*-value
Muscle and spinal function	**2Way-ANOVA followed by Tukey test**			
B1-XYM	26.333 ± 0.414	Ab	$F_{(1,64)} = 0.236$	0.798
C6-XYM	25.571 ± 0.369	Genotype	$F_{(2,64)} = 0.331$	0.719
B1-XYF	26.642 ± 0.561	B1-XYM vs C6-XYM	$q = 0.751$	0.99
C6-XYF	25.857 ± 0.962	B1-XYF vs. C6-XYF	$q = 1.055$	0.97
B1-XXM	26.231 ± 0.482	B1-XXM vs. C6-XXM	$q = 1.066$	0.97
C6-XXM	26.083 ± 0.609			
Spino-Cerebellar function	**2Way-ANOVA followed by Tukey test**			
B1-XYM	20.16667 ± 0.112	Ab	$F_{(1,64)} = 0.716$	0.4
C6-XYM	19.57143 ± 0.202	genotype	$F_{(2,64)} = 1.399$	0.255
B1-XYF	20.35714 ± 0.169	B1-XYM vs. C6-XYM	$q = 0.551$	0.99
C6-XYF	20.28571 ± 0.184	B1-XYF vs. C6-XYF	$q = 3.097$	0.257
B1-XXM	20.23077 ± 0.231	B1-XXM vs. C6-XXM	$q = 1.999$	0.718
C6-XXM	20 ± 0.213			
Sensory function	**2Way-ANOVA followed by Tukey test**			
B1-XYM	11.625 ± 0.186	Ab	$F_{(1,64)} = 0.17$	0.681
C6-XYM	12.071 ± 0.229	Genotype	$F_{(2,64)} = 1.161$	0.32
B1-XYF	11.679 ± 0.219	B1-XYM vs. C6-XYM	$q = 0.336$	0.99
C6-XYF	11.714 ± 0.486	B1-XYF vs. C6-XYF	$q = 0.125$	0.99
B1-XXM	12.038 ± 0.215	B1-XXM vs. C6-XXM	$q = 0.894$	0.99
C6-XXM	11.875 ± 0.175			
Neuro-Psychiatric function	**2Way-ANOVA followed by Tukey test**			
B1-XYM	38.333 ± 1.558	Ab	$F_{(1,64)} = 0.681$	0.412
C6-XYM	31.714 ± 1.714	Genotype	$F_{(2,64)} = 0.64$	0.52
B1-XYF	40.143 ± 1.123	B1-XYM vs. C6-XYM	$q = 0.122$	0.99
C6-XYF	38.142 ± 1.404	B1-XYF vs. C6-XYF	$q = 1.93$	0.747
B1-XXM	34.692 ± 1.184	B1-XXM vs. C6-XXM	$q = 0.147$	0.99
C6-XXM	40.333 ± 1.514			
Autonomic function	**2Way-ANOVA followed by Tukey test**			
B1-XYM	7.75 ± 0.25	Ab	$F_{(1,64)} = 0.689$	0.409
C6-XYM	7.857 ± 0.634	Genotype	$F_{(2,64)} = 1.495$	0.232
B1-XYF	8 ± 0.392	B1-XYM vs. C6-XYM	$q = 2.033$	0.707
C6-XYF	6.857 ± 0.404	B1-XYF vs. C6-XYF	$q = 0.508$	0.99
B1-XXM	8.077 ± 0.309	B1-XXM vs. C6-XXM	$q = 0.458$	0.99
C6-XXM	7.833 ± 0.441			

Variables in the second column (assessing multiple aspects of each function) were considered, with their individual scores being added per function. The statistical analysis of the functions from the observational screen showed that in utero exposure to C6 did not significantly alter the five functions. The number of mice per group was: B1-XYM = 12, C6-XYM = 7, B1-XYF = 7, C6-XYF = 13, B1- XXM = 14, and C6-XXM = 12. Two-way ANOVA with Tukey correction, which did not reach significance ($P < 0.05$); Ab, antibody.

2021b (64-bit) SR2, OriginLab, Northampton, MA] was used for statistical tests. $P < 0.05$ were considered statistically significant.

RESULTS

Effects of *in utero* Exposure to C6 on Cortical Thickness Depend on Sex Chromosome Complement

We established mating pairs between wild type C57Bl/6J female and XY^- *TgSry* male mice (**Figure 1A**), which delivered offspring with the genotypes XY^- *TgSry* (termed XYM), *XX TgSry* (termed XXM), XY^- (termed XYF), and *XX* (termed XXF) (**Figure 1A**). We administered intravenous C6 or B1 antibody to pregnant mice on embryonic day E13.5 and harvested the fetuses on day E15.5 (7) (**Figure 1B**). We used the XYM and XXF mice as internal controls to confirm that, as in wild type C57BL/6J mice, *in utero* exposure to C6 led to ASD-like phenotypes in males but not females in this mouse strain. Offspring from 5 to 7 litters for each antibody were analyzed, with no more than two offspring per genotype selected from each litter. Not all genotypes were present in all litters.

We measured the CP/CZ ratio (**Figure 2A**) in hormonal and chromosomal males and females exposed to C6 or B1, as we had shown this ratio to be diminished in C57BL/6 males, but not female mice exposed to C6 *in utero* (7). Crucially, we observed no effect of C6 administration in XXF offspring (**Figures 2B,C,** $P > 0.1$, **Table 1**) and a decrease in the CP/CZ ratio in XYM offspring (**Figure 2C**), replicating our previous results in C57BL/6 mice (7). Indeed, we found that C6-exposed XYM fetuses had a significantly smaller CP/CZ ratio when compared to B1-XYM control fetuses (**Figure 2C;** $q = 4.89$, $P = 0.029$, see **Table 1** and **Supplementary Table 1** for details on statistical tests), which was likely due to a decrease in CP area specifically and not to smaller SP, IZ or VZ**.** Of note, the C6-treated fetuses displayed high variability in the CP/CZ ratio and, predictably, two-way ANOVA revealed a significant effect for the "antibody" factor [C6 vs. B1 groups, $F_{(1, 41)} = 9.1$, $P = 0.0048$] and the antibody × genotype interaction [$F_{(3, 41)} = 3.29$, $P = 0.03$], while the *post-hoc* Tukey correction confirmed the C6 vs. B1 effect ($q = 4.41$, $P = 0.004$). However, the comparisons of the interactions for all the other groups failed to reach statistical significance (**Supplementary Table 1**).

Importantly, the CP/CZ ratio of B1-XYM and B1-XYF offspring did not differ (**Figure 2C,** $P > 0.1$, **Table 1**) suggesting that sex hormones do not determine the CP size in XY mice. Also, B1-XXM and B1-XXF mice had an equivalent CP/CZ ratio (**Figure 2C,** $P > 0.1$, **Table 1**), suggesting again that sex hormones do not regulate cortical structure in XX mice.

Additionally, when compared to their respective control group, the CP area was significantly smaller in C6-XYM fetuses (**Figure 2D,** $P < 0.05$, **Table 1**). As in the case of the CP/CZ ratio, two-way ANOVA showed significant effects for antibody [$F_{(1, 41)} = 6.74$, $P = 0.001$] and antibody × genotype interaction [$F_{(3, 41)} = 3.42$, $P = 0.027$], whereas the Tukey test confirmed the C6 vs. B1 effect ($q = 3.82$, $P = 0.001$), a significant C6-XYM vs. B1-XYM interaction ($q = 4.98$, $P = 0.024$) and lack of significance for all other interactions (**Supplementary Table 1**). Moreover, *in utero* exposure to C6 maternal antibody did not alter the CZ area in any of the groups (**Figure 2E,** $P > 0.1$, **Table 1**), which was verified by two-way ANOVA followed by Tukey test (**Supplementary Table 1**). To further confirm this point, we performed separate measurements of the areas of the subplate, intermediate zone, and ventricular zone (**Figure 2A**) and, again, found no differences across the groups ($P > 0.5$, **Supplementary Table 1**). Hormones were not identified as a contributing factor to the male bias of a C6-induced decrease in CP area at the E15.5 stage of development because neither gonadal female nor gonadal male XX fetuses were significantly affected by antibody exposure.

C6-Mediated ASD-Like Phenotypes Are Influenced by Sex Chromosome Complement

To evaluate the role of sex chromosomes and gonadal hormones on the male bias of C6-induced behavioral deficits, we conducted a series of behavioral studies on adult FCG mice that were exposed to C6 or B1 *in utero* on E13.5. We include 3 groups in these studies (XYM, XYF and XXM) as our previous studies in wildtype C57BL/6 mice revealed no effect of C6 exposure on female offspring and there was no structural phenotype associated with C6 exposure in XXF offspring (**Figures 2B,C**). Initially, we performed an observational screen and surveyed several variables to assess muscle, spinal, spinocerebellar, sensory, neuropsychiatric, and autonomic functions (**Table 2**). We found that, for each genotype, there were no significant differences in the scores obtained for C6 and B1 mice (**Table 2**).

A set of behavioral assessments was focused on key ASD-like phenotypes, such as the presence of anxiety, repetitive behaviors, and social impairments. We studied adult mice from eight litters exposed to C6 and six litters exposed to B1. Not all the genotypes were represented in each litter. Anxiety is often a comorbid psychiatric condition in patients with ASD. Therefore, we evaluated C6-exposed FCG mice for increased anxiety-like behavior in an open-field task in which the animals were allowed to freely explore a well-lit square arena during two sessions (S1 and S2), lasting 10 min each**,** and separated by 24 h (**Figure 3A**). In the context of the open-field task, anxiety-like behavior is defined as avoidance to explore the center of the apparatus, which some claim occurs more prominently at the early stage of the task. However, it is clear that initial exposure to the chamber triggers habituation, a type of non-associative learning, in which the mice adapt their behavioral responses due to the continual exposure to the novel environment. Therefore, in this study, we decided to define sustained anxiety-like behavior as a mouse spending significantly less time in the center of the arena during S2, after the initial S1 habituation session. We, thus, calculated 'time-in-center' scores for consecutive 10-s intervals in S1 and S2, which we used to build time series graphs (**Figure 3B**). During S1, we found that all groups (regardless of antibody exposure or genotype) displayed similar time-in-center scores (**Figure 3B,** $P > 0.1$, **Table 1**). During S2, C6-XYM mice and C6-XYF mice did not increase their time-in-center scores while

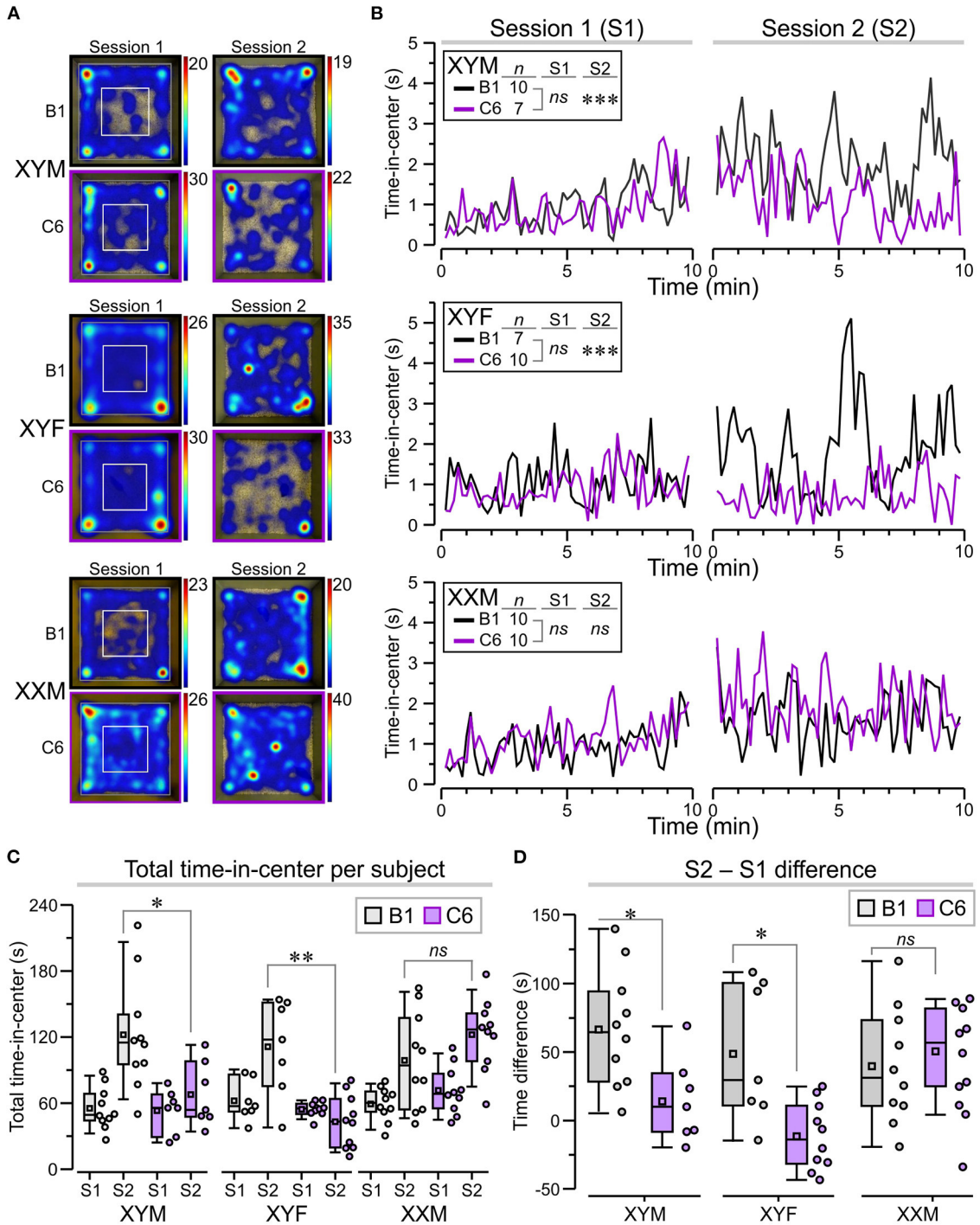

FIGURE 3 | Sustained anxiety-like behavior in C6-exposed XYM and XYF mice during the open-field task. **(A)** Top-view heatmaps of the open-field task for representative XYM, XYF, and XXM mice that were exposed *in utero* to anti-Caspr2 antibody (C6) or control antibody (B1). The color scale at the right of each heatmap represents seconds. **(B)** Graphs show the time spent at the center of the arena, taken over regular 10-s intervals during session 1 (S1) and session 2 (S2), for all groups. RMANOVA with Bonferroni *post-hoc* tests reveal significantly lower time-in-center, during S2, for C6-XYM mice compared to B1-XYM mice as well as C6-XYF mice compared to B1-XYF mice. **(C)** Box-and-whisker plots for time-in-center show mean (small square), median, Q1–Q3 quartiles (box), and 10–90 range (whiskers) for S1 and S2. Dots represent individual mice; 3-way ANOVA, followed by Tukey test, was used for statistical comparisons. **(D)** Difference for time-in-center between S2 and S1 show statistical differences for the XYM and XYF cohorts; 2-way ANOVA with Tukey test was used for statistical comparisons. See **Table 1** and **Supplementary Table 2** for details of statistical testing; *ns* = non-significant, $^{*}P < 0.05$, $^{**}P < 0.01$, $^{***}P < 0.001$.

the other groups spent significantly more time in the center area than they had during S1 (**Figure 3B**, $P < 0.01$, **Table 1**, **Supplementary Table 2**).

To further demonstrate the anxiety-like effect in C6-XYM and C6-XYF groups, we computed the overall time-in-center for each subject during S1 and S2 (**Figure 3C**) and found that neither C6-XYM nor C6-XYF mice increased the amount of time spent in the center during S2 ($P = 0.99$ for both groups, **Table 1**, **Supplementary Table 2**). In contrast, C6-XXM mice significantly increased their time-in-center during S2 ($P < 0.05$, **Table 1**, **Supplementary Table 2**). Also, B1-XYM mice had higher time-in-center during S2 (**Figure 3C**, $P < 0.05$, **Table 1**, **Supplementary Table 2**). Furthermore, a comparison of B1 vs C6 groups during S2 confirmed that C6-XYM and C6-XYF mice spent significantly less time-in-center than their B1 counterparts (**Figure 3C**, $P < 0.05$ for both groups, **Table 1**, **Supplementary Table 2),** whereas C6-XXM and B1-XXM animals spent a similar amount time in the center of the arena (**Figure 3C**, $P = 0.796$, **Table 1**, **Supplementary Table 2**). Finally, we computed the time difference for time-in-center during the two sessions (S2–S1) and found that the C6-XYM and C6-XYF groups had significantly lower scores than B1-XYM and B1-XYF groups, respectively (**Figure 3D**, $P < 0.05$ for both groups, **Table 1**, **Supplementary Table 2**). Taken together, these data show a sustained anxiety-like phenotype associated with sex chromosome complement.

We also assessed locomotor activity in the open-field task by measuring the total time moving and the total distance traveled during each period to ensure that this was not a confounding variable. We focused on S2 as it was in S2 that we observed differences related to genotype and antibody exposure. During S2, all the groups showed significantly less time moving when compared to S1 (**Figure 4A**, $P < 0.05$, **Table 1**, **Supplementary Table 2**); nevertheless, the C6-exposed offspring had similar time-moving scores when compared to B1 control mice (**Figure 4A**, $P > 0.5$, **Table 1**, **Supplementary Table 2**). Additionally, there were no significant differences in distance traveled during S2 for C6-exposed mice compared to their respective B1-exposed controls (**Figure 4A**, $P > 0.05$, **Table 1**, **Supplementary Table 2**).

We evaluated the C6-exposed FCG mice for stereotypic and compulsive behaviors using cumulative time self-grooming and number of marbles buried. We found that XYM, XYF, and XXM mice exposed to C6 *in utero* did not display an increase in repetitive behaviors when compared to their respective B1 controls in either self-grooming (**Figure 4B**, $P > 0.4$, **Table 1**, **Supplementary Table 2**) or the marble burying task (**Figure 4C**, $P > 0.6$, **Table 1**, **Supplementary Table 2**).

Lastly, we used the three-chamber task [adapted from Yang et al. (26)] to explore the influence of sex chromosomes and gonadal hormones on the decreased social interactions produced by *in utero* exposure to C6 in male mice (7) (**Figure 5A**). We defined social approach as the total amount of time spent interacting with an unfamiliar mouse (referred to as "mouse-stimulus") compared

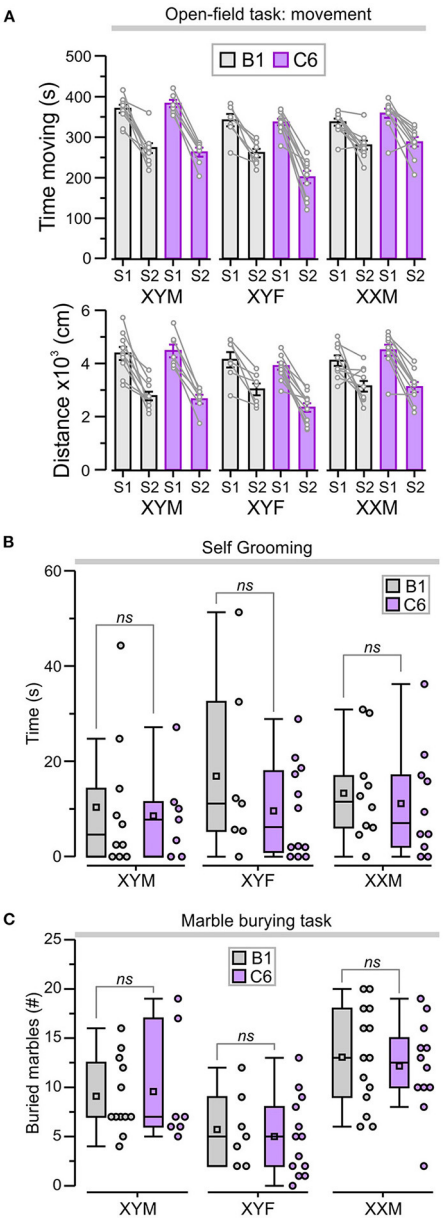

FIGURE 4 | C6 exposure *in utero* did not lead to an increase in repetitive behaviors. **(A)** *Top*, graph shows the total time (mean ± SEM) moving during sessions 1 and 2 (S1 and S2). *Bottom*, total distance traveled (mean ± SEM) as a measure of locomotor activity in the open-field task. The lines linking each S1 and S2 represent the scores for individual animals. **(B)** Box-and-whisker plots for cumulative time self-grooming show median and Q1–Q3 quartiles (whiskers are 10–90 range). Dots represent individual animals. C6-exposed mice did not exhibit increased self-grooming compared to B1 control groups, irrespective of genotype. **(C)** Box-and-whisker plots show the number of marbles buried (more than 50% of the surface area covered by bedding) during the marble-burying task. The number of marbles buried was not significantly different between B1- and C6-exposed mice, irrespective of genotype; 2-way ANOVA with Tukey test was used for statistical comparisons. See **Table 1** and **Supplementary Table 2** for details of statistical testing; *ns* = non-significant.

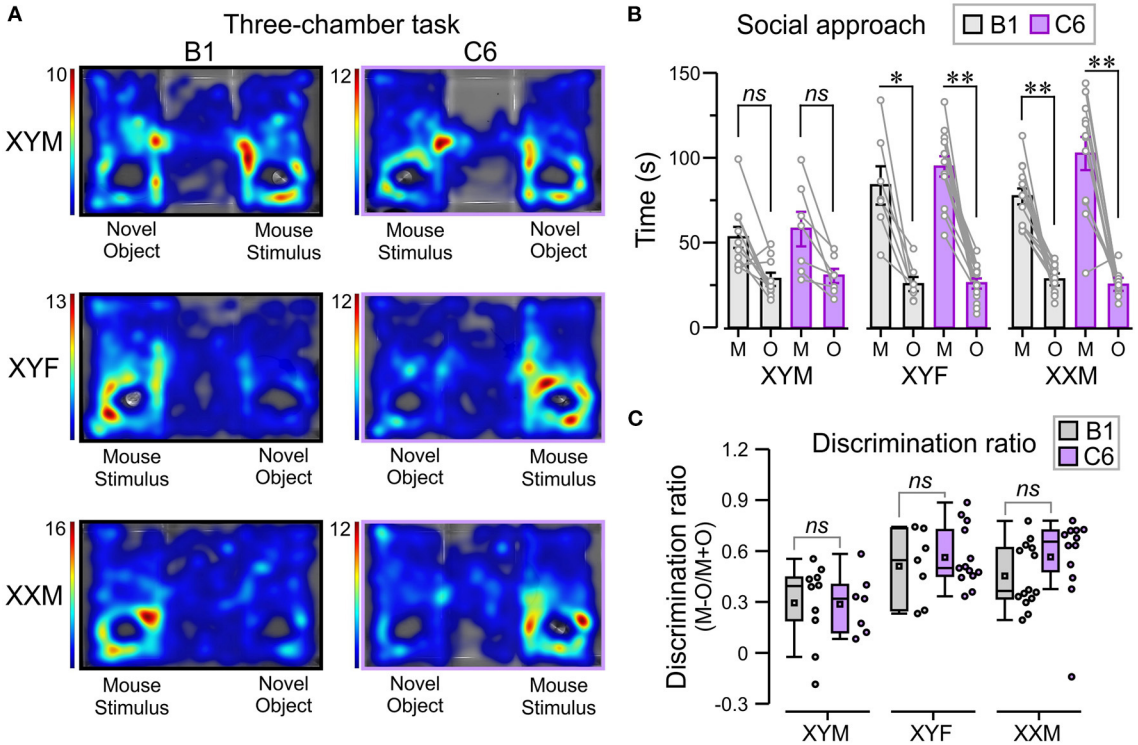

FIGURE 5 | *In utero* C6 exposure did not affect social approach. We used the three-chamber task to evaluate social approach. The number of mice per group was: B1-XYM = 10, C6-XYM = 7, B1-XYF = 7, C6-XYF = 13, B1-XXM = 14, and C6-XXM = 12. **(A)** Representative trials of the social approach session displayed as top-view heatmaps for individual B1- and C6-exposed XYM, XYF, and XXM mice. **(B)** Time (mean ± SEM) spent interacting with the novel object (O) and the "mouse-stimulus" (M). The lines linking each mouse-stimulus and object represent the scores for individual subjects. All the groups tested showed social preference for the mouse-stimulus compared to the novel object; 3-way ANOVA with Tukey test was used for these comparisons. **(C)** Box-and-whisker plots show the discrimination ratio for social interaction. C6- and B1-exposed mice displayed similar discrimination between mouse-stimulus and novel object, irrespective of genotype; 2-way ANOVA with Tukey test was used for these comparisons. See **Table 1** and **Supplementary Table 2** for details of statistical testing; *ns*, non-significant, $^{*}P < 0.05$, $^{**}P < 0.001$.

to the amount of time spent interacting with a novel object. Normal social approach was defined as spending more time near the mouse-stimulus and less time near the object. We found that XYF and XXM mice, regardless of C6 or B1 exposure, preferred the mouse-stimulus compared to the object (**Figures 5A,B**, $P < 0.01$, **Table 1**, **Supplementary Table 2**). Interestingly, C6-XYM mice did not show significantly higher exploration of the mouse-stimulus but, paradoxically, B1-XYM mice failed to show a preference for the mouse-stimulus (**Figures 5A,B**, $P > 0.1$, **Table 1**, **Supplementary Table 2**). Additionally, we computed social discrimination ratios (for which positive values reflect a predilection for the mouse-stimulus), which further demonstrated that B1- and C6-exposed mice of all groups preferred the mouse-stimulus instead of the object (**Figure 5C**, **Table 1**, **Supplementary Table 2**). These results indicate that XYM, XYF and XXM mice exposed to C6 displayed normal social approach. We were unable to replicate the phenotype seen in C6 exposed male wild type mice (7) in the FCG model.

DISCUSSION

In this study we used the FCG mouse model to distinguish the contributions of sex chromosomes and gonadal hormones to abnormal cortical development and adult ASD-like phenotypes in a model of maternally-induced ASD by the anti-Caspr2 antibody, C6. Analysis of the fetal brains showed that C6-exposed XYM fetuses had significantly smaller CP/CZ ratio and CP area, when compared to B1-XYM control fetuses. Remarkably, the B1-XYM and B1-XYF fetal cortices did not differ in their CP/CZ ratio and CP area, and this was also the case for the B1-XXM and B1-XXF groups, which strongly suggest that sex hormones were not responsible for determining the CP size in either XY or XX mice. Moreover, behavioral assessment of adult offspring revealed a behavioral pattern of sustained anxiety-like behavior in C6-XYM and C6-YXF mice, in which they spent significantly less time in the center of an open-field arena during a second exposure after the initial habituation session. Additionally, adult

C6-exposed XYM, XYF and XXM mice did not seem to exhibit abnormalities in locomotion, self-grooming, the marble-burying task and the three-chamber social approach task.

C6 antibody exposure in our model occurs throughout a limited window during *in utero* development, from time of antibody administration on E13.5 to IgG exclusion by the blood brain barrier between E16.5 and E17.5. Thus, we propose that the sex-biased effects of the C6 antibody depend on the roles that sex chromosome genes and gonadal hormones have on the critical brain developmental processes ongoing at the time of exposure. Our findings support a predominant influence of sex chromosome complement on the susceptibility to C6-induced ASD-like phenotypes in mice exposed mid-gestation.

Changes in cortical thickness, including thinning (27–32) and thickening (33–35), have been observed in ASD. We have previously shown that *in utero* exposure to C6 antibody leads to thinning of the CP in male mice (7). Using the FCG mouse model, we found that both XYM and XYF but not XXM or XXF mice had a significantly smaller CP/CZ ratio when exposed to C6. Thus, presence of the Y chromosome or lack of two copies of the X chromosome is key in determining the susceptibility to cortical thinning, irrespective of gonadal hormones. The mechanism for the thinned cortical plate has not yet been determined. Sex chromosome complement has previously been identified to be important for brain development and the establishment of brain sex differences (21, 36–40). In congruence with our findings, the analysis of MR brain images from individuals with complete androgen insensitivity syndrome (CAIS) and Klinefelter syndrome suggests a sex chromosome gene-dosage effect on the thickness of the motor cortex (39) and the temporal, orbitofrontal and lingual cortices (41), respectively. Savic and Arver (41) propose that sex differences in motor cortex development are predominantly established by X-chromosome genes that escape inactivation and lack a Y-chromosome homolog whereas in the superior temporal cortex these differences are likely influenced by X-chromosome escapee genes with Y-chromosome homologs. Similar potential sex chromosome gene dosage relationships have been proposed to account for the brain structural differences identified in individuals with sex chromosome aneuploidies (42–44). Indeed, Vawter et al. (45) identified fourteen X-chromosome genes that are differentially expressed in XXY compared to XY individuals, twelve of which were significantly correlated with measure of verbal cognition. Furthermore, Good et al. (42) propose that haploinsufficiency of a subset of X-linked genes, including the gene encoding monoamine oxidase B, contribute to the brain structural abnormalities and neurocognitive deficits observed in Turner syndrome. The increased prevalence of ASD in individuals with sex chromosome aneuploidies [reviewed in (46–51)] supports the hypothesis that sex chromosome gene dosage contributes to ASD susceptibility and suggests that it may contribute to the sex bias in our model.

While sex chromosomes are essential for brain differentiation and sex specific behaviors (21, 37, 52–59), gonadal hormones also modulate developmental processes and contribute to sex differences in brain anatomy. Indeed, both human and animal studies have found a mixed contribution of gonadal hormones and sex chromosomes to sex differences in brain structure, with the predominant factor being region specific (38, 39, 41, 43, 6041; 39). In particular, testosterone exposure has been implicated in determining parietal and occipital cortical thickness in individuals with CAIS and sex chromosome aneuploidies (39, 41). Additionally, data from the FCG mouse model also suggest a predominant gonadal hormone contribution to differences in cortical thickness and volume in the adult brain as we found in the comparison of B1-exposed XXF and XXM mice in the fetal brain (38, 60). Based on these data, gonadal hormones might have been predicted to modulate the effects of C6 on fetal cortical thickness, however, they mainly address hormone exposure during puberty (61, 62). Furthermore, gonadal hormone and signaling deficiencies observed in individuals with CAIS and sex chromosome aneuploidies may act as confounders when studying the association between sex chromosomes and brain sexual differentiation.

While sex hormones act on the brain throughout post-partum life, for gonadal hormones to modulate the susceptibility to C6-induced phenotypes, both the hormones and their receptors must be expressed at the time of antibody exposure. Androgen receptor (AR) mRNA has been detected in the fetal mouse brain as early as E11, with expression in the neocortex, hippocampal cortex, and hypothalamus peaking on E15–16 (63). Estrogen receptor (ER) α protein has been detected as early as E12–14 in the mouse embryonic ventricular and subventricular zones (64) whereas mRNA has been detected as early as E16.5 in the mouse fetal brain (65) and follows a similar pattern in the ventricular zone and cerebral cortex in rats, with the earliest expression on E16 (66). ERβ protein has been detected as early as E12.5 in the mouse brain and was first appreciated in the deep layers of the cerebral cortex on E15.5–16.5 (67). Signaling through AR and ERs has been found to regulate developmental processes in the cortex. Zhang et al. (68) observed an effect of testosterone and estrogen on the differentiation but not proliferation of cortical neurons isolated from rat fetuses on E14. They proposed that these effects are mediated by signaling through the AR and not ERα as its expression was low. In mice, Wang et al. (69) proposed that estrogen regulates neuronal survival and migration through ERβ and that decreased signaling leads to cortical thinning likely secondary to impairments in these processes. While the beginning of the period during which decreased signaling through ERβ in the mouse fetal brain leads to cortical thinning was narrowed down to E14.5 at the earliest, thus overlapping with the period of antibody exposure in our model, no sex bias was observed. This lack of sex bias in the effects of altered signaling through ERβ on cortical structure could account for the insignificant influence of gonadal hormones in our ASD model as one would expect C6 to interact with processes that when altered have different outcomes in males compared to females.

Both testosterone and estrogens are present in mouse fetal circulation at the time of C6 exposure. Fetal Leydig cells in mice arise on E12.5 [reviewed in (70)] and proteins required for testosterone synthesis are first detected between E12.5 and E13.5, coinciding with the earliest reported testosterone production (71). Given that fetal rodent ovaries are thought to

produce minimal amounts of estrogen (72), estrogens in the fetal peripheral circulation likely originate from maternal and placental sources. However, of these hormones, only peripherally derived testosterone crosses the blood brain barrier in a form that can be actively used. Estrogens in the peripheral circulation are bound by alpha-fetoprotein, rendering them inaccessible for cell signaling in the brain (73). Thus, alpha-fetoprotein protects the female rodent brain from masculinization and defeminization by estrogen (73) while testosterone aromatization to estrogen masculinizes and defeminizes the male rodent brain. While alpha-fetoprotein may sequester peripheral estrogens, other sources of estrogen including aromatization of testosterone and *de novo* synthesis from cholesterol have been identified in the developing rodent brain (74–83). Moreover, Martínez-Cerdeño et al. (64) detected aromatase expression in the mouse ventricular and subventricular zones as early as E9. Interestingly, alpha-fetoprotein is also strongly expressed in the ventricular zone from E12 (64). Hence, while there may be differences in the level of estrogen in the brain during development between males and females, C6 may alter brain developmental processes in regions where estrogen signaling is diminished by locally produced alpha-fetoprotein. Furthermore, sex chromosome genes may modulate aromatase and gonadal hormone receptor expression in the brain (84, 85), potentially accounting for the observed dominant genetic effect on C6 susceptibility. In accordance with this hypothesis, decreased expression of aromatase has been detected in individuals with ASD (86, 87).

The behavioral assessment of adult mice revealed that the time spent in the center of an open-field arena did not significantly increase upon repeat exposure in C6-XYM and C6-XYF mice. Furthermore, C6-XYM and C6-XYF mice spent significantly less time in the center of the arena during repeat exposure compared to the control B1 counterparts. We have termed this response sustained anxiety-like behavior, as anxiety has been defined by others as avoidance of the center of an arena in the first exposure. Together, these observations indicate an abnormal behavioral pattern due to *in utero* C6 exposure in XYM and XYF mice. Conversely, XXM mice showed a significant difference in time spent in the center between the first and repeated exposures independent of C6 or B1 exposure, suggesting that the anxiety phenotypes are driven by sex chromosome complement. Indeed, individuals with sex chromosome aneuploidies, including Klinefelter and Turner Syndromes, have been reported to have an increased prevalence of anxiety (88–90). Additional tests including the elevated plus maze and light-dark box tests may be useful to further characterize the anxiogenic effects of C6 and the relationship to sex chromosome complement.

In this study we identified sex chromosome complement to be essential for the effects of *in utero* exposure to C6 maternal antibody on fetal brain cortical development and adult behavior. Differences in gene dosage is one potential mechanism through which sex chromosome complement may be increasing the susceptibility of XY mice to C6. Indeed, Xu et al. (59) identified a subset of genes outside the pseudo-autosomal region of the sex chromosomes whose level of expression in the brain shows a sex bias. Furthermore, while X chromosome inactivation is a compensatory mechanism for differences in gene dosage between XX and XY complements (91), an estimated 10–15% of the X chromosome genes outside the pseudo-autosomal region escape inactivation in humans and are therefore more highly expressed in XX compared to XY individuals (92, 93). Finally, imprinting can affect expression levels of X chromosome genes in the brain (94–96) and has been associated with impairments in social behavior in Turner Syndrome (97) and cognitive function in a mouse model of this condition (94). Of note, the mouse Y chromosome encodes for 10× more genes than the human Y chromosome (98). Consequently, if Y chromosome genes account for the male bias observed in our mouse model of maternal antibody induced ASD, our findings may not completely translate to the pathogenesis of ASD in humans exposed *in utero* to anti-Caspr2 antibody.

While the establishment of sexual dimorphisms involves both gonadal hormones and sex chromosomes, both of which are operative not just during the window of fetal brain exposure to maternal antibody our data suggest that gonadal hormones have a limited role in determining the susceptibility to C6-induced phenotypes, at least in these genetically manipulated mice. It should be noted that sex hormone levels in these mice are not the same as in the C57BL/6 strain in which the C6 model was established. Nevertheless, C6 likely impairs development processes that are regulated by sex chromosome genes. It is possible that these sex chromosome genes modulate gonadal hormone signaling pathways. For example, sex chromosome complement determines sex differences in aromatase and ERβ expression levels in the developing mouse amygdala (84, 85). Given the proposed relationship between cortical thickness and sociability (30) and symptom severity (99) in ASD, further inquiry into the exact mechanism by which sex chromosome complement influences the risk to develop ASD-like phenotypes due to C6 exposure *in utero* is important. Deciphering the exact mechanisms through which sex chromosome genes compensate for or exacerbate the effects of *in utero* C6 exposure in females and males, respectively, will be key for expanding our knowledge of brain development and identifying potential therapeutic targets for ASD.

DATA AVAILABILITY STATEMENT

The original contributions presented in the study are included in the article/**Supplementary Material**, further inquiries can be directed to the corresponding author/s.

ETHICS STATEMENT

The animal study was reviewed and approved by Institutional Animal Care and Use Committee (IACUC) of the Feinstein Institutes for Medical Research.

AUTHOR CONTRIBUTIONS

AG-G, AP, LB, BV, PH, and BD designed the experiments. AG-G, AP, BV, and PH performed experiments and analyzed the data.

AG-G and PH made the final figures. AG-G, PH, and BD wrote the manuscript. All authors approved the manuscript.

FUNDING

This work was supported by the National Institutes of Health (NIH) grant 5P01AI102852 and NIH grant 5P01AI073693 to BD. It was also supported by the Nancy Lurie Marks Family Foundation (BD). PH was supported by DOD Impact Award W81XWH1910759.

ACKNOWLEDGMENTS

We thank Andrea La Bella for help with experiments.

SUPPLEMENTARY MATERIAL

The Supplementary Material for this article can be found online at: https://www.frontiersin.org/articles/10.3389/fneur.2021.721108/full#supplementary-material

REFERENCES

1. Baio J, Wiggins L, Christensen DL, Maenner MJ, Daniels J, Warren Z, et al. Prevalence of autism spectrum disorder among children aged 8 years - autism and developmental disabilities monitoring network, 11 sites, United States, 2014. *MMWR Surveill Summ.* (2018) 67:1–23. doi: 10.15585/mmwr.ss6706a1
2. Gata-Garcia A, Diamond B. Maternal antibody and ASD: clinical data and animal models. *Front Immunol.* (2019) 10:1129. doi: 10.3389/fimmu.2019.01129
3. Bai D, Yip BHK, Windham GC, Sourander A, Francis R, Yoffe R, et al. Association of genetic and environmental factors with autism in a 5-country cohort. *JAMA Psychiatry.* (2019) 76:1035–43. doi: 10.1001/jamapsychiatry.2019.1411
4. Baron-Cohen S, Lombardo MV, Auyeung B, Ashwin E, Chakrabarti B, Knickmeyer R. Why are autism spectrum conditions more prevalent in males? *PLoS Biol.* (2011) 9:e1001081. doi: 10.1371/journal.pbio.1001081
5. Nolen-Hoeksema S, Girgus JS. The emergence of gender differences in depression during adolescence. *Psychol Bull.* (1994) 115:424–43. doi: 10.1037/0033-2909.115.3.424
6. Rutter M, Caspi A, Moffitt TE. Using sex differences in psychopathology to study causal mechanisms: unifying issues and research strategies. *J Child Psychol Psychiatry.* (2003) 44:1092–115. doi: 10.1111/1469-7610.00194
7. Brimberg L, Mader S, Jeganathan V, Berlin R, Coleman TR, Gregersen PK, et al. Caspr2-reactive antibody cloned from a mother of an ASD child mediates an ASD-like phenotype in mice. *Mol Psychiatry.* (2016) 21:1663–71. doi: 10.1038/mp.2016.165
8. Bel C, Oguievetskaia K, Pitaval C, Goutebroze L, Faivre-Sarrailh C. Axonal targeting of Caspr2 in hippocampal neurons via selective somatodendritic endocytosis. *J Cell Sci.* (2009) 122 (Pt. 18):3403–13. doi: 10.1242/jcs.050526
9. Poliak S, Gollan L, Martinez R, Custer A, Einheber S, Salzer JL, et al. Caspr2, a new member of the neurexin superfamily, is localized at the juxtaparanodes of myelinated axons and associates with K+ channels. *Neuron.* (1999) 24:1037–47. doi: 10.1016/S0896-6273(00)81049-1
10. Alarcón M, Abrahams BS, Stone JL, Duvall JA, Perederiy JV, Bomar JM, et al. Linkage, association, and gene-expression analyses identify CNTNAP2 as an autism-susceptibility gene. *Am J Hum Genet.* (2008) 82:150–9. doi: 10.1016/j.ajhg.2007.09.005
11. Arking DE, Cutler DJ, Brune CW, Teslovich TM, West K, Ikeda M, et al. A common genetic variant in the neurexin superfamily member CNTNAP2 increases familial risk of autism. *Am J Hum Genet.* (2008) 82:160–4. doi: 10.1016/j.ajhg.2007.09.015
12. Bakkaloglu B, O'Roak BJ, Louvi A, Gupta AR, Abelson JF, Morgan TM, et al. Molecular cytogenetic analysis and resequencing of contactin associated protein-like 2 in autism spectrum disorders. *Am J Hum Genet.* (2008) 82:165–73. doi: 10.1016/j.ajhg.2007.09.017
13. Newbury DF, Paracchini S, Scerri TS, Winchester L, Addis L, Richardson AJ, et al. Investigation of dyslexia and SLI risk variants in reading- and language-impaired subjects. *Behav Genet.* (2011) 41:90–104. doi: 10.1007/s10519-010-9424-3
14. Nord AS, Roeb W, Dickel DE, Walsh T, Kusenda M, O'Connor KL, et al. Reduced transcript expression of genes affected by inherited and *de novo* CNVs in autism. *Eur J Hum Genet.* (2011) 19:727–31. doi: 10.1038/ejhg.2011.24
15. O'Roak BJ, Deriziotis P, Lee C, Vives L, Schwartz JJ, Girirajan S, et al. Exome sequencing in sporadic autism spectrum disorders identifies severe de novo mutations. *Nat Genet.* (2011) 43:585–9. doi: 10.1038/ng.835
16. Poot M, Beyer V, Schwaab I, Damatova N, Van't Slot R, Prothero J, et al. Disruption of CNTNAP2 and additional structural genome changes in a boy with speech delay and autism spectrum disorder. *Neurogenetics.* (2010) 11:81–9. doi: 10.1007/s10048-009-0205-1
17. Sehested LT, Møller RS, Bache I, Andersen NB, Ullmann R, Tommerup N, et al. Deletion of 7q34-q36.2 in two siblings with mental retardation, language delay, primary amenorrhea, dysmorphic features. *Am J Med Genet A.* (2010) 152A:3115–9. doi: 10.1002/ajmg.a.33476
18. Steer CD, Golding J, Bolton PF. Traits contributing to the autistic spectrum. *PLoS ONE.* (2010) 5:e12633. doi: 10.1371/journal.pone.0012633
19. Strauss KA, Puffenberger EG, Huentelman MJ, Gottlieb S, Dobrin SE, Parod JM, et al. Recessive symptomatic focal epilepsy and mutant contactin-associated protein-like 2. *N Engl J Med.* (2006) 354:1370–7. doi: 10.1056/NEJMoa052773
20. Vernes SC, Newbury DF, Abrahams BS, Winchester L, Nicod J, Groszer M, et al. A functional genetic link between distinct developmental language disorders. *N Engl J Med.* (2008) 359:2337–45. doi: 10.1056/NEJMoa0802828
21. De Vries GJ, Rissman EF, Simerly RB, Yang LY, Scordalakes EM, Auger CJ, et al. A model system for study of sex chromosome effects on sexually dimorphic neural and behavioral traits. *J Neurosci.* (2002) 22:9005–14. doi: 10.1523/JNEUROSCI.22-20-09005.2002
22. Itoh Y, Mackie R, Kampf K, Domadia S, Brown JD, O'Neill R, et al. Four core genotypes mouse model: localization of the sry transgene and bioassay for testicular hormone levels. *BMC Res Notes.* (2015) 8:69. doi: 10.1186/s13104-015-0986-2
23. Schambra UB. *Prenatal Mouse Brain Atlas*. 1st edn. Boston, MA: Springer (2008). doi: 10.1007/978-0-387-47093-1
24. Lee JY, Huerta PT, Zhang J, Kowal C, Bertini E, Volpe BT, et al. Neurotoxic autoantibodies mediate congenital cortical impairment of offspring in maternal lupus. *Nat Med.* (2009) 15:91–6. doi: 10.1038/nm.1892
25. Thomas A, Burant A, Bui N, Graham D, Yuva-Paylor LA, Paylor R. Marble burying reflects a repetitive and perseverative behavior more than novelty-induced anxiety. *Psychopharmacology.* (2009) 204:361–73. doi: 10.1007/s00213-009-1466-y
26. Yang M, Silverman JL, Crawley JN. Automated three-chambered social approach task for mice. *Curr Protoc Neurosci.* (2011) Chapter 8:Unit 8.26. doi: 10.1002/0471142301.ns0826s56
27. Chung MK, Robbins SM, Dalton KM, Davidson RJ, Alexander AL, Evans AC. Cortical thickness analysis in autism with heat kernel smoothing. *Neuroimage.* (2005) 25:1256–65. doi: 10.1016/j.neuroimage.2004.12.052
28. Hadjikhani N, Joseph RM, Snyder J, Tager-Flusberg H. Anatomical differences in the mirror neuron system and social cognition network in autism. *Cereb Cortex.* (2006) 16:1276–82. doi: 10.1093/cercor/bhj069
29. Hyde KL, Samson F, Evans AC, Mottron L. Neuroanatomical differences in brain areas implicated in perceptual and other core features of autism revealed by cortical thickness analysis and voxel-based morphometry. *Hum Brain Mapp.* (2010) 31:556–66. doi: 10.1002/hbm.20887
30. Richter J, Henze R, Vomstein K, Stieltjes B, Parzer P, Haffner J, et al. Reduced cortical thickness and its association with social reactivity in

children with autism spectrum disorder. *Psychiatry Res.* (2015) 234:15–24. doi: 10.1016/j.pscychresns.2015.06.011
31. Scheel C, Rotarska-Jagiela A, Schilbach L, Lehnhardt FG, Krug B, Vogeley K, et al. Imaging derived cortical thickness reduction in high-functioning autism: key regions and temporal slope. *Neuroimage.* (2011) 58:391–400. doi: 10.1016/j.neuroimage.2011.06.040
32. Wallace GL, Dankner N, Kenworthy L, Giedd JN, Martin A. Age-related temporal and parietal cortical thinning in autism spectrum disorders. *Brain.* (2010) 133 (Pt. 12):3745–54. doi: 10.1093/brain/awq279
33. Hardan AY, Muddasani S, Vemulapalli M, Keshavan MS, Minshew NJ. An MRI study of increased cortical thickness in autism. *Am J Psychiatry.* (2006) 163:1290–2. doi: 10.1176/ajp.2006.163.7.1290
34. Jou RJ, Minshew NJ, Keshavan MS, Vitale MP, Hardan AY. Enlarged right superior temporal gyrus in children and adolescents with autism. *Brain Res.* (2010) 1360:205–12. doi: 10.1016/j.brainres.2010.09.005
35. Khundrakpam BS, Lewis JD, Kostopoulos P, Carbonell F, Evans AC. Cortical thickness abnormalities in autism spectrum disorders through late childhood, adolescence, and adulthood: a large-scale MRI study. *Cereb Cortex.* (2017) 27:1721–31. doi: 10.1093/cercor/bhx038
36. Abel JM, Witt DM, Rissman EF. Sex differences in the cerebellum and frontal cortex: roles of estrogen receptor alpha and sex chromosome genes. *Neuroendocrinology.* (2011) 93:230–40. doi: 10.1159/000324402
37. Carruth LL, Reisert I, Arnold AP. Sex chromosome genes directly affect brain sexual differentiation. *Nat Neurosci.* (2002) 5:933–4. doi: 10.1038/nn922
38. Corre C, Friedel M, Vousden DA, Metcalf A, Spring S, Qiu LR, et al. Separate effects of sex hormones and sex chromosomes on brain structure and function revealed by high-resolution magnetic resonance imaging and spatial navigation assessment of the four core genotype mouse model. *Brain Struct Funct.* (2016) 221:997–1016. doi: 10.1007/s00429-014-0952-0
39. Savic I, Frisen L, Manzouri A, Nordenstrom A, Lindén Hirschberg A. Role of testosterone and Y chromosome genes for the masculinization of the human brain. *Hum Brain Mapp.* (2017) 38:1801–14. doi: 10.1002/hbm.23483
40. Seney ML, Ekong KI, Ding Y, Tseng GC, Sibille E. Sex chromosome complement regulates expression of mood-related genes. *Biol Sex Differ.* (2013) 4:20. doi: 10.1186/2042-6410-4-20
41. Savic I, Arver S. Sex differences in cortical thickness and their possible genetic and sex hormonal underpinnings. *Cereb Cortex.* (2014) 24:3246–57. doi: 10.1093/cercor/bht180
42. Good CD, Lawrence K, Thomas NS, Price CJ, Ashburner J, Friston KJ, et al. Dosage-sensitive X-linked locus influences the development of amygdala and orbitofrontal cortex, and fear recognition in humans. *Brain.* (2003) 126 (Pt. 11):2431–46. doi: 10.1093/brain/awg242
43. Lentini E, Kasahara M, Arver S, Savic I. Sex differences in the human brain and the impact of sex chromosomes and sex hormones. *Cereb Cortex.* (2013) 23:2322–36. doi: 10.1093/cercor/bhs222
44. Lepage JF, Hong DS, Mazaika PK, Raman M, Sheau K, Marzelli MJ, et al. Genomic imprinting effects of the X chromosome on brain morphology. *J Neurosci.* (2013) 33:8567–74. doi: 10.1523/JNEUROSCI.5810-12.2013
45. Vawter MP, Harvey PD, DeLisi LE. Dysregulation of X-linked gene expression in Klinefelter's syndrome and association with verbal cognition. *Am J Med Genet B Neuropsychiatr Genet.* (2007) 144B:728–34. doi: 10.1002/ajmg.b.30454
46. Green T, Flash S, Reiss AL. Sex differences in psychiatric disorders: what we can learn from sex chromosome aneuploidies. *Neuropsychopharmacology.* (2019) 44:9–21. doi: 10.1038/s41386-018-0153-2
47. Bishop DV, Jacobs PA, Lachlan K, Wellesley D, Barnicoat A, Boyd PA, et al. Autism, language and communication in children with sex chromosome trisomies. *Arch Dis Child.* (2011) 96:954–9. doi: 10.1136/adc.2009.179747
48. Bruining H, Swaab H, Kas M, van Engeland H. Psychiatric characteristics in a self-selected sample of boys with Klinefelter syndrome. *Pediatrics.* (2009) 123:e865–70. doi: 10.1542/peds.2008-1954
49. Tartaglia N, Davis S, Hench A, Nimishakavi S, Beauregard R, Reynolds A, et al. A new look at XXYY syndrome: medical and psychological features. *Am J Med Genet A.* (2008) 146A:1509–22. doi: 10.1002/ajmg.a.32366
50. Tartaglia NR, Wilson R, Miller JS, Rafalko J, Cordeiro L, Davis S, et al. Autism spectrum disorder in males with sex chromosome aneuploidy: XXY/klinefelter syndrome, XYY, and XXYY. *J Dev Behav Pediatr.* (2017) 38:197–207. doi: 10.1097/DBP.0000000000000429
51. van Rijn S, Swaab H. Vulnerability for psychopathology in Klinefelter syndrome: age-specific and cognitive-specific risk profiles. *Acta Paediatr.* (2011) 100:908–16. doi: 10.1111/j.1651-2227.2011.02289.x
52. Cox KH, Rissman EF. Sex differences in juvenile mouse social behavior are influenced by sex chromosomes and social context. *Genes Brain Behav.* (2011) 10:465–72. doi: 10.1111/j.1601-183X.2011.00688.x
53. Dewing P, Chiang CW, Sinchak K, Sim H, Fernagut PO, Kelly S, et al. Direct regulation of adult brain function by the male-specific factor SRY. *Curr Biol.* (2006) 16:415–20. doi: 10.1016/j.cub.2006.01.017
54. Gatewood JD, Wills A, Shetty S, Xu J, Arnold AP, Burgoyne PS, et al. Sex chromosome complement and gonadal sex influence aggressive and parental behaviors in mice. *J Neurosci.* (2006) 26:2335–42. doi: 10.1523/JNEUROSCI.3743-05.2006
55. Kopsida E, Lynn PM, Humby T, Wilkinson LS, Davies W. Dissociable effects of sry and sex chromosome complement on activity, feeding and anxiety-related behaviours in mice. *PLoS ONE.* (2013) 8:e73699. doi: 10.1371/journal.pone.0073699
56. Maxson SC, Didier-Erickson A, Ogawa S. The Y chromosome, social signals, and offense in mice. *Behav Neural Biol.* (1989) 52:251–9. doi: 10.1016/S0163-1047(89)90369-5
57. McPhie-Lalmansingh AA, Tejada LD, Weaver JL, Rissman EF. Sex chromosome complement affects social interactions in mice. *Horm Behav.* (2008) 54:565–70. doi: 10.1016/j.yhbeh.2008.05.016
58. Sluyter F, Bohus B, Beldhuis HJ, van Oortmerssen GA. Autosomal and Y chromosomal effects on the stereotyped response to apomorphine in wild house mice. *Pharmacol Biochem Behav.* (1995) 52:17–22. doi: 10.1016/0091-3057(95)00092-B
59. Xu J, Burgoyne PS, Arnold AP. Sex differences in sex chromosome gene expression in mouse brain. *Hum Mol Genet.* (2002) 11:1409–19. doi: 10.1093/hmg/11.12.1409
60. Markham JA, Jurgens HA, Auger CJ, De Vries GJ, Arnold AP, Juraska JM. Sex differences in mouse cortical thickness are independent of the complement of sex chromosomes. *Neuroscience.* (2003) 116:71–5. doi: 10.1016/S0306-4522(02)00554-7
61. Bramen JE, Hranilovich JA, Dahl RE, Chen J, Rosso C, Forbes EE, et al. Sex matters during adolescence: testosterone-related cortical thickness maturation differs between boys and girls. *PLoS ONE.* (2012) 7:e33850. doi: 10.1371/journal.pone.0033850
62. Nguyen TV, McCracken J, Ducharme S, Botteron KN, Mahabir M, Johnson W, et al. Testosterone-related cortical maturation across childhood and adolescence. *Cereb Cortex.* (2013) 23:1424–32. doi: 10.1093/cercor/bhs125
63. Young WJ, Chang C. Ontogeny and autoregulation of androgen receptor mRNA expression in the nervous system. *Endocrine.* (1998) 9:79–88. doi: 10.1385/ENDO:9:1:79
64. Martínez-Cerdeño V, Noctor SC, Kriegstein AR. Estradiol stimulates progenitor cell division in the ventricular and subventricular zones of the embryonic neocortex. *Eur J Neurosci.* (2006) 24:3475–88. doi: 10.1111/j.1460-9568.2006.05239.x
65. Lemmen JG, Broekhof JL, Kuiper GG, Gustafsson JA, van der Saag PT, van der Burg B. Expression of estrogen receptor alpha and beta during mouse embryogenesis. *Mech Dev.* (1999) 81:163–7. doi: 10.1016/S0925-4773(98)00223-8
66. Miranda RC, Toran-Allerand CD. Developmental expression of estrogen receptor mRNA in the rat cerebral cortex: a nonisotopic in situ hybridization histochemistry study. *Cereb Cortex.* (1992) 2:1–15. doi: 10.1093/cercor/2.1.1
67. Fan X, Warner M, Gustafsson JA. Estrogen receptor beta expression in the embryonic brain regulates development of calretinin-immunoreactive GABAergic interneurons. *Proc Natl Acad Sci USA.* (2006) 103:19338–43. doi: 10.1073/pnas.0609663103
68. Zhang L, Chang YH, Barker JL, Hu Q, Maric D, Li BS, et al. Testosterone and estrogen affect neuronal differentiation but not proliferation in early embryonic cortex of the rat: the possible roles of androgen and estrogen receptors. *Neurosci Lett.* (2000) 281:57–60. doi: 10.1016/S0304-3940(99)00942-8
69. Wang L, Andersson S, Warner M, Gustafsson JA. Estrogen receptor (ER)beta knockout mice reveal a role for ERbeta in migration of cortical

neurons in the developing brain. *Proc Natl Acad Sci USA*. (2003) 100:703–8. doi: 10.1073/pnas.242735799
70. O'Shaughnessy PJ, Baker PJ, Johnston H. The foetal leydig cell–differentiation, function and regulation. *Int J Androl.* (2006) 29:90–5; discussion 105–108. doi: 10.1111/j.1365-2605.2005.00555.x
71. Büdefeld T, Jezek D, Rozman D, Majdic G. Initiation of steroidogenesis precedes expression of cholesterologenic enzymes in the fetal mouse testes. *Anat Histol Embryol.* (2009) 38:461–6. doi: 10.1111/j.1439-0264.2009.00975.x
72. Lamprecht SA, Kohen F, Ausher J, Zor U, Lindner HR. Hormonal stimulation of oestradiol-17 beta release from the rat ovary during early postnatal development. *J Endocrinol.* (1976) 68:343–4. doi: 10.1677/joe.0.0680343
73. Bakker J, De Mees C, Douhard Q, Balthazart J, Gabant P, Szpirer J, et al. Alpha-fetoprotein protects the developing female mouse brain from masculinization and defeminization by estrogens. *Nat Neurosci.* (2006) 9:220–6. doi: 10.1038/nn1624
74. Amateau SK, Alt JJ, Stamps CL, McCarthy MM. Brain estradiol content in newborn rats: sex differences, regional heterogeneity, and possible de novo synthesis by the female telencephalon. *Endocrinology.* (2004) 145:2906–17. doi: 10.1210/en.2003-1363
75. Hojo Y, Hattori TA, Enami T, Furukawa A, Suzuki K, Ishii HT, et al. Adult male rat hippocampus synthesizes estradiol from pregnenolone by cytochromes P45017alpha and P450 aromatase localized in neurons. *Proc Natl Acad Sci USA*. (2004) 101:865–70. doi: 10.1073/pnas.2630225100
76. Kimoto T, Tsurugizawa T, Ohta Y, Makino J, Tamura, H.o, et al. Neurosteroid synthesis by cytochrome p450-containing systems localized in the rat brain hippocampal neurons: N-methyl-D-aspartate and calcium-dependent synthesis. *Endocrinology.* (2001) 142:3578–89. doi: 10.1210/endo.142.8.8327
77. MacLusky NJ, Walters MJ, Clark AS, Toran-Allerand CD. Aromatase in the cerebral cortex, hippocampus, and mid-brain: ontogeny and developmental implications. *Mol Cell Neurosci.* (1994) 5:691–8. doi: 10.1006/mcne.1994.1083
78. McEwen BS, Lieberburg I, Chaptal C, Krey LC. Aromatization: important for sexual differentiation of the neonatal rat brain. *Horm Behav.* (1977) 9:249–63. doi: 10.1016/0018-506X(77)90060-5
79. Naftolin F, Ryan KJ, Davies IJ, Reddy VV, Flores F, Petro Z, et al. The formation of estrogens by central neuroendocrine tissues. *Recent Prog Horm Res.* (1975) 31:295–319. doi: 10.1016/B978-0-12-571131-9.50012-8
80. Prange-Kiel J, Wehrenberg U, Jarry H, Rune GM. Para/autocrine regulation of estrogen receptors in hippocampal neurons. *Hippocampus.* (2003) 13:226–34. doi: 10.1002/hipo.10075
81. Rhoda J, Corbier P, Roffi J. Gonadal steroid concentrations in serum and hypothalamus of the rat at birth: aromatization of testosterone to 17 beta-estradiol. *Endocrinology.* (1984) 114:1754–60. doi: 10.1210/endo-114-5-1754
82. Rune GM, Frotscher M. Neurosteroid synthesis in the hippocampus: role in synaptic plasticity. *Neuroscience.* (2005) 136:833–42. doi: 10.1016/j.neuroscience.2005.03.056
83. Vreeburg JT, van der Vaart PD, van der Schoot P. Prevention of central defeminization but not masculinization in male rats by inhibition neonatally of oestrogen biosynthesis. *J Endocrinol.* (1977) 74:375–82. doi: 10.1677/joe.0.0740375
84. Cisternas CD, Tome K, Caeiro XE, Dadam FM, Garcia-Segura LM, Cambiasso MJ. Sex chromosome complement determines sex differences in aromatase expression and regulation in the stria terminalis and anterior amygdala of the developing mouse brain. *Mol Cell Endocrinol.* (2015) 414:99–110. doi: 10.1016/j.mce.2015.07.027
85. Cisternas CD, Cabrera Zapata LE, Arevalo MA, Garcia-Segura LM, Cambiasso MJ. Regulation of aromatase expression in the anterior amygdala of the developing mouse brain depends on ERβ and sex chromosome complement. *Sci Rep.* (2017) 7:5320. doi: 10.1038/s41598-017-05658-6
86. Crider A, Thakkar R, Ahmed AO, Pillai A. Dysregulation of estrogen receptor beta (ERβ), aromatase (CYP19A1), and ER co-activators in the middle frontal gyrus of autism spectrum disorder subjects. *Mol Autism.* (2014) 5:46. doi: 10.1186/2040-2392-5-46
87. Sarachana T, Xu M, Wu RC, Hu VW. Sex hormones in autism: androgens and estrogens differentially and reciprocally regulate RORA. A novel candidate gene for autism. *PLoS ONE.* (2011) 6:e17116. doi: 10.1371/journal.pone.0017116
88. Kili,ç BG, Ergür AT, Ocal G. Depression, levels of anxiety and self-concept in girls with Turner's syndrome. *J Pediatr Endocrinol Metab.* (2005) 18:1111–7. doi: 10.1515/JPEM.2005.18.11.1111
89. Schmidt PJ, Cardoso GM, Ross JL, Haq N, Rubinow DR, Bondy CA. Shyness, social anxiety, and impaired self-esteem in Turner syndrome and premature ovarian failure. *JAMA*. (2006) 295:1374–6. doi: 10.1001/jama.295.12.1374
90. Tartaglia N, Cordeiro L, Howell S, Wilson R, Janusz J. The spectrum of the behavioral phenotype in boys and adolescents 47,XXY (Klinefelter syndrome). *Pediatr Endocrinol Rev*. (2010) 8 (Suppl. 1):151–9.
91. Lyon MF. Gene action in the X-chromosome of the mouse (*Mus musculus* L.). *Nature.* (1961) 190:372–3. doi: 10.1038/190372a0
92. Carrel L, Cottle AA, Goglin KC, Willard HF. A first-generation X-inactivation profile of the human X chromosome. *Proc Natl Acad Sci USA.* (1999) 96:14440–4. doi: 10.1073/pnas.96.25.14440
93. Carrel L, Willard HF. X-inactivation profile reveals extensive variability in X-linked gene expression in females. *Nature.* (2005) 434:400–4. doi: 10.1038/nature03479
94. Davies W, Isles A, Smith R, Karunadasa D, Burrmann D, Humby T, et al. Xlr3b is a new imprinted candidate for X-linked parent-of-origin effects on cognitive function in mice. *Nat Genet.* (2005) 37:625–9. doi: 10.1038/ng1577
95. Gregg C, Zhang J, Butler JE, Haig D, Dulac C. Sex-specific parent-of-origin allelic expression in the mouse brain. *Science.* (2010) 329:682–5. doi: 10.1126/science.1190831
96. Raefski AS, O'Neill MJ. Identification of a cluster of X-linked imprinted genes in mice. *Nat Genet.* (2005) 37:620–4. doi: 10.1038/ng1567
97. Skuse DH, James RS, Bishop DV, Coppin B, Dalton P, Aamodt-Leeper G, et al. Evidence from turner's syndrome of an imprinted X-linked locus affecting cognitive function. *Nature.* (1997) 387:705–8. doi: 10.1038/42706
98. Hughes JF, Page DC. The biology and evolution of mammalian Y chromosomes. *Annu Rev Genet.* (2015) 49:507–27. doi: 10.1146/annurev-genet-112414-055311
99. Ecker C, Ginestet C, Feng Y, Johnston P, Lombardo MV, Lai MC, et al. Brain surface anatomy in adults with autism: the relationship between surface area, cortical thickness, autistic symptoms. *JAMA Psychiatry.* (2013) 70:59–70. doi: 10.1001/jamapsychiatry.2013.265

Conflict of Interest: The authors declare that the research was conducted in the absence of any commercial or financial relationships that could be construed as a potential conflict of interest.

AUTOIMMUNITY

In utero exposure to maternal anti–aquaporin-4 antibodies alters brain vasculature and neural dynamics in male mouse offspring

Simone Mader[1,2]*†, Lior Brimberg[1]†, An Vo[1], Joshua J. Strohl[1,3], James M. Crawford[4], Alexandre Bonnin[5], Joseph Carrión[1], Delcora Campbell[1], Tomás S. Huerta[1,3], Andrea La Bella[1], Roseann Berlin[1], Stephen L. Dewey[1], Matthew Hellman[1], David Eidelberg[1], Irena Dujmovic[6,7], Jelena Drulovic[6], Jeffrey L. Bennett[8], Bruce T. Volpe[1], Patricio T. Huerta[1,3], Betty Diamond[1]

The fetal brain is constantly exposed to maternal IgG before the formation of an effective blood-brain barrier (BBB). Here, we studied the consequences of fetal brain exposure to an antibody to the astrocytic protein aquaporin-4 (AQP4-IgG) in mice. AQP4-IgG was cloned from a patient with neuromyelitis optica spectrum disorder (NMOSD), an autoimmune disease that can affect women of childbearing age. We found that embryonic radial glia cells in neocortex express AQP4. These cells are critical for blood vessel and BBB formation through modulation of the WNT signaling pathway. Male fetuses exposed to AQP4-IgG had abnormal cortical vasculature and lower expression of WNT signaling molecules *Wnt*5a and *Wnt*7a. Positron emission tomography of adult male mice exposed in utero to AQP4-IgG revealed increased blood flow and BBB leakiness in the entorhinal cortex. Adult male mice exposed in utero to AQP4-IgG had abnormal cortical vessels, fewer dendritic spines in pyramidal and stellate neurons, and more S100β$^+$ astrocytes in the entorhinal cortex. Behaviorally, they showed impairments in the object-place memory task. Neural recordings indicated that their grid cell system, within the medial entorhinal cortex, did not map the local environment appropriately. Collectively, these data implicate in utero binding of AQP4-IgG to radial glia cells as a mechanism for alterations of the developing male brain and adds NMOSD to the conditions in which maternal IgG may cause persistent brain dysfunction in offspring.

INTRODUCTION

A family history of autoimmune diseases is associated with an increased risk of neurodevelopmental and neuropsychiatric disorders in the offspring. An increased risk for brain defects has been described in children born to mothers, but not fathers, with celiac disease, rheumatoid arthritis, and systemic lupus erythematosus (SLE) (*1*, *2*). Neuromyelitis optica spectrum disorder (NMOSD) is an autoimmune disease causing demyelination of the optic nerves, brainstem, and spinal cord (*3*) affecting women of childbearing age (*4*). NMOSD is characterized by the presence of antibodies against the astrocytic protein aquaporin-4 (AQP4)–immunoglobulin G (IgG); these are present in nearly 80% of patients (*5*, *6*) and contribute to disease pathogenesis. Administration of monoclonal AQP4-IgGs cloned from a patient with NMOSD into rodent models of experimental autoimmune encephalitis (*7*–*9*), or direct injection of AQP4-IgG into rodent brain (*10*), results in a phenotype that closely resembles NMOSD. Complement-dependent cytotoxicity (CDC) appears to be a major mechanism of tissue damage by AQP4-IgG (*8*, *10*–*12*), but pathogenic T cells have also been implicated in brain injury (*13*, *14*). Most studies in pregnant women with NMOSD focus on the effect of pregnancy on disease activity (*15*–*18*), although there are some reports of increased miscarriage and preeclampsia (*4*, *19*), sometimes accompanied by multiple infarcts in the placenta (*19*). The available follow-up evidence for an effect of AQP4-IgG on neonates is sparse but includes cases of infants with hydrocephalus and persistent neurological impairment (*4*, *20*). There are no long-term follow-up studies of children born to AQP4-IgG–positive mothers.

It is well established that in utero exposure to maternal autoantibodies present in other conditions can alter neurodevelopment as IgG can access the developing before the blood brain barrier (BBB) matures (*21*–*23*). For example, maternal antibodies that cross-react with the *N*-methyl-D-aspartate receptor found in SLE lead to cognitive impairment in male offspring (*24*) and nonviability of female fetuses (*25*). Moreover, in a mouse model of autism spectrum disorders (ASDs), maternal antibodies against Contactin-associated protein-like 2 (Caspr2) are associated with deficits in social interaction and repetitive behaviors in the offspring (*26*).

During embryonic development, AQP4 is expressed in radial glial cells (RGCs) of the developing cortex; however, by postpartum days 1 to 3, its expression is restricted to astrocytes (*27*). RGCs initially guide neuronal development, are the precursor cells for astrocytes (*28*–*30*), contribute to central nervous system (CNS) vascularization (*31*–*34*), and modulate wingless-type MMTV integration site family (WNT) signaling pathways in endothelial cells to stabilize newly formed blood vessels in the late embryonic brain (*35*). Although gene expression studies show that RGCs express *Aqp4* (*36*), its function in these cells is not completely elucidated. In the

[1]The Feinstein Institutes for Medical Research, Northwell Health, Manhasset NY 11030, USA. [2]Institute of Clinical Neuroimmunology, Biomedical Center of the Ludwig Maximilian University of Munich, Munich 82152, Germany. [3]Department of Molecular Medicine, Zucker School of Medicine at Hofstra/Northwell, Manhasset, NY 11030, USA. [4]Department of Pathology and Laboratory Medicine, Northwell Health, Manhasset, NY 11030, USA. [5]Department of Physiology and Neurosciences, Zilkha Neurogenetic Institute, University of Southern California, Keck School of Medicine, Los Angeles, CA 90033, USA. [6]Clinical Center of Serbia University School of Medicine, Belgrade, 11000, Serbia. [7]Department of Neurology, University of North Carolina, School of Medicine, Chapel Hill, NC 27517, USA. [8]Department of Neurology and Ophthalmology, Programs in Neuroscience and Immunology, University of Colorado Denver, School of Medicine, Denver, CO 80045, USA.
*Corresponding author Email: simone.mader@med.uni-muenchen.de
†These authors contributed equally to this work.

adult brain, AQP4 functions as a water channel that is localized in a polarized form at the endfeet of astrocytes that surround blood vessels.

Given the central role of RGCs in neurovascular development and the dearth of information about the cognitive outcome of children exposed in utero to maternal AQP4-IgG, we studied whether in utero exposure to an NMOSD patient-derived monoclonal AQP4-IgG would alter CNS vasculature development or lead to persistent functional and neurocognitive deficits.

RESULTS

AQP4 is expressed on radial glia in the fetal brain

We used quantitative polymerase chain reaction (qPCR) to quantify *Aqp4* gene expression in the fetal brain of mice and found that it increased steadily from embryonic day 11.5 (E11.5) to E18.5, whereas placental *Aqp4* expression was low throughout gestation (Fig. 1A). No differences in expression of *Aqp4* transcripts were observed between male and female fetal brains (Fig. 1A). The expression of embryonic AQP4 protein was demonstrated also by Western blot (Fig. 1B). Before E18.5, the dominant AQP4 band had a lower molecular weight than the adult form (Fig. 1B), which we reasoned might reflect the absence of glycosylation. AQP4 has two N-glycosylation sites. When we subjected adult AQP4 to enzymatic deglycosylation, it exhibited the same molecular weight as embryonic AQP4, suggesting that before E18.5, AQP4 was predominantly expressed as a nonglycosylated protein (fig. S1A).

We next confirmed a gene expression study showing that *Aqp4* is expressed in RGCs (*36*), by immunostaining of the fetal cortex at E14.5 with an antibody against the glutamate/aspartate transporter (GLAST), a marker for RGCs, and a commercially available anti-AQP4 antibody that recognizes embryonic AQP4 (Fig. 1C). At E14.5, AQP4 was expressed on both the soma and processes of GLAST$^+$ RGCs in the developing cortex (Fig. 1C).

Maternal AQP4-IgG causes vasculature impairment in the fetal brain

We verified that the monoclonal AQP4-IgG cloned from a patient with NMOSD (*8*), which gets transferred during pregnancy into the embryonic brain (*37*), was able to bind to fetal mouse brain (fig. S1B) and to human embryonic kidney (HEK)–293T cells expressing either AQP4 containing both glycosylation sites and AQP4 with mutations in both sites that prevent glycosylation (fig. S1C). An isotype-matched antibody, 2B4-IgG, which is specific for measles virus (*38*) without any brain reactivity (fig. S1B), was used as a

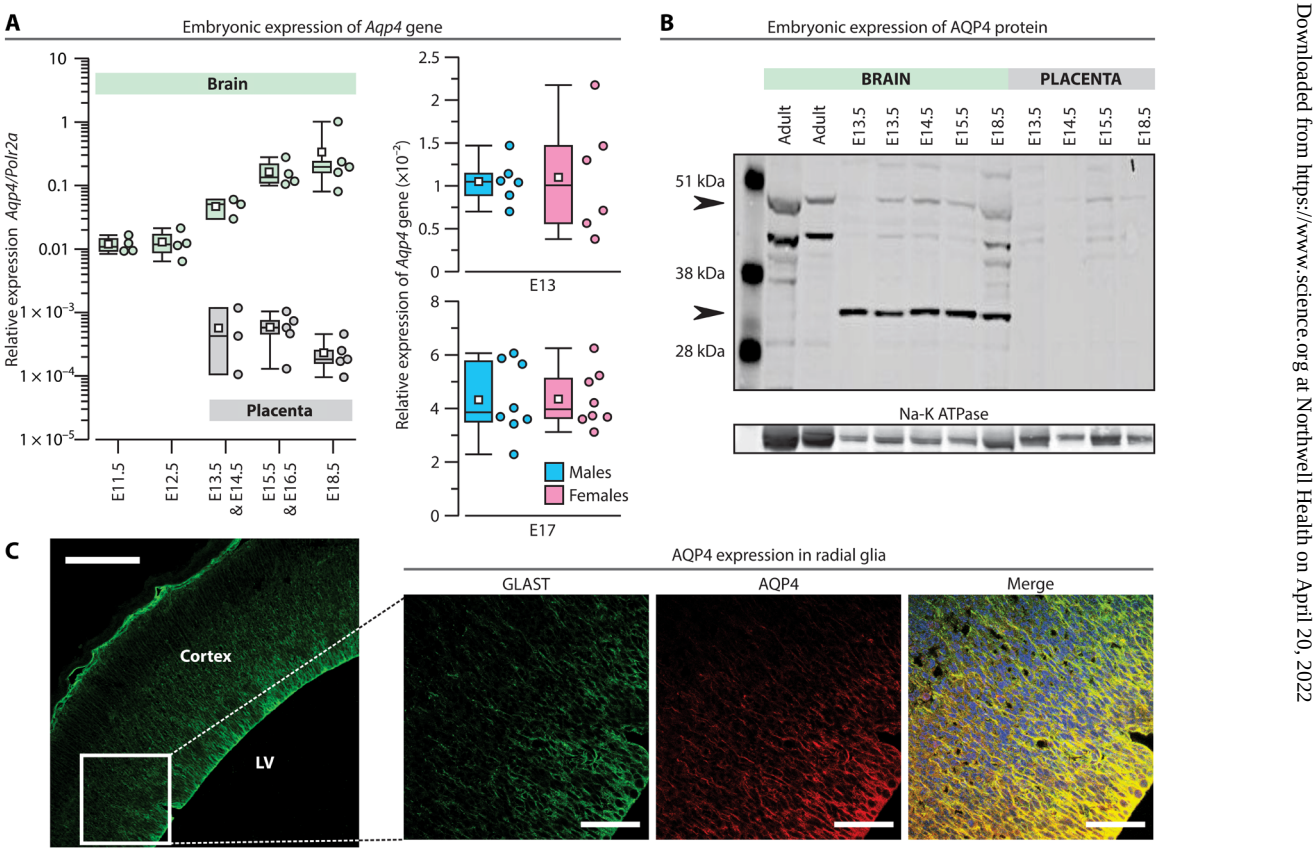

Fig. 1. The expression of AQP4 in the fetal mouse brain. (**A**) Left: *Aqp4*-gene expression (relative to *Polr2A*) across embryonic days, in brain and placenta (box-and-whisker plot; brain at E11.5, $n = 4$; brain at E12.5, $n = 4$; brain at E13.5, $n = 3$; brain at E15.5, $n = 4$; brain at E18.5, $n = 5$; placenta at E13.5, $n = 3$; placenta at E15.5, $n = 5$; placenta at E18.5, $n = 5$). Right: *Aqp4*-gene expression in brain at E13 (top, six male and six female) and E17 (bottom, eight male and eight female). (**B**) Brain and placenta were analyzed for AQP4 expression by Western blot. Upper arrowhead points to adult (50 kDa) and lower arrowhead points to embryonic AQP4 (32 kDa) (representative of three experiments). Na-K ATPase (sodium–potassium adenosine triphosphatase) was used as loading control. (**C**) Left: Coronal section of cerebral cortex (E15.5) stained with anti-GLAST antibody (green) and anti-AQP4 (red). Boxed area corresponds to magnified sections (at right); LV, lateral ventricle. Right: Merge image showing colocalization of AQP4-signal with GLAST$^+$ RGCs (yellow). DAPI-stained nuclei are in blue (representative of three experiments). Scale bars, 250 μm (left) and 25 μm (right).

control (*37*). For our murine model of maternal IgG transfer, AQP4-IgG or 2B4-IgG was administered, by retro-orbital injection, to dams at E14.5 to generate offspring exposed in utero to AQP4-IgG (termed AQP4 mice henceforth) or 2B4-IgG (termed 2B4 mice). We chose E14.5 since, at this embryonic age, there is increased expression of AQP4 (Fig. 1A), and maternal antibodies can cross the placenta and access the brain before the embryonic BBB restricts antibody access (*21*, *37*).

Because RGCs express AQP4 and are involved in blood vessel ingression in the developing cortex and stabilization of newly formed blood vessels in the late embryonic brain (*35*, *39*), we analyzed the cortical vasculature of AQP4 and 2B4 fetal brains. Isolectin B4 (IB4) was used to stain vascular endothelial cells at E18.5, a time point when the vast majority of cortical vessels have reached their mature form (*35*). Comparisons of vessel length revealed that AQP4 males had longer blood vessels, which extended radially within the developing cortex, when compared to 2B4 males (Fig. 2A). In female offspring, there were no differences in vasculature in the developing cortex between AQP4 and 2B4 mice (fig. S2A).

In parallel, we found decreased expression of the WNT signaling molecules, *Wnt*5A and *Wnt*7A, in the cortex of AQP4 males compared to 2B4 males at postnatal day 0 (P0) (Fig. 2B). We found that *Wnt*5A expression was decreased around cortical endothelial cells of AQP4 males (Fig. 2C), suggesting that RGCs that are affected by AQP4-IgG may alter the cortical vasculature of AQP4 males (*35*).

The pathology of NMOSD involves AQP4-IgG–mediated CDC (*10*–*12*, *40*). Eculizumab, a U.S. Food and Drug Administration–approved complement inhibitor, is effective in patients with NMOSD (*12*, *41*). It was previously suggested that transfer of AQP4-IgG to pregnant dams together with coinjection of the human complement factor C1q would damage the placenta (*42*). We did not detect any overt placental defects in dams given AQP4-IgG. There was no placental neutrophilic inflammation, and there was comparable microscopic necrosis in the placentas of AQP4-IgG– and 2B4-IgG–exposed dams 48 hours after antibody administration (fig. S2B).

Maternal AQP4-IgG acts through CDC

CDC is the main process by which AQP4-IgG mediates tissue destruction in NMOSD (*8*, *11*, *43*–*45*). We asked whether the altered cortical vasculature in the AQP4-IgG–exposed fetal brain was mediated by CDC. To address this question, we first demonstrated that C1q was present in the fetal cortex. We quantified *C1q* gene expression by qPCR in C57BL/6 nonmanipulated fetuses and found that *C1q* was increasingly expressed in the cortex, starting at E11.5 to E18.5, until it reached adult expression (Fig. 2D). The placenta showed low *C1q* expression throughout gestation (Fig. 2D).

Next, we showed that AQP4-IgG could activate the mouse complement cascade, leading to membrane-attack-complex (MAC) formation. Specifically, HEK-293T cells transfected with either wild-type AQP4 or AQP4 with mutations in both glycosylation sites, fused with green fluorescent protein, were incubated with AQP4-IgG and serum obtained from a male mouse (containing active complement). MAC formation was observed in HEK-293T cells expressing either wild-type or mutant AQP4 (Fig. 2E). Conversely, no to negligible MAC formation was detected on cells incubated with 2B4-IgG and mouse serum (Fig. 2E). MAC depositions were also evident in the cortex of AQP4 males at E16.5 (48 hours after dams were given AQP4-IgG or 2B4-IgG) by staining with antibody targeting the complement component C5b-9 (fig. S2C).

To strengthen the causal link between AQP4-IgG and C1q activation, we evaluated the effect of AQP4-IgG administration to pregnant *C1q* knockout ($C1q^{-/-}$) dams. Analysis of cortical blood vessels in E18.5 brains, with isolectin-IB4 staining, revealed no vascular abnormalities in AQP4-$C1q^{-/-}$ male mice compared to 2B4-$C1q^{-/-}$ male mice (Fig. 2F).

Adult AQP4 males have an impaired BBB in the entorhinal cortex

Because of the dense expression of AQP4 at the BBB and on the basis of our findings of vascular changes in the fetal brain, we assessed BBB integrity in the adult brain by conducting a positron emission tomography (PET) study with three different tracers: [^{18}F]-fluorodeoxyglucose (FDG) to assess metabolism, [^{11}C]-isoaminobutyric acid (AIB) to assess BBB permeability, and [^{15}O]-labeled water (H_2O) to measure blood flow. We found enhanced [^{11}C]-AIB and [^{15}O]-H_2O signals in the entorhinal cortex of AQP4 males compared to 2B4 males (Fig. 3, A and B, and Table 1), indicating increased blood flow and a compromised BBB. We found no change in [^{18}F]-FDG in the entorhinal cortex of the same mice, suggesting no differences in metabolism between groups (Table 1). Moreover, there were no differences between AQP4 and 2B4 females for [^{11}C]-AIB, [^{15}O]-H_2O, or [^{18}F]-FDG (Fig. 3B and Table 1). In addition, analysis of [^{11}C]-AIB signals in the entorhinal cortex of $C1q^{-/-}$ males revealed no differences between AQP4-$C1q^{-/-}$ mice and 2B4-$C1q^{-/-}$ controls (Fig. 3B and Table 1). Using an independent region-of-interest approach, based on standard anatomical atlases (*46*, *47*), we confirmed increased blood flow and BBB permeability in AQP4 males in the entorhinal cortex, but not in other brain regions (table S1).

To understand whether the compromised BBB was associated with an altered volume of the compartments that contain cerebrospinal fluid (CSF) in the brain, we used images from [^{18}F]-FDG PET analyzed with a CSF template as previously published (*48*). AQP4 male but not APQ4 female mice had an increased CSF volume (Table 2). Moreover, expression of claudin-5, an essential tight-junction protein in endothelial cells, was reduced in AQP4 males compared to 2B4 controls (Fig. 3C). There was significantly more IgG in the CSF of AQP4 males compared to 2B4 controls ($P = 0.02$; Fig. 3D), further supporting that the BBB is compromised in AQP4 males.

Adult AQP4 males show impaired object-place memory

Behavioral assessments showed that AQP4 males exhibited no abnormalities compared to the 2B4 males in an observational screen, which revealed no differences in body weight, coat, grip strength, body tone, and several reflexes (table S2). Moreover, AQP4 males had no deficit in an olfaction test (fig. S3A), the open-field test (fig. S3, B and C), the novel object recognition task (fig. S3D), and the Morris water-maze task (fig. S3E). AQP4 females were also not different from 2B4 females in these assays (table S2 and fig. S3).

In addition, we assessed AQP4 mice in the object-place memory (OPM) task, a spatial cognition test in which an animal recognizes that an object has been relocated to a novel location (Fig. 4A) (*49*). AQP4 male, but not AQP4 female, animals failed to discriminate between the moved object and the stable object (remaining in the same location), as tested by their OPM ratios (Fig 4, B and C). Conversely, 2B4 males and 2B4 females exhibited the expected bias toward the moved object in the test phase (Fig 4, B and C). To confirm that brain injury occurred through a complement-dependent

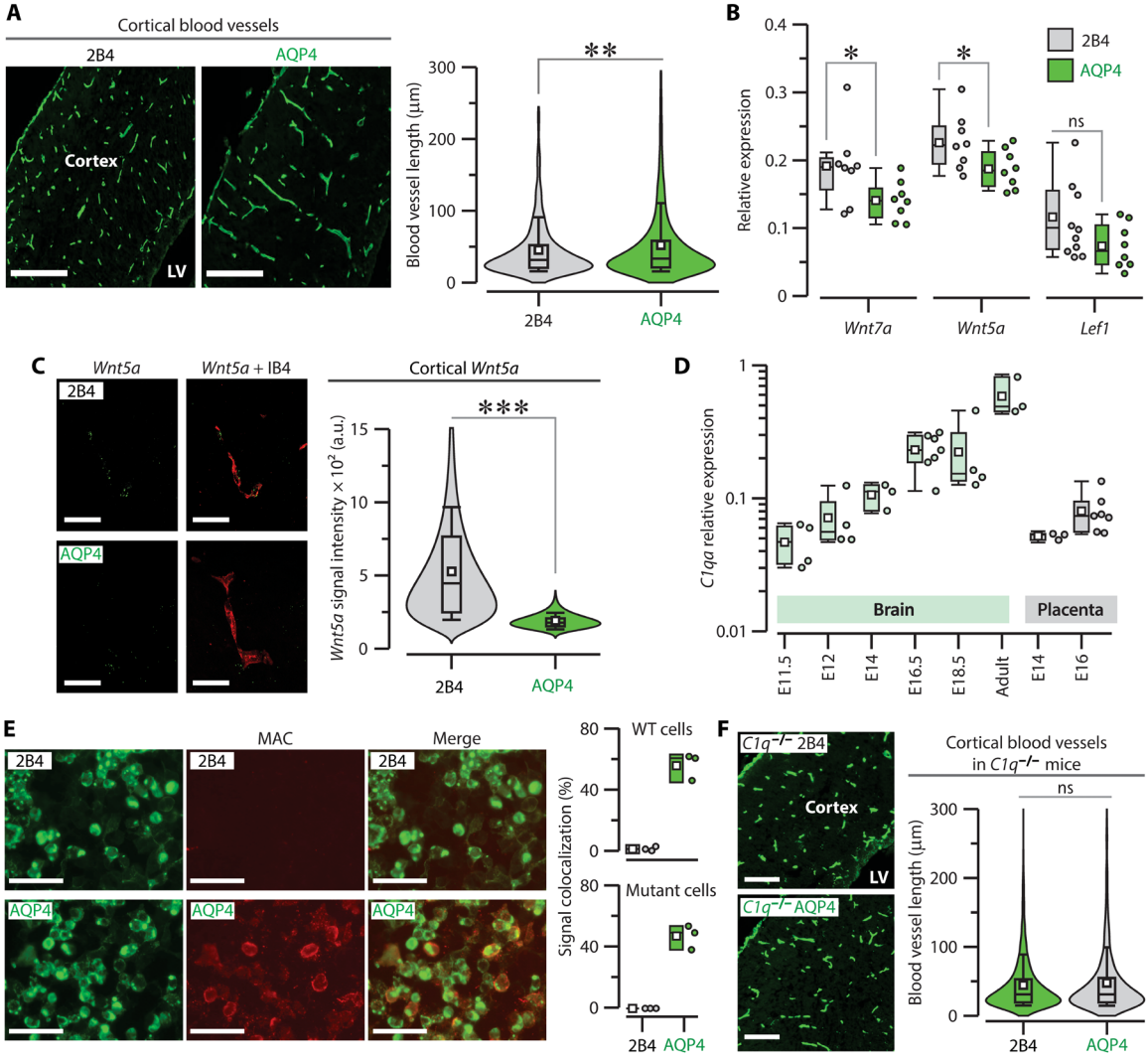

Fig. 2. Maternal AQP4-IgG causes abnormal vasculature in the fetal brain. (**A**) Left: Representative cortical sections stained with isolectin-IB4 for blood vessels. Right: Violin plots show length of vessels, at E18.5, in AQP4 males [$n = 2238$ vessel segments (VS), six mice, range: 108 to 245 VS per animal] compared to 2B4 males ($n = 2221$ VS, six mice, range: 102 to 279 VS per animal); $^{**}P = 0.005$, Kolmogorov-Smirnov (KS) test. (**B**) Box-and-whisker plot shows relative expression of WNT signaling genes ($^{*}P = 0.03$ for *Wnt*7a, $^{*}P = 0.04$ for *Wnt*5a, and $P = 0.08$ for *Lef*1, Student's *t* test). The cortex was extracted from AQP4 and 2B4 males ($n = 8$ mice, 2 liters, for each group), at P0; gene expression was measured by qPCR and normalized to *Polr*2A. (**C**) Left: Representative images of cortical blood vessels (Ib4, red signal) and *Wnt*5a RNA expression (green signal). Right: Violin plots show cortical *Wnt*5a signal intensity near the AQP4 vessels at E18.5 (2B4 males, $n = 114$, four mice, AQP4 males, $n = 120$, four mice; $^{**}P = 1.2 \times 10^{-25}$, KS test). a.u., arbitrary units. (**D**) Box-and-whisker plot shows *C1qa* transcript expression (relative to *Polr2A*) in the developing brain (E11.5, $n = 4$; E12, $n = 4$; E14, $n = 3$; E16.5, $n = 7$; E18.5, $n = 5$; adult, $n = 3$) and in the placenta (E14, $n = 3$; E16, $n = 7$) of untreated C57BL/6 mice. (**E**) Left: Mouse MAC formation (red signal) was analyzed in HEK cells expressing the nonglycosylated AQP4-fused with green fluorescent protein (GFP) (green signal, left) in the presence of the monoclonal AQP4-IgG or 2B4-IgG and mouse serum (middle and right panels, representative of three experiments). Right: Box-and-whisker plot shows the percentage of colocalization. Mean (95% confidence interval): wild-type (WT) cells; 2B4 = 1.21 (−2.18 to 4.6), AQP4 = 55.7 (34 to 77.4). Mutant cells; 2B4 = 0 (0 to 0), AQP4 = 47.1 (27.27 to 66.93). (**F**) Left: Representative images of embryonic cortex stained with isolectin-IB4. Right: Violin plots for cortical blood vessels of $C1q^{-/-}$ males at E18.5 (2B4, $n = 1390$ VS, four mice, 206 to 276 VS per animal; AQP4, $n = 1407$ VS, 6 mice, 115 to 272 VS per animal); $C1q^{-/-}$ AQP4 and $C1q^{-/-}$ 2B4 males ($P = 0.71$, KS test). (A and F) LV, lateral ventricle; ns, not significant. Scale bars, 250 µm (A and F), 20 µm (C), and 50 µm (E).

pathway, we subjected $C1q^{-/-}$ mice to the OPM task and found normal OPM ratios for both male and female AQP4-$C1q^{-/-}$ and 2B4-$C1q^{-/-}$ mice (Fig. 4C).

Adult AQP4 males show disorganized grid cells in the medial entorhinal cortex

Because the OPM data indicated impaired spatial cognition in AQP4 males, and the PET results demonstrated that the entorhinal cortex was a particularly sensitive brain region, we sought to investigate its network function in vivo. Mice were preselected for these recordings based on their performance in the OPM task so that AQP4 males with the lowest OPM ratios and 2B4 males with positive OPM ratios were chosen. Mice were implanted with four-tetrode arrays targeted to the medial entorhinal cortex (fig. S4 for electrode location). After implantation surgery, the tetrodes were slowly lowered until clear single units were observed at a final depth of ~1 mm

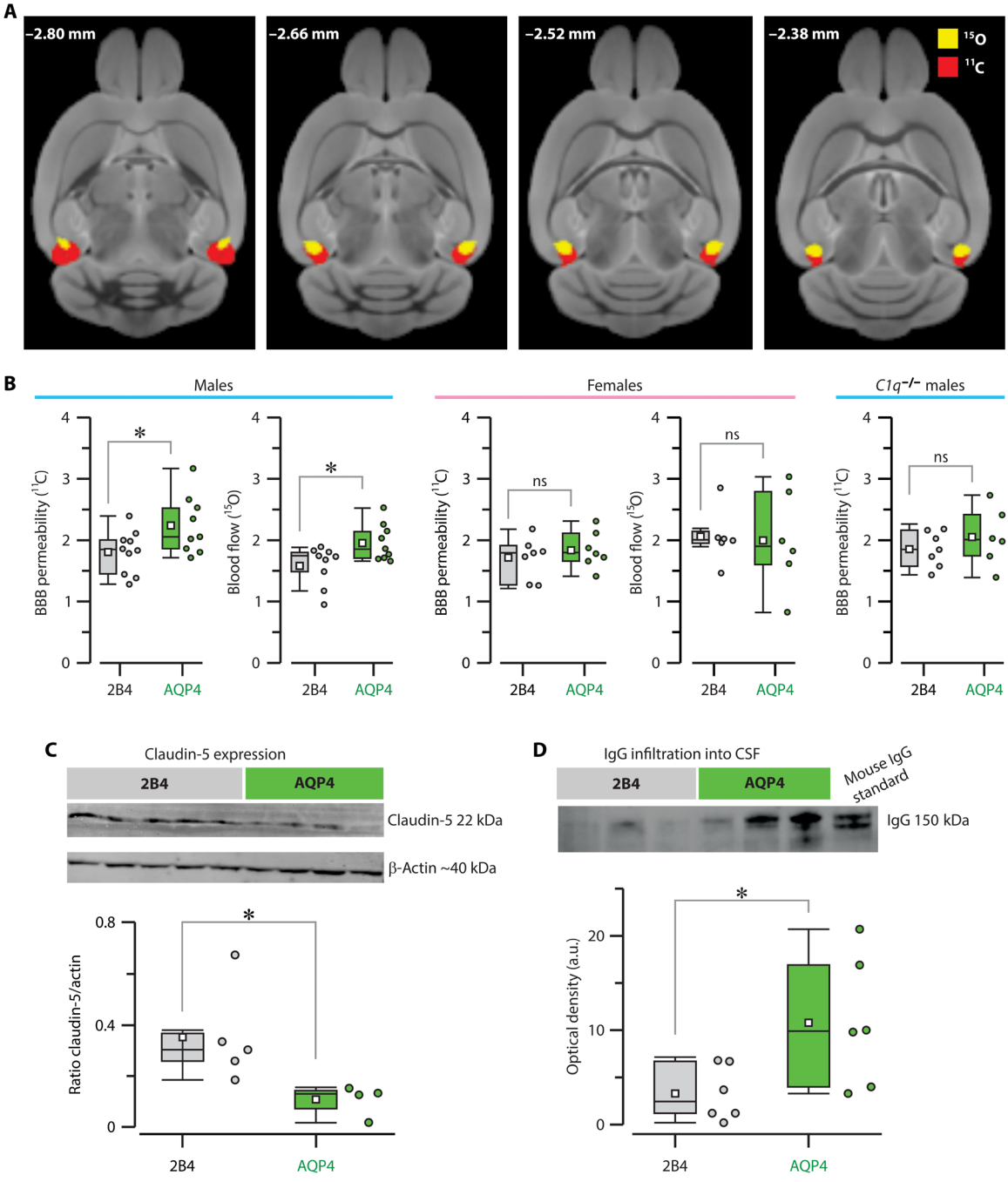

Fig. 3. MicroPET reveals impaired BBB in entorhinal cortex of adult AQP4 male mice. (**A**) Voxel-wise search over the whole-brain volume shows a distinct region in which BBB permeability ([^{11}C]-AIB; red right cluster) and blood flow ([^{15}O]-H_2O; yellow right cluster) are increased at a threshold of $P < 0.001$ (voxel-level uncorrected) in AQP4 males compared to 2B4 males. The significant clusters from these two analyses are located in the right entorhinal cortex and overlap in this region. BBB permeability and blood flow values were measured post hoc in these clusters (right) and in the contralateral "mirror" regions (left) and averaged for the individual mice. (**B**) Box-and-whisker plots of mean BBB permeability and blood flow in the bilateral entorhinal cortex. Left: Comparing between AQP4 and 2B4 males for BBB permeability (2B4, $n = 10$; AQP4, $n = 9$; $^*P = 0.036$, Student's t test) and blood flow (2B4, $n = 9$; AQP4, $n = 9$; $^*P = 0.023$, Student's t test). Middle: Comparing AQP4 and 2B4 females for changes in BBB permeability (2B4, $n = 7$; AQP4, $n = 7$) and blood flow [2B4, $n = 6$; AQP4, $n = 6$; ns, $P = 0.6$, Mann-Whitney U (MWU) test]. Right: Comparing BBB permeability in AQP4 and 2B4 $C1q^{-/-}$ males (2B4, $n = 7$; AQP4, $n = 6$; ns, $P = 0.5$, MWU test). (**C**) Top: Western blot shows claudin-5 protein expression in the cortex. Bottom, box-and-whisker plot shows claudin-5 expression (normalized to β-actin) in the AQP4 males compared to 2B4 males (2B4, $n = 5$; AQP4, $n = 4$; $^*P = 0.04$, MWU test). (**D**) Top: Western blot shows IgG in the CSF. Bottom: box-and-whisker plot shows the optical density of IgG in the CSF in AQP4 and 2B4 males (2B4, $n = 6$; AQP4, $n = 6$; $^*P = 0.02$, MWU test).

Table 1. Micro-PET brain analysis of adult AQP4 mice. Values represent the means ± SD in the entorhinal cortex for FDG, ^{11}C, and ^{15}O injected to AQP4 and 2B4 mice. *P* values were calculated using Student's *t* test, two-tailed, with Welsch correction (equal variance not assumed). Whole-brain voxel-wise comparisons were done by analyzing across appropriate groups, on a voxel-by-voxel basis, and searching for any location with a significant difference. Preprocessed images have units in mCi (dose-corrected). Once brought into statistical parametric mapping (SPM), averaged images are ratio normalized by global mean.

Male	**FDG (*n* = 29)**	**^{11}C (*n* = 19)**	**^{15}O (*n* = 18)**
	17 2B4, 12 AQP4	**10 2B4, 9 AQP4**	**9 2B4, 9 AQP4**
2B4	1.93 ± 0.10	1.82 ± 0.35	1.59 ± 0.33
AQP4	1.91 ± 0.08	2.25 ± 0.48	1.96 ± 0.30
P [*t* value]	0.64 [0.47]	0.04 [2.27]	0.02 [2.51]
Female	**FDG (*n* = 15)**	**^{11}C (*n* = 14)**	**^{15}O (*n* = 12)**
	7 2B4, 8 AQP4	**7 2B4, 7 AQP4**	**6 2B4, 6 AQP4**
2B4	1.93 ± 0.03	1.71 ± 0.34	2.06 ± 0.45
AQP4	1.94 ± 0.06	1.84 ± 0.30	2.01 ± 0.81
P [*t* value]	0.9 [0.13]	0.46 [0.77]	0.90 [0.13]
***C1q*$^{-/-}$ Male**	**FDG (*n* = 13)**	**^{11}C (*n* = 13)**	
	7 2B4, 6 AQP4	**7 2B4, 6 AQP4**	
2B4	1.97 ± 0.09	1.85 ± 0.29	
AQP4	1.96 ± 0.15	2.05 ± 0.47	
P [*t* value]	0.98 [0.02]	0.37 [0.89]	

Table 2. Micro-PET analysis of CSF in adult AQP4 mice. Percent change in CSF volume (means ± SD) calculated from FDG scans from AQP4 and 2B4 groups. *P* values were calculated using Student's *t* test.

Male	**2B4 (*n* = 17)**	**AQP4 (*n* = 12)**	***P* value**
Left	2.26% ± 0.17%	2.41% ± 0.23%	0.065
Right	2.33% ± 0.09%	2.43% ± 0.13%	0.018
Left and right	4.59% ± 0.23%	4.84% ± 0.34%	0.027
Female	**2B4 (*n* = 7)**	**AQP4 (*n* = 8)**	***P* value**
Left	2.46% ± 0.10%	2.38% ± 0.20%	0.31
Right	2.44% ± 0.09%	2.54% ± 0.11%	0.09
Left and right	4.91% ± 0.14%	4.92% ± 0.24%	0.92

(superficial layers of the medial entorhinal cortex). Single-unit recordings were obtained in both groups, and individual units were isolated and classified as grid cells (*50*, *51*) for further analysis (Fig. 4D). Firing-rate maps in 2B4 mice formed evenly spaced hexagonal grids across the environment, and the spatial autocorrelation for these maps showed a center with hexagonally arranged correlation peaks surrounding it. In the AQP4 group, the firing maps did not show evenly spaced hexagonal grids, and when the spatial autocorrelation was determined, peaks were distorted and did not form well-defined hexagons (Fig. 4E). Grid cells recorded in the AQP4 males had significantly lower firing rates ($P = 0.028$) and grid scores ($P = 0.027$) compared to the 2B4 males (Fig. 4F).

Adult AQP4 males have structural abnormalities in the entorhinal cortex

Blood vessels in the entorhinal cortex of adult male mice were stained with lectin. There was longer length and diameter in the AQP4 males compared to the 2B4 group (Fig. 5, A and B). Moreover, adult AQP4 males exhibited altered entorhinal AQP4 expression; specifically, they had increased AQP4 expression around blood vessels (fig. S5A).

Quantification of Golgi-stained entorhinal stellate neurons (Fig. 5C) and pyramidal cells (Fig. 5D) revealed that the dendritic length for each neuronal type was not different between AQP4 and 2B4 males (Fig. 5E). However, we observed a reduced number of dendritic spines on pyramidal and stellate cells in the AQP4 males when compared to 2B4 males (Fig. 5F). These differences appear to be specific to the entorhinal cortex, as pyramidal neurons of the CA1 region of the hippocampus were similar in their dendritic length and number of spines between the AQP4 and 2B4 males (fig. S6). We also found an increased number of S100β-labeled astrocytes, counted in stereologically similar entorhinal regions in AQP4 males compared to 2B4 males (Fig. 5G).

AQP4 staining was not altered in the kidney of adult AQP4 males (fig. S5B) where AQP4 is abundantly expressed (*52*). The amount of albumin in the urine was not different between adult AQP4 and 2B4 mice (fig. S5C), further emphasizing that maternal AQP4-IgG exposure did not affect kidney development.

Human NMOSD serum antibodies bind both embryonic and adult AQP4

Because we found that, before E18.5, AQP4 was predominantly expressed as a nonglycosylated protein, we wanted to investigate whether patients' autoantibodies differentially bind to glycosylated ("adult") or nonglycosylated ("embryonic") AQP4. Patients with antibody to nonglycosylated AQP4 may be more at-risk having offspring affected by antibody exposure. We analyzed serum samples from 38 female patients with NMOSD for binding to wild-type AQP4 and AQP4 containing mutations in both glycosylation sites, using a cell-based assay (Table 3). Most sera (69%) exhibited binding to both forms of AQP4; however, 31% preferentially bound to wild-type AQP4 and less to AQP4 with mutations in both glycosylation sites, suggesting that the antibodies present in these patients might be less damaging to fetal brains.

DISCUSSION

Our study provides evidence that exposure to AQP4-IgG during pregnancy promotes neurodevelopmental impairment that persists throughout adulthood in the male mouse brain. Structural alteration of brain vasculature was associated with BBB impairment, disrupted neuronal function, and impaired cognitive performance. Our data strongly suggest that the effect of maternal AQP4-IgG is mediated through targeting of AQP4-IgG to RGCs that shape several processes in the developing cortex, including the architecture of the cortical vessels.

The adult brain typically requires an insult to the BBB in order for antibodies to penetrate brain tissue (*22*); alternatively, the entry of AQP4-IgG to the brain can occur at the BBB-deficient sites such as the area postrema (*53*), whereas the fetal brain with its developing, therefore incomplete, BBB is exposed to circulating maternal antibodies from E12.5 until around E16.5 (*21*). In a prior study, we

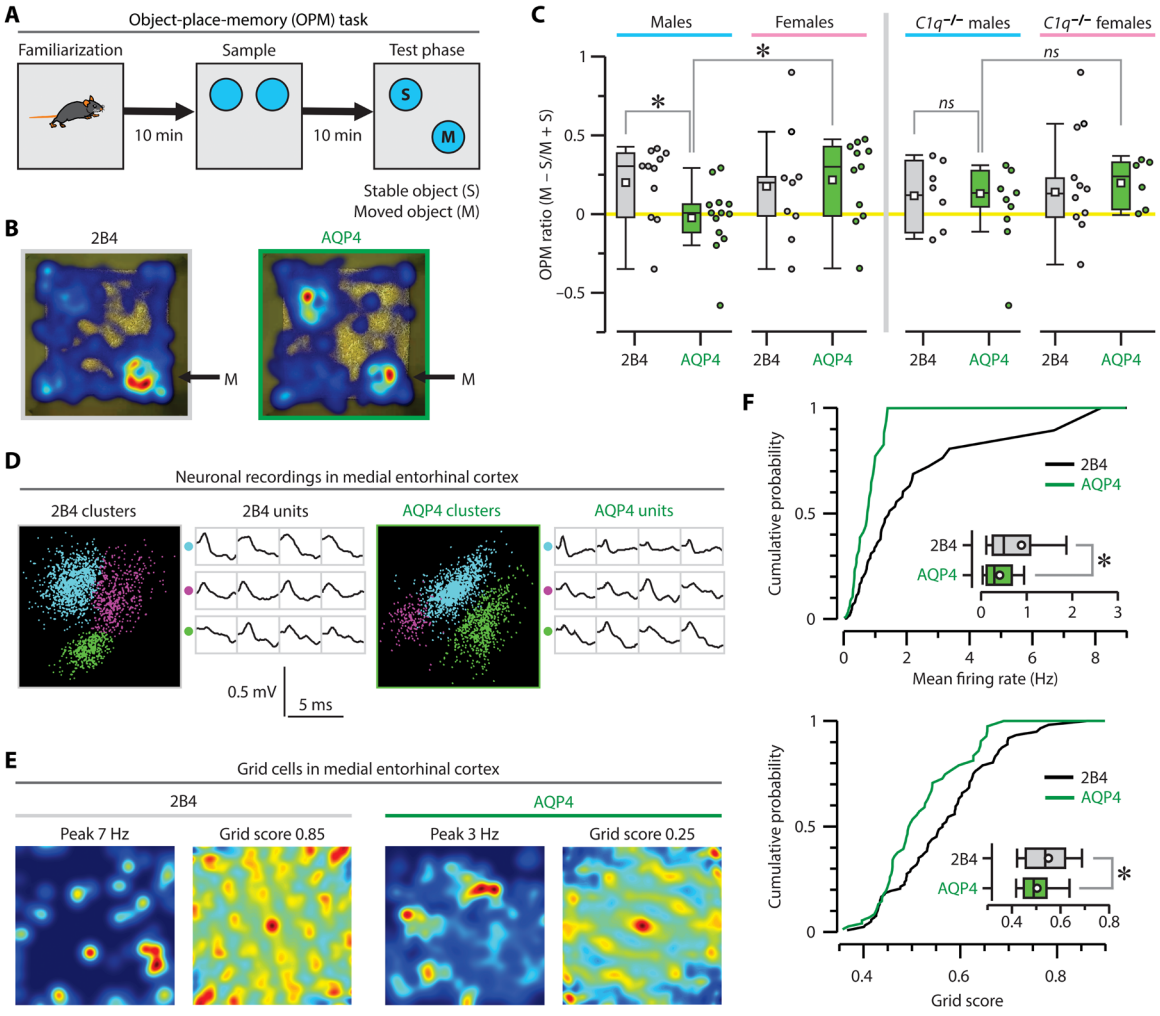

Fig. 4. Adult AQP4 male mice show impaired spatial cognition and disorganized entorhinal grid cells. (**A**) Diagram of the OPM task. Each mouse is familiarized to the chamber and then exposed to two objects (sample phase, 5 min). For the test phase (5 min), one of the objects is moved to a different location. (**B**) Representative heatmaps of the test phase depicting the location of the nose of the mouse. 2B4 mice had a strong bias toward the moved object (M), which was lacking in AQP4 mice. (**C**) Box-and-whisker plots of OPM ratios (2B4 males, $n = 11$; AQP4 males, $n = 13$; 2B4 females, $n = 9$; AQP4 females, $n = 11$; $^*P = 0.025$, AQP4 versus 2B4 males; $^*P = 0.023$, AQP4 males versus AQP4 females; Student's t test). $C1q^{-/-}$ mice have normal OPM ratios for all groups (2B4 males, $n = 6$; AQP4 males, $n = 7$; 2B4 females, $n = 10$; AQP4 females, $n = 6$; ns, $P = 0.88$, AQP4-$C1q^{-/-}$ versus 2B4-$C1q^{-/-}$ males; ns, $P = 0.42$, AQP4-$C1q^{-/-}$ males versus AQP4-$C1q^{-/-}$ females; Student's t test). (**D**) Example cluster plots (left for each group) showing three simultaneously recorded neurons from a tetrode. Colors allow visualization of each clustered unit. The waveforms (right for each group) are the action potentials in each channel of the tetrode. (**E**) Representative rate maps showing the firing rate of a single grid cell with respect to the location of the mouse (left for each group), and representative autocorrelation maps constructed from the displayed rate maps (right for AQP4 and 2B4 males). (**F**) Top: cumulative probability plot showing grid cell mean firing rates (2B4, $n = 87$ cells, four mice; AQP4, $n = 55$ cells, four mice; $^*P = 0.0277$, KS test). Bottom: cumulative probability plot showing cell firing in AQP4 mice ($n = 55$) and 2B4 mice ($n = 87$), as calculated using the grid score metric; $^*P = 0.0269$, KS test.

showed that maternal AQP4-IgG penetrates rodent fetal brain tissue (*37*). Since the discovery of AQP4-IgG, in 2005 (*6*), few reports have described the effect of in utero exposure to AQP4-IgG on the developing fetus. In mice, intraperitoneal injection of high titers of AQP4-IgG together with human complement resulted in fetal death and placental inflammation, whereas administration of lower amount of AQP4-IgG and human complement resulted in normal litter size, but no other observations of the offspring were performed (*42*). We did not observe any inflammation of the placenta. It is possible that higher concentrations of AQP4-IgG could affect the placenta or that high amount of human complement contributed to the placental damage. Our pregnancy model does not entirely recapitulate the features of the human disease; we cannot exclude that inflammation present in patients with NMOSD may have additional deleterious effects on pregnancy. Clinical studies have reported a higher rate of miscarriages in AQP4-IgG–seropositive patients with NMOSD, which might reflect either placental or fetal injury (*4*). There are also two case reports of children with hydrocephalus born to AQP4-IgG–seropositive patients with NMOSD (*4*, *20*), yet mostly normal births have been reported (*4*, *20*). However, to our knowledge, there are no long-term epidemiological studies assessing cognitive function and neurodevelopmental outcomes in boys and girls born to AQP4-IgG–positive mothers with NMOSD.

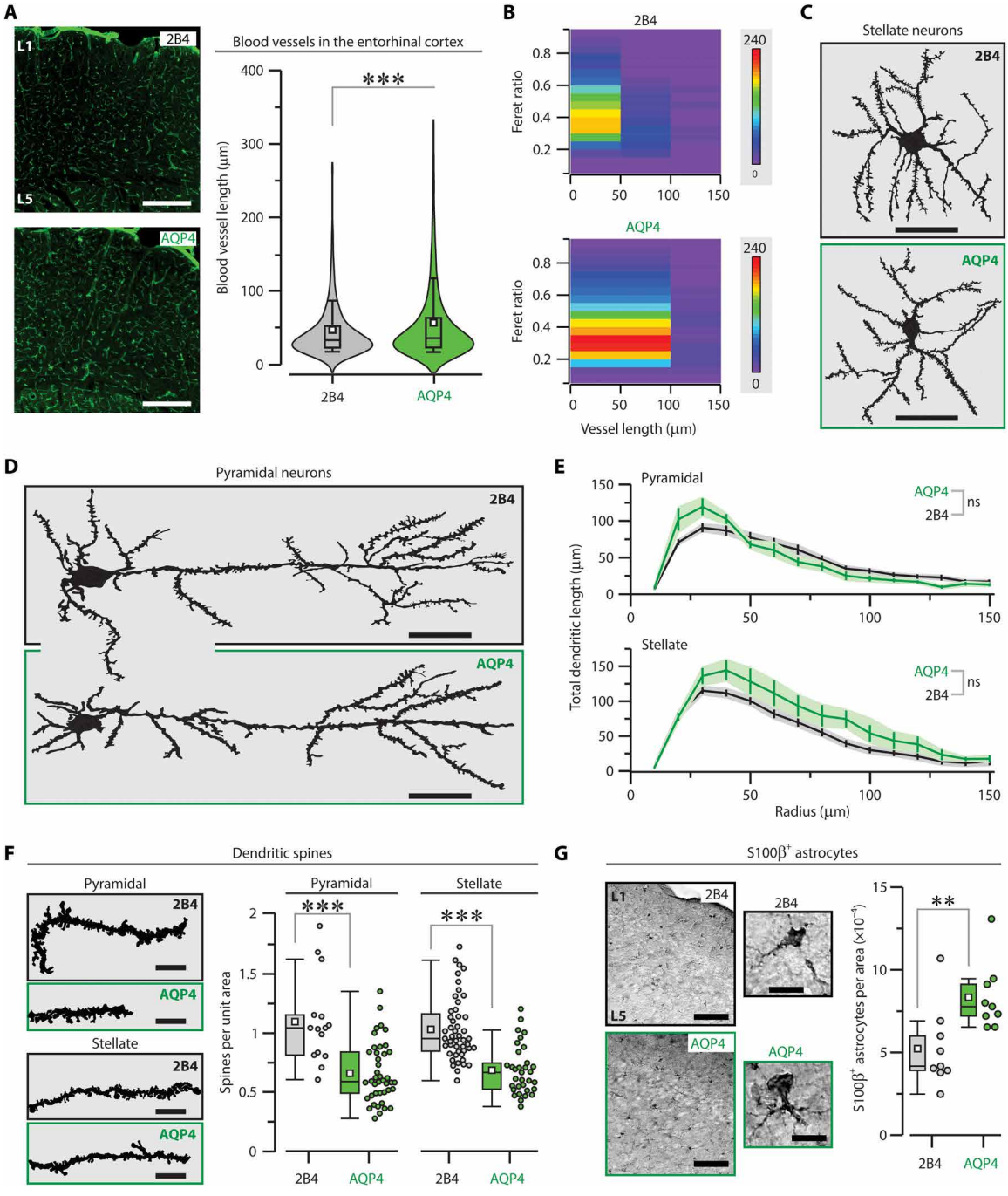

Fig. 5. Adult AQP4 male mice exhibit abnormal blood vessels and dendritic spines in the entorhinal neurons. (**A**) Left: Representative sections were stained with lectin for blood vessels in the entorhinal cortex. Right: Violin plots show cortical vessel length in AQP4 males ($n = 1898$ VS, nine mice, range: 108 to 245 VS per animal) compared to 2B4 males ($n = 1879$ VS, eight mice, 102 to 279 VS per animal); $^{***}P = 3.5 \times 10^{-5}$, KS test. (**B**) Heatmap plots of vessel length in AQP4 male and 2B4 male mice (2B4, $n = 1879$ VS, eight mice; AQP4, $n = 1898$ VS, 9 mice; $P = 1.4 \times 10^{-9}$, KS test). The Feret ratio is calculated as F_{min}/F_{max}, where F_{max} is the greatest width of the vessel contour and F_{min} is the least width; low ratios depict elongated objects, and values approaching 1 depict compact or circular objects. (**C**) Representative tracings of stellate neurons stained with Golgi method. (**D**) Example tracings of Golgi-stained pyramidal neurons. (**E**) Sholl analysis quantifies the total dendritic length (means ± SEM) in concentric rings (radius) from the cell body of pyramidal and stellate cells (2B4, $n = 49$ pyramidal, 59 stellate, four mice; AQP4, $n = 10$ pyramidal, 15 stellate, four mice; ns, $P = 0.4$, linear mixed model). (**F**) Analysis of dendritic spines (number of spines per unit area) in neurons of the entorhinal cortex in AQP4 and 2B4 males, for pyramidal cells (2B4, $n = 15$ dendrites, four mice; AQP4, $n = 42$ dendrites, four mice; $^{***}P = 0.00047$, Student's t test) and stellate cells (2B4, $n = 48$ dendrites, four mice; AQP4, $n = 33$ dendrites, four mice; $^{***}P = 6.4 \times 10^{-9}$, Student's t test). (**G**) Left: Sections show S100β-labeled astrocytes in the entorhinal cortex, with insets showing a magnified astrocytic cell. Right: Box-and-whisker plots show S100β$^+$ astrocytes per unit area in both groups of male mice (2B4, $n = 9$ sections, four mice; AQP4, $n = 9$ sections, four mice; $^{**}P = 0.008$, MWU test). L1, layer 1; L5, layer 5. Scale bars, 500 μm (A), 20 μm (C), 20 μm (D), 5 μm (F), 500 μm (G), and 10 μm (G, inset).

Table 3. Level of anti-AQP4 antibodies in serum of patients with NMOSD. We used a cell-based assay to measure binding of NMOSD patient antibodies in serum to wild-type AQP4 (glycosylated) and to AQP4-containing mutations in the two glycosylation sites (nonglycosylated AQP4). We determined the highest dilution (titer) that still bound transfected cells. Antibody titers are shown as median (range, minimum to maximum) of patients showing no difference in binding (defined as a maximum of one titer level difference) compared to patients showing a difference in binding (defined as more than two titer levels difference) to glycosylated AQP4 and nonglycosylated AQP4. Age, sex, and gender or ethnicity for all study participants are included in data file S1.

	Patients with no difference in AQP4-IgG binding	Patients showing less binding to AQP4 nonglycosylated
Number	26/38 (69%)	12/38 (31%)
Glycosylated AQP4 titer	1280 (20–20,480)	1600 (40–20,480)
Nonglycosylated AQP4 titer	1280 (20–10,240)	240 (0–5120)

We have found that AQP4 is expressed in the brain at a time when maternal antibodies can penetrate the embryonic brain in mice. In the adult brain, AQP4 is expressed on astrocytic endfeet. Since astrocytes appear rather late in development, we asked which cells express AQP4 in the fetal brain. A previous study reported AQP4 expression on RGCs in the developing cortex (*27*). In addition, whole transcriptome data during mouse brain development showed that *Aqp4* is expressed in proliferating progenitor cells, much less in differentiating progenitor cells, and not in postmitotic neurons (*36*). This pattern of *Aqp4* expression is similar to the expression of *Sox2* (*36*), a marker for RGCs. We have found that the AQP4 protein is expressed in GLAST$^+$ RGCs as early as E14.5. Furthermore, we established that AQP4 expressed in the fetal brain has a lower molecular weight than the adult brain, likely due to lack of glycosylation.

In our model, male but not female mice exposed in utero to AQP4-IgG showed altered brain vasculature associated with changes in expression of WNT signaling molecules. A critical clue to this sex-specific phenotype comes from the observation that *C1q*$^{-/-}$ male mice exposed in utero to AQP4-IgG did not have alterations in brain vasculature. This result clearly implicates the complement cascade in the effect of AQP4-IgG. Complement genes are expressed in a sexually dimorphic pattern, so that during neocortical development, complement genes are more highly expressed in males than females (*54*). In adulthood, the pattern reverses, and complement genes are more expressed in females (*54*). Thus, a differential expression of complement components may explain why males, but not females, are affected when they are exposed in utero to AQP4-IgG. Of note, maternal antibodies have also been shown to affect neurodevelopment in a sex-dependent manner in SLE and ASD (*24*, *26*).

Our study suggests that maternal AQP4-IgG–mediated fetal brain injury is complement dependent. Although mouse complement can be activated in vivo by antibodies with a human Fc region (*55*, *56*), we are also aware of data showing that human AQP4-IgG needs to be coinjected with human complement to cause pathology in mouse models of NMOSD (*10*, *57*, *58*). The discrepancy between our data and previous reports may reflect differences in the abundance and/or function of complement components between the fetal and adult complement systems.

It is likely that AQP4-IgG interferes with the normal interaction of RGCs and endothelial cells leading to abnormal vasculature in the cortex at a critical developmental time. Ablation of RGCs interferes with the sprouting of the trunk vessels in the spinal cord of zebrafish embryos (*59*) and alters the vasculature in the fetal cortex of rodents (*35*). Deletion of AQP4 in mice has been linked to impaired synaptic plasticity and poor performance in the OPM task (*60*, *61*). We found that in utero exposure to maternal AQP4-IgG produced a vasculature phenotype in the male brain, by E18.5, which continued into adulthood. Our data point to the entorhinal cortex as a focal node in the adult brain for the persistence of the neurodevelopmental impairment. More studies are needed to understand the specific fragility of the entorhinal cortex to AQP4-IgG, but our work demonstrates that both structural and functional abnormalities associate with impaired spatial cognition.

Deficient vasculature development can lead to neurodevelopmental defects. For instance, glucose transporter 1 (GLUT1) deficiency syndrome, a genetic disease characterized by a lack of GLUT1 in the brain, leads to delayed brain angiogenesis and reduced size of microvasculature without affecting BBB integrity (*62*). Early repletion of GLUT1 restores cerebral microvasculature (*62*). Several studies have associated BBB dysfunction with cognitive impairment (*63*–*65*). For example, mice lacking apolipoprotein E (ApoE), a model for late Alzheimer's disease, show BBB leakage accompanied by cognitive deficits including memory impairment (*66*–*68*). Aging ApoE-deficient mice exhibit altered AQP4 expression, which possibly contributes to the BBB impairment. BBB leakage can result in disturbance of ionic homeostasis and thus can lead to neuronal dysregulation. Vascular pathology can lead to increased S100β expression (*69*). Furthermore, stress can also lead to increased S100β expression (*70*). It is intriguing that investigators have demonstrated elevated S100β concentration in the CSF of patients with NMOSD, which may reflect astrocytic damage due to pathogenic AQP4-IgG (*71*–*73*).

We demonstrated that a vasculature phenotype may be caused by maternal AQP4-IgG affecting RGCs and blood vessel structure via WNT signaling. The combination of neuronal alterations and leaky BBB in the entorhinal cortex suggests that a dysfunctional BBB may be driving the neuronal phenotype (*74*, *75*). We cannot exclude the idea that early exposure to AQP4-IgG affects neuronal/astrocyte precursors leading to long-term neuronal dysfunction. Note that BBB impairment was specific to the entorhinal cortex. The entorhinal cortex is one of the first cortical regions to initiate neurogenesis (*76*), and AQP4 is highly expressed in adult entorhinal cortex (*77*), possibly making it more vulnerable to the effect of circulating AQP4-IgG during a critical time of development.

The main limitation of our study is that murine models might have different effector functions, and thus humanized models or studies in nonhuman primates are warranted to further elucidate the role of maternal AQP4 antibodies. In addition, there is only limited information regarding the effect of in utero exposure to AQP4-IgG in humans with no longitudinal follow-up studies. Future studies are needed to assess larger cohorts of children born to mothers with AQP4-IgG, which also need to address the effects of maternal medication or indirect effects of maternal illness, such as cytokines or pathogenic T cells. It is also possible that additional factors such as genetics and in utero environmental variables contribute to the effect of maternal AQP4-IgG on development.

Our study is particularly important, as earlier diagnosis and appropriate treatment greatly improve clinical outcome of patients and may increase the number of successful pregnancies of patients with NMOSD. Demonstrating how maternal brain-reactive autoantibodies can interfere with the developing brain and lead to a durable effect represents an important step toward the initiation of long-term studies in humans and the development of future therapeutic interventions. It also increases our understanding of the development of the brain microvasculature.

MATERIALS AND METHODS

Study design

Our goal was to investigate the acute and long-term effect of in utero exposure to maternal AQP4-IgG on the developing brain. AQP4 expression was assessed in the developing brain. The brains of embryos and adult AQP4 mice, as well as 2B4 mice, were analyzed histologically for alterations in endothelial cells, astrocytes, and neurons. Adult mice were evaluated with a microPET study to measure BBB integrity and IgG infiltration into the CSF. Adult mice were also assessed with behavioral tests, including the OPM task for spatial cognition, and an electrophysiological study of the entorhinal cortex. No statistical methods were used to predetermine sample size. No data were excluded from analyses. The animals were randomly assigned to the behavioral testing, microPET, and histological analysis except for the preselection of animals for neuronal recordings, as stated in the appropriate section. All animals were run in random order by investigators blinded to the treatment group of each animal. Information regarding number of samples and experimental replicates is indicated per experiment in each figure legend.

Animals

We used adult C57BL/6 mice (the Jackson Laboratory, strain #000664) as well as $C1q^{-/-}$ mice on a C57BL/6 background, which were bred to C57BL/6-H2d haplotype. Mice were, on average, 3 to 5 months old unless otherwise specified. $C1q^{-/-}$ mice were obtained from V. S. Ten (Department of Pediatrics, Columbia University). All mice were housed with ad libitum access to food and water. The animals' care was in accordance with the National Institutes of Health Guidelines under protocols reviewed and approved by the Institutional Animal Care and Use Committee (2009-048 and 2013-014) of the Feinstein Institutes for Medical Research.

Human monoclonal antibodies

AQP4-IgG rAb-53 was cloned from a patient with NMOSD, and specificity of the antibody for AQP4 binding was previously confirmed (*8*). The isotype-control recombinant 2B4-IgG binds to measles virus nucleocapsid protein (*38*). Antibody concentrations were measured by IgG enzyme-linked immunosorbent assay (*37*) and Nanodrop. Each new batch of recombinant human AQP4-IgG (1 μg/ml) is verified to bind to human AQP4 using a cell-based assay with HEK-293T cells (American Type Culture Collection, CRL 11268TM) transiently transfected with AQP4 (*78*). Monoclonal antibody was tested for binding to cells expressing AQP4 (M23 isoform) as well as cells expressing nonglycosylated AQP4 as described below. Nontransfected cells and cells expressing a nonrelevant protein (Caspr2) were included as negative controls.

Serum binding to glycosylated and nonglycosylated forms of AQP4

Serum of patients was collected at the Clinic of Neurology, Clinical Center of Serbia. All patients met the revised diagnostic criteria of NMOSD (*3*). Individuals provided informed consent through the appropriate institutional review boards. Participation in this research was approved by the University of Belgrade Faculty of Medicine Institutional Review Board (approval number 29/X-8, amendment approval number 1322/XII-22). Serum of 38 patients with NMSOD was tested for IgG binding to human AQP4 (plasmid provided as a gift from M. Reindl) and nonglycosylated human AQP4 (see the Supplementary Materials) expressed on the cell surface of HEK-293T cells as previously described (*78*, *79*). Antibody titers were analyzed by serial dilution until no more signal of AQP4-IgG binding was observed.

Statistical analysis

All raw, individual-level data are presented in data file S1. We performed the Shapiro-Wilk normality test in each dataset to determine whether the sample was drawn from a normally distributed population. We then used Student's t test for datasets that were normally distributed (and with samples larger than 10). For small datasets that were not normally distributed (sample sizes less than 10), we performed the Mann-Whitney U test. For large datasets that were not normally distributed, we used the Kolmogorov-Smirnov test. For dendritic branching datasets from neurons, we used a linear mixed model. To analyze categorical data, we used a χ^2-test for independence. All tests were performed with the statistical toolbox of OriginPro (version 2021b, 64 bit, SR2, OriginLab Corp.) and are indicated in the text. Values were considered significant for $P < 0.05$. Data are presented as mean, and error bars represent standard error. All tests were performed two-tailed.

SUPPLEMENTARY MATERIALS

http://www.science.org/doi/10.1126/scitranslmed.abe9726
Materials and Methods
Figs. S1 to S6
Tables S1 and S2
Data file S1
MDAR Reproducibility Checklist
References (*80*–*92*)
View/request a protocol for this paper from *Bio-protocol*.

REFERENCES AND NOTES

1. H. O. Atladottir, M. G. Pedersen, P. Thorsen, P. B. Mortensen, B. Deleuran, W. W. Eaton, E. T. Parner, Association of family history of autoimmune diseases and autism spectrum disorders. *Pediatrics* **124**, 687–694 (2009).
2. E. Vinet, C. A. Pineau, A. E. Clarke, S. Scott, E. Fombonne, L. Joseph, R. W. Platt, S. Bernatsky, Increased risk of autism spectrum disorders in children born to women with systemic lupus erythematosus: Results from a large population-based cohort. *Arthritis Rheumatol.* **67**, 3201–3208 (2015).
3. D. M. Wingerchuk, B. Banwell, J. L. Bennett, P. Cabre, W. Carroll, T. Chitnis, J. de Seze, K. Fujihara, B. Greenberg, A. Jacob, S. Jarius, M. Lana-Peixoto, M. Levy, J. H. Simon, S. Tenembaum, A. L. Traboulsee, P. Waters, K. E. Wellik, B. G. Weinshenker; International Panel for NMO Diagnosis, International consensus diagnostic criteria for neuromyelitis optica spectrum disorders. *Neurology* **85**, 177–189 (2015).
4. M. M. Nour, I. Nakashima, E. Coutinho, M. Woodhall, F. Sousa, J. Revis, Y. Takai, J. George, J. Kitley, M. E. Santos, J. M. Nour, F. Cheng, H. Kuroda, T. Misu, A. Martins-da-Silva, G. C. DeLuca, A. Vincent, J. Palace, P. Waters, K. Fujihara, M. I. Leite, Pregnancy outcomes in aquaporin-4-positive neuromyelitis optica spectrum disorder. *Neurology* **86**, 79–87 (2016).
5. P. Waters, S. Jarius, E. Littleton, M. I. Leite, S. Jacob, B. Gray, R. Geraldes, T. Vale, A. Jacob, J. Palace, S. Maxwell, D. Beeson, A. Vincent, Aquaporin-4 antibodies in neuromyelitis optica and longitudinally extensive transverse myelitis. *Arch. Neurol.* **65**, 913–919 (2008).

6. V. A. Lennon, T. J. Kryzer, S. J. Pittock, A. S. Verkman, S. R. Hinson, IgG marker of optic-spinal multiple sclerosis binds to the aquaporin-4 water channel. *J. Exp. Med.* **202**, 473–477 (2005).
7. M. Bradl, T. Misu, T. Takahashi, M. Watanabe, S. Mader, M. Reindl, M. Adzemovic, J. Bauer, T. Berger, K. Fujihara, Y. Itoyama, H. Lassmann, Neuromyelitis optica: Pathogenicity of patient immunoglobulin in vivo. *Ann. Neurol.* **66**, 630–643 (2009).
8. J. L. Bennett, C. Lam, S. R. Kalluri, P. Saikali, K. Bautista, C. Dupree, M. Glogowska, D. Case, J. P. Antel, G. P. Owens, D. Gilden, S. Nessler, C. Stadelmann, B. Hemmer, Intrathecal pathogenic anti-aquaporin-4 antibodies in early neuromyelitis optica. *Ann. Neurol.* **66**, 617–629 (2009).
9. S. Hillebrand, K. Schanda, M. Nigritinou, I. Tsymala, D. Bohm, P. Peschl, Y. Takai, K. Fujihara, I. Nakashima, T. Misu, M. Reindl, H. Lassmann, M. Bradl, Circulating AQP4-specific auto-antibodies alone can induce neuromyelitis optica spectrum disorder in the rat. *Acta Neuropathol.* **137**, 467–485 (2019).
10. S. Saadoun, P. Waters, B. A. Bell, A. Vincent, A. S. Verkman, M. C. Papadopoulos, Intra-cerebral injection of neuromyelitis optica immunoglobulin G and human complement produces neuromyelitis optica lesions in mice. *Brain* **133**, 349–361 (2010).
11. J. Soltys, Y. Liu, A. Ritchie, S. Wemlinger, K. Schaller, H. Schumann, G. P. Owens, J. L. Bennett, Membrane assembly of aquaporin-4 autoantibodies regulates classical complement activation in neuromyelitis optica. *J. Clin. Invest.* **129**, 2000–2013 (2019).
12. S. J. Pittock, A. Berthele, K. Fujihara, H. J. Kim, M. Levy, J. Palace, I. Nakashima, M. Terzi, N. Totolyan, S. Viswanathan, K. C. Wang, A. Pace, K. P. Fujita, R. Armstrong, D. M. Wingerchuk, Eculizumab in aquaporin-4-positive neuromyelitis optica spectrum disorder. *N. Engl. J. Med.* **381**, 614–625 (2019).
13. B. Zeka, M. Hastermann, S. Hochmeister, N. Kogl, N. Kaufmann, K. Schanda, S. Mader, T. Misu, P. Rommer, K. Fujihara, Z. Illes, F. Leutmezer, D. K. Sato, I. Nakashima, M. Reindl, H. Lassmann, M. Bradl, Highly encephalitogenic aquaporin 4-specific T cells and NMO-IgG jointly orchestrate lesion location and tissue damage in the CNS. *Acta Neuropathol.* **130**, 783–798 (2015).
14. M. Pohl, N. Kawakami, M. Kitic, J. Bauer, R. Martins, M. T. Fischer, J. Machado-Santos, S. Mader, J. W. Ellwart, T. Misu, K. Fujihara, H. Wekerle, M. Reindl, H. Lassmann, M. Bradl, T cell-activation in neuromyelitis optica lesions plays a role in their formation. *Acta Neuropathol. Commun.* **1**, 85 (2013).
15. W. Kim, S. H. Kim, I. Nakashima, Y. Takai, K. Fujihara, M. I. Leite, J. Kitley, J. Palace, E. Santos, E. Coutinho, A. M. Silva, B. J. Kim, B. J. Kim, S. W. Ahn, H. J. Kim, Influence of pregnancy on neuromyelitis optica spectrum disorder. *Neurology* **78**, 1264–1267 (2012).
16. Y. D. Fragoso, T. Adoni, D. B. Bichuetti, J. B. Brooks, M. L. Ferreira, E. M. Oliveira, C. L. Oliveira, S. B. Ribeiro, A. E. Silva, F. Siquineli, Neuromyelitis optica and pregnancy. *J. Neurol.* **260**, 2614–2619 (2013).
17. B. Bourre, R. Marignier, H. Zephir, C. Papeix, D. Brassat, G. Castelnovo, N. Collongues, S. Vukusic, P. Labauge, O. Outteryck, B. Fontaine, P. Vermersch, C. Confavreux, J. de Seze; NOMADMUS Study Group, Neuromyelitis optica and pregnancy. *Neurology* **78**, 875–879 (2012).
18. Y. Shimizu, K. Fujihara, T. Ohashi, I. Nakashima, K. Yokoyama, R. Ikeguch, T. Takahashi, T. Misu, S. Shimizu, M. Aoki, K. Kitagawa, Pregnancy-related relapse risk factors in women with anti-AQP4 antibody positivity and neuromyelitis optica spectrum disorder. *Mult. Scler.* **22**, 1413–1420 (2016).
19. R. Reuss, P. S. Rommer, W. Bruck, F. Paul, M. Bolz, S. Jarius, T. Boettcher, A. Grossmann, A. Bock, F. Zipp, R. Benecke, U. K. Zettl, A woman with acute myelopathy in pregnancy: Case outcome. *BMJ* **339**, b4026 (2009).
20. Y. Huang, Y. Wang, Y. Zhou, Q. Huang, X. Sun, C. Chen, L. Fang, Y. Long, H. Yang, H. Wang, C. Li, Z. Lu, X. Hu, A. G. Kermode, W. Qiu, Pregnancy in neuromyelitis optica spectrum disorder: A multicenter study from South China. *J. Neurol. Sci.* **372**, 152–156 (2017).
21. V. Braniste, M. Al-Asmakh, C. Kowal, F. Anuar, A. Abbaspour, M. Toth, A. Korecka, N. Bakocevic, L. G. Ng, P. Kundu, B. Gulyas, C. Halldin, K. Hultenby, H. Nilsson, H. Hebert, B. T. Volpe, B. Diamond, S. Pettersson, The gut microbiota influences blood-brain barrier permeability in mice. *Sci. Transl. Med.* **6**, 263ra158 (2014).
22. B. Diamond, G. Honig, S. Mader, L. Brimberg, B. T. Volpe, Brain-reactive antibodies and disease. *Annu. Rev. Immunol.* **31**, 345–385 (2013).
23. L. Brimberg, S. Mader, Y. Fujieda, Y. Arinuma, C. Kowal, B. T. Volpe, B. Diamond, Antibodies as mediators of brain pathology. *Trends Immunol.* **36**, 709–724 (2015).
24. J. Y. Lee, P. T. Huerta, J. Zhang, C. Kowal, E. Bertini, B. T. Volpe, B. Diamond, Neurotoxic autoantibodies mediate congenital cortical impairment of offspring in maternal lupus. *Nat. Med.* **15**, 91–96 (2009).
25. L. Wang, D. Zhou, J. Lee, H. Niu, T. W. Faust, S. Frattini, C. Kowal, P. T. Huerta, B. T. Volpe, B. Diamond, Female mouse fetal loss mediated by maternal autoantibody. *J. Exp. Med.* **209**, 1083–1089 (2012).
26. L. Brimberg, S. Mader, V. Jeganathan, R. Berlin, T. R. Coleman, P. K. Gregersen, P. T. Huerta, B. T. Volpe, B. Diamond, Caspr2-reactive antibody cloned from a mother of an ASD child mediates an ASD-like phenotype in mice. *Mol. Psychiatry* **21**, 1663–1671 (2016).
27. P. Fallier-Becker, J. P. Vollmer, H. C. Bauer, S. Noell, H. Wolburg, A. F. Mack, Onset of aquaporin-4 expression in the developing mouse brain. *Int. J. Dev. Neurosci.* **36**, 81–89 (2014).
28. O. Marin, J. L. Rubenstein, Cell migration in the forebrain. *Annu. Rev. Neurosci.* **26**, 441–483 (2003).
29. P. Rakic, Elusive radial glial cells: Historical and evolutionary perspective. *Glia* **43**, 19–32 (2003).
30. M. Segarra, B. C. Kirchmaier, A. Acker-Palmer, A vascular perspective on neuronal migration. *Mech. Dev.* **138** Pt 1, 17–25 (2015).
31. S. Liebner, M. Corada, T. Bangsow, J. Babbage, A. Taddei, C. J. Czupalla, M. Reis, A. Felici, H. Wolburg, M. Fruttiger, M. M. Taketo, H. von Melchner, K. H. Plate, H. Gerhardt, E. Dejana, Wnt/beta-catenin signaling controls development of the blood-brain barrier. *J. Cell Biol.* **183**, 409–417 (2008).
32. R. Daneman, D. Agalliu, L. Zhou, F. Kuhnert, C. J. Kuo, B. A. Barres, Wnt/beta-catenin signaling is required for CNS, but not non-CNS, angiogenesis. *Proc. Natl. Acad. Sci. U.S.A.* **106**, 641–646 (2009).
33. J. M. Stenman, J. Rajagopal, T. J. Carroll, M. Ishibashi, J. McMahon, A. P. McMahon, Canonical Wnt signaling regulates organ-specific assembly and differentiation of CNS vasculature. *Science* **322**, 1247–1250 (2008).
34. S. Raab, H. Beck, A. Gaumann, A. Yuce, H. P. Gerber, K. Plate, H. P. Hammes, N. Ferrara, G. Breier, Impaired brain angiogenesis and neuronal apoptosis induced by conditional homozygous inactivation of vascular endothelial growth factor. *Thromb. Haemost.* **91**, 595–605 (2004).
35. S. Ma, H. J. Kwon, H. Johng, K. Zang, Z. Huang, Radial glial neural progenitors regulate nascent brain vascular network stabilization via inhibition of Wnt signaling. *PLoS Biol.* **11**, e1001469 (2013).
36. J. Aprea, S. Prenninger, M. Dori, T. Ghosh, L. S. Monasor, E. Wessendorf, S. Zocher, S. Massalini, D. Alexopoulou, M. Lesche, A. Dahl, M. Groszer, M. Hiller, F. Calegari, Transcriptome sequencing during mouse brain development identifies long non-coding RNAs functionally involved in neurogenic commitment. *EMBO J.* **32**, 3145–3160 (2013).
37. S. Mader, L. Brimberg, J. N. Soltys, J. L. Bennett, B. Diamond, Mutations of recombinant aquaporin-4 antibody in the Fc domain can impair complement-dependent cellular cytotoxicity and transplacental transport. *Front. Immunol.* **9**, 1599 (2018).
38. M. P. Burgoon, R. A. Williamson, G. P. Owens, O. Ghausi, R. B. Bastidas, D. R. Burton, D. H. Gilden, Cloning the antibody response in humans with inflammatory CNS disease: Isolation of measles virus-specific antibodies from phage display libraries of a subacute sclerosing panencephalitis brain. *J. Neuroimmunol.* **94**, 204–211 (1999).
39. R. L. Matsuoka, A. Rossi, O. A. Stone, D. Y. R. Stainier, CNS-resident progenitors direct the vascularization of neighboring tissues. *Proc. Natl. Acad. Sci. U.S.A.* **114**, 10137–10142 (2017).
40. S. R. Hinson, M. F. Romero, B. F. Popescu, C. F. Lucchinetti, J. P. Fryer, H. Wolburg, P. Fallier-Becker, S. Noell, V. A. Lennon, Molecular outcomes of neuromyelitis optica (NMO)-IgG binding to aquaporin-4 in astrocytes. *Proc. Natl. Acad. Sci. U.S.A.* **109**, 1245–1250 (2012).
41. J. Palace, D. M. Wingerchuk, K. Fujihara, A. Berthele, C. Oreja-Guevara, H. J. Kim, I. Nakashima, M. Levy, M. Terzi, N. Totolyan, S. Viswanathan, K. C. Wang, A. Pace, M. Yountz, L. Miller, R. Armstrong, S. Pittock; PREVENT Study Group, Benefits of eculizumab in AQP4+ neuromyelitis optica spectrum disorder: Subgroup analyses of the randomized controlled phase 3 PREVENT trial. *Mult. Scler. Relat. Disord.* **47**, 102641 (2021).
42. S. Saadoun, P. Waters, M. I. Leite, J. L. Bennett, A. Vincent, M. C. Papadopoulos, Neuromyelitis optica IgG causes placental inflammation and fetal death. *J. Immunol.* **191**, 2999–3005 (2013).
43. S. R. Hinson, A. McKeon, J. P. Fryer, M. Apiwattanakul, V. A. Lennon, S. J. Pittock, Prediction of neuromyelitis optica attack severity by quantitation of complement-mediated injury to aquaporin-4-expressing cells. *Arch. Neurol.* **66**, 1164–1167 (2009).
44. S. F. Roemer, J. E. Parisi, V. A. Lennon, E. E. Benarroch, H. Lassmann, W. Bruck, R. N. Mandler, B. G. Weinshenker, S. J. Pittock, D. M. Wingerchuk, C. F. Lucchinetti, Pattern-specific loss of aquaporin-4 immunoreactivity distinguishes neuromyelitis optica from multiple sclerosis. *Brain* **130**, 1194–1205 (2007).
45. L. Sabater, A. Giralt, A. Boronat, K. Hankiewicz, Y. Blanco, S. Llufriu, J. Alberch, F. Graus, A. Saiz, Cytotoxic effect of neuromyelitis optica antibody (NMO-IgG) to astrocytes: An in vitro study. *J. Neuroimmunol.* **215**, 31–35 (2009).
46. G. A. Johnson, A. Badea, J. Brandenburg, G. Cofer, B. Fubara, S. Liu, J. Nissanov, Waxholm space: An image-based reference for coordinating mouse brain research. *Neuroimage* **53**, 365–372 (2010).
47. J. F. P. Ullmann, C. Watson, A. L. Janke, N. D. Kurniawan, D. C. Reutens, A segmentation protocol and MRI atlas of the C57BL/6J mouse neocortex. *Neuroimage* **78**, 196–203 (2013).
48. S. J. Sawiak, N. I. Wood, G. B. Williams, A. J. Morton, T. A. Carpenter, Voxel-based morphometry in the R6/2 transgenic mouse reveals differences between genotypes not seen with manual 2D morphometry. *Neurobiol. Dis.* **33**, 20–27 (2009).

49. T. W. Faust, S. Robbiati, T. S. Huerta, P. T. Huerta, Dynamic NMDAR-mediated properties of place cells during the object place memory task. *Front. Behav. Neurosci.* **7**, 202 (2013).
50. M. Fyhn, T. Hafting, M. P. Witter, E. I. Moser, M. B. Moser, Grid cells in mice. *Hippocampus* **18**, 1230–1238 (2008).
51. C. Miao, Q. Cao, M. B. Moser, E. I. Moser, Parvalbumin and somatostatin interneurons control different space-coding networks in the medial entorhinal cortex. *Cell* **171**, 507–521.e17 (2017).
52. S. Nielsen, P. Agre, The aquaporin family of water channels in kidney. *Kidney Int.* **48**, 1057–1068 (1995).
53. E. Shosha, D. Dubey, J. Palace, I. Nakashima, A. Jacob, K. Fujihara, T. Takahashi, D. Whittam, M. I. Leite, T. Misu, T. Yoshiki, S. Messina, L. Elsone, M. Majed, E. Flanagan, A. Gadoth, C. Huebert, J. Sagen, B. M. Greenberg, M. Levy, A. Banerjee, B. Weinshenker, S. J. Pittock, Area postrema syndrome: Frequency, criteria, and severity in AQP4-IgG-positive NMOSD. *Neurology* **91**, e1642–e1651 (2018).
54. D. Prilutsky, A. Kho, A. Feiglin, T. Hammond, B. Stevens, I. S. Kohane, Sexual dimorphism of complement-dependent microglial synaptic pruning and other immune pathways in the developing brain. biorxiv 204412 [**Preprint**] (2017). https://doi.org/10.1101/204412.
55. N. Di Gaetano, E. Cittera, R. Nota, A. Vecchi, V. Grieco, E. Scanziani, M. Botto, M. Introna, J. Golay, Complement activation determines the therapeutic activity of rituximab in vivo. *J. Immunol.* **171**, 1581–1587 (2003).
56. E. Saeland, G. Vidarsson, J. H. Leusen, E. Van Garderen, M. H. Nahm, H. Vile-Weekhout, V. Walraven, A. M. Stemerding, J. S. Verbeek, G. T. Rijkers, W. Kuis, E. A. Sanders, J. G. Van De Winkel, Central role of complement in passive protection by human IgG1 and IgG2 anti-pneumococcal antibodies in mice. *J. Immunol.* **170**, 6158–6164 (2003).
57. H. Zhang, A. S. Verkman, Longitudinally extensive NMO spinal cord pathology produced by passive transfer of NMO-IgG in mice lacking complement inhibitor CD59. *J. Autoimmun.* **53**, 67–77 (2014).
58. N. Asavapanumas, J. Ratelade, M. C. Papadopoulos, J. L. Bennett, M. H. Levin, A. S. Verkman, Experimental mouse model of optic neuritis with inflammatory demyelination produced by passive transfer of neuromyelitis optica-immunoglobulin G. *J. Neuroinflammation* **11**, 16 (2014).
59. R. L. Matsuoka, M. Marass, A. Avdesh, C. S. Helker, H. M. Maischein, A. S. Grosse, H. Kaur, N. D. Lawson, W. Herzog, D. Y. Stainier, Radial glia regulate vascular patterning around the developing spinal cord. *eLife* **5**, e20253 (2016).
60. V. A. Skucas, I. B. Mathews, J. Yang, Q. Cheng, A. Treister, A. M. Duffy, A. S. Verkman, B. L. Hempstead, M. A. Wood, D. K. Binder, H. E. Scharfman, Impairment of select forms of spatial memory and neurotrophin-dependent synaptic plasticity by deletion of glial aquaporin-4. *J. Neurosci.* **31**, 6392–6397 (2011).
61. H. E. Scharfman, D. K. Binder, Aquaporin-4 water channels and synaptic plasticity in the hippocampus. *Neurochem. Int.* **63**, 702–711 (2013).
62. M. Tang, G. Gao, C. B. Rueda, H. Yu, D. N. Thibodeaux, T. Awano, K. M. Engelstad, M. J. Sanchez-Quintero, H. Yang, F. Li, H. Li, Q. Su, K. E. Shetler, L. Jones, R. Seo, J. McConathy, E. M. Hillman, J. L. Noebels, D. C. De Vivo, U. R. Monani, Brain microvasculature defects and Glut1 deficiency syndrome averted by early repletion of the glucose transporter-1 protein. *Nat. Commun.* **8**, 14152 (2017).
63. J. Geng, L. Wang, L. Zhang, C. Qin, Y. Song, Y. Ma, Y. Chen, S. Chen, Y. Wang, Z. Zhang, G. Y. Yang, Blood-brain barrier disruption induced cognitive impairment is associated with increase of inflammatory cytokine. *Front. Aging Neurosci.* **10**, 129 (2018).
64. M. Mogi, M. Horiuchi, Neurovascular coupling in cognitive impairment associated with diabetes mellitus. *Circ. J.* **75**, 1042–1048 (2011).
65. S. Taheri, C. Gasparovic, B. N. Huisa, J. C. Adair, E. Edmonds, J. Prestopnik, M. Grossetete, N. J. Shah, J. Wills, C. Qualls, G. A. Rosenberg, Blood-brain barrier permeability abnormalities in vascular cognitive impairment. *Stroke* **42**, 2158–2163 (2011).
66. A. Hafezi-Moghadam, K. L. Thomas, D. D. Wagner, ApoE deficiency leads to a progressive age-dependent blood-brain barrier leakage. *Am. J. Phys. Cell Physiol.* **292**, C1256–C1262 (2007).
67. S. M. Fullerton, G. A. Shirman, W. J. Strittmatter, W. D. Matthew, Impairment of the blood-nerve and blood-brain barriers in apolipoprotein E knockout mice. *Exp. Neurol.* **169**, 13–22 (2001).
68. N. Methia, P. Andre, A. Hafezi-Moghadam, M. Economopoulos, K. L. Thomas, D. D. Wagner, ApoE deficiency compromises the blood brain barrier especially after injury. *Mol. Med.* **7**, 810–815 (2001).
69. S. G. Kalinichenko, A. V. Korobtsov, N. Y. Matveeva, I. I. Pushchin, Structural and chemical changes in glial cells in the rat neocortex induced by constant occlusion of the middle cerebral artery. *Acta Histochem.* **122**, 151573 (2020).
70. R. Gerlai, J. M. Wojtowicz, A. Marks, J. Roder, Overexpression of a calcium-binding protein, S100 beta, in astrocytes alters synaptic plasticity and impairs spatial learning in transgenic mice. *Learn. Mem.* **2**, 26–39 (1995).
71. R. Takano, T. Misu, T. Takahashi, S. Sato, K. Fujihara, Y. Itoyama, Astrocytic damage is far more severe than demyelination in NMO: A clinical CSF biomarker study. *Neurology* **75**, 208–216 (2010).
72. Y. Wei, H. Chang, X. Li, L. Du, W. Xu, H. Cong, Y. Yao, X. Zhang, L. Yin, CSF-S100B is a potential candidate biomarker for neuromyelitis optica spectrum disorders. *Biomed. Res. Int.* **2018**, 5381239 (2018).
73. T. Misu, R. Takano, K. Fujihara, T. Takahashi, S. Sato, Y. Itoyama, Marked increase in cerebrospinal fluid glial fibrillar acidic protein in neuromyelitis optica: An astrocytic damage marker. *J. Neurol. Neurosurg. Psychiatry* **80**, 575–577 (2009).
74. B. V. Zlokovic, The blood-brain barrier in health and chronic neurodegenerative disorders. *Neuron* **57**, 178–201 (2008).
75. F. Ju, Y. Ran, L. Zhu, X. Cheng, H. Gao, X. Xi, Z. Yang, S. Zhang, Increased BBB permeability enhances activation of microglia and exacerbates loss of dendritic spines after transient global cerebral ischemia. *Front. Cell. Neurosci.* **12**, 236 (2018).
76. Y. Liu, T. Bergmann, Y. Mori, J. M. Peralvo Vidal, M. Pihl, N. A. Vasistha, P. D. Thomsen, S. E. Seemann, J. Gorodkin, P. Hyttel, K. Khodosevich, M. P. Witter, V. J. Hall, Development of the entorhinal cortex occurs via parallel lamination during neurogenesis. *Front. Neuroanat.* **15**, 663667 (2021).
77. M. Aoyama, H. Kakita, S. Kato, M. Tomita, K. Asai, Region-specific expression of a water channel protein, aquaporin 4, on brain astrocytes. *J. Neurosci. Res.* **90**, 2272–2280 (2012).
78. S. Mader, A. Lutterotti, F. Di Pauli, B. Kuenz, K. Schanda, F. Aboul-Enein, M. Khalil, M. K. Storch, S. Jarius, W. Kristoferitsch, T. Berger, M. Reindl, Patterns of antibody binding to aquaporin-4 isoforms in neuromyelitis optica. *PLOS ONE* **5**, e10455 (2010).
79. S. Mader, V. Gredler, K. Schanda, K. Rostasy, I. Dujmovic, K. Pfaller, A. Lutterotti, S. Jarius, F. Di Pauli, B. Kuenz, R. Ehling, H. Hegen, F. Deisenhammer, F. Aboul-Enein, M. K. Storch, P. Koson, J. Drulovic, W. Kristoferitsch, T. Berger, M. Reindl, Complement activating antibodies to myelin oligodendrocyte glycoprotein in neuromyelitis optica and related disorders. *J. Neuroinflammation* **8**, 184 (2011).
80. M. M. Ruseva, V. Ramaglia, B. P. Morgan, C. L. Harris, An anticomplement agent that homes to the damaged brain and promotes recovery after traumatic brain injury in mice. *Proc. Natl. Acad. Sci. U.S.A.* **112**, 14319–14324 (2015).
81. W. K. Schiffer, M. M. Mirrione, S. L. Dewey, Optimizing experimental protocols for quantitative behavioral imaging with 18F-FDG in rodents. *J. Nucl. Med.* **48**, 277–287 (2007).
82. S. J. Sawiak, N. I. Wood, G. B. Williams, A. J. Morton, T. A. Carpenter, Use of magnetic resonance imaging for anatomical phenotyping of the R6/2 mouse model of Huntington's disease. *Neurobiol. Dis.* **33**, 12–19 (2009).
83. D. C. Rogers, E. M. Fisher, S. D. Brown, J. Peters, A. J. Hunter, J. E. Martin, Behavioral and functional analysis of mouse phenotype: SHIRPA, a proposed protocol for comprehensive phenotype assessment. *Mamm. Genome* **8**, 711–713 (1997).
84. S. S. Chavan, P. T. Huerta, S. Robbiati, S. I. Valdes-Ferrer, M. Ochani, M. Dancho, M. Frankfurt, B. T. Volpe, K. J. Tracey, B. Diamond, HMGB1 mediates cognitive impairment in sepsis survivors. *Mol. Med.* **18**, 930–937 (2012).
85. M. Yang, J. N. Crawley, Simple behavioral assessment of mouse olfaction. *Curr. Protoc. Neurosci.* **Chapter 8**, Unit 8.24 (2009).
86. E. H. Chang, B. T. Volpe, M. Mackay, C. Aranow, P. Watson, C. Kowal, J. Storbeck, P. Mattis, R. Berlin, H. Chen, S. Mader, T. S. Huerta, P. T. Huerta, B. Diamond, Selective impairment of spatial cognition caused by autoantibodies to the N-methyl-D-aspartate receptor. *EBioMedicine* **2**, 755–764 (2015).
87. J. Nestor, Y. Arinuma, T. S. Huerta, C. Kowal, E. Nasiri, N. Kello, Y. Fujieda, A. Bialas, T. Hammond, U. Sriram, B. Stevens, P. T. Huerta, B. T. Volpe, B. Diamond, Lupus antibodies induce behavioral changes mediated by microglia and blocked by ACE inhibitors. *J. Exp. Med.* **215**, 2554–2566 (2018).
88. C. Kowal, L. A. DeGiorgio, T. Nakaoka, H. Hetherington, P. T. Huerta, B. Diamond, B. T. Volpe, Cognition and immunity; antibody impairs memory. *Immunity* **21**, 179–188 (2004).
89. Y. Ma, P. R. Hof, S. C. Grant, S. J. Blackband, R. Bennett, L. Slatest, M. D. McGuigan, H. Benveniste, A three-dimensional digital atlas database of the adult C57BL/6J mouse brain by magnetic resonance microscopy. *Neuroscience* **135**, 1203–1215 (2005).
90. E. H. Chang, P. T. Huerta, Neurophysiological correlates of object recognition in the dorsal subiculum. *Front. Behav. Neurosci.* **6**, 46 (2012).
91. J. Z. Tsien, P. T. Huerta, S. Tonegawa, The essential role of hippocampal CA1 NMDA receptor-dependent synaptic plasticity in spatial memory. *Cell* **87**, 1327–1338 (1996).
92. R. Sankowski, T. S. Huerta, R. Kalra, T. J. Klein, J. J. Strohl, Y. Al-Abed, S. Robbiati, P. T. Huerta, Large-scale validation of the paddling pool task in the clockmaze for studying hippocampus-based spatial cognition in mice. *Front. Behav. Neurosci.* **13**, 121 (2019).

Acknowledgments: We thank C. Kowal for assistance in perfusing embryos, J. Nestor for assistance in obtaining CSF through cisterna-magna-puncture, C. Bagnall-Moreau for assistance with MBF ImageJ software, and C. Haupt for helpful discussions. **Funding:** This work was supported by NIH Grants 5P01AI102852 (to B.D.), 5P01AI073693 (to B.D.), and 2R01EY022936 (to J.L.B.); by the DOD impact award W81XWH1910759 (to P.T.H.); and by the Guthy Jackson Charitable Foundation (to J.L.B.). **Author contributions:** S.M. designed and performed experiments involving immunohistology of embryonic and adult brains, qPCR,

site-directed mutagenesis, Western blot, mouse behavior, microPET, cell-based assay, brain deglycosylation, and enzyme-linked immunosorbent assay (ELISA); performed statistical analysis; prepared figures; and wrote the manuscript. L.B. designed and performed experiments involving immunohistology of embryonic and adult brains, qPCR, mouse behavior, in situ hybridization; performed statistical analysis; prepared figures; and wrote the manuscript. A.V. and D.E. designed experiments involving microPET, analyzed the microPET data, prepared figures, and contributed to manuscript preparation. J.C., S.L.D., and M.H. designed and conducted experiments involving microPET and contributed to manuscript preparation. J.J.S. performed experiments involving mouse behavior and neuronal recordings and contributed in the preparation of figures and the manuscript. J.M.C. and A.B. designed and analyzed the experiments involving placenta pathology and contributed in the preparation of the manuscript. D.C. designed and performed experiments involving immunohistology of brains and in situ hybridization and contributed in the preparation of the manuscript. T.S.H. and A.L.B. contributed in experiments involving mouse behavior and contributed in the preparation of figures and the manuscript. R.B. contributed in immunohistology staining and preparation of figures. I.D. and J.D. contributed in sample collection of patients with NMOSD and analysis of data and manuscript preparation. J.L.B. contributed human monoclonal antibodies, performed experiments for validation of antibodies, and contributed in the preparation of the manuscript. B.T.V. supervised and designed experimental procedures involving histology, analyzed data, and prepared the manuscript. P.T.H. supervised and analyzed experimental procedures for mouse behavior and neuronal recordings, prepared figures, and prepared the manuscript. B.D. conceived, designed, and supervised experimental procedures and prepared the manuscript.
Competing interests: The authors declare that they have no competing interests. **Data and materials availability:** All data associated with this study are present in the paper or the Supplementary Materials.

Submitted 25 September 2020
Resubmitted 8 December 2021
Accepted 11 March 2022
Published 20 April 2022
10.1126/scitranslmed.abe9726

Science Translational Medicine

In utero exposure to maternal anti–aquaporin-4 antibodies alters brain vasculature and neural dynamics in male mouse offspring

Simone MaderLior BrimbergAn VoJoshua J. StrohlJames M. CrawfordAlexandre BonninJoseph CarriónDelcora CampbellTomás S. HuertaAndrea La BellaRoseann BerlinStephen L. DeweyMatthew HellmanDavid EidelbergIrena DujmovicJelena DrulovicJeffrey L. BennettBruce T. VolpePatricio T. HuertaBetty Diamond

Sci. Transl. Med., 14 (641), eabe9726. • DOI: 10.1126/scitranslmed.abe9726

Transferring maternal autoantibodies

Recent data have shown that family history of autoimmune diseases is associated with increased risk of neurological disorders. Here, Mader *et al.* investigated the effects of prenatal brain exposure to antibodies targeting the astrocytic protein aquaporin-4 (AQP4-IgG), that are present in most of the patients with neuromyelitis optica spectrum disorder (NMOSD). The authors showed that mice exposed in utero to AQP4-IgG developed abnormal brain vasculature and impaired blood-brain barrier in cortical areas by modulating WNT signaling in radial glia. Once they reached adult age, the animals developed neuronal and astrocytic abnormalities as well as cognitive impairments, suggesting that maternal IgG might impair brain development in the offspring.

Science Translational Medicine (ISSN) is published by the American Association for the Advancement of Science. 1200 New York Avenue NW, Washington, DC 20005. The title *Science Translational Medicine* is a registered trademark of AAAS.

Science Translational Medicine
AAAS

Supplementary Materials for

In utero exposure to maternal anti–aquaporin-4 antibodies alters brain vasculature and neural dynamics in male mouse offspring

Simone Mader *et al.*

Corresponding author: Simone Mader, simone.mader@med.uni-muenchen.de

Sci. Transl. Med. **14**, eabe9726 (2022)
DOI: 10.1126/scitranslmed.abe9726

The PDF file includes:

Other Supplementary Material for this manuscript includes the following:

Materials and Methods

SECTION 1: Fetal Studies

Antibody administration to pregnant dams: For timed pregnancy, 2 females either C57BL/6 wild type or *C1q* -/- and 1 male mouse (corresponding genotype) were housed together for 14 h. The time when the male mouse was removed from the cage was designated E0.5. We injected human monoclonal AQP4-IgG or 2B4-IgG (60 µg in a total volume of 200 µl PBS) into pregnant dams at E14.5, retro-orbitally, under light anesthesia. Embryos were either harvested at E15.5, E16.5 or E18.5 or pregnancies were allowed to progress full term. Retro-orbital injection was chosen to allow intravenous vascular access of AQP4-IgG and 2B4-IgG and we have previously demonstrated that this is an effective route in the maternal antibody model (*26*).

qPCR for analyzing Aqp4, Wnt signaling, and C1q: We performed qPCR in embryonic and adult brain and placenta. *Tissue* was homogenized in Trizol (Life Technologies). Total RNA was purified from the homogenized tissue using PicoPure RNA Isolation Kit (Applied Biosystems) following manufactory's instruction. Briefly, 1 µg of RNA was transcribed into cDNA using an iScript cDNA synthesis kit (Bio Rad) and including a DNase digestion step (DNA-free DNA removal kit, Invitrogen). We measured gene expression using Roche's LightCycler 480 Probes Master mix and Mm00437347_m1 (*Wnt5*a, Applied Biosystems), Mm00550265_m1 (*Lef1*, Applied Biosystems), Mm00437356_m1 (*Wnt7*, Applied Biosystems), Mm00802131_m1 (*Aqp*, Applied Biosystems) and Mm00432142_m1 (*C1qa*, Applied Biosystems) on a LightCycler 480 II instrument (Roche). The results were normalized by Mm00839493_m1 probe (*Polr*2A, Applied Biosystems) and relative induction was calculated by delta Ct.

Site directed mutagenesis of AQP4: We modified both glycosylation sites of human M23 AQP4 (at position 153 and at position 206) by site-directed mutagenesis according to the manufacturer's instructions (Invitrogen). The glycosylation site at position 153 is located in the extracellular domain and at position 206 in the cytoplasmic domain. The amino acids at both sites were modified from asparagine (N) to glycine (G) and thus generated the double mutant AQP4 N153G/N206G. We confirmed the site directed mutagenesis by sequencing (Genewiz).

Immunohistology of fetal brains: Embryos or E18 brains were fixed in 4% PFA containing 4% sucrose (4 h, 4°C), gradually transferred to increased sucrose concentrations up to 30% sucrose. Tissue was embedded in OCT compound (VWK) on dry ice and stored at -80°C. Sections were cut (12 µm thickness, Cryostat, Leica) and mounted on gelatin-coated slides and stored (-80˚C).

Staining of the vasculature in embryonic brain: E18.5 brains were stained for isolectin-B4 (IB4, biotin conjugate, Sigma-Aldrich, #L2140) with modifications (*80*). Briefly, sections were thawed (20 min at RT), washed with TBS and IB4 was added in TBS (1:50 dilution, overnight, 4°C). Sections were washed (3x, 20 min) in TBS and streptavidin Alexa-488 (Life Technologies, #S32354) was added (1:300 dilution, 1 h, at RT). Sections were washed (3x) in TBS and DAPI (Thermofisher) was added. Sections were mounted (DAKO-mounting medium #S3023) and cover-slipped (Fisher). The hippocampus was identified and used an internal landmark from which an identical volume of cortical region superior to the hippocampus was framed ($1.5x10^5 \mu m^2$). Targets that were antibody positive were counted and measured on tiled images within the frame (NA= 0.8; Axio-Imager. Z-1, Axio-Vision 4.8, Zeiss).

Staining of complement-MAC in embryonic brain: E18.5 brains were stained for complement-MAC deposits with anti-C5b9 antibody, a kind gift provided by B. Paul Morgan (*80*). In short, tissue sections were blocked for 1 h with PBS with 5% bovine serum albumin (BSA, Sigma Aldrich) in Triton X100 (0.1%) at RT. Anti-C5b9 antibody (1:250) and anti-GLAST antibody (1:150 Frontier Institute Co. Lt., Japan, #AB_2571716) were added overnight at 4°C. After washing in PBS/0.1%Tween, antibody binding

was detected using Alexa 488 Donkey anti-rabbit (Thermo Fisher, #A21208) and 594 Donkey anti-goat (Life Technologies, #A-11058). Finally, DAPI (1 µg per ml, Life Technologies) was added. Comparable sections from each animal (n = 5 or 6) and comparable cortical regions within those sections were imaged with tiling and Z-stack functions at 63x oil under identical super-resolution (Airy scan) conditions (LSM900, Zeiss,). C5b9 deposits were identified by threshold techniques and areas were quantified (Zen 3.1, Zeiss).

Histology of E15 perfused embryos and AQP4 expression analysis: After sacrificing the pregnant dam, embryos were perfused by removing the placental sac (with embryo and attached placenta) in ice cold HBSS (Life Technologies). Cardiac perfusion was performed under a surgical microscope (*21*, *58*). Embryos were fixed in 4% PFA-containing 1% sucrose (4 h, 4°C), 1 h in 20% sucrose, and overnight in 30% sucrose (all at 4°C). Embryos or brains were incubated (at RT) in 1:1 mixture of 30% sucrose and OCT-compound, frozen in OCT-compound on dry ice and stored (-80°C). Sagittal sections were cut (12 µm thickness, Cryostat), mounted on gelatin-coated slides, dried (1 h) and stored (-80°C). Sections were dried (1 h, at RT) prior to staining. Slides were rinsed in PBS (2x, 5 min each) and blocked (PBS-3% BSA-3% FBS in 0.1% TritonX-100, 1 h) and then incubated with goat anti-GLAST (Frontier Institute Co. Lt.,) and rabbit-anti-AQP4 (Abcam, #ab46182) diluted in blocking buffer (1 h). Slides were washed (3x, PBS-T) and antibody binding was detected using secondary antibodies from Alexa (Alexa488 and Alexa594, 400x dilutions). DAPI staining was added and sections were DAKO-mounted and cover-slipped.

Wnt5a in situ hybridization: E18.5 brains were prepared as described above. *Wnt5a* (#316791, ACD) in situ hybridization, was performed using RNAscope Multiplex Fluorescent Reagent Kit v2 (cat # 323110) according to the manufacture's manual. After developing the *Wnt5a* signal, we stained for IB4 as described above. Comparable regions from comparable sections were imaged as before and IB4 anchored a fixed zone of influence in which the *Wnt*5A could be identified and quantified (ZOI, Zen 3.1, Zeiss).

Western Blot for AQP4 and tight-junction proteins: Brain and placentas were harvested, frozen in liquid-nitrogen and stored (-80°C). For AQP4 expression, membrane and cytosolic fractions were prepared. To process the tissue for Western Blot, brain and placenta were homogenized (ice-cold Homogenizing Buffer: 0.32M sucrose, 10mM HEPES, 2mM EDTA, protease inhibitors) and centrifuged (1000g, 15 min). Supernatant was centrifuged (200,000g) and pellet was resuspended in buffer and centrifuged (200,000g). The pellet was suspended (Lysis Buffer: 20 mM Tris-HCl pH8, 137 mM NaCl, 10%glycerol, 1%NP-40 and 2 mM EDTA, protease inhibitors). For tight-junction expression analysis, the cortex of adult mice was dissected, weighted and processed in Lysis Buffer containing protease-inhibitors and homogenized. All protein concentrations were determined using a BCA protein assay kit (Pierce) according to instructions (Thermo Scientific).

For protein detection, 10 µg of protein (membrane, cytosolic fraction, or whole cell lysate) was loaded on a Novex 4–12% Bis-Tris gel system (Invitrogen). Gels were electrophoresed (60 min, 200V, MOPS-running-buffer) and proteins were transferred to an Immoblot-PDVF membrane (30V, 2.5 h). Following blocking (4% non-fat dry milk in PBS containing 0.1% tween, 1h, at RT), the blot was overnight-incubated at 4°C with rabbit anti-AQP4 (Abcam) or anti-Claudin-V (Invitrogen) diluted in 4% non-fat dry milk. As loading control, anti-actin (1:1000, Abcam, #ab8226) or sodium potassium ATPase for the membrane fraction (Abcam, #ab76020) were used. The blot was washed (3x, 15 min, PBS + 0.1% tween) and incubated with secondary antibodies (680CW and 800CW Odyssey, 10,000x, in 4% non-fat dry milk in PBS + 0.1% tween, 1 h, at RT). Following four washing steps, image acquisition was performed with an Odyssey Imaging System (LI-COR Biosciences).

Sex determination: The sex of embryos was either determined as previously described (*25*) or analyzed at Transnetyx.

SECTION 2: Adult offspring studies

MicroPET acquisition: AQP4- and 2B4-mice were used for these studies. Weight of all mice was obtained and they received isoflurane before imaging and until the end of acquisition. Tail vein catheters were temporarily inserted and mice were placed into the scanner platform. The animals were run in random order by investigators blinded to the treatment group of each animal. [^{15}O]-H_2O was intravenously injected (average dose: 1.43 mCi) and immediately thereafter the scan was started, as it has a half-life of 122 sec. After a waiting period of 20 min, mice were injected through the tail vein catheter with [^{11}C]-isoaminobutyric acid ([^{11}C]-AIB) (average dosage: 1.22 mCi, half-life 20.3 min). The scan was started immediately after injection and the camera was set to acquire the first 10 min of ^{11}C uptake into the brain and the remaining 40 min were used to allow two half-lives to decay before introduction of [^{18}F]-FDG. After this scan the animals received [^{18}F]-FDG intraperitoneally (an average of 1.68 mCi, half-life 110 min) as they were in the same position in the camera and a second 10-min scan was acquired after 45 min asleep uptake period. Animals were allowed to recover in a clean cage with constant monitoring. After the radioactive material was decayed, mice were euthanized and brains and CSF were obtained as described.

Image analysis of microPET data: Imaging data was processed using the FMRIB software library, abbreviated FSL (http://www.fmrib.ox.ac.uk/fsl/). [^{18}F]-FDG scans from each animal were registered to an [^{18}F]-FDG template (*81*) and then to a common MRI template (*89*). The transformations from the [^{18}F]-FDG scan to the template were then applied to the corresponding [^{15}O]-H_2O and [^{11}C]-AIB scans in each animal. Regarding the [^{11}C]-AIB scan, the final three frames of each scan were averaged and used for analysis. Images were smoothed with an isotropic Gaussian kernel FWHM (full width at half maximum) 0.56 mm at all directions. These processing steps were applied for each male and female animal. For each tracer, to identify brain regions in which there was significant difference between AQP4- and 2B4-mice, we performed separate whole brain voxel-wise searches using SPM-Mouse software (Wolfson Brain Imaging Centre, University of Cambridge, Cambridge, UK; www.spmmouse.org) (*48*). These comparisons were performed separately for male and female populations. Group differences were considered significant at a voxel-level threshold of $P < 0.001$ with a cluster cutoff of 500 voxels. Individual data from each significant cluster identified through the whole-brain searches were measured using post-hoc volume-of-interest (VOI) analyses. Values for each significant cluster were compared across groups by using Student t tests and were considered significant at $P < 0.05$.

CSF volume estimation: We used [^{18}F]-FDG scans and the CSF template of SPM-Mouse (*48, 82*) to estimate the CSF volume and the CSF percentage of entire brain volume for each individual animal. Based on the histograms of normalized metabolic activity in each animal brain, a cutoff threshold of 1.15 was selected for the discrimination between the gray matter and white matter/CSF. Voxels which are in the CSF template and have the normalized metabolic activity less than the cutoff threshold were identified. These CSF volumes were compared across groups by using Student t tests and were considered significant at $P < 0.05$.

Measurement of mouse IgG in CSF: CSF was obtained by a cisterna magna puncture and loaded on Novex 4–12% Bis-Tris gels (Invitrogen). Gels were electrophoresed (60 min, 200V) using non reducing conditions and proteins were transferred to an Immunoblot PDVF membrane (30V, 2.5 h). Following blocking with 4% non-fat dry milk in PBS containing 0.1% tween (1h, at RT), the blot was developed with anti-human 800CW Odyssey in 4% non-fat dry milk in PBS + 0.1% tween (1:5000, 1 h, at RT). Following washing (4x), image acquisition was performed (Odyssey Imaging System). Blood contamination was excluded by analyzing the fluid under the microscope and also by Western Blot using TER-119 antibody (R&D Systems, #MAB1125, 400x) in 4% non-fat dry milk (1h, at RT). Following washing (3x), secondary antibody was added (anti human 680CW Odyssey, 1:5000 dilution, 1 h, at RT). Following washing (4x), image acquisition was performed.

Behavioral assessments: AQP4- and 2B4-mice were maintained on a reverse-light schedule (dark: 09:00–21:00, light: 21:00–9:00), with *ad libitum* access to food and water, and were analyzed in a blinded fashion. One week before testing, mice were handled for 5 days in sessions of 5 to 10 min during the dark period of their circadian cycle. Animal behavior was recorded with a centrally-placed video camera using video tracking software (EthoVision XT8.5, Noldus) that recorded the animal's position. Animals of the same sex were tested in cohorts of 8–10 2B4 or AQP4 in an observational screen (*83, 84*), olfactory habituation-dishabituation task (*85*), OPM task (*49, 86, 87*), open-field test, novel-object-recognition (NOR) task (*90*)**,** and Morris water maze (MWM) task (*88*). Mice undergoing behavioral assessments were analyzed according to their cage number, which did not indicate the type of antibody the mice were exposed to in utero; therefore, the testing was performed in a blinded fashion.

Observational screen: This assessment was adapted from the first stage of the SHIRPA procedure (*83, 84*). It consisted in measuring 48 variables (V), using a categorical scale for each category. It began by observing some anatomical parameters, such as coat length (V1: 0 = normal, 1 = diluted, 2 = spotty, 3 = change in color, 4 = other), hair length (V2: 0 = normal, 1 = alopecia, 2 = short, 3 = long) and hair morphology (V3: 0 = normal, 1 = curly, 2 = other). This was followed by observation in a cylindrical glass flask of body position (V4: 0 = flat, 1 = lying on side, 2 = prone, 3 = upright, 4 = sitting up, 5 = some standing in hind legs, 6 = frequent hind leg standing, 7 = some vertical leaping, 8 = frequent leaping), spontaneous activity (V5: 0 = inactive, 1 = mostly resting, 2 = scratch and groom, 3 = slow, 4 = sporadic, 5 = medium and grooming, 6 = high, 7 = vigorous, 8 = nonstop), respiratory rate (V6: 0 = gasping, 1 = slow and labored, 2 = normal, 3 = hyperventilation), tremor occurrence (V7: 0 = none, 1 = mild, 2 = marked), defecation (V8: number of boli), and urination (V9: 0 = absent, 1 = present). Subsequently, mice were transferred to an arena (55 cm x 33 cm, with the floor marked with 9 equal squares) and transfer arousal (V10: 0 = comatose, 2 = ~25s freeze, 3 = ~20s freeze, 4 = ~5s freeze, 5 = no freezing, 6 = extremely excited), latency to move (V11: in seconds), and locomotion in the arena (V12: number of squares entered in 30 s) were measured. We further assessed piloerection (V13: 0 = none, 1 = coat stood on end), palpebral closure (V14: 0 = eyes wide open, 1 = eyes half closed, 2 = eyes closed), startle response (V15: 0 = none, 1 = backward ear flip, 2 = jump less than 1 cm, 3 = high jump), gait (V16: 0 = normal, 1 = fluid but abnormal, 2 = limited, 3 = incapacity), pelvic elevation (V17: 0 – markedly flat pelvis, 1 = ~1mm elevation, 2 = normal [~3 mm], 3 = elevated [>3mm]), tail elevation (V18: 0 = dragging, 1 = horizontal, 2 = elevated), touch escape (V19, response to finger stroke from above: 0 = none, 1 = mild, 2 = moderate, 3 = vigorous), positional passivity (V20, struggle to sequential handling when: 0 = held by tail, 1 = held by neck, 2 = laid supine, 3 = held by hind legs, 4 = no struggle), trunk curl (V21: 0 = absent, 1 = present), limb grasping (V22: 0 = absent, 1 = present), visual placing (V23, extension of forelimbs when mouse is lowered by base of tail from a height of ~15cm above a wire grid: 0 = none, 1 = upon nose contact, 2 = ~9mm upon vibrissae contact, 3 = ~18mm before vibrissae contact, 4 = 25mm early vigorous extension), grip strength (V24, lower the mouse and allow it to grip the grid then apply a gentle horizontal backwards pull: 0 = none, 1 = slight, 2 = moderate, 3 = active, 4 = unusually effective grip), body tone (V25, compress sides of the mouse between thumb and index finger: 0 = flaccid [no return to normal], 1 = slight resistance, 2 = extreme resistance [board-like]), pinna reflex (V26, during the time the mouse is gently restrained on the grid, touch the proximal part of the inner canthus lightly with the tip of the fine wire probe and look at ear retraction: 0 = none, 1 = active retraction, 2 = hyperactive), corneal reflex (V27, touch the cornea lightly with the side of the fine wire probe and look at eye blink response: 0 = none, 1 = single eye blink, 2 = multiple eye blinks), toe pinch (V28, apply gentle lateral compression of mid digit and check withdrawal response: 0 = none, 1 = slight, 2 = moderate, 3 = rapid, 4 = very brisk), body length (V29: in cm), tail length (V30: in cm), lacrimation (V31: 0 = absent, 1 = present), whisker morphology (V32: 0 = normal, 1 = abnormal), provoked biting (V33, insert dowel rod between teeth and the side of the mouth: 0 = absent, 1 = present), salivation (V34: 0 = none, 1 = slight, 2 = wet zone), heart rate (V35, felt by palpation below sternum: 0 = bradycardia, 1 = normal, 2 = tachycardia), abdominal tone (V36, palpation of abdomen: 0 = flaccid, 2 = slight resistance, 3 = board-like), skin color (V37 color gradations of plantar surface: 0 = blanched, 1 = pink tone, 2 = bright red flush), limb tone (V38, resistance to gentle finger-tip pressure on plantar surface: 0 = none, 1 = slight,

2 = moderate, 3 = marked, 4 = extreme resistance), wire maneuver (V39, animal is held above a wire by tail suspension, it is lowered to allow the forelimbs to grip the horizontal wire, held in extension, rotated around to the horizontal and released: 0 = active grip with hind legs, 1 = difficulty to grasp with hind legs, 2 = unable to grasp with hind legs, 3 = falls within 5 s, 4 = falls immediately), righting reflex (V40, animal is held by tail and flicked backwards through the air such that it performs a backward somersault when released. Observe the landing position: 0 = no impairment, 1 = lands on side, 2 = lands on back, 3 = fails to right when placed on back), contact righting (V41, place the animal into the plastic tube and turn mouse upside down: 0 = absent, 1 = present), and negative geotaxis (V42, place animal on horizontal grid. This is then raised to the vertical with the animal facing the floor. Observe for 30 s: 0 = turns and climbs the grid, 1 = turns but then freezes, 2 = moves but fails to turn, 3 = does not move within 30 s, 4 = falls off). Throughout the screen, incidences of the freeze response (V43: 0 = none, 1 = freezes during transfer arousal or other arena transfers), irritability (V44: 0 = none, 1 = struggle during supine restraint or other maneuvers), aggressivity (V45: 0 = none, 1 = bites the experimenter), vocalizations (V46: 0 = absent, 1 = present) and 'bizarre' behaviors (V47: 0 = absent, 1 = present) were assessed. Finally, body weight (V48: in grams) was measured. The observed parameters were grouped according to five functional categories, which were: muscle and spinal function (summed V4, V5, V8, V9, V16, V17, V18, V20, V21, V22, V23, V24, V25, V36, V38, V39, V40, V41); spinocerebellar function (summed V4, V16, V17, V18, V21, V22, V23, V24, V25, V36, V38, V40, V41); sensory function (summed V10, V16, V19, V23, V26, V27, V28, V33, V40, V42); neuropsychiatric function (summed V4, V5, V7, V10, V11, V12, V19, V20, V25, V33, V39, V40, V41, V42, V43, V44, V45, V46, V47); and autonomic function (summed V8, V6, V9, V13, V14, V18, V31, V34, V35, V37). The summed scores for each function were averaged across mice from the same group (2B4 or AQP4) and these were then subjected to statistical analysis.

Olfactory habituation-dishabituation task: AQP4- and 2B4-mice were tested according to prior protocols with minor modifications (*85*). Almond extract (1:50 dilution, McCormick, Hunt Valley) and banana extract (1:100 dilution, McCormick, Hunt Valley) were chosen as odorants with non-emotional value. Dilutions were made fresh in distilled water, on the same day when animals were tested, and dilutions were prepared in a different environment than the testing room. Animals were assessed in a 22.5 x 22.5 x 29.5 cm Plexiglas chamber, with 1 cm of bedding in the floor, and made of solid light green walls and a hole of 1 cm of diameter in one of the sides, located 8 cm above the ground and 11.2 cm from the lateral corners. A cotton stick was inserted into the hole. Indirect dim light was used during testing. A video camera was fixed above the chamber to track mice. Nose point, center point and tail point of the animal were recorded by behavioral tracking software (EthoVision XT8.5), and the nose point was used for analysis of mice sniffing the cotton stick. Bedding was not changed between mice of the same sex. On day 1, each mouse was gently placed in the testing chamber for 10 min. After this period, a dry cotton stick was placed in the hole, and the mouse continued in the chamber for 10 min. On day 2, each mouse was first familiarized to the chamber with a dry cotton stick present (10 min) and then a cotton stick soaked in water was introduced. The stick protruded from the wall ~3 cm and was held in place for 2 min. The mouse was exposed 3 times to a water-soaked stick followed by 1 min of 'rest' without exposure to the stick. After 3 trials with the non-odorant stimulus, the mouse was exposed to 3 presentations of almond-soaked stick (2 min each, 1 min break in-between) and followed by 3 exposures to banana-soaked stick (2 min each, 1 min breaks).

OPM task: AQP4- and 2B4-mice were tested in accordance to previously described protocols (*49, 86, 87*). The apparatus consisted of a chamber with a square base (40-cm on the side) and 60-cm high walls built of grey polyvinyl chloride. The floor was covered with a thin layer of bedding. A light bulb (50 W) of orange hue illuminated the chamber from above. A video camera above the chamber was connected to the video input of the behavioral-tracking-software (Ethovision XT8.5). Mice were transported inside their home cages into the darkened experimental room and placed in the empty chamber, one at a time, for 4 sessions (2 per day) of 15 min. On the third day, mice were subjected to the OPM task, which consisted of a familiarization trial (T1), a sample trial (T2), and a choice trial (T3), interspersed by 10-min delays that were spent in a highly habituated holding chamber. For T1, animals were placed in the empty chamber for

15 min. For T2, mice explored the chamber for 5-min in the presence of two identical objects, which were located in 2 of 4 possible sites at the center of the NW, NE, SW or SE quadrants of the chamber. For T3, which lasted 5-min, one object (chosen at random) remained in the familiar position during which the second object was moved to a location that was the center of the adjacent quadrant, 20-cm apart from its previous position. Object exploration was measured with a software algorithm (Ethovision) that assigned a circular zone (diameter, 6.5-cm) around each object and recorded the episodes in which the animal's snout was in close proximity (<1 cm) to the object's periphery. The number of visits and the times spent exploring each object on T2 and T3 were used for statistical comparisons. For T2, an exploration ratio was defined as the time exploring the right object (in either NE- or SE-zone) divided by the sum of the times exploring both objects. For T3, an OPM ratio was defined as the time exploring the moved object minus the time exploring the stable object over the sum of the times exploring both objects.

Open-field test: AQP4- and 2B4-mice were tested in an apparatus that consists of a chamber with a square base (25-cm on the side) and 60-cm high walls, with open ceiling, constructed of white plastic. The floor was covered with a thin layer of bedding. It was illuminated from the top by a 40-W red bulb. A CCD camera was also mounted on top and was connected to the video input of the behavioral-tracking-software (Ethovision). Each mouse was placed in the empty chamber and allowed to explore it for 15 min. For analysis, the chamber was subdivided into 3 concentric areas (Fig. S3B) consisting of a peripheral area (3-cm from the wall), a central area (square at center, 10 cm on the side), and a ring area between the center and periphery. The times spent exploring each area were used for statistical comparisons.

NOR task: AQP4- and 2B4-mice were tested according to our prior protocol (*87*), in the same apparatus used for the open field test. Before formal testing, each mouse was allowed to familiarize with the empty chamber for 3 sessions (10 min each) over a period of 2 days (one on day 1 and two on day 2). For the NOR task (Fig. S3C), a single trial consisted of 3 phases: sample, delay, and test. For the sample phase, mice were placed in the chamber and explored two identical objects for a period of 5 min. For the delay phase, mice were placed in their home cage for ~1 min. During this interval, test objects replaced sample objects. One of them was identical to those in the sample phase ("familiar object") whereas the other was different ("novel object"). For the test phase, mice explored the chamber with the familiar and novel objects for 5 min. Object exploration was scored when the nose of the mouse was near the object, and it was measured with a software algorithm (Ethovision) that assigned a circular zone (diameter, 6.5-cm) around each object and recorded the episodes in which the animal's snout was in close proximity (<1 cm) to the object's periphery. The NOR ratio was defined as the time exploring the novel object minus the time exploring the familiar object over the sum of the times exploring both objects.

Morris water maze (MWM) task: AQP4- and 2B4-mice were tested in the MWM task according to protocols we have described extensively (*88, 91, 92*). Briefly, we implemented the hidden platform variant of the MWM with the use of a circular pool (diameter, 160 cm) filled with clear water (21°±1°C). The experimental area was dimly illuminated except for 4 large distal cues, which were strongly illuminated with focal lights. We trained the animals in blocks of 4 trials per day for a total of 12 trials (3 days). A mouse was lowered into the pool at one of four starting points in the periphery and had to swim and climb to a hidden platform (diameter, 16 cm), located at the center of the south-west quadrant, in >60 sec (cutoff time). Subjects who failed a trial were guided to the platform and stayed on it for ~5 sec. One day after the training phase, all mice received a probe test in which the platform was absent and the animals had to swim for 60 sec. For analysis, the paths traversed by the mice, the latency to find the platform, and the amount of time in each quadrant of the pool were recorded by Ethovision software. The quadrants were defined as target (SW, in which the platform was located during training), opposite (NE), left (NW) and right (SE).

Neural recordings in the medial entorhinal cortex of freely-behaving mice: The electrophysiological recordings were performed as described previously (*49, 86, 87*). Electrode arrays consisted of 4 tetrodes mounted onto custom 3D-printed micro-drives, and attached to an Omnetics EIB-16 (Neuralynx, Boseman,

MT). The body of the microdrive was printed using a 3D-printer (Form-2, Formlabs, Somerville, MA) and the EIB attached to the top using small machine screws. Tetrodes were wound from 17-µm wire (90% platinum, 10% iridium, California Fine Wire, Grover Beach, CA) and electroplated with platinum black solution (Neuralynx) so that impedances were under 350 kΩ. Tetrodes were glued to a block within the body of the microdrive which could be lowered in precise steps by turning a machine screw. For implantation and lowering of electrodes, mice were anesthetized with 2.5%-isoflurane and maintained at 2%, with anesthesia depth regularly checked by tail or toe pinch reflex. Prior to start of surgery, the surgical site was prepared by shaving and wiping with betadine solution and isopropyl alcohol. An incision was made along the midline, and the skull covered with Metabond Quick Adhesive Cement (Parkell, Edgewood, NY). Using a drill, a craniotomy was made above the cerebellum and the ground screw inserted into the skull. The second craniotomy was made on the right side, 0.38 mm anterior to the transverse sinus and 3.3 mm lateral to midline, and the dura was removed using fine forceps. Tetrodes were inserted at a 5° angle to the sagittal plane so that the tips were pointed in the posterior direction, and slowly lowered to a depth of 0.8 mm below the surface of the brain. Once the tetrodes were in place, the microdrive was affixed to the skull using Ortho-Jet dental acrylic (Lang Dental Inc, Wheeling IL). The ground screw was attached to the EIB-16 using a copper wire, and a 3D-printed cap was glued in place around the microdrive for protection. Buprenorphine (Buprenex, 0.03 mg/kg) was injected subcutaneously for pain relief and the mouse was allowed to recover from anesthesia in a fresh cage placed on a heating pad. Prior to start of recordings, tetrodes were lowered over the course of a week until well-separated units were observed, to a final depth of ~1 mm.

For grid cell recordings, a headstage preamplifier (HS-18-CNR-LED-MDR50, Neuralynx) was connected to the EIB-16 and signals were passed to a programmable amplifier (Lynx-8, Neuralynx). Signals were collected and stored on a PC using Cheetah 4 (Neuralynx) acquisition software. All tetrodes were referenced to the ground screw in the skull. Single units were band-pass filtered (600–9000 Hz) and captured at a rate of 30 kHz. The position of the mouse was tracked at 30-Hz using a camera which was mounted on the ceiling above the recording chamber which tracked a red LED on the headstage and saved the position using Cheetah 4. Recordings consisted of 15-min sessions in a square chamber (1-m on the side, 40-cm tall walls) in which the mouse was allowed to roam freely (*49*, *86*, *87*).

For grid cell analysis, spike sorting was performed using Spike2 (CED). The firing rate of each neuron was calculated as the number of spikes for each isolated unit recorded in a single session divided by the duration of the session. Sorted spikes and position data were imported into NeuroExplorer 5 (NEX Technologies, Colorado Springs, CO), and the chamber was split up into 2 x 2 cm spatial bins. The firing rate for each bin was calculated as the number of spikes divided by the occupancy time of the mouse for that bin and smoothed using Gaussian kernel with a 6-cm radius. If a unit had three or more locations with a firing rate greater than 20% of the peak firing rate spread throughout the chamber and a mean firing rate of less than 5 Hz, it was classified as a grid cell, all other cell types with discarded from further analysis. Firing rate maps were then exported to the MATLAB environment and grid scores and spatial autocorrelation maps were generated using MATLAB scripts that we adopted from scripts kindly supplied by Edvard Moser's laboratory. The spatial autocorrelation is defined as:

$$r(\tau_x, \tau_y) = \frac{n\sum\gamma(x,y)\gamma(x-\tau_x, y-\tau_y) - \sum\gamma(x,y)\sum\gamma(x,y)\gamma(x-\tau_x, y-\tau_y)}{\sqrt{n\sum\gamma(x,y)^2 - (\sum\gamma(x,y))^2}\sqrt{n\sum\gamma(x-\tau_x, y-\tau_y)^2 - \sum\gamma\,(x-\tau_x, y-\tau_y))^2}}$$

where $\gamma(x,y)$ is the average firing rate of a cell at location (x,y), and τ_x, τ_y are spatial lags for which the autocorrelation is calculated. From the autocorrelogram, the grid score is determined by calculating the Pearson correlation of a circle around the center point rotated at angels of 30°, 90°, and 150° on one side and 60° and 120° on the other side taking the minimum difference between the two sides. The rotational symmetry of the autocorrelation maps was quantified using the grid score metric (*50, 51*).

Immunohistology of adult brains: Mice were perfused with 4%PFA following replacement of blood with heparinized pre-perfusion buffer. Brains were sectioned (40 µm, microtome), collected in 0.1 M phosphate buffer (PB, pH 7.4) and mounted on gelatin-coated slides. Slides were air dried and incubated with rabbit anti-AQP4-IgG (Millipore, 1:400), S100β antibody (Abcam, 1:500) or biotinylated lectin (Vector Labs, 1:400) in 0.1 M PBS (pH 7.4) overnight at 4°C. Sections were washed and incubated with appropriate secondary antibodies labeled with Alexa488 or Alexa594 (Life Technologies) for 1h (at RT) and washed three times. DAPI was included in the last washing step. Sections were mounted, cover-slipped, and visualized with an Axio-Imager (Z-1, Zen 3.1, Zeiss). Using stereological sampling procedures that ensured comparability across regions of interest, we examined either the cortex superior to the hippocampus (Bregma, -2.06 mm) or the medial entorhinal cortex (Bregma, -4.04 mm). An example of the entorhinal stereological strategy follows: the rhinal fissure was identified and then posterior sections were explored so that the ventral cortex at the base of the alveus and external capsule was used as a landmark bilaterally (bregma, -4.04 mm). Then a fixed frame ($8.45x10^5$ μm^2) was imposed on the medial entorhinal cortex bilaterally (layers 3–6; 2B4, n = 7; AQP, n = 9), and a tiled image was obtained and stitched (63x oil, numerical aperture [NA] = 1.4; Axio-Imager. Z-1, Zen 3,1, Zeiss). Z-stack (2-µm steps) images were low-pass-Gaussian filtered and collapsed into a maximal intensity plane. Targets that were antibody positive were counted and measured. Determination of the vessel length (L_V) incorporated a measure of the vessel perimeter (P_V) and the vessel area (A_V) that was expressed by the following formula (see fiber length measure, Zen3.1, Zeiss):

$$Lv = \frac{1}{4}\left(P_v + \sqrt{P_v^2 - 16 * A_v}\right)$$

Along these lines, we calculated the Feret ratio for the vessels in adult mice with the following formula (Zen3.1, Zeiss):

Feret ratio = Feret (minimum) / Feret (maximum)

Feret (minimum) was determined by the distance between two parallel lines positioned on opposite sides of a target, and a sliding caliper measured 32 angle positions and the distance between the lines. The minimum value was taken from the 32 measures. Likewise, for Feret (maximum), the maximum value was taken from the 32 measures. Low values represent long or elongated targets, and values approaching 1 indicate compact or circular objects.

Golgi staining of neurons and analysis: Preparation of brains and Golgi staining were done by FD Rapid GolgiStain Kit, as previously described (*26*). For dendrite analysis, the cell bodies and dendrites were identified (40x, NA = 0.8, Axio-Imager. Z-1, Zen 3.1, Zeiss) and a tiled image was obtained (Z-stack steps = 2µm). Images were transferred to be traced and quantified (Neurolucida 360, MBF). For spine analysis, secondary dendrites from neurons in layers 3–6 of the medial entorhinal cortex, or from neurons in CA1 hippocampus, were imaged (100x oil, NA = 1.4; Axio-Imager. Z-1, Zen 3.1, Zeiss) and tiled (Z-stack steps = 0.5-µm). Image stacks were transferred to a software program (Neurolucida360, MBF) so that the soma was identified and the dendrites were visualized and traced. The Sholl protocol (Neurolucida360, MBF) surrounds the soma, and, in shells of expanding (10µm) diameters, quantifies the total length of the dendrites in each shell. Image stacks of spines were identified on dendrites and were quantified by software (Neurolucida360, MBF).

SECTION 3: Additional studies

Brain deglycosylation: The brain membrane lysate from an adult mouse (20 µg) as well as an embryo (20 µg) was de-glycosylated following the instructions of the protein deglycosylation mix from the manufacturer (Bio Labs). Briefly, 5 µl of 10x glycoprotein denaturation buffer was added to 50 µl of total reaction volume. Following a denaturation of the lysate by heating the reaction at 100°C for 10 min, the lysate was chilled on ice and centrifuged for 10 sec. We added 5 µl of 10x glycol-buffer, 2, 5 ul of 10% NP_40 and 15 µl of H_2O. We added 5 µl of deglycosylation enzyme cocktail and mixed it gently. After incubating the reaction at 37°C for 4 h, we analyzed the sample by Western blot. As a control, we performed the same steps with identical lysate but omitted the deglycosylation enzyme.

Cell-based assay for MAC: We analyzed the ability of mouse serum to activate the complement cascade and result in MAC formation in human AQP4-transfected cells upon adding human monoclonal AQP4-IgG or 2B4-IgG. HEK293T cells were transfected either with wildtype or mutant non-glycosylated AQP4. The assay was performed as described, with modifications (*79*). We collected fresh serum from male C57Bl6 mice, and used it immediately for the CDC assay. DMEM-medium without serum was supplemented at 20x with mouse serum and 1 µg/ml AQP4-IgG or 2B4-IgG. Following 1-h incubation at 37°C, we washed the plate with HBSS and added Rabbit Anti-C5b-9 antibody (Abcam) in DMEM-medium (1 h, 4°C). We washed the plate and added Anti-Rabbit Alexa594 antibody (400x dilution in DMEM-medium, 30 min). Following 3 washing steps, we incubated the cells for 5 min with DAPI diluted in HBSS, washed 2x, and fixed the cells with 4%PFA. Fluorescent images were acquired using the Zeiss Axio- Imager microscope with a 20x objective. Images were quantified for the presence of MAC (red signal) on AQP4 transfected cells (green signal) using the Image J (NIH) colocalization program. The percentage of the signal colocalized in the images was calculated as the sum of the pixel intensities from the colocalized signal (yellow in merged image) divided by the sum of the pixel intensities from AQP4 channel signal (green).

Measurement of proteinuria: Urine of male and female mice was collected and frozen at -20°C. We quantified proteinuria in male and female mice using the Mouse Albumin ELISA Quantitation Set (Bethyl Laboratories) according to manufactory's instructions.

Kidney staining: Kidneys from adult AQP4 and 2B4 mice were sectioned at 12 µm on a Cryostat (Leica) and mounted on gelatin-coated slides, which were stored at -80°C. Section were thawed for 30 min (at RT) and stained with biotinylated *Lycopersicon esculentum* (tomato) Lectin (Vector Labs) and AQP4-IgG (Millipore), following the staining procedure performed for adult mouse brain.

Hematoxylin-eosin staining of placenta: Placentas were fixed in 4% PFA/PBS overnight at 4°C followed by equilibration in 30% sucrose/PBS. They were embedded in OCT, and 20-µm sections of placentas were obtained with a cryostat. Sections were frozen in closed containers at -80°C. For histologic staining, frozen sections were air-dried overnight at room temperature. The following day, placentas were incubated for 2 min in absolute ethanol, 2 min in 95% ethanol, 10 dips in 95% ethanol, and 10 dips in 75% ethanol. Slides were briefly rinsed in running water followed by 3-min incubation in Harris Haematoxylin. After rinsing the slides till they were clear they were quickly dipped (for one dip) in acidic alcohol, rinsed under running water, incubated for one dip in Ammonia water/bluing solution, rinsed under running water, incubated for 8 sec in Eosin Y, 10 dips in 95% ethanol, 10 dips in absolute ethanol, 10 min in absolute ethanol, followed by 10 min in Xylene before mounting with clear mount.
Analysis was performed by one observer (JMC) in a blinded fashion at the Department of Pathology and Laboratory Medicine Northwell Health. Each slide was scanned at medium power (100x), to get oriented to the slide and identify the locations of the chorionic plate, chorionic membrane, and placental villus compartment. The slide was then scanned at high power (400x), focusing on the chorionic plate and sub-plate region (scored as "Plate"), and the placental villus compartment moving from the sub-plate region to

the region closest to the maternal interface (scored as “Villus”). Semi quantitative scoring was performed for necrosis in the villus and plate as well as for polymorphonuclear leukocytes (PMN) infiltration.

FIGURE S1

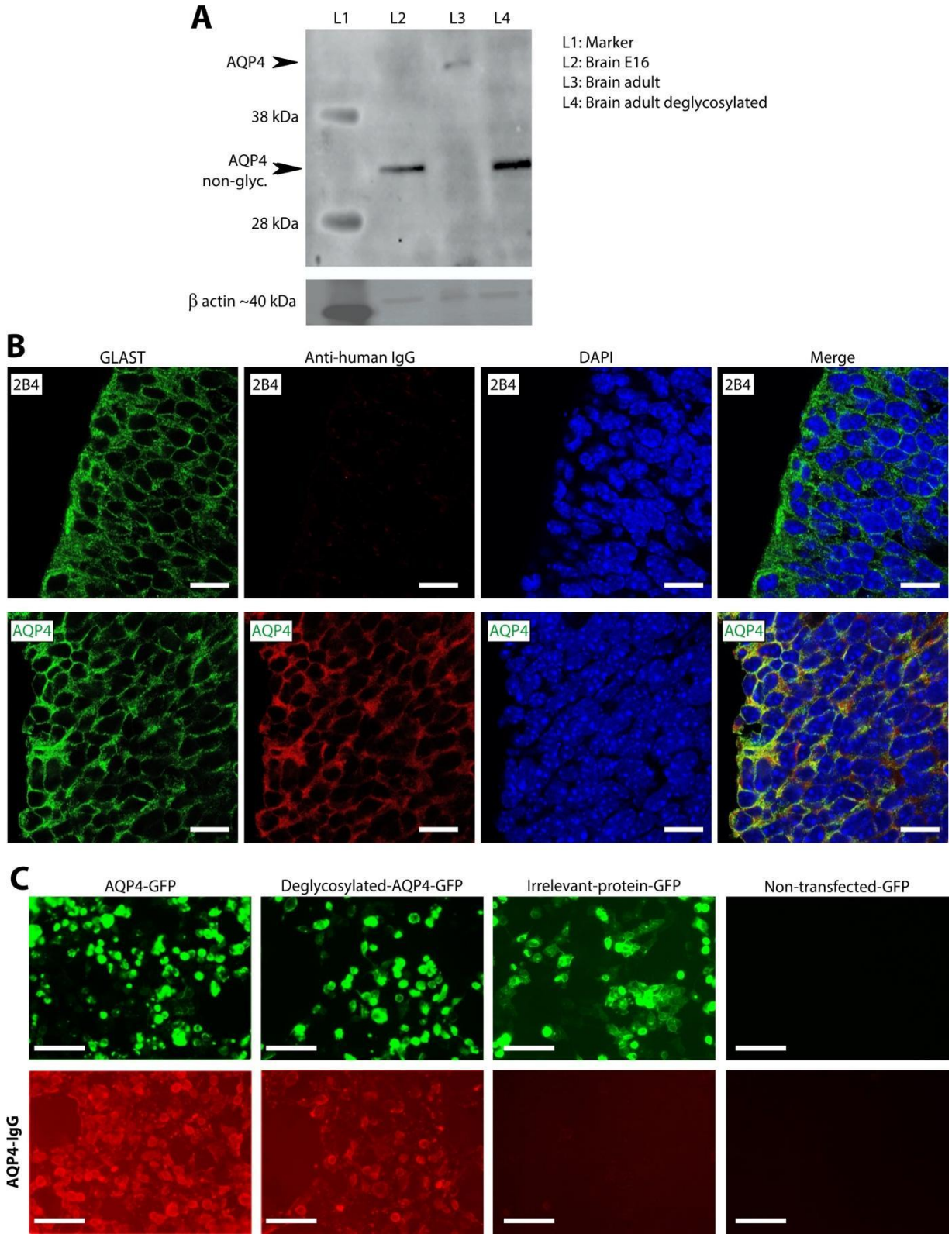
A
L1
L2
L3
L4
AQP4
38 kDa
AQP4
non-glyc.
28 kDa
β actin ~40 kDa
L1: Marker
L2: Brain E16
L3: Brain adult
L4: Brain adult deglycosylated
B
GLAST
Anti-human IgG
DAPI
Merge
2B4
AQP4
C
AQP4-GFP
Deglycosylated-AQP4-GFP
Irrelevant-protein-GFP
Non-transfected-GFP
AQP4-IgG

Fig. S1: Characterization of AQP4 expression in the developing brain. (A) We performed Western blot and observed an AQP4 band in the membrane lysate of embryonic brain at E16 of C57BL/6 mice (L2, lower arrowhead), compared to AQP4 in the brain membrane lysate of adult mice (L3, upper arrowhead). We performed enzymatic deglycosylation of adult brain membrane (L4, lower arrowhead). β-actin was used as a loading control. The Western blot was developed with commercially available anti-AQP4 antibody (representative of 3 experiments). **(B)** Coronal sections of cerebral cortex (E15.5) were analysed for binding of human monoclonal AQP4-IgG (generated from a CSF plasma cell of a patient with NMOSD) compared to 2B4-IgG (control antibody) . *Left to right:* RGCs were stained with GLAST antibody (green signal) and human anti-AQP4-IgG or 2B4-IgG (red signal). Cell nuclei were stained with DAPI (blue signal), and merged image show colocalization of GLAST, DAPI and AQP4 signals (representative of 3 experiments). Scale bar, 20 μm. **(C)** Binding of human monoclonal AQP4-IgG (red signal) was investigated with live cell-based assays using HEK-239T cells. Left to right: Binding of human AQP4-IgG was analyzed to cells expressing glycosylated AQP4-GFP or cells expressing deglycosylated AQP4-GFP (generated by site directed mutagenesis of the glycosylation site of the human N153/N206 AQP4). Cells expressing Caspr2-GFP (an irrelevant protein) as well as non-transfected cells (which do not express GFP) were included as controls (representative of 3 experiments). Scale bar, 50 μm. Abbreviations: L, lane, AQP4 non-glyc., non-glycosylated AQP4.

FIGURE S2

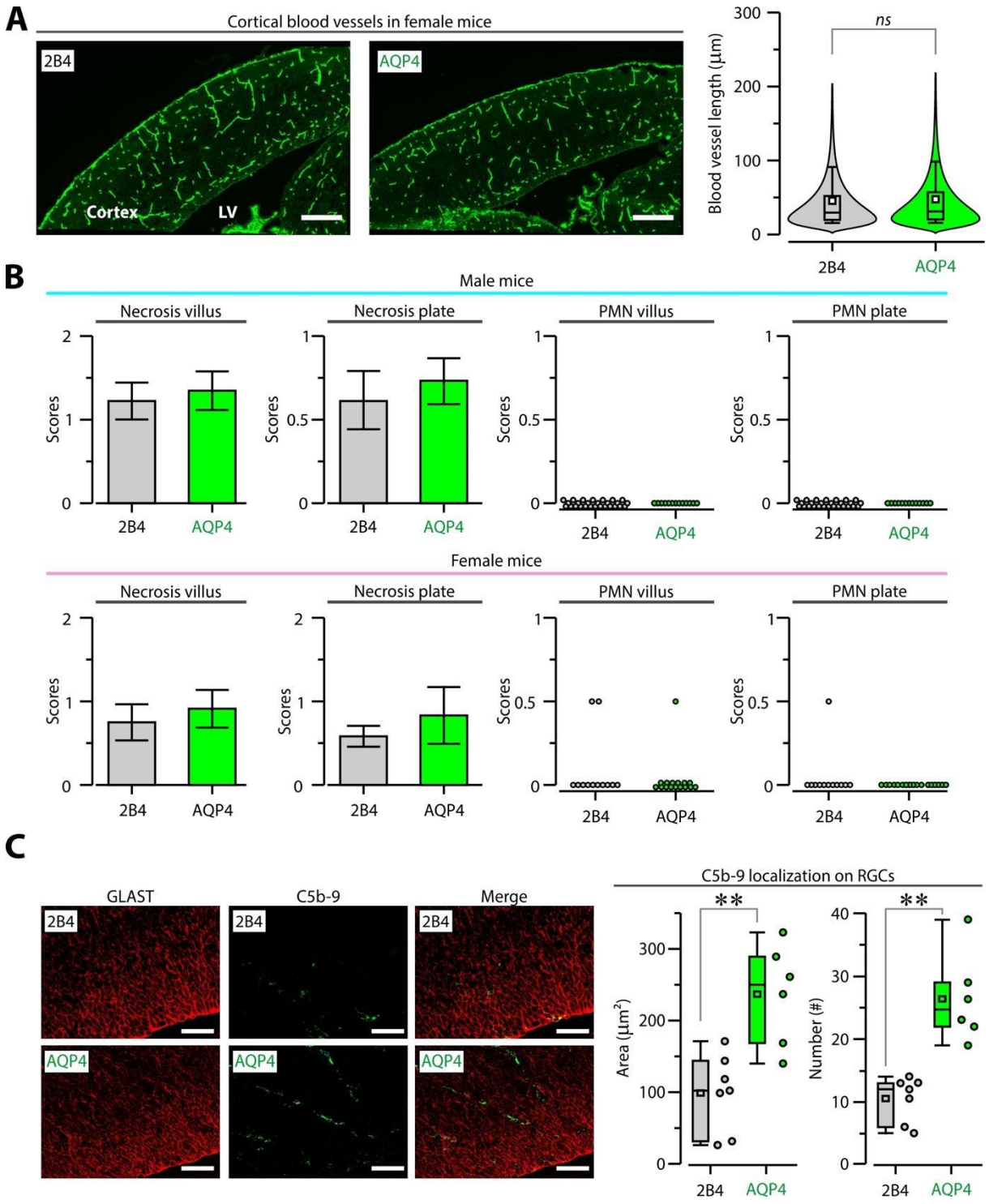
A
Cortical blood vessels in female mice
2B4
AQP4
Cortex
LV
Blood vessel length (µm)
ns
2B4
AQP4
B
Male mice
Necrosis villus
Necrosis plate
PMN villus
PMN plate
Scores
Female mice
C
GLAST
C5b-9
Merge
C5b-9 localization on RGCs
Area (µm²)
Number (#)
**

Fig. S2: Blood vessels in female fetal brains, placenta studies, and C5b-9 in AQP4-males. (A) *Left*, representative cortical sections of female brains (E18.5) stained with isolectin-IB4 for blood vessels. *Right*, violin plots show the length of developing vessels in the fetal cortex of AQP4-females (n = 1775 vessel segments, 8 mice, range: 136–203 vessel segments per animal) and 2B4-females (n = 1762 vessel segments, 10 mice; 164–221 vessel segments per animal); P = 0.15, Kolmogorov-Smirnov test. Scale bar, 200 μm. **(B)** Using a blinded, semi-quantitative scoring system for placental histological sections, the graphs show the score of necrosis and neutrophilic inflammation (polymorphonuclear cells, PMN), in placentas obtained from male fetuses from dams receiving AQP4-IgG (3 mice, 13 sections) or 2B4- IgG (4 mice, 27 sections), as well as placentas obtained from female fetuses from dams receiving AQP4-IgG (3 mice, 15 sections) or 2B4-IgG (2 mice, 12 sections), 48 h after antibody administration. **(C)** *Left*, representative cortical sections (E16.5) of 2B4- and AQP4-males stained with anti-GLAST antibody (red) for radial glia cells (RGCs) and anti-C5b-9 antibody (green), showing the presence of membrane attack complex (MAC) in AQP4-males and 2B4-males. *Right*, Box-and-whisker plots shows the co-localization of C59-b and GLAST signals as total area (** P = 0.012, Mann-Whitney U test) and number (** P = 0.0033, Mann-Whitney U test) of co-localized signals, within stereologically-comparable fetal sections (fixed dimension of sampled cortex, 8.45 x 10^5 μm^2). The cortex was extracted from AQP4- and 2B4-males (n = 6 mice, 2 litters, for each group), at E16.5. Scale bar, 20 μm.

FIGURE S3

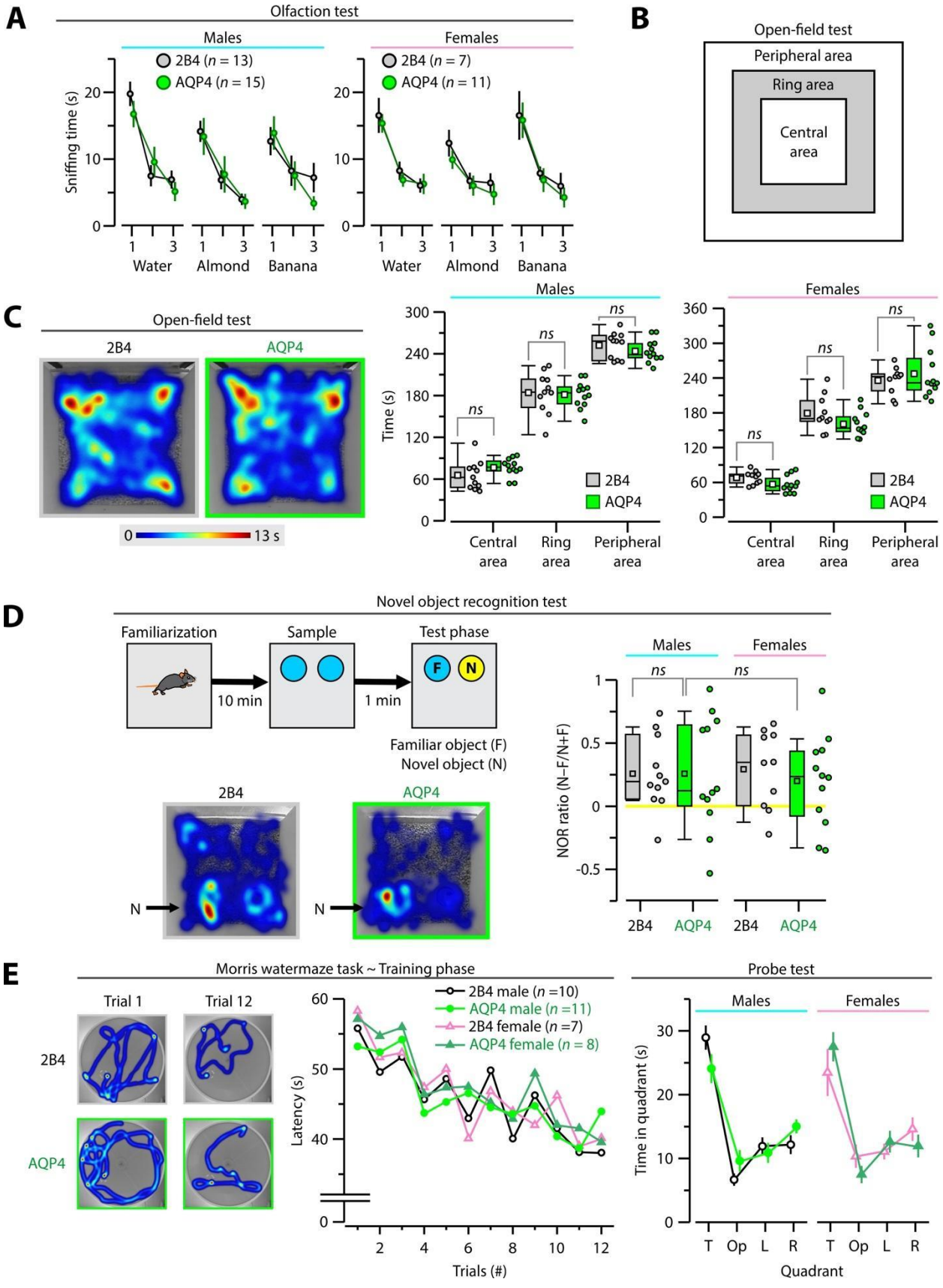
A
Olfaction test
Males
Females
2B4 (n = 13)
AQP4 (n = 15)
2B4 (n = 7)
AQP4 (n = 11)
Sniffing time (s)
Water
Almond
Banana
B
Open-field test
Peripheral area
Ring area
Central area
C
Open-field test
2B4
AQP4
0
13 s
Males
Females
Time (s)
ns
Central area
Ring area
Peripheral area
D
Novel object recognition test
Familiarization
Sample
Test phase
10 min
1 min
F
N
Familiar object (F)
Novel object (N)
NOR ratio (N–F/N+F)
E
Morris watermaze task ~ Training phase
Trial 1
Trial 12
2B4 male (n =10)
AQP4 male (n =11)
2B4 female (n =7)
AQP4 female (n = 8)
Latency (s)
Trials (#)
Probe test
Time in quadrant (s)
T
Op
L
R
Quadrant

Fig. S3: Behavior assessments of AQP4- and 2B4-mice. (A) The olfactory habituation-dishabituation test measures the time the mice spent smelling the water, almond extract, and banana extract of either sex (2B4-males, $n = 13$, vs. AQP4-males, $n = 15$, $F_{(1,26)} = 0.834$, $P = 0.41$; 2B4-females, $n = 7$, vs. AQP4-females, $n = 11$, $F_{(1,16)} = 1.564$, $P = 0.137$; 2-way repeated measures ANOVA of sniffing times with Bonferroni correction). **(B)** Schematic of the regions of the arena that are used for occupancy analysis in the open-field test. **(C)** *Left*, representative heatmaps of mice in the open-field test. *Right*, box-and-whisker plots showing the times the mice spent in the central, ring, and peripheral areas during the open-field test for both 2B4 and AQP4 groups (2B4-males, $n = 11$; AQP4-males, $n = 12$; 2B4-females, $n = 10$; AQP4-females, $n = 12$), of either sex (*ns*, non-significant; males: central, $P = 0.15$, ring, $P = 0.78$, periphery, $P = 0.26$; females: central, $P = 0.05$, ring, $P = 0.12$, periphery, $P = 0.43$; Student *t* test). **(D)** *Top left*, diagram of the NOR task. Each mouse is familiarized to the chamber and then exposed to two identical objects (sample phase, 5 min). Subsequently, for the test phase (5 min), one object is swapped with a novel and dissimilar object. *Bottom left*, representative heatmaps of the test phase show that both 2B4- and AQP4-males have a strong bias towards the novel object (N). *Right*, box-and-whisker plots of NOR ratios (2B4-males, $n = 11$; AQP4-males, $n = 12$; 2B4-females, $n = 10$; AQP4-females, $n = 12$); (2B4- vs. AQP4-males, $P = 0.99$; 2B4- vs. AQP4-females, $P = 0.53$; AQP4-males vs. AQP4-females, $P = 0.73$; Student *t* test). **(E)** *Left*, representative heatmaps for trials 1 and 12 of the Morris watermaze task in which mice learn to find a hidden platform located in the SW quadrant. *Middle*, latency (mean ± SEM) to find the platform across trials in all the groups (2B4-males, $n = 10$; AQP4-males, $n = 11$; 2B4-females, $n = 7$; AQP4-females, $n = 8$), The task acquisition is compared across groups (2B4- vs. AQP4-males, $F_{(1,19)} = 0.34$, $P = 0.735$; 2B4- vs. AQP4-females, $F_{(1,13)} = 0.44$, $P = 0.66$; 2-way repeated measures ANOVA of $\log_{10}$ transformed latencies with Bonferroni correction). *Right*, probe test (performed 24 h after the last training trial, assessing hippocampus-based spatial memory) measures the time in the SW quadrant (target quadrant; 2B4- vs. AQP4-males, $P = 0.11$; 2B4- vs. AQP4-females, $P = 0.37$; Student *t* test),. Abbreviations for quadrants: T, target; Op, opposite; L, left; R, right.

FIGURE S4

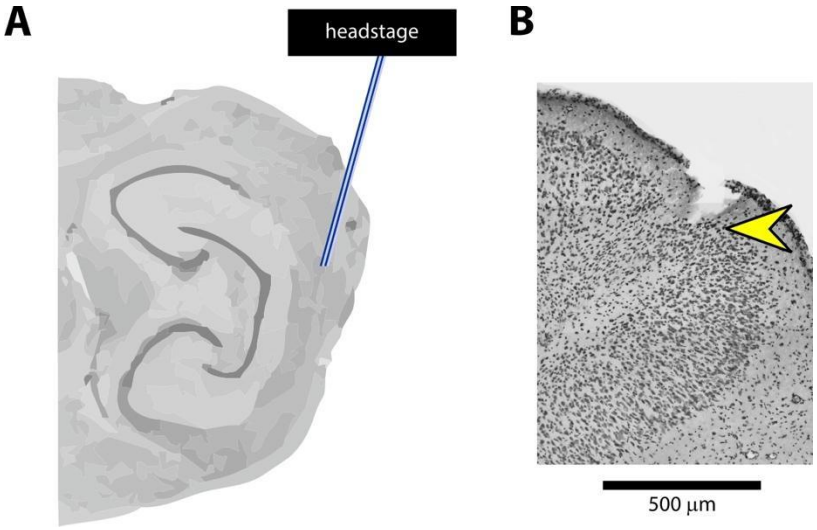

Fig. S4: The location of electrodes implanted in the medial entorhinal cortex. (A) Cartoon of a sagittal brain section (+2.75mm from the midline) showing the medial entorhinal cortex that is targeted by the electrode array (4 tetrodes). **(B)** Representative micrograph of a Nissl-stained section from AQP4 mouse, with the track made by the tetrode bundle (indicated by yellow arrow) as it reached the superficial cortical layers of the medial entorhinal cortex.

FIGURE S5

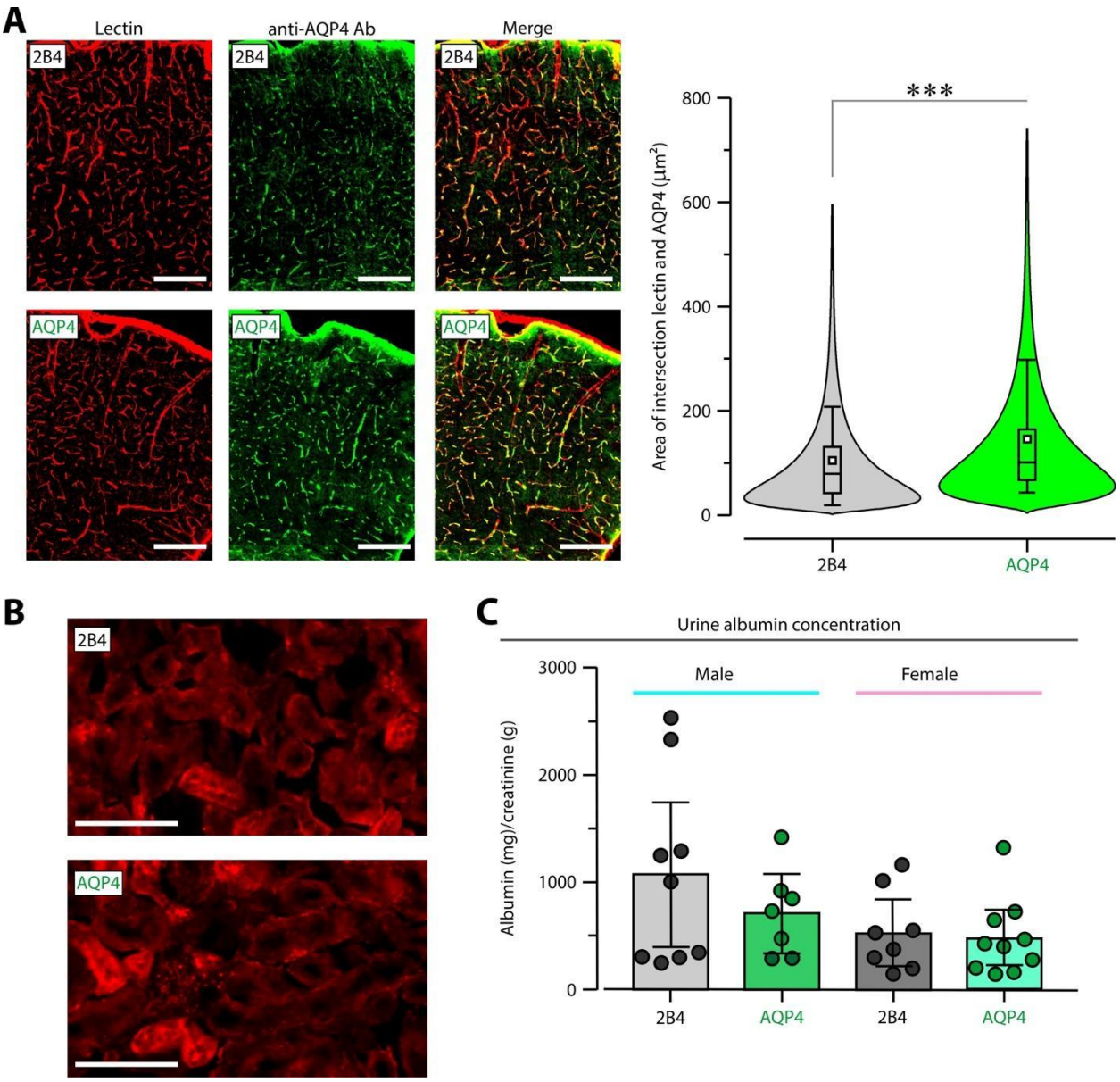

Fig. S5: Characterization of AQP4 expression in brain and kidney of adult AQP4- and 2B4- **mice. (A)** Analysis of AQP4 expression around vessels**.** *Left*, representative cortical sections (bregma –4.04 mm) of adult males stained for blood vessels (lectin, red) and AQP4 (commercial anti-AQP4-antibody, green) in AQP4-and 2B4-males. *Right*, violin plots show that the area of intersection between the lectin and AQP4 signals (μm^2) in AQP4-males (n = 7 mice, 923 counts) compared to 2B4-males (n = 7 mice, 565 counts); *** $P = 1.2x10^{-8}$, Kolmogorov-Smirnov test. We sampled stereologically aligned sections of similar size (6.71×10^5 μm^2) in all animals. Scale bar, 100 µm. **(B)** Analysis of AQP4 expression in the kidney through histology (commercial anti-AQP4-antibody, red signal) in adult AQP4- and 2B4-males (representative image). Scale bar, 20 µm. **(C)**Urinary albumin concentrations between adult AQP4-mice (male, n = 7; female, n = 10) and 2B4-mice (male, n = 9; female, n = 8).

FIGURE S6

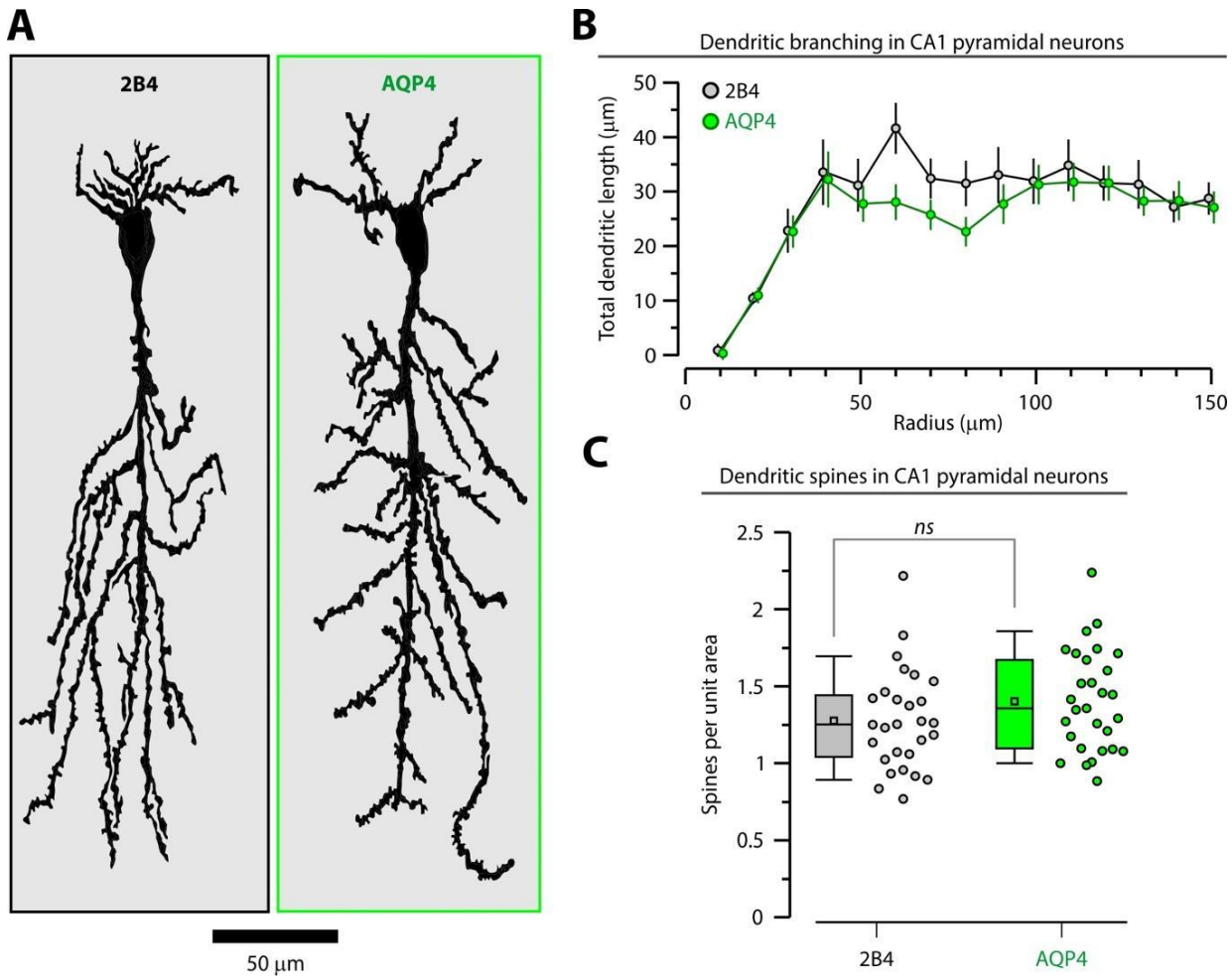

Fig. S6. Histological analysis of CA1 pyramidal cells in the hippocampus. (A) Representative tracings of Golgi-stained CA1 pyramidal neurons. (B) Sholl analysis quantifies the total dendritic length in concentric rings (radii) from the cell body of CA1 neurons and shows the architecture in AQP4 mice (n = 4) and 2B4 mice (n = 4) (*ns*, P = 0.288, ICC = 0.087, mixed linear model). A comparable analysis of the intersections of each dendrite with the concentric rings was performed between the groups (*ns*, P = 0.644, ICC = 0.118, mixed linear model**). (C)** Analysis of density of dendritic spines in CA1 neurons in AQP4 mice (n = 4) and 2B4 mice (n = 4) (*ns*, P = 0.15, Student t test). Abbreviation: ICC, intraclass correlation coefficient.

TABLE S1

Males	**FDG** (*n* = 29) 17 2B4, 12 AQP4			**11C** (*n* = 19) 10 2B4, 9 AQP4			**15O** (*n* = 18) 9 2B4, 9 AQP4		
ROI §	2B4	AQP4	*P*	2B4	AQP4	*P*	2B4	AQP4	*P*
Entorhinal cortex ¶	1.88 ± 0.05	1.87 ± 0.05	0.74	1.81 ± 0.31	2.10 ± 0.22	**0.03**	1.56 ± 0.48	1.97 ± 0.22	**0.03**
Accumbens	2.02 ± 0.08	2.02 ± 0.07	0.84	2.41 ± 0.68	1.97 ± 0.39	0.13	2.52 ± 0.51	2.19 ± 0.34	0.15
Amygdala	1.77 ± 0.13	1.77 ± 0.08	0.87	2.81 ± 0.88	2.48 ± 0.31	0.33	2.30 ± 0.63	1.83 ± 0.26	0.07
Caudate putamen	2.00 ± 0.08	2.06 ± 0.08	0.07	1.97 ± 0.44	1.71 ± 0.38	0.21	2.12 ± 0.34	2.16 ± 0.15	0.77
Globus pallidus	1.99 ± 0.08	2.04 ± 0.06	0.12	2.62 ± 0.97	1.90 ± 0.49	0.08	2.52 ± 0.50	2.20 ± 0.18	0.11
Hippocampus	2.01 ± 0.06	2.04 ± 0.07	0.19	2.62 ± 0.97	2.15 ± 0.27	0.11	1.93 ± 0.28	2.09 ± 0.07	0.12
Hypothalamus	2.09 ± 0.09	2.08 ± 0.12	0.81	1.94 ± 0.25	2.79 ± 0.76	0.58	2.79 ± 0.96	2.00 ± 0.37	0.05
Neocortex ‡	1.60 ± 0.05	1.60 ± 0.06	0.79	1.16 ± 0.35	1.38 ± 0.11	0.11	1.17 ± 0.41	1.44 ± 0.20	0.11
Olfactory-Pyriform	1.33 ± 0.04	1.31 ± 0.06	0.23	1.37 ± 0.27	1.17 ± 0.23	0.12	1.22 ± 0.16	1.18 ± 0.26	0.71
Periaqueductal gray	2.16 ± 0.15	2.23 ± 0.15	0.23	1.88 ± 0.27	1.74 ± 0.34	0.36	2.30 ± 0.15	2.40 ± 0.23	0.32
Thalamus	2.05 ± 0.11	2.14 ± 0.12	0.06	2.18 ± 0.60	1.90 ± 0.39	0.27	2.53 ± 0.24	2.46 ± 0.10	0.48

Females	**FDG** (*n* = 15) 7 2B4, 8 AQP4			**11C** (*n* = 14) 7 2B4, 7 AQP4			**15O** (*n* = 12) 6 2B4, 6 AQP4		
ROI §	2B4	AQP4	*P*	2B4	AQP4	*P*	2B4	AQP4	*P*
Entorhinal cortex ¶	1.87 ± 0.04	1.86 ± 0.05	0.73	1.80 ± 0.19	1.90 ± 0.16	0.31	2.13 ± 0.51	2.06 ± 0.57	0.82
Accumbens	1.96 ± 0.05	2.02 ± 0.05	0.07	2.15 ± 0.28	2.01 ± 0.32	0.45	1.97 ± 0.66	2.05 ± 0.82	0.87
Amygdala	1.75 ± 0.11	1.76 ± 0.06	0.89	2.85 ± 0.30	2.93 ± 0.24	0.60	1.64 ± 0.29	1.44 ± 0.73	0.57
Caudate putamen	2.01 ± 0.07	2.07 ± 0.08	0.22	1.18 ± 0.15	1.26 ± 0.08	0.28	1.89 ± 0.48	1.97 ± 0.56	0.83
Globus pallidus	1.97 ± 0.07	2.06 ± 0.11	0.10	1.57 ± 0.32	1.53 ± 0.21	0.76	2.10 ± 0.35	1.70 ± 0.87	0.36
Hippocampus	1.99 ± 0.05	2.04 ± 0.06	0.16	1.58 ± 0.14	1.74 ± 0.13	0.07	2.02 ± 0.15	2.11 ± 0.04	0.23
Hypothalamus	2.02 ± 0.06	2.08 ± 0.06	0.09	3.44 ± 0.41	3.36 ± 0.45	0.75	1.89 ± 0.21	1.57 ± 0.76	0.38
Neocortex ‡	1.63 ± 0.06	1.57 ± 0.07	0.11	1.59 ± 0.25	1.49 ± 0.11	0.38	1.67 ± 0.24	1.82 ± 0.32	0.41
Olfactory-Pyriform	1.30 ± 0.02	1.27 ± 0.04	0.13	1.27 ± 0.13	1.20 ± 0.09	0.28	1.26 ± 0.15	1.04 ± 0.36	0.24
Periaqueductal gray	2.13 ± 0.14	2.29 ± 0.15	0.07	1.26 ± 0.15	1.28 ± 0.36	0.90	2.19 ± 0.37	1.87 ± 0.36	0.19
Thalamus	2.07 ± 0.10	2.17 ± 0.15	0.19	1.45 ± 0.25	1.42 ± 0.16	0.77	2.17 ± 0.17	1.97 ± 0.71	0.54

Table S1: Micro-PET brain analysis using region-of-interest (ROI) approach. Values are the mean ± SD in anatomically-defined brain regions for [18F]-fluorodeoxyglucose (FDG), [11C]-isoaminobutyric acid (11C), and [15O]-labeled water (15O) injected to AQP4- and 2B4- male mice (upper Table) and AQP4- and 2B4- female mice (lower Table). *P* values were calculated using Student's t test, two-tailed.The brain areas used for the ROI analysis were taken from anatomical atlases (*46*, *47*) Note that the values for the entorhinal cortex in this Table differ slightly from those in Table 1. This is because the exact locations in the brain where the values were obtained differed across techniques. The values in Table 1 were acquired by comparing the groups on a voxel-by-voxel basis, and the significantly-different values corresponded to a cluster of voxels that coincided with the entorhinal cortex. Conversely, in the ROI analysis, the values for each region were taken from locations corresponding to anatomical structures as determined using mouse

brain atlases. Notes: [§] Waxholm Space Atlas (*46*); [¶] Neocortex Atlas (*47*); [‡] neocortex ROI excludes the entorhinal cortex. Pre-processed images have units in mCi (dose corrected). Once brought into SPM, averaged images are ratio normalized by global mean

TABLE S2

Observational screen		**Males** (*n* = 28) 13 2B4, 15 AQP4				**Females** (*n* = 18) 7 2B4, 11 AQP4			
Variable	Range	2B4	AQP4	X^2	*P*	2B4	AQP4	X^2	*P*
V1: coat length	0–4	0 (0/0)	0 (0/0)	0	1	0 (0/0)	0 (0/0)	0	1
V2: hair length	0–3	0 (0/0)	0 (0/0)	0	1	0 (0/0)	0 (0/0)	0	1
V3: hair morphology	0–2	0 (0/0)	0 (0/0)	0	1	0 (0/0)	0 (0/0)	0	1
V4: body position	0–8	5 (5/5)	5 (5/5)	0	0.73	5 (5/5)	5 (4/5)	0.67	0.22
V5: spontaneous activity	0–8	5 (5/5)	5 (5/5)	2.18	0.16	5 (5/6)	5 (4/5)	1.29	0.09
V6: respiratory rate	0–3	2 (2/2)	2 (2/2)	0	1	2 (2/2)	2 (2/2)	0	1
V7: tremor occurrence	0–2	0 (0/0)	0 (0/0)	0	1	0 (0/0)	0 (0/0)	0	1
V8: defecation	0–4	0 (0/1.5)	0 (0/2)	0.74	0.43	0 (0/2)	1 (0/3)	0.23	0.47
V9: urination	0–1	0 (0/0)	0 (0/0)	0	1	0 (0/0)	0 (0/0)	0	1
V10: transfer arousal	0–6	5 (4/5)	5 (4/5)	0	0.81	4 (4/5)	4 (4/5)	0.003	0.95
V11: latency to move	0–32	1 (0.5/2)	2 (2/3)	0.53	0.07	2 (1/3)	2 (2/3)	0.12	0.7
V12: locomotion in arena	0–35	21 (16/24)	17 (15/20)	2.23	0.1	20 (16/22)	19 (16/22)	0.23	0.93
V13: piloerection	0–1	0 (0/0)	0 (0/0)	0	1	0 (0/0)	0 (0/0)	0	1
V14: palpebral closure	0–2	0 (0/0)	0 (0/0)	0	1	0 (0/0)	0 (0/0)	0	1
V15: startle response	0–3	2 (1/2)	1 (1/2)	0	0.48	1 (1/2)	1 (1/2)	0.51	0.5
V16: gait	0–3	0 (0/0)	0 (0/0)	0	1	0 (0/0)	0 (0/0)	0	1
V17: pelvic elevation	0–3	2 (2/2)	2 (2/2)	0	1	2 (2/2)	2 (2/2)	0	1
V18: tail elevation	0–2	1 (1/1)	1 (1/1)	2.49	0.12	1 (1/1)	1 (1/1)	0	1
V19: touch escape	0–3	2 (2/2)	2 (2/2)	1.2	0.05	2 (2/2)	2 (2/3)	2.29	0.42
V20: positional passivity	0–4	0 (0/0)	0 (0/0)	1.87	0.18	0 (0/0)	0 (0/0)	0	1
V21: trunk curl	0–1	1 (1/1)	1 (1/1)	0	1	1 (1/1)	1 (1/1)	0	1
V22: limb grasping	0–1	0 (0/1)	0 (0/1)	0.19	0.68	1 (0/1)	0 (0/1)	0.23	0.66
V23: visual placing	0–4	2 (2/2.5)	2 (2/3)	0.05	0.83	3 (2/3)	2 (2/3)	1.6	0.2
V24: grip strength	0–4	3 (2/3)	2 (2/3)	0	0.41	3 (2/3)	3 (3/3)	0	0.56
V25: body tone	0–2	1 (1/1)	1 (1/1)	0	1	1 (1/1)	1 (1/1)	0	1
V26: pinna reflex	0–2	1 (1/1)	1 (1/1)	0	1	1 (1/1)	1 (1/1)	0	1
V27: corneal reflex	0–3	0 (0/1)	1 (1/1)	0	1	1 (1/1)	1 (1/1)	1.66	0.21
V28: toe pinch	0–4	2 (2/3)	2 (2/2.5)	0.44	0.47	2 (2/2)	3 (2/3)	2.92	0.13
V29: body length (cm)	0–9	8 (7.75/8.5)	8 (8/8.5)	0.19	0.46	8 (8/8.5)	8 (7/8.5)	0.51	0.82
V30: tail length (cm)	0–8	7.5 (7/7.5)	7 (6.5/7.5)	2.16	0.08	7 (7/7.5)	6.5 (6.5/7)	1.17	0.14

V31: lacrimation	0–1	0 (0/0)	0 (0/0)	0	1	0 (0/0)	0 (0/0)	0	1
V32: whisker morphology	0–1	0 (0/0)	0 (0/0)	1.19	0.28	0 (0/0)	0 (0/0)	0	1
V33: provoked biting	0–1	1 (0/1)	1 (0/1)	0	0.98	1 (0/1)	1 (0/1)	0	0.82
V34: salivation	0–2	0 (0/0)	0 (0/0)	0.01	0.92	0 (0/1)	0 (0/1)	0.003	0.95
V35: heart rate	0–2	1 (1/1)	1 (1/1)	0	1	1 (1/1)	1 (1/1)	0	1
V36: abdominal tone	0–2	1 (1/2)	1 (1/2)	0.08	0.79	1 (1/2)	1 (1/2)	0.01	0.92
V37: skin color	0–2	1 (1/1)	1 (1/1)	0	1	1 (1/1)	1 (1/1)	0	1
V38: limb tone	0–4	2 (1.5/2.5)	2 (2/2)	0.04	1	2 (1/3)	2 (2/3)	0.004	0.44
V39: wire maneuver	0–4	0 (0/0.5)	0 (0/1)	0.36	0.45	0 (0/0)	0 (0/1)	0.42	0.49
V40: righting reflex	0–3	0 (0/0)	0 (0/0)	0	1	1 (0/1)	0 (0/0)	0	1
V41: contact righting	0–1	1 (1/1)	1 (1/1)	0	1	1 (0/1)	1 (1/1)	0	0.13
V42: negative geotaxis	0–4	0 (0/0)	0 (0/0)	0	1	0 (0/0)	0 (0/0)	0	1
V43: freeze response	0–1	0 (0/0)	0 (0/0)	0.01	0.92	0 (0/0)	0 (0/1)	1.87	0.2
V44: irritability	0–1	0 (0/0)	0 (0/0)	0	1	0 (0/0)	0 (0/0)	0	1
V45: aggressivity	0–1	0 (0/0)	0 (0/0)	1.87	0.18	0 (0/0)	0 (0/0)	1.43	0.25
V46: vocalizations	0–1	0 (0/1)	0 (0/1)	0.74	0.42	0 (0/1)	0 (0/1)	0.12	0.75
V47: abnormal behavior	0–1	0 (0/0)	0 (0/0)	0.9	0.35	0 (0/0)	0 (0/0)	0.67	0.43
V48: body weight	g	24 (22.2/24.75)	25.2 (19.8/27.3)	1.29	0.22	18.9 (17.8/23)	19.5 (15.1/21.6)	0.23	0.42

Observational screen	**Males** (*n* = 28) 13 2B4, 15 AQP4				**Females** (*n* = 18) 7 2B4, 11 AQP4			
Functions	2B4	AQP4	*t*	*P*	2B4	AQP4	*t*	*P*
F1: muscle and spinal function	28.08 ± 0.75	28.6 ± 0.61	0.54	0.59	26.86 ± 1.01	26.64 ± 0.41	0.2	0.82
F2: spinocerebellar function	21.69 ± 0.61	21.47 ± 0.39	0.31	0.76	20.43 ± 0.61	19.9 ± 0.53	0.64	0.53
F3: sensory function	18.08 ± 0.49	17.6 ± 0.43	0.73	0.47	14.0 ± 0.44	13.73 ± 0.36	0.48	0.64
F4: neuropsychiatric function	24.02 ± 0.27	24.93 ± 0.62	1.36	0.19	23.59 ± 0.62	23.83 ± 0.55	0.29	0.77
F5: autonomic function	5.92 ± 0.37	6.13 ± 0.31	0.44	0.66	6.14 ± 0.55	6.82 ± 0.42	0.97	0.35

Table S2: Observational screen of AQP4- and 2B4-mice. The top section of the table shows the values for the 48 variables as medians (25%/75% interquartile) in the order they were measured during the screen. The nonparametric Mood's median test was used to examine statistical significance. The chi-square (X^2) and probability (*P*) values for each comparison are shown. The bottom section of the table shows the values (mean ± SEM) for the observational functions, and P values across different In this case, Student's *t* test (two-tailed) was used to estimate statistical significance. Mice were 6 week old on average per group.

Datafile S1: Raw data